

Metal Halide Perovskites for Photocatalytic Solar-to-Chemical Energy Conversion

Chunhua Wang

Supervisor:

Prof. Johan Hofkens, KU Leuven

Co-supervisor:

Prof. Maarten B.J. Roeffaers, KU Leuven

Examination committee:

Prof. Jeremy Harvey, KU Leuven, Chairman

Prof. Maarten B.J. Roeffaers, KU Leuven

Prof. Mark Van der Auweraer, KU Leuven

Prof. Rob Ameloot, KU Leuven

Prof. Elke Debroye, KU Leuven

Prof. Giacomo Bergamini, University of Bologna

Dissertation presented in
partial fulfilment of the
requirements for the degree
of Doctor of Science (PhD):
Chemistry

August 2022

© 2022 KU Leuven, Science, Engineering & Technology
Uitgegeven in eigen beheer, Chunhua Wang, Leuven

Alle rechten voorbehouden. Niets uit deze uitgave mag worden vermenigvuldigd en/of openbaar gemaakt worden door middel van druk, fotokopie, microfilm, elektronisch of op welke andere wijze ook zonder voorafgaandelijke schriftelijke toestemming van de uitgever.

All rights reserved. No part of the publication may be reproduced in any form by print, photoprint, microfilm, electronic or any other means without written permission from the publisher.

Acknowledgement

With a strong interest in science and curiosity about the unknown, I have always longed to be able to study in an open and prestigious university worldwide. I still remember that moment when I received the invitation letter from my promoter four years ago; while life is like a journey, all good things come to an end. In the past four years, too many people have supported me in both my scientific research and daily life, therefore here I would like to take the time to express my gratitude to all of them.

First, I would like to thank my supervisor Prof. Johan Hofkens. He gave me this opportunity to join his group, and provided me a free and creative platform to pursue my research which lays a solid ground for me to become an independent researcher. I would then like to thank my co-supervisor Prof. Maarten Roeffaers, all my research work was finished under his direct supervision. He guided me the research details and helped with the manuscript revision, and each story in this doctoral thesis was born with his valuable suggestions and support. Without his help, I could not finish my doctoral thesis. I would also like to thank my assessors Prof. Mark Van der Auweraer and Prof. Rob Ameloot for offering me valuable suggestions in supervisory committee meetings.

I sincerely want to thank Haowei and Bo for their support during my PhD. Besides the academic field, Bo is also like an elder brother, thanks to his deep conversations and his understanding of my circumstances. A special thanks to Masoumeh and Julian for their discussions in experiments and paper publication. I want to thank my Chinese collaborators, Prof. Biao Liu and Dr. Yang Ding, who gave me lots of help and suggestions for my research.

Thanks also go to members of MIP group, Carine, Filip, Eduard, Bjorn, Ann, Rik, Sabina, etc. for their technical and administrative help. I also want to thank other colleagues, Haifeng, Handong, Gang, Li, Yujie, Rui, Yiyue, Hongwen, Yangshan, Giacomo, Lotte, Davy, Michiel, Imran, Michael, Bapi and Tim, and I can't give these people enough gratitude. I sincerely need to thank Handong and Gang, not only for the plenty of help for my lab work, but also for the fun in our daily life after work. I still remember that morning Gang picked me up at the

station when I arrived at Leuven, and you two guys helped me to fit into Leuven quickly. When I encountered depression and frustration during the first year, both of you always stands by my side and give me plenty of support. The company from you guys made the colorful of my life in Leuven, and I will never forget every happy moment and humorous chats we had.

I would also like to thank the China Scholarship Council and KU Leuven for the financial support, and the cheerful working atmosphere. Without financial support and a comfortable research environment, I could not be able to undertake this PhD.

Lastly but most importantly, I must express my heartfelt thanks to my family. I am so appreciative of them for always being there, even though my parents maybe don't always know or understand what I am doing. I am very appreciative of their continued love and support, and all aspects of my life. I could not be here without their support.

All in all, thanks to this precious experience. It means a lot to me and has helped shape me into a better person. Looking forward to the next better journey.

Chunhua Wang

July 2022 in Leuven

Abstract

Energy and environmental issues faced on a global scale are among the biggest challenges in the 21st century. The worldwide industrial growth still relies heavily on fossil fuels as energy sources resulting in the atmospheric emission of vast amounts of hazardous, greenhouse gasses such as SO_x, NO_x and CO₂. As non-renewable natural resources, fossil fuels will also be exhausted one day. A sustainable energy supply to replace fossil fuels and environmental remediation is hence urgently. Among the alternative energy resources, the utilization of solar energy is among the most promising to address future challenges. Solar energy needs to be converted for example into chemicals to make efficient use of it, and this is where photocatalysts play a key role in driving redox reactions utilizing the energy of the absorbed photons. Up to now, various photocatalysts have been reported, including inorganic oxides, nitrides, sulfides, carbon-based materials and metal-coordination compounds. However, most of them generally exhibit modest photocatalytic performance with most of the absorbed photon energy converted into heat. This asks for exploring and developing more efficient photocatalysts.

Metal halide perovskites (MHPs) have recently emerged as promising photocatalysts due to their excellent optoelectronic properties and low-cost solution processing. To date, MHPs-based composites have been applied in various photocatalysis reactions including CO₂ reduction, H₂ evolution, organic synthesis and pollutant degradation. Although much progress has been made, the catalytic performance of pure MHPs can still be improved by (1) minimizing charge carrier recombination, (2) stabilizing the “soft” ionic structure from degradation. To improve the photoactivity, some methods have been explored, such as cocatalyst loading, heterojunction formation by coupling MHP to semiconductor photocatalyst materials, and morphology modification, while the MHP photocatalysis research is in its infancy, and more efficient strategies are still desired for achieving high photocatalytic performance. Besides, many efforts have been made to improve the stability of the MHPs. Currently, the use of low polarity organic solvents can be considered to provide a stable environment for MHP photocatalysis. Nevertheless, even in apolar solvents,

MHP photocatalysts still experience stability issues for example because of the formation of polar products during the photocatalytic processes. Therefore, further practical/industry applications need to overcome these drawbacks.

This PhD thesis has focused on developing efficient strategies to improve the photocatalytic performance and stability of MHP photocatalyst for solar-to-chemical conversion. The main contents are as follows:

In the first part of this dissertation (Chapter 1), the energy crisis and environmental pollution issues we are facing nowadays are analysed, and the potential of photocatalytic processes is highlighted. Next, the photoelectronic properties of MHPs that match the requirement of efficient photocatalysts are outlined. Afterwards, the drawbacks of MHPs hampering their further practical applications are pointed out, and the feasible solutions to address these issues are clarified. Lastly, the current use of MHPs for photocatalytic solar-to-chemical energy conversions, i.e., H₂ evolution, CO₂ reduction, organic transformation, and pollutant degradation, is summarized and discussed.

In the experimental Chapters 2, 3 and 4, the main research results of my PhD work are presented:

In Chapter 2, a Schottky junction by the decoration of the Pd nanocubes (NCs) on the CsPbBr₃ surface was designed to promote the separation of photogenerated electron-hole pairs in CsPbBr₃. This Pd/CsPbBr₃ composite was applied to the Suzuki coupling reaction to study the catalytic performance. Benefiting from the improved charge separation and reduced activation energy, the activity of Pd/CsPbBr₃ is 11.3 folds higher than that of CsPbBr₃. Besides, the temperature-dependent catalytic performance of the photocatalytic Suzuki reaction and the reaction mechanism were investigated.

Chapter 3 expands the concept of Schottky junction by using a phase-engineered crystalline-amorphous core@shell Pd (APd) cube, to further improve the photocatalytic performance of simultaneous H₂ evolution and organic synthesis over Cs₃Bi₂Br₉ photocatalyst. Experimental and theoretical results revealed that the APd offers a robust route to tune both charge transfer kinetics and surface redox dynamics. As a result, the optimized APd/Cs₃Bi₂Br₉ photocatalyst exhibits H₂ and benzaldehyde production rates exceeding 1400 μmol h⁻¹ g⁻¹.

To simultaneously enhance the photocatalytic activity and stability of MHP photocatalysts, in Chapter 4, a planar heterojunction solar photocatalytic cell ($\text{NiO}_x/\text{CsPbBr}_3/\text{TiO}_2$) was constructed, where NiO_x and TiO_2 serve as charge extraction materials and MHP protecting layers. When applied to selective benzyl alcohol oxidation reaction, this solar photocatalytic cell presents a 7-time higher photocatalytic activity and enhanced stability (> 90 h) as compared to pure CsPbBr_3 . Besides, it is found that trace amounts of water could enhance the MHP photocatalyst performance. This improvement was attributed to the water-induced structural reorganization of CsPbBr_3 , resulting in the reduced charge effective mass and enhanced charge separation.

Finally, Chapter 5 describes the conclusion and outlook. First of all, the main results of this thesis, i.e., the construction of a Schottky junction by coupling MHP with Pd and phase engineered crystalline-amorphous Pd cocatalyst to boost the photocatalytic conversion efficiency of MHPs, and the construction of a stable solar photocatalyst cell to boost the photoactivity and stability of MHP photocatalysts, were summarized. Afterwards, the challenges of the MHP-based photocatalysis applications, i.e., the modest photocatalytic activity and the stability issues of MHPs, are pointed out, and some strategies that can be used to solve these problems are offered.

Through this dissertation, useful approaches for enhancing both photocatalytic activity and stability of MHPs are developed, and the great promise of the MHP-based photocatalyst materials for solar-to-chemical conversion is demonstrated and expanded. Overall, this thesis opens a window for efficient solar-to-fuel conversion using MHP-based photocatalysts.

Samenvatting

Energie- en milieuproblemen waarmee we wereldwijd worden geconfronteerd, behoren tot de grootste uitdagingen van de 21e eeuw. De wereldwijde industriële groei is nog steeds sterk afhankelijk van fossiele brandstoffen als energiebron, wat resulteert in de atmosferische uitstoot van enorme hoeveelheden gevaarlijke broeikasgassen zoals SO_x , NO_x en CO_2 . Als niet-hernieuwbare natuurlijke hulpbronnen zullen fossiele brandstoffen op een dag ook uitgeput raken. Een duurzame energievoorziening ter vervanging van fossiele brandstoffen en de milieusanering zijn dan ook noodzakelijk. Zonne-energie is één van de meest veelbelovende alternatieve energiebronnen om deze toekomstige uitdaging aan te gaan. Zonne-energie kan omgezet worden in chemicaliën, dit is waar fotokatalysatoren een sleutelrol spelen door middel van het aansturen van redoxreacties die gebruikmaken van de energie van geabsorbeerde fotonen. Verschillende fotokatalysatoren zijn tot op heden gerapporteerd, zoals anorganische oxiden, nitride, sulfiden, koolstof gebaseerde materialen en metaalcoördinatieverbindingen. De meeste van deze materialen vertonen over het algemeen gelimiteerde fotokatalytische activiteit, waarbij het grootste deel van de geabsorbeerde fotonenergie wordt omgezet in warmte. Dit vraagt voor de ontwikkeling van efficiëntere fotokatalysatoren.

Metaalhalogenideperovskieten (MHP's) zijn onlangs ontdekt als veelbelovende fotokatalysatoren vanwege hun vele voordelen, zoals een hoge absorptiecoëfficiënt, lage excitonbindingsenergie, lange dragerdiffusielengte en goedkope oplossingsverwerking. Tot op heden zijn op MHP's gebaseerde composiet fotokatalysatoren toegepast in verschillende reacties, zoals CO_2 -reductie, H_2 -evolutie, organische synthese en degradatie van verontreinigende stoffen. Hoewel er veel vooruitgang is geboekt, kunnen de fotokatalytische prestaties van pure MHP's nog steeds worden verbeterd door (1) de recombinatie van ladingsdragers te minimaliseren, (2) de "zachte" ionische structuur te stabiliseren tegen degradatie. Enkele methoden zijn onderzocht om de fotoactiviteit te verbeteren, zoals het impregneren met cokatalysatoren, heterojunctievorming door MHP te koppelen aan halfgeleider fotokatalysatormaterialen en morfologiemodificatie. Het onderzoek naar MHP-

fotokatalyse staat echter nog in zijn kinderschoenen en efficiëntere strategieën zijn noodzakelijk om betere fotokatalytische prestaties te bereiken. Daarnaast zijn er veel inspanningen geleverd om de stabiliteit van de MHP's te verbeteren. Organische solventen met een lage polariteit kunnen worden beschouwd als een stabiele omgeving voor MHP-fotokatalyse. Desalniettemin ervaren MHP-fotokatalysatoren zelfs in apolaire oplosmiddelen nog steeds stabiliteitsproblemen, bijvoorbeeld door de vorming van polaire producten tijdens de fotokatalytische processen. Daarom dienen deze uitdagingen eerst aangepakt te worden voordat verdere praktische toepassingen kunnen uitgewerkt worden.

Dit proefschrift richt zich op het verbeteren van de fotokatalytische prestaties en stabiliteit van MHP-fotokatalysatoren voor omzetting van zonne-energie naar chemische energie. De belangrijkste inhoud is als volgt:

In het eerste deel van dit proefschrift (hoofdstuk 1) worden de energiecrisis en milieuvuulingsproblemen waarmee we tegenwoordig worden geconfronteerd geanalyseerd, en wordt het potentieel van fotokatalytische processen toegelicht. Vervolgens worden de optische en elektronische eigenschappen van MHP's die voldoen aan de vereisten van efficiënte fotokatalysatoren geschetst. Daarna wordt gewezen op de nadelen van MHP's die hun verdere praktische toepassingen in de weg staan en worden enkele haalbare oplossingen om deze problemen aan te pakken verduidelijkt. Ten slotte wordt het huidige gebruik van MHP's voor fotokatalytische omzettingen van zonne-naar-chemische energie, d.w.z. H₂-evolutie, CO₂-reductie, organische synthese en afbraak van verontreinigende stoffen, samengevat en besproken. In de experimentele hoofdstukken 2, 3 en 4 worden de belangrijkste onderzoeksresultaten van dit proefschrift gepresenteerd:

In hoofdstuk 2 werd een Schottky-junctie ontworpen door decoratie van Pd nanocubes (NCs) op het CsPbBr₃-oppervlak om de scheiding van fotogegenererde elektronen en gaten in CsPbBr₃ te bevorderen. Deze Pd/CsPbBr₃-compositie werd toegepast op de Suzuki-koppelingsreactie om de katalytische prestaties te bestuderen. Dankzij de verbeterde ladingsscheiding en verminderde activeringsenergie is de activiteit van Pd/CsPbBr₃ 11.3 keer hoger dan die van zuiver CsPbBr₃. Daarnaast werden de

temperatuurafhankelijke prestatie van de fotokatalytische Suzuki-reactie en het reactiemechanisme onderzocht.

Hoofdstuk 3 breidt het concept van de Schottky-junctie uit door gebruik te maken van eenkristallijn-amorfe kern@shell Pd (APd) kubus gedecoreerde Cs₃Bi₂Br₉ fotokatalysator, om de fotokatalytische prestatie van de H₂-evolutie reactie in combinatie met de organische synthese van kostbare chemicaliën verder te verbeteren. Experimentele en theoretische resultaten lieten zien dat APd een robuuste route biedt om zowel de ladingsoverdrachtskinetiek als de oppervlakte-redoxdynamiek te verbeteren. Dit resulteert in een H₂- en benzaldehydeproductiesnelheden van meer dan 1400 μmol h⁻¹ g⁻¹ voor de geoptimaliseerde APd/Cs₃Bi₂Br₉-fotokatalysator.

Om zowel de fotoactiviteit alsook de stabiliteit van MHP-fotokatalysatoren te verbeteren, werd in Hoofdstuk 4 een vlakke heterojunctie (NiO_x/CsPbBr₃/TiO₂) geconstrueerd, waarbij NiO_x en TiO₂ niet alleen dienen als ladingsdrager-transportlagen, maar ook als beschermplagen voor de MHP. Toegepast op de selectieve fotokatalytische oxidatie van benzylalcohol, vertoont dit systeem een 7-voudige verbetering van de fotoactiviteit en verbeterde stabiliteit gedurende meer dan 90 uur in vergelijking met zuiver CsPbBr₃. Bovendien werd vastgesteld dat sporen van water de prestaties van de MHP-fotokatalysator kan verbeteren, dit werd toegeschreven aan de door water geïnduceerde structurele reorganisatie van MHP, wat leidde tot een verminderde effectieve massa van de lading en een verbeterde ladings scheiding.

Tot slot beschrijft hoofdstuk 5 de conclusies en vooruitzichten. Allereerst zijn de belangrijkste resultaten van dit proefschrift samengevat. Dit zijn de constructie van een Schottky-junctie door MHP te koppelen met Pd nanobuisjes en fasegemanipuleerde kristallijn-amorfe Pd-cokatalysator om de fotokatalytische prestatie van MHP's te verbeteren, en de constructie van een stabiele zonne-fotokatalysatorcel om gelijktijdig de fotoactiviteit en stabiliteit van MHP-fotokatalysatoren te verhogen. Daarna wordt gewezen op de uitdagingen voor de toepassing van de op MHP gebaseerde fotokatalysatoren. Deze zijn de bescheiden fotokatalytische activiteit van pure MHP-fotokatalysatoren en de stabiliteitsproblemen van MHP's. Ook worden er enkele

strategieën aangeboden die onderzocht kunnen worden om deze problemen op te lossen.

Door middel van dit proefschrift worden bruikbare methodes voor het verbeteren van de fotokatalytische activiteit en stabiliteit van MHP's ontwikkeld, en wordt het grote potentieel van de op MHP gebaseerde fotokatalysatoren voor de conversie van zonne-energie naar chemische energie aangetoond en uitgebreid. Over het algemeen effent dit proefschrift het pad voor een efficiënte conversie van zonne-energie naar brandstof met behulp van op MHP gebaseerde fotokatalysatoren.

List of symbols and abbreviations

APd	Amorphous palladium
BA	Benzyl alcohol
BAD	Benzaldehyde
CB	Conduction band
CO ₂	Carbon dioxide
CsPbBr ₃	Cesium lead bromide
DMSO	Dimethyl sulfoxide
DFT	Density functional theory
DRS	UV-vis diffuse reflectance spectra
E _g	Bandgap energy
eV	Electron volt
ESR	Electron spin resonance
EDS	Energy-dispersive X-ray spectroscopy
EIS	Electrochemical impedance spectroscopy
FA	Formamidinium (HC(NH ₂) ₂)
g-C ₃ N ₄	Graphitic carbon nitride
GC	Gas chromatography
GC-MS	Gas chromatography-mass spectrometry
H ₂	Hydrogen
MA	Methylammonium (CH ₃ NH ₃)
MHP	Metal halide perovskite
NCs	Nanocubes
nm	Nanometre
$\cdot\text{O}_2^-$	Superoxide free radical
PL	Photoluminescence
SEM	Scanning electron microscope
TCD	Thermal conductivity detector
TEM	Transmission electron microscopy
HRTEM	High resolution TEM micrograph
TON	Turnover number
TOF	Turnover frequency

TEOA	Triethanolamine
UV-Vis	Ultraviolet-Visible
VB	Valence band
XRD	X-ray diffraction
XPS	X-ray photoelectron spectroscopy

Table of Contents

Acknowledgement.....	I
Abstract.....	III
Samenvatting.....	VI
List of symbols and abbreviations.....	X
Chapter 1. General introduction.....	1
1.1 Photocatalysis concept.....	2
1.2 Metal halide perovskites (MHPs).....	4
1.2.1 Crystal structure.....	4
1.2.2 Electronic and optical properties.....	5
1.2.3 Stability.....	6
1.3 Approaches for photocatalyst modification.....	8
1.3.1 Loading cocatalysts.....	8
1.3.2 Heterojunction structure.....	10
1.3.3 Defect engineering.....	12
1.4 Applications of MHPs in photocatalysis.....	14
1.4.1 H ₂ evolution.....	15
1.4.2 CO ₂ reduction.....	19
1.4.3 Organic synthesis.....	21
1.4.4 Pollutant degradation.....	24
1.5 Motivation and objectives.....	28
1.5.1 Motivation.....	28
1.5.2 Research objectives.....	29
1.6 References.....	29
Chapter 2. Photothermal Suzuki coupling over a metal halide perovskite/Pd nanocube composite catalyst.....	41
2.1 Introduction.....	43

2.2 Results and discussion	44
2.3 Conclusions	55
2.4 Experimental section.....	56
2.5 References.....	60
2.6 Appendix to Chapter 2	65
Chapter 3. Simultaneous photocatalytic H ₂ generation and organic synthesis over crystalline-amorphous Pd nanocube decorated Cs ₃ Bi ₂ Br ₉	94
3.1 Introduction	96
3.2 Results and discussion	97
3.3 Conclusions	102
3.4 References.....	103
3.5 Appendix to Chapter 3	105
Chapter 4. Planar heterojunction boosts solar-driven photocatalytic performance and stability of halide perovskite solar photocatalyst cell	126
4.1 Introduction	128
4.2 Experimental section.....	129
4.3 Results and discussion	134
4.4 Conclusions	148
4.5 References.....	149
4.6 Appendix to Chapter 4	154
Chapter 5. Conclusion and outlook.....	169
Safety Aspects	172
List of publications	173

Chapter 1. General introduction

The rapid industrialization and growth in global activity are the driving forces for the increasing energy demand. For instance, global energy utilization is predicted to increase by around 35 % by 2050, which is almost double compared to 2000.¹ Until now, economic prosperity and development heavily rely on non-renewable fossil fuels. These fossil fuels are not infinitely available and will be exhausted one day. Furthermore, the combustion of fossil fuels results in the atmospheric emission of greenhouse and hazardous gases such as CO₂, SO₂, and NO_x.² Thus, there is an urgent need for alternative energy sources and methods to decrease environmental pollution and our dependency on fossil fuels.

The establishment of eco-friendly and sustainable energy resources is a good starting point to fulfill this goal. So far, many alternative approaches such as wind power, hydroelectric power, geothermal energy biomass power and solar energy have been developed. Solar energy, which abundantly reaches the earth's surface every day, is a clean and sustainable source of energy. The energy of the sunlight that reaches the earth in 1 h is estimated to be equal to the energy needed for humans for 1 year ($\sim 4.6 \times 10^{20}$ joules).³ The utilization of sunlight is therefore considered one of the most promising green energy strategies.

Among the various solar technologies, photocatalysis – a process that utilizes the energy of photons to accelerate/initiate a chemical reaction, has shown great potential in solar-to-chemical conversion. In 1972, Fujishima and coworkers showed TiO₂ as a photo(electro)catalyst to split water into H₂ and O₂.⁴ From then on, photocatalysis has attracted increasing attention.

Contributions

This literature overview was written by Chunhua Wang with critical input from Bo Weng, Maarten B.J. Roeffaers, and Johan Hofkens.

1.1 Photocatalysis concept

Photocatalysis is the acceleration of chemical reactions by light. When using sunlight, solar energy is converted into chemical fuels. In general, photocatalysis is particularly interesting for green and sustainable chemistry since it combines the efficiency of catalysis with the usage of sunlight. Following the first work reported by Fujishima et al.,⁴ photocatalytic applications have attracted growing attention. The photocatalyst plays a key role in the catalytic reaction process since the chemical reactions occur on the catalysts surface, and thus the photocatalyst directly determines the photocatalytic performance of the reaction. Two types of photocatalysis can be identified depending on the physical form of the catalyst and the reaction medium: homogeneous and heterogeneous photocatalysis.⁵ In homogeneous photocatalysis both the photocatalyst and reactant are in the same phase. If they are not in the same phase, the photocatalytic reactions are categorized as heterogeneous photocatalysis. The latter is often a solid material in contact with a reaction medium in gas- or liquid-phase. Homogeneous catalytic systems generally suffer from the difficulty in separation and recovery of catalysts from the reaction mixtures. This makes the heterogeneous alternative much more interesting for industrial applications.⁶ Therefore, much attention has been paid to the heterogeneous photocatalytic reactions. The work in this thesis is focused on heterogeneous photocatalysis.

Semiconductor-based heterogeneous photocatalytic reactions take place by utilizing light as an energy source and a semiconductor material as the catalyst. The basic principle of this kind of photocatalytic process starts at the semiconductor electronic band structure. The bandgap is the energy distance between the conduction band (CB) and the valence band (VB). Generally, semiconductor-based photocatalysis involves three major steps:⁷ (1) light harvesting and photoinduced electron excitation, (2) charge separation and migration from bulk to surface, and (3) photoredox reactions that take place at the surface of the photocatalyst. Taking the widely used semiconductor TiO_2 as an example, the general photocatalytic process is shown in Figure 1a.⁸ Firstly, under light illumination, the photocatalyst (TiO_2) absorbs photons with an energy larger than the bandgap. This causes the excitation of electrons from

the VB to the CB generating holes in the VB. Secondly, the photogenerated charge carriers migrate to the surface. Meanwhile, a part of the generated electrons in the CB will move back to VB and recombine with the holes. Finally, the separated charge carriers react with the adsorbed reactant molecules. The electrons are involved in reduction reactions and holes participate in oxidation reactions.

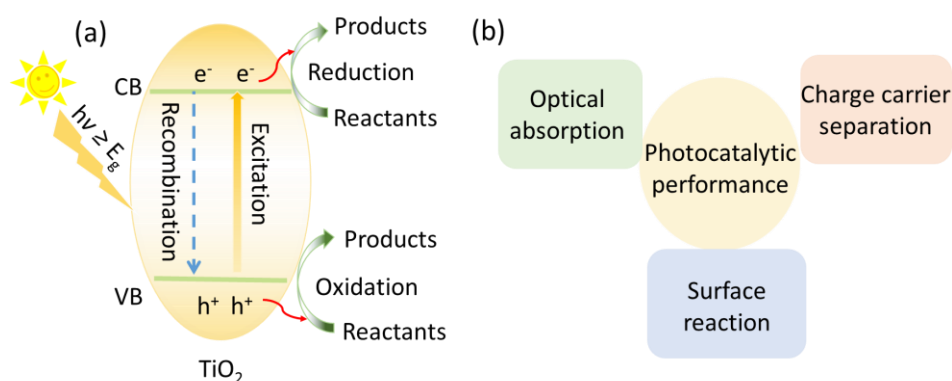


Figure 1. (a) Schematic illustration of a semiconductor-based (TiO₂) photocatalytic process. (b) Three key kinetic parameters affecting the catalytic performance of semiconductor photocatalysts.

For photocatalysis, the catalytic reaction efficiency is mainly determined by three kinetic parameters:^{9, 10} optical absorption, the separation of photoinduced electron-hole pairs, and surface reaction (Figure 1b).

- Firstly, the light absorption of a photocatalyst is associated with its bandgap and absorption coefficient. Generally, a smaller bandgap results in a broader light absorption range. While in a photocatalytic reaction, a small bandgap leads to a limited redox ability of the photocatalyst.¹¹ Therefore, balancing the bandgap, the absorption coefficient and the reaction is very important. The absorption coefficient of the material expresses the likelihood of a photon with specific energy to be absorbed.
- Secondly, the efficient separation of photogenerated charge carriers is necessary to make sure the generated electrons and holes can effectively participate in redox reactions.¹² The lower exciton binding energy and longer charge carrier diffusion length of semiconductor materials are key to achieving this.

- Thirdly, since the redox reactions take place at the surface of the photocatalysts, efficient migration of electrons and holes from the bulk to the catalysts surface to participate in chemical reactions is very important.⁷ Besides charge carriers reaching the surface, reactant absorption and product desorption also play an important role.

It is well known that these three key factors influencing photocatalytic performance are highly related to the photocatalyst itself. So far, many studies have been carried out to develop various photocatalysts.¹³⁻¹⁶ Unfortunately, the conversion efficiency of most photocatalysts is generally unsatisfactory mainly due to limited light utilization and/or fast charge recombination. Future practical applications need to address these challenges.

Inspired by the great advances in solar cells, metal halide perovskites (MHPs) have recently emerged as promising photocatalysts due to their excellent optical and electronic properties.^{2,11,12} The following section first gives a brief introduction to MHP materials. Secondly, some strategies that can be used to improve the catalytic performance of the photocatalyst are introduced. Thirdly, the recent applications of MHPs in photocatalysis including H₂ evolution, CO₂ reduction, organic transformation, and pollutant degradation are summarized and discussed. Finally, the motivation and objectives of this thesis are summarized.

1.2 Metal halide perovskites (MHPs)

1.2.1 Crystal structure

Metal Halide perovskites (MHPs) are a group of semiconductor materials with a similar crystal structure as the natural mineral CaTiO₃ – the earliest perovskite material brought to light by Gustav Rose 1839 while named after Russian mineralogist Lev Perovski, with the chemical formula ABX₃.¹⁷ In this formula A is a monovalent cation (CH₃NH₃⁺, MA⁺; CH(NH₂)₂⁺, FA⁺; Cs⁺), B is a bivalent metal cation (Pb²⁺, Sn²⁺) and X is a halide anion (I⁻, Br⁻ and Cl⁻)¹⁸. Typically, A occupies a corner of a unit cell, B sits in a body-centered position, and X occupies a face-centered position, with a corner-sharing [BX₆]⁴⁻ octahedra,¹⁹ as exhibited in Figure 2.

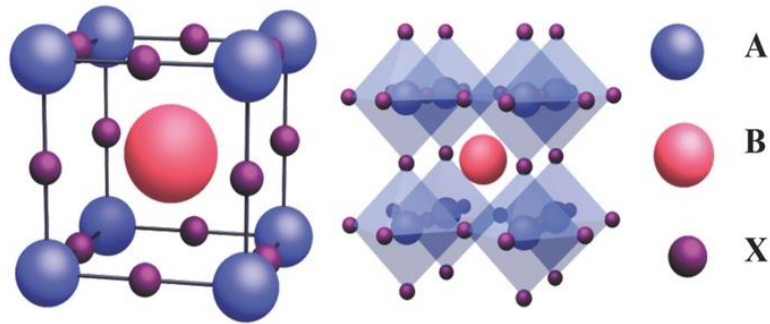


Figure. 2 Unit cell crystal structure of MHPs (left) and the extended crystalline structure connected by corner-sharing $[BX_6]^{4-}$ octahedra (right).¹⁹ Reproduced with permission from ref 19. Copyright 2017 Wiley.

The structure of MHPs is associated with BX_6 octahedra and A cation, and their crystal structures can be tuned by regulating its octahedral factor (μ) (Equation 1), and long-standing Goldschmidt's tolerance factor τ (Equation 2):²⁰

$$\mu = \frac{r_B}{r_X} \quad (1)$$

$$\tau = \mu^{-1} - n_A \left[n_A - \frac{\frac{r_A}{r_B}}{\ln\left(\frac{r_A}{r_B}\right)} \right] \quad (2)$$

where r_A , r_B and r_X stand for the radius of A, B and X ions, respectively,^{20,21} n_A is the varied oxidation state of A. For all-inorganic MHPs involving alkali A^+ cations, $n_A = 1$. Typically, τ is used to assess the degrees of size matching between the A cation and BX_6 octahedra. The formation of the perovskite structure is reported to require $\tau < 0.418$. To meet the requirement of forming the octahedra, the radius of r_A needs to be larger than $0.442 r_X$, i.e., $\mu > 0.442$.²⁰

22

1.2.2 Electronic and optical properties

The excellent optoelectronic performance of MHPs is mainly attributed to their distinctive electronic properties.² Through investigation of the electronic structure such as band structure and density of states, their photoelectric properties including light absorption coefficient, exciton binding energy, carrier mobility, effective mass, and charge recombination rate, can be analyzed.²³

Theoretical simulations such as density functional theory (DFT) have been widely employed to calculate the band structure of halide perovskites.^{23, 24} The

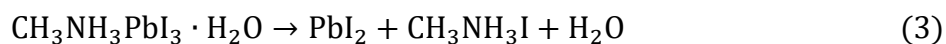
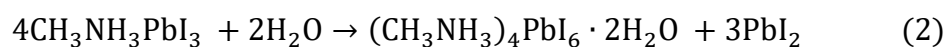
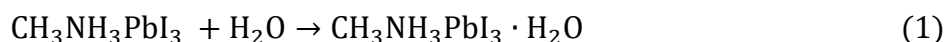
electronic structures of MHPs with different halides possess similar features. For instance, in typical 3D CsPbX₃ MHPs, the VB is constituted by the antibonding hybridized 6s orbitals of Pb and X np orbitals of the halides (n= 5, 4, and 3 for I, Br, and Cl, respectively), and the CB is mainly composed of Pb 6p orbitals.^{24, 25} The band structures are rarely dependent on X composition, while X ions affect the bandgap (E_g).²⁵ The excitation and charge carrier recombination are mainly confined within the PbX₆ octahedra.²⁴

Compared to other materials, MHPs possess excellent optical properties including high absorption coefficient (> 10⁵ cm⁻¹), small exciton binding energy (E_b < k_BT for iodide-based family) and tunable bandgap (1.24-3.55 eV).^{18, 26} The optical bandgap is one of the most important photoelectronic properties since it directly determines the absorbance range. The bandgap of MHPs can be tuned over the visible light region, which meets the requirements regarding catalysis. Taking CsPbX₃ MHP as an example, when changing X site halide from I to Br and Cl, the energy levels of the X np6 orbitals decrease, shifting the CB position toward more positive potentials, thus yielding different bandgaps.²⁷ Specifically, CsPbI₃ with cubic phase has a bandgap (E_g) of 1.73 eV, a wider was found for CsPbBr₃ (2.3 eV) and CsPbCl₃ (2.99 eV). Besides, the E_g is tunable by mixing different halides. For example, CsPbI_xBr_{3-x} like CsPbI₂Br and CsPbIBr₂ has a E_g of 1.92 eV and 2.05 eV, respectively.²¹

1.2.3 Stability

The stability of photocatalytic materials is another key factor affecting their applicability.^{2,12} The structural and electronic properties of MHPs can change dramatically upon air exposure (moisture, O₂) and UV illumination.¹² For instance, MHPs easily degrade into PbX₂ components, MA or FA and halide ions in contact with water due to the fragile organic moieties (MA⁺, FA⁺).^{18, 20, 28, 29} Over the past decade, the degradation mechanisms of MHPs have been widely explored using in-situ grazing incidence XRD, transient absorption spectroscopy techniques and ab initio molecular dynamics simulations. These investigations showed that the absorbed H₂O quickly penetrates the inner structure of MHPs and reacts with BX₆ octahedra, resulting in the formation of monohydrate and dihydrate compounds. Taking CH₃NH₃PbI₃ as an example,

its degradation processes when exposed to water can be expressed by the following equations:¹²



Furthermore, the stability of MHPs is also weak in the presence of oxygen and light.¹² Through UV-vis and XRD characterizations, Hitoshi et al. reported that $\text{CH}_3\text{NH}_3\text{PbI}_3$ decomposes into PbI_2 under light exposure for 12 h.³⁰ The degradation mechanism was further investigated by Haque et al.³¹ They showed that this photoinduced degradation process is associated with iodide vacancies, in which O_2 will be inserted into the crystal lattice of MHPs. The molecular O_2 will react with photogenerated electrons at the site of I vacancies to form reactive superoxide species. Then, the superoxide radicals interact with MA and produce the decomposition products H_2O , CH_3NH_2 , PbI_2 , and I_2 .³¹ Furthermore, light irradiation also influences the bandgap of MHPs.³² The light soaking alters the position of the CB and VB of MHPs and thus changes the bandgap. McGehee et al. symmetrically investigated this change using $\text{MAPbBr}_{x-1}\text{I}_{3-x}$ MHPs as a model MHP material.³² Under light irradiation for a few minutes, a red-shift in PL peak and an increase in PL intensity of the $\text{MAPbBr}_{x-1}\text{I}_{3-x}$ film were observed.

The instability issues of MHP photocatalysts have recently been highlighted by Roeffaers and coworkers in a review.¹² Overall, the stability of MHPs originates from their crystal structures. Owing to the ionic nature of MHPs, they generally have a “soft” structure. This causes the fast degradation of MHPs under photocatalytic conditions. Given that, several proven or potential strategies were suggested to stabilize the MHP photocatalysts, these include replacing organic cations (MA^+ and FA^+) with inorganic components (Cs^+), using saturated haloacid HX ($\text{X}=\text{I}, \text{Br}$) solutions, low-polarity solvents (acetonitrile, toluene, ethyl acetate, trifluorotoluene, isopropanol, etc.), adding drying agents (such as Na_2SO_4), encapsulation or surface capping the MHP, etc. One of the targets of this thesis is to develop efficient approaches to improve the stability of MHP photocatalysts, which will be discussed in detail in Chapter 4.

1.3 Approaches for photocatalyst modification

As stated above, the typical photocatalytic reaction process consists of three main steps: (1) the photocatalyst absorbs light to produce photogenerated electron-hole pairs; (2) the separation and transfer of the generated charge carriers; (3) the reduction and oxidation reactions on the photocatalysts surface.⁷ For most pure photocatalysts, the solar-to-chemical conversion efficiency is generally modest, originating from inefficient charge separation.² To boost the photocatalytic activity, effective strategies are required to minimize the charge recombination.¹² So far, enormous efforts have been made by loading cocatalysts, construction a heterojunction, and defect engineering.² In this section, these approaches are summarized and discussed.

1.3.1 Loading cocatalysts

The loading of cocatalyst on the photocatalysts surface has been shown to efficiently improve the photocatalytic performance.^{2,12} Taking metal cocatalyst as an example, generally, when metal nanoparticles are in close contact with a semiconductor material, charge redistribution between the metal and semiconductor will occur because of their different Fermi level (E_F) positions (Figure 3a), which leads to band bending of the semiconductor. Electrons transfer from semiconductor to metal until the E_F of the metal and the semiconductor reaches equilibrium, resulting in the formation of a Schottky barrier (Figure 3b).³³ Under light irradiation, the photogenerated charges are influenced by this band bending. Specifically, electrons in the semiconductor are transferred to the metal cocatalyst driven by the built-in electric field at the interface, and the as-formed Schottky barrier at the interface will block the backflow of electrons from the metal to semiconductor (Figure 3c), leading to efficient separation of photogenerated charge carriers. Besides, the cocatalyst can also offer more reactive sites for redox reactions. Until now, noble metals such as Au,³⁴ Pd,³⁵ Pt,³⁶ Ag,³⁷ Ru,³⁸ and Rh,³⁹ noble metal oxides like RuO₂⁴⁰ and IrO₂,⁴¹ and noble-metal-free cocatalysts such as Ni complexes,^{42, 43} hydrogenase mimics,^{44, 45} carbon nanotubes,⁴⁶ graphene nanosheets,⁴⁷ B₂O_{3-x}N_x,⁴⁸ and MoS₂,⁴⁹⁻⁵¹ have been explored as cocatalysts for photocatalysis. An example of an MHP-metal cocatalyst composite for the

photocatalytic degradation of dyes is presented in Figure 3d.² The metal cocatalyst (Pt or Au) serves as an electron reservoir to capture the photoinduced electrons, leading to a dramatical enhancement in the production rate of the MHP photocatalyst. In this thesis, coupling MHP with metal cocatalyst (Pd) was adopted to promote charge separation, and thus enhancing solar-to-chemical conversion efficiency of MHP photocatalyst (Chapter 2).

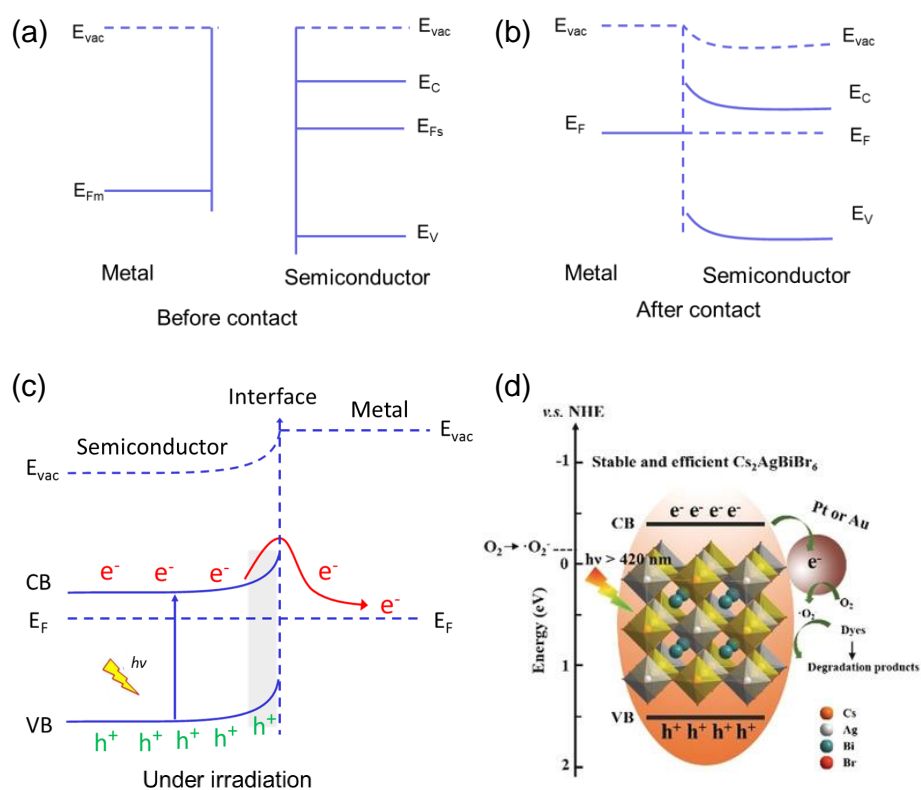


Figure 3. Schematic band diagram of a n-type semiconductor/metal composite (a) before and (b) after contact and (c) the electron transfer within a Schottky junction under light irradiation, where E_F , E_{vac} , represent Fermi level and vacuum level, respectively, and CB, VB, e^- , and h^+ stand for conduction band, valence band, electron and hole, respectively. (d) An example of photocatalytic degradation of dyes using an MHP/metal composite.² Reproduced with permission from ref 2. Copyright 2020 Elsevier.

Cocatalysts have various functions: (1) promote the separation and migration of photogenerated electron-hole pairs.^{7, 52} (2) offer more active sites for the targeted surface photocatalytic reaction. (3) plasmon metals cocatalyst (Au, Ag, Cu) can improve the light absorption originating from the localized surface plasmon resonance effect.^{7, 52, 53} (4) extend the stability of the photocatalysts

through the consumption of electrons and/or holes.^{7, 52} (5) lower the overpotential of H₂ evolution reactions.⁷ (6) enhance the selectivity of CO₂ reduction.⁵³

On the other hand, tuning the crystallinity of cocatalysts has been demonstrated to improve the photocatalytic performance.^{53,54} Normally, highly crystalline materials have a higher charge migration rate, while materials with low crystallinity, such as amorphous structures can serve as surface active sites.⁵³ For example, by integrating a low crystallinity Pd cocatalyst to CdS, the production rate of CO₂ over Pd/CdS composite improves significantly.⁵⁴ Similarly, a semi crystalline-amorphous Pd cocatalyst was found to be beneficial for charge separation and offers multiple reaction sites, thus enhancing the photoactivity and selectivity of the CO₂ reduction.⁵³ In this dissertation, phase-engineered crystalline-amorphous core@shell Pd nanocubes were designed to enhance the photocatalytic efficiency of H₂ evolution and organic synthesis (Chapter 3).

1.3.2 Heterojunction structure

Engineering of heterojunctions is one of the most promising approaches to improve photocatalytic performance.^{56, 57} For traditional semiconductor photocatalysts such as TiO₂, CdS, ZnO and C₃N₄, the construction of a heterojunction to minimize the recombination of charges has been demonstrated.^{56,57} Similarly, recent studies also confirmed that this strategy could dramatically enhance the conversion efficiency of MHP photocatalyst.^{2,12,55} Very recently, MHP-based heterojunctions (such as type II and Z-scheme) have been summarized in detail by Roeffaers group.⁵⁵ More specifically, the underlying photophysical principles of different types of heterojunctions were clarified, and techniques to identify the type of heterojunctions were highlighted.

In general, when semiconductor A and semiconductor B are in contact, three types of band alignments can be formed:⁵⁶⁻⁵⁸ type I, type II, and type III (Figure 4).⁵⁸ For a type I heterojunction (Figure 4a), the VB and CB of semiconductor B are located in the middle of the bandgap of semiconductor A. In this heterojunction system, photogenerated charge carriers migrate to

semiconductor B, and accumulate at the VB and CB of semiconductor B for targeted redox reaction. Considering electrons and holes flow to a single semiconductor, the charge carriers generally cannot be separated efficiently due to the inevitable charge accumulation.⁵⁸ For a type II system (Figure 4b), semiconductor A has a higher VB and CB position compared to semiconductor B. As a result, the opposite transfer and confinement of the charge carriers will occur, leading to a transfer of the electrons in semiconductor A to semiconductor B, and holes migrate from semiconductor B to semiconductor A. Due to the opposite flow directions of electrons and holes, the charge carriers can be separated effectively.⁵⁷ For a type III heterojunction (Figure 4c), the band edges of the two semiconductors are not overlapped. Thus, the shuttle of holes or/and electrons between the two semiconductors will not occur.

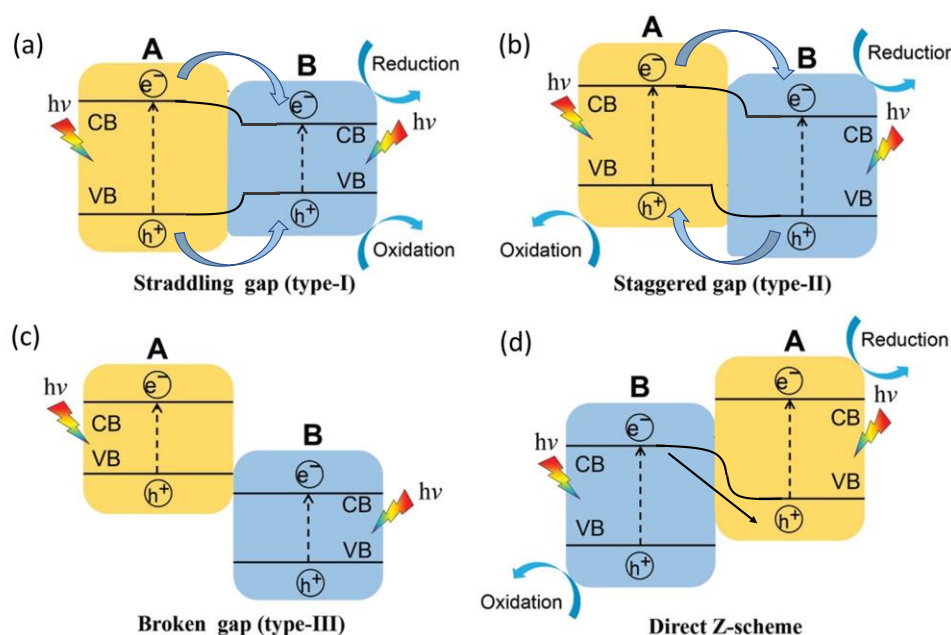


Figure 4. Schematic illustration of electrons and holes separation and migration under light illumination in four different heterojunction systems. (a) Type-I, (b) Type-II, (c) Type-III heterojunction, and (g) direct Z-scheme photocatalytic system,⁵⁸ where CB, VB, e^- , and h^+ stand for conduction band, valence band, electron and hole, respectively. Reproduced with permission from ref 58. Copyright 2020 Wiley.

If the two materials are an n- type and a p-type semiconductors, the electrons in the n-type semiconductor will migrate to the p–n interface while the holes are remained. This process originates from the offset of E_F .⁵⁷ Meanwhile, the holes

generated in the p-type semiconductor material transfer to the n-type semiconductor. As a result, a p–n heterojunction will be generated when the E_F reaches an equilibration, forming an internal electric field.⁵⁷ Under light irradiation, driven by the internal electric field, photogenerated electrons transfer to the CB of the n-type semiconductor quickly, while holes will be shuttled to the VB of the p-type semiconductor.⁵⁸ Although p–n heterojunction and Type-II systems have a similar configuration, the charge separation in a p–n heterojunction is generally faster than in a Type-II system, attributing to the synergistic effect of band alignment and internal electric field.^{56, 57}

However, the redox ability of these heterojunctions is generally limited.⁵⁵ To maximize the redox potentials, Yu et al. constructed a direct Z-scheme heterojunction (Figure 4d).⁵⁹ Although this system possesses an identical configuration to a type-II system, the charge separation mechanism is different.^{57, 58} Because of the strong electrostatic repulsion, a direct Z-scheme blocks the transfer of electrons within the CB between semiconductors A and B. Alternatively, the photogenerated electrons in the CB of semiconductor A directly combine with holes in the VB of semiconductor B. In this case, the photogenerated electrons in semiconductor A and holes in B are spatially separated.^{56, 57} As a result, the strong redox ability of both semiconductors is maintained.⁵⁸

To sum up, the construction of heterojunction is one of the most promising strategies to enhance photocatalytic performance.^{55,57,58} By tuning the type of the heterojunction, both the charge separation and redox potential can be adjusted.⁵⁸

1.3.3 Defect engineering

Defects exist in almost all semiconductor materials at room temperature.¹⁰ Although defects in semiconductors are widely recognized as charge recombination centers detrimental to photocatalytic performance, some recent studies have shown that when precisely engineered, certain types of defects, in small amounts, can improve the photocatalytic performance of the photocatalyst (e.g. TiO_2 , Bi_2WO_6 and $\text{g-C}_3\text{N}_4$). These defects optimize the electronic structure, tune the light absorption, influence the charge separation,

and offer more reactive sites.^{7,11} Hence, defect engineering provides a feasible strategy to improve the overall photocatalytic performance.¹¹ Despite the great promise, it is difficult to accurately modulate the defect concentration and location during the synthesis process.

Specifically, for MHPs, two categories of defects are generally identified: intrinsic and extrinsic defects. Intrinsic point defects include vacancies, interstitials and anti-sites,¹⁷⁻¹⁹ are listed in order of increasing formation energy (Figure 5a). The defects in MHPs generally lie near the band edges or within the bands making MHPs generally very defect-tolerant (Figure 5b).^{10,18} This is in contrast to traditional defect intolerant semiconductors (e.g. CdSe, GaAs) (Figure 5b).¹⁸ Extrinsic surface defects, originating from unsaturated surface bonds or surrounding environment, are a major concern in solution processed MHPs.¹⁸

So far, defect engineering has not been reported to improve the photocatalytic performance of MHP photocatalysts. On the contrary, defects are shown to be detrimental to photocatalytic performance, and the defect passivation can enhance the photoactivity. For example, Wang et al. reported that the defects treatment of CsPbBr₃ (uncoordinated Pb) nanocrystals can dramatically improve the photocatalytic CO₂ activity.¹⁵ Similarly, Ou et al. confirmed that the surface passivation of CsPbBr₃ quantum dots promotes the photocatalytic performance.¹⁶ Until now, passivating the defects of MHPs is still a mainstream approach for improving their photocatalytic properties (Figure 5c). Especially, post-treatment with proper ligand molecules or metal salts have been employed to passivate the surface defects (Figure 5d).⁶ However, very recently, a DFT study showed that the defect modified (Br-vacancy) Cs₂AgBiBr₆ will be beneficial for CO₂ adsorption compared to pristine Cs₂AgBiBr₆.²⁹ Therefore, the relationship between defects and catalytic activity of MHP photocatalysts still needs to be investigated systematically.

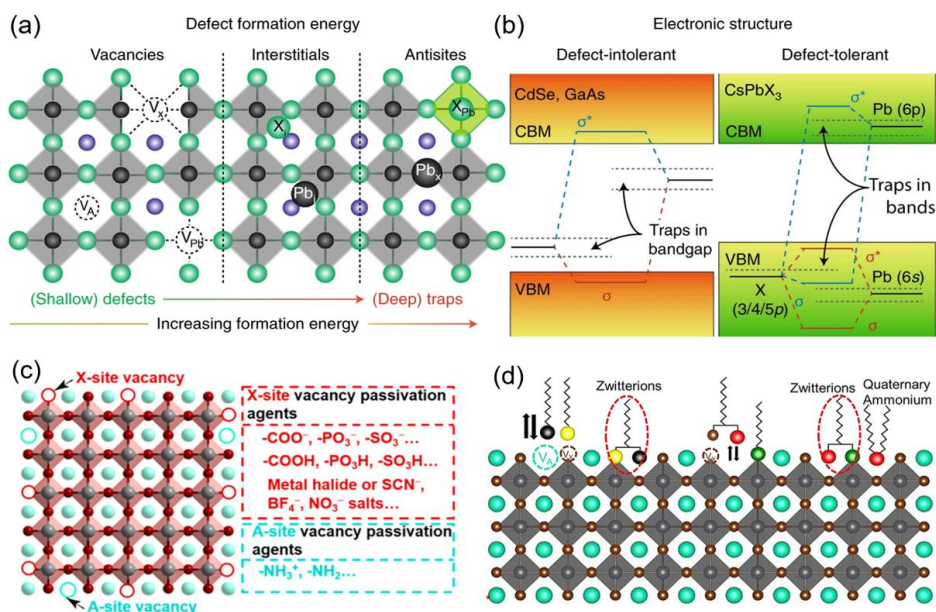


Figure 5. (a) Schematic overview of typical point defects in MHPs and (b) comparison of electronic band structure of traditional defect-intolerant semiconductors (e.g. CdSe, GaAs) and defect-tolerant MHPs (e.g. CsPbX₃). Reproduced with permission from ref 8. Copyright 2018 Springer Nature Publishing AG. (c) Summary of ligand modification of MHPs with different types of passivation ligands. Reproduced with permission from ref 6. Copyright 2022 American Chemical Society. (d) Schematic illustration of defects passivation with various surface ligands. Reproduced with permission from ref 10. Copyright 2021 Wiley-VCH.

1.4 Applications of MHPs in photocatalysis

So far, great efforts have been made to enable MHPs for solar-to-chemical fuel conversion. In this section, recent progress in the development of MHP-based composites for various photocatalytic reactions is summarized and discussed, such as photocatalytic H₂ evolution, photocatalytic CO₂ reduction, photocatalytic organic synthesis and photocatalytic pollutant degradation (Figure 6).

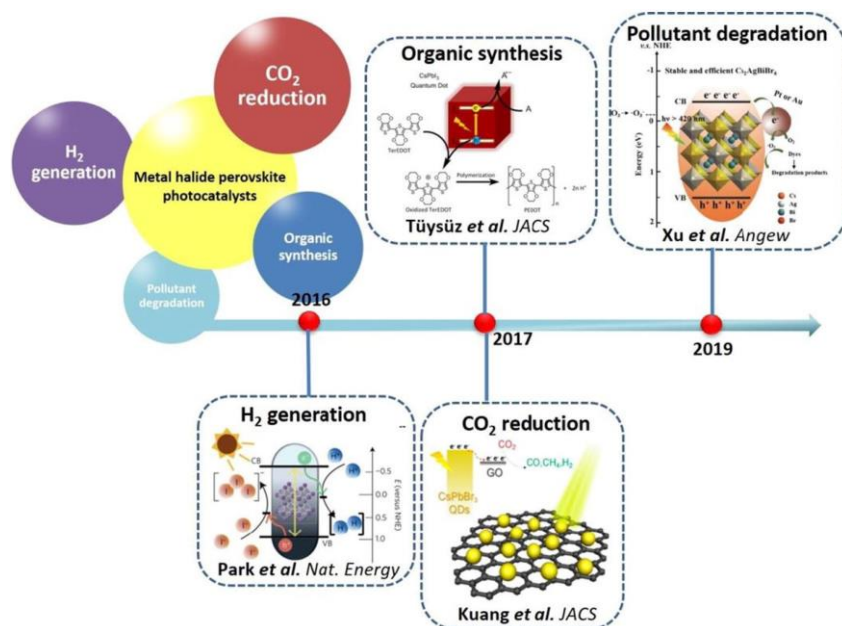


Figure 6. MHP-based photocatalytic applications and the corresponding representative work.² Reproduced with permission from ref 2. Copyright 2020 Elsevier.

1.4.1 H₂ evolution

H₂ is one of the most promising clean and sustainable energy sources to replace traditional nonrenewable fossil fuels.⁶⁰ Photocatalytic H₂ evolution, generated from water splitting, hydrohalic acid, or alcohols, is an attractive renewable technology.⁶⁰ Despite TiO₂-based materials have shown great promise as photocatalysts for H₂ generation, their poor light utilization efficiency, fast charge carrier recombination and low performance limit their practical applications.^{12, 61} Therefore, the development of new semiconductor materials is necessary.

In 2016, Park et al. first demonstrated H₂ evolution over MHP photocatalyst.⁶² To address the instability issue of MHPs, a precipitation-solubility dynamic equilibrium strategy was developed. Under visible light illumination, MAPbI₃ exhibited a stable H₂ production rate of 2.9 μmol g⁻¹ h⁻¹ (Figure 7a). Though loading the Pt on the surface of MAPbI₃ to facilitate the charge separation in MAPbI₃, the production rate was enhanced to 57 μmol g⁻¹ h⁻¹. Since then, the application of MHPs in H₂ evolution was further developed through coupling MHPs with other semiconductors or electron cocatalysts (Figures 7 b-e). For example, Huang et al.⁶³ synthesized a MAPbI₃/rGO catalyst using reduced

graphene oxide (rGO) to promote the separation of photogenerated electrons in MAPbI₃ (Figure 7b). As a result, the MAPbI₃/rGO composite exhibited a photocatalytic conversion rate of 939 μmol g⁻¹ h⁻¹, which is 67-fold higher than that of pure MAPbI₃. Afterwards, they also synthesized a MAPbBr_{3-x}I_x catalyst via a halide exchange strategy.⁶⁴ A production rate of 651.2 μmol h⁻¹ was achieved with MAPbBr_{3-x}I_x/Pt composite under visible light illumination. Followed by these studies, coupling of MHPs with semiconductor materials to improve the charge separation was further explored. Li and coworkers designed a MAPbI₃/TiO₂ composite to facilitate the charge transportation efficiency of MAPbI₃, thus enhancing the production rate of H₂ evolution from HI splitting (Figure 7c).⁶⁵ Similarly, Tao et al. constructed a Ni₃C/MAPbI₃ photocatalyst,⁶⁶ which resulted in an H₂ generation rate of 2362 μmol g⁻¹ h⁻¹, 55 times higher than that of pure MAPbI₃ (Figure 7d). Furthermore, Li et al. designed a dual-channel transport photocatalyst to better promote the extraction of photogenerated charge carriers.⁶⁷ This photocatalyst system has a structure of Pt/Ta₂O₅/MAPbBr₃/PEDOT:PSS, using Pt/Ta₂O₅ and PEDOT:PSS as electron extraction material and hole extraction material, respectively (Figure 7e). Benefiting from the promoted charge separation, the H₂ generation rate of MAPbBr₃ is improved 52 times, reaching 105 μmol h⁻¹ under visible light illumination.

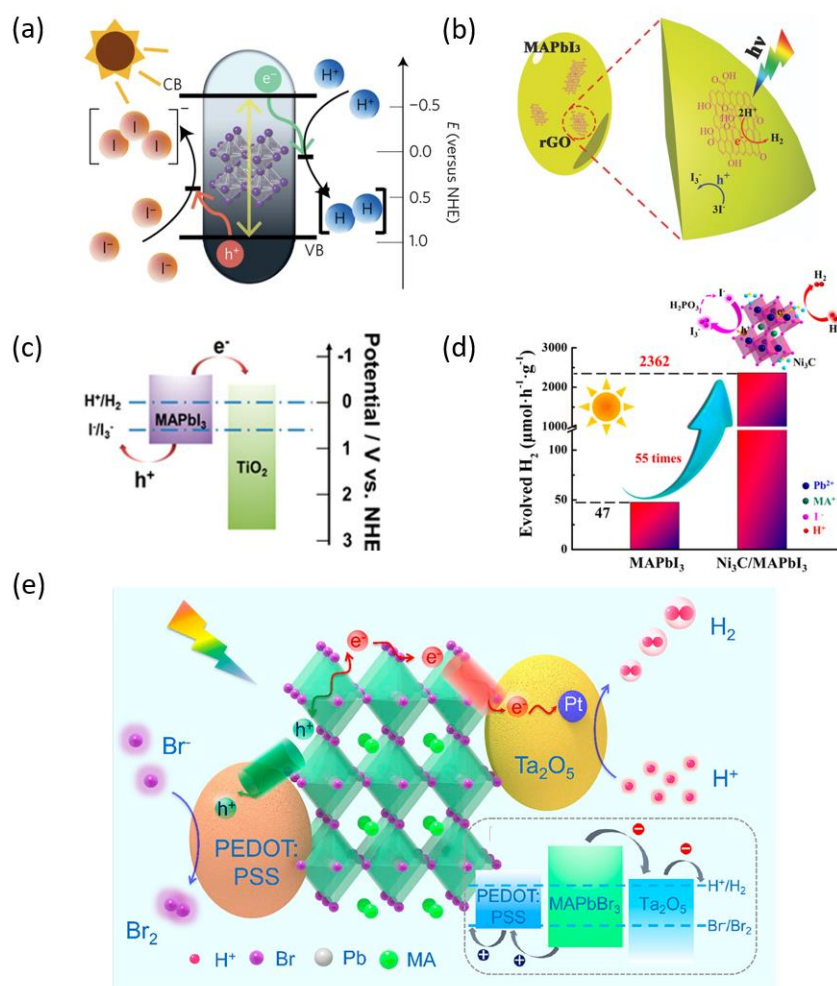


Figure 7. (a) Schematic band diagram of MAPbI₃ for H₂ generation in saturated HI aqueous solution.⁶² Reproduced with permission from ref 62. Copyright 2017 Springer Nature. (b) Schematic illustration of MAPbI₃/rGO for enhanced H₂ production.⁶³ Reprinted with permission from ref 63. Copyright 2018 Wiley. (c) Band energy structure of MAPbI₃ and TiO₂.⁶⁵ Reprinted with permission from ref 65. Copyright 2018 American Chemical Society. (d) Schematic illustration of the production rate of MAPbI₃ and Ni₃C/MAPbI₃.⁶⁶ Reprinted with permission from ref 66. Copyright 2019 American Chemical Society. (e) Schematic band diagram and reaction mechanism of Pt/Ta₂O₅/MAPbBr₃/PEDOT:PSS, using PEDOT:PSS and Pt/Ta₂O₅ as hole and electron extraction materials, respectively.⁶⁷ Reproduced with permission from ref 67. Copyright 2019 American Chemical Society.

In summary, great efforts have been made to improve the photocatalytic performance of MHPs in the photocatalytic H₂ evolution (Table 1). However,

the photoactivity for the H₂ evolution is still relatively low and needs to be further improved. Material engineering such as developing MHPs with a suitable bandgap, higher reduction potential, and excellent charge separation ability, are promising pathways to improve the photocatalytic performance.² On the other hand, most experiments on the MHP-based H₂ evolution reaction are performed in saturated aqueous haloacid HX (X=Br and I). During the photocatalytic process, the halide X⁻ will be oxidized to X₃⁻, which requires additional reducing agents (such as H₃PO₂) to regenerate X⁻. This leads to a rise in the cost and limits the real-world large-scale applicability.^{12, 35} Moreover, the strong acidity and corrosive ability of HX make the operational conditions harsher and more dangerous, and prevents the use of specific cocatalysts.¹² Therefore, further applications need to be explored as alternative MHP-based H₂ evolution routes.

Table 1. Summary of photocatalytic H₂ evolution using MHP-based photocatalysts.

Photocatalyst	light source	Medium	H ₂ rate $\mu\text{mol g}^{-1} \text{h}^{-1}$	Ref.
MAPbI ₃ /Pt	$\lambda \geq 475 \text{ nm}$	HI acid	11.31	62
CsAgBiBr ₄ /rGO	$\lambda \geq 420 \text{ nm}$, 300 W Xe	HBr acid	50	68
CsPbBr ₃ /Ru@TiO ₂	445 nm, 50 mW laser	Triethanolamine	160	69
MAPbI ₃ /TiO ₂	$\lambda \geq 420 \text{ nm}$	HI acid	436.6	65
MAPbI ₃ /CoP	$\lambda \geq 420 \text{ nm}$, 150 W Xe	HI acid	785.9	70
DMASnBr ₃ /g-C ₃ N ₄	500 mW cm ⁻² Xe	Glucose solution	925	71
MAPbI ₃ /rGO	$\lambda \geq 420 \text{ nm}$, 300 W Xe	HI acid	939	63
PEASnBr ₄ /g-C ₃ N ₄	$\lambda \geq 420 \text{ nm}$, 300 W Xe	Triethanolamine	1613	72
Pt/TiO ₂ -MAPbI ₃	$\lambda \geq 420 \text{ nm}$	HI acid	1986.67	65
MAPbI ₃ /Ni ₃ C	$\lambda \geq 420 \text{ nm}$, 300 W Xe	HI acid	2362	66

MAPbBr _{3-x} I _x /Pt	$\lambda \geq 420 \text{ nm}$	mixed HI/HBr acid	2604.80	64
MAPbI ₃ /BP	$\lambda \geq 420 \text{ nm}$, 300 mW cm ⁻² ² Xe	HI acid	3742	73

1.4.2 CO₂ reduction

As a greenhouse gas, CO₂ has been well recognized as the main reason for the increase in surface temperature of our planet. The conversion of CO₂ to fuels does not only provide a new way for obtaining chemical fuels but can also slow down climate change.⁷⁴ Photocatalytic CO₂ reduction, supported by solar energy and a photocatalyst, has attracted increasing attention to convert CO₂ to chemical fuels, such as CO, CH₄, HCOOH, HCHO and CH₃OH.⁷⁵

Recently, MHPs have been employed as promising photocatalysts for CO₂ reduction due to their many advantages. Until now, different MHP-based composites have been employed, and their photocatalytic performance is summarized in Table 2. Kuang et al. reported the use of a CsPbBr₃ MHP for the photocatalytic CO₂ reduction (Figure 8a), in which the photocatalytic reaction was performed in ethyl acetate to stabilize the MHP.⁷⁶ To promote the charge separation in CsPbBr₃ MHP, GO, an excellent charge mediator, was decorated onto the surface of CsPbBr₃, resulting in a production rate of 30 and 59 $\mu\text{mol g}^{-1} \text{h}^{-1}$ for CH₄ and CO, respectively (Figure 8b). Inspired by this work, more strategies for photocatalytic CO₂ reduction with MHPs have been developed. Kuang and coworkers⁷⁷ reported a CsPbBr₃ NCs/Pd composite by coupling MHPs with Pd cocatalyst, The Pd not only serves as an electron acceptor to facilitate charge separation but can also modify the kinetics to catalyze the reaction. The CO, CH₄ and H₂ production rate is improved to 5.8 and 10.4 and 3.3 $\mu\text{mol g}^{-1} \text{h}^{-1}$, respectively, corresponding to a 2.4-fold enhancement compared to pure CsPbBr₃. This concept was also followed by Pan et al. where MXene was used to facilitate the separation of photogenerated electrons and holes. In addition, coupling MHPs with other semiconductor materials such as g-C₃N₄ (Figure 8c)⁷⁸ and ZnO⁷⁹ to form a Type-II heterojunction, or encapsulating MHPs into MOFs,⁸⁰ were further developed. The construction of Z-scheme heterojunctions, such as Fe₂O₃/RGO/CsPbBr₃ (Figure 8d),⁸¹ was also developed to efficiently promote the separation of

charge carriers while retaining the high redox potentials in MHPs to achieve high photocatalytic performance.

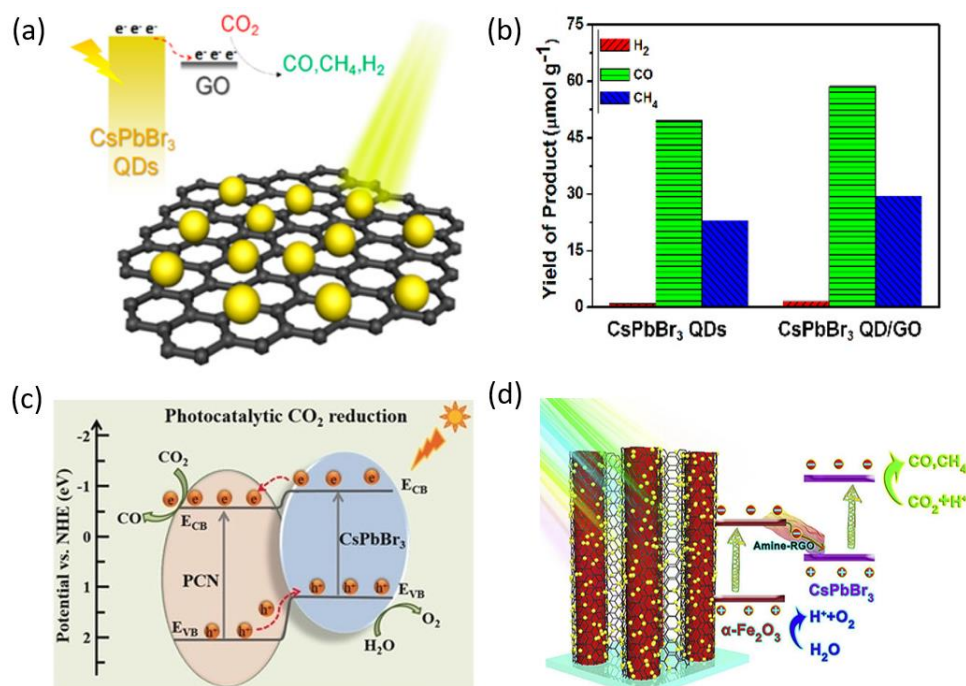


Figure 8. (a) Scheme of CsPbBr₃/GO composite for the photocatalytic CO₂ reduction and (b) comparison of the main products of the reaction with and without GO as a cocatalyst.⁷⁶ Reproduced from ref 76. Copyright 2017 American Chemical Society. (c) Schematic illustration of the CO₂ reduction over CsPbBr₃/g-C₃N₄ photocatalyst.⁷⁸ Reproduced with permission from ref 78. Copyright 2018 Wiley. (d) Scheme of the α-Fe₂O₃/Amine-RGO/CsPbBr₃ Z-scheme photocatalyst for CO₂ reduction.⁸¹ Reproduced from ref 81. Copyright 2020 Elsevier.

To sum up, great success has been achieved to promote charge separation and facilitate surface redox reactions in MHPs, thus enhancing their photocatalytic performance in CO₂ reduction. However, the relatively low photoactivity still does not meet the requirements for practical applications.² Therefore, more efforts are still needed to improve the MHP-based CO₂ reduction for further applications. Furthermore, the MHP-based photocatalytic CO₂ reduction faces poor selectivity, where CO, CH₄ and H₂ are generally produced simultaneously.¹²

Table 2. Summary of photocatalytic CO₂ reduction using MHP-based photocatalysts.

Photocatalyst	light source	Medium	products and activities (μmol/g/h)	Ref.
CsPbBr ₃ QDs	300 W Xe, AM 1.5G	ethyl acetate/water	CO (4.25), CH ₄ (1.5), H ₂ (0.1)	82
CsPbBr ₃ QDs/GO	300 W Xe, AM 1.5G	ethyl acetate	CO (4.89), CH ₄ (2.47), H ₂ (0.13)	76
CsPbBr ₃ @ZIF-67	100 W Xe, AM 1.5G	water vapor	CO (0.77), CH ₄ (3.51)	83
CsPbBr ₃ NC/ZnO/graphene	150 W Xe, AM 1.5G	water vapor	CO (0.85), CH ₄ (6.29)	79
Cs ₂ AgBiBr ₆	300 W Xe, AM 1.5G	ethyl acetate	CO (0.92), CH ₄ (0.11)	84
CsPbBr ₃ @TiO ₂	300 W Xe, AM 1.5G	ethyl acetate/isopropanol	CO (3.9), CH ₄ (6.72), H ₂ (1.46)	85
MAPbI ₃ @Fe-MOF	300 W Xe	ethyl acetate/water	CO (4.16), CH ₄ (13)	80
Cs ₃ Bi ₂ I ₉	UV (32 W, 305 nm)	water vapor	CO (7.76), CH ₄ (1.49)	86
Co@CsPbBr ₃ /Cs ₄ PbBr ₆	300 W Xe	water	CO (11.95)	87
CsPbBr ₃ /TiO ₂ -g-C ₃ N ₄	300 W Xe	ethyl acetate/water	CO (12.9)	88
CsPbBr ₃ /MXene	300 W Xe	ethyl acetate	CO (32.15), CH ₄ (14.64)	89
CsPbBr ₃ QDs/g-C ₃ N ₄	300 W Xe, λ ≥ 420 nm	ethyl acetate/water	CO (70)	78
CsPbBr _{3-x} Cl _x QDs	300 W Xe, AM 1.5G	ethyl acetate	CO (85), CH ₄ (12)	90
Cs ₂ SnI ₆ /SnS ₂	300 W Xe, λ ≥ 400 nm	water/methanol	CH ₄ (6.09)	91

1.4.3 Organic synthesis

Organic chemicals are essential to produce many of our daily products such as pharmaceuticals, flavorings, food additives and pesticides. Well-stabilized industrial organic synthesis routes normally require harsh operating conditions (high temperature and pressure).⁷⁵ The photocatalytic reactions have been considered as desirable alternative approaches in organic chemistry. Unfortunately, many traditional catalysts have certain limits, such as the high cost of noble metals, complicated preparations and moderate activity.⁷⁵

Therefore, the development of economical and effective alternative photocatalysts is of great importance.

Among various potential photoactive materials, MHPs have shown great promise. The first report on MHP organic synthesis was the polymerization of TerEDOT (2,2',5',2"-ter-3,4-ethylenedioxythiophene) into PEDOT over CsPbI₃ QDs (Figure 9a).⁹² TerEDOT is a hole acceptor and is oxidized by photogenerated holes, with benzoquinone or molecular oxygen as an electron acceptor. Afterwards, many advances have been made,⁹³⁻⁹⁸ as summarized in Table 3. Roeffaers et al. demonstrated that FAPbBr₃ is an efficient photocatalyst for the selective photocatalytic oxidation of benzyl alcohol (Figure 9b).⁹⁶ Through loading the FAPbBr₃ on the surface of TiO₂, the photoactivity of FAPbBr₃ could be improved drastically. This was attributed to the improved charge separation in FAPbBr₃ due to the photogenerated electrons transfer from FAPbBr₃ to TiO₂.⁹⁶ Many studies regarding C–H bond activation were also reported.^{97, 98} Yan and co-workers demonstrated that CsPbX₃ MHPs can be used for C–C, C–N and C–O formation (C–C bond formations via C–H activation, C–N, and C–O formations via N-heterocyclizations and aryl-esterifications) (Figure 9c).⁹³ A detailed understanding of the reaction mechanisms (Figure 9d), investigated by Chen et al. through transient absorption spectroscopy,⁹⁴ offers a guideline for designing new MHP-based systems for photosynthesis of a larger class of small molecules.

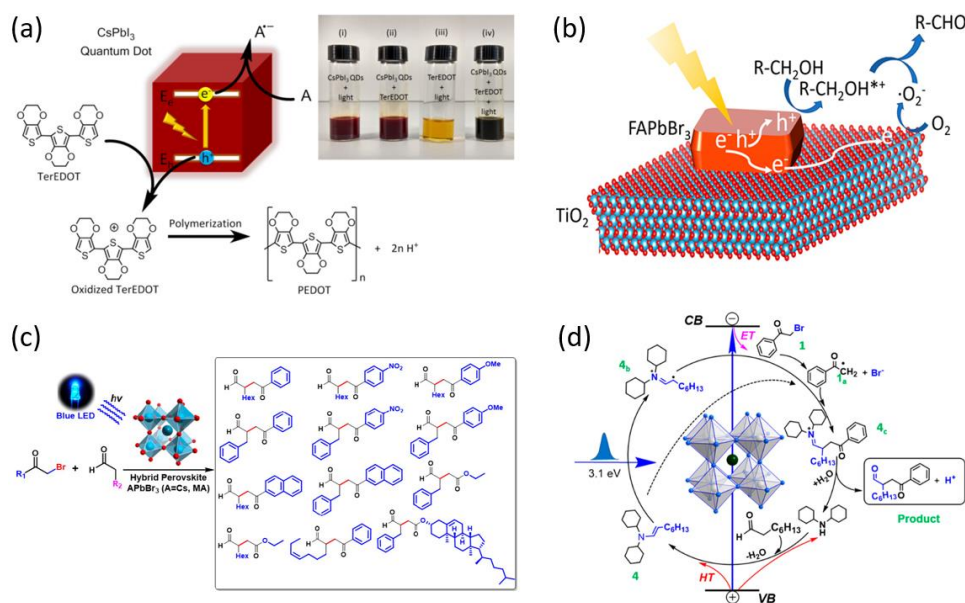


Figure 9. (a) Schematic illustration of the CsPbI₃ QDs used for photocatalytic polymerization of TerEDOT.⁹² Reproduced with permission from ref 92. Copyright 2017 American Chemical Society. (b) Scheme of the CsPbBr₃/TiO₂ for selective photocatalytic oxidation of benzyl alcohol.⁹⁶ Reproduced with permission from ref 96. Copyright 2018 American Chemical Society. (c) Photocatalytic α -alkylation of aldehydes by APbBr₃ (A=Cs and MA) in organic solvents.⁹³ Reproduced from ref 93. Copyright 2019 American Chemical Society. (d) Schematic illustration of the mechanism for C-C bond formation over CsPbBr₃.⁹⁴ Reproduced with permission from ref 94. Copyright 2020 American Chemical Society.

In summary, the current literature shows the promise of MHPs for photocatalytic organic synthesis. However, most of these studies mainly focus on traditional catalytic reactions, more efforts can be made to explore some novel reactions to expand the application of MHPs.^{2,12} Besides, in some organic synthesis reactions such as selective benzyl alcohol oxidation, the photogenerated electrons and holes cannot be effectively used to generate value-added products.² Therefore, the combination of oxidized organic reaction and reduction reactions to simultaneously utilize the photogenerated charge carriers,¹¹ such as coupling benzyl alcohol oxidation and CO₂ reduction, or simultaneous oxidation of benzyl alcohol into benzaldehyde and H₂ evolution, offers a promising new direction for research on MHPs.

Table 3. Comparison of the photocatalytic performance of MHP-based photocatalysts for organic synthesis.

Photocatalyst	Light source	Reaction condition	Conversion (%)	Selectivity (%)	Ref.
FAPbBr ₃	AM 1.5	Benzyl alcohol	15	99	96
FAPbBr ₃ /TiO ₂	G, 150 W Xe	/toluene	63	99	
CsPbBr ₃ /TiO ₂	$\lambda > 420$ nm, 300 W Xe	Benzyl alcohol /toluene Benzyl alcohol /Hexene	50 25	90 82	97
CsPbX ₃ /W ₁₈ O ₄₉	AM 1.5 G, 150 W Xe	Benzyl alcohol /Hexene	72	99	98
CsPbBr ₃	Blue LED, 12 W	aldehyde	85	-	93
CsPbBr ₃	Visible LED	tertiary amines	98	-	99
CsPbBr ₂ Cl			98		
CsPbBr _{0.5} Cl _{0.5}		Thiophenol/	68		
CsPbI ₃		disulfide	58		
CsPbCl ₃			35		
Cs ₃ Bi ₂ Br ₉	$\lambda > 420$ nm	styrene oxide	99	-	100
CsPbBr ₃			91		
CsPbI ₃	$\lambda > 495$ nm	3,4-ethylenedioxythiophene	33	-	92
CsPbBr ₃	Blue LED	aldehydes	99	96	95

1.4.4 Pollutant degradation

Environmental pollution is currently a serious issue in the whole world threatening human health and ecosystems.^{75, 101} Conventional treatment methods for pollution such as membrane filtration, chemical precipitation, and biological methods have already been adopted and thoroughly investigated.

However, these approaches face some limitations like high operating costs and non-biodegradable products, and are rather time-consuming.¹⁰¹ Establishing environmentally friendly and sustainable photocatalysis technologies to solve these problems is therefore highly desirable. So far, various photocatalyst materials (TiO_2 , $\text{g-C}_3\text{N}_4$ and CdS) have been explored to achieve this goal. However, the rapid charge recombination and low light absorption of most photocatalysts restrict their photocatalytic performance.⁷⁵

In recent years, MHPs have been demonstrated as promising photocatalysts for pollutant degradation. Table 4 summarizes the recent progress of the application of MHPs in various pollutant degradation applications. For example, Xu et al. reported that CsPbX_3 ($X = \text{Cl}, \text{Br}, \text{and I}$) QDs (Figure 10a) can rapidly degrade methyl orange into a colorless solution within 80 minutes (Figure 10b).¹⁰² Xu and co-workers synthesized $\text{Cs}_2\text{AgBiBr}_6$ MHPs for organic dye degradation (Rhodamine B (RhB), Rhodamine 110 (Rh110), Methyl red (MR), and Methyl orange (MO)) through an alcohol-based photocatalytic system irradiated under visible light (Figure 10c).¹⁰³ Monitoring of this photocatalytic degradation process showed that the dye molecules can be mineralized completely within 2 h (Figure 10d), and the reaction rate of $\text{Cs}_2\text{AgBiBr}_6$ is comparable to that of CdS . Following this concept, MHP-based type II heterostructures were developed to improve the production rate of pollutant degradation reactions. For instance, an MHP/ C_3N_4 catalyst was synthesized for photocatalytic pollutant degradation.¹⁰⁴⁻¹⁰⁶ Through modulation of the interfacial charge carrier dynamics of MAPbBr_3 (CsPbBr_3)/ $\text{g-C}_3\text{N}_4$, the activity of this composition became much higher than those of pure MAPbBr_3 (CsPbBr_3). Similarly, Liu and co-workers designated a $\text{CsPbBr}_3/\text{C}_3\text{N}_4$ composite coupling Ag for 7-aminocephalosporanic acid degradation (Figure 10e);¹⁰⁵ Fan et al. constructed $\text{CsPbCl}_3/\text{C}_3\text{N}_4$ for penicillin 6-aminopenicillanic acid degradation,¹⁰⁶ the formation of the heterojunction is beneficial for charge separation, thus enhancing the photocatalytic activity of MHPs.

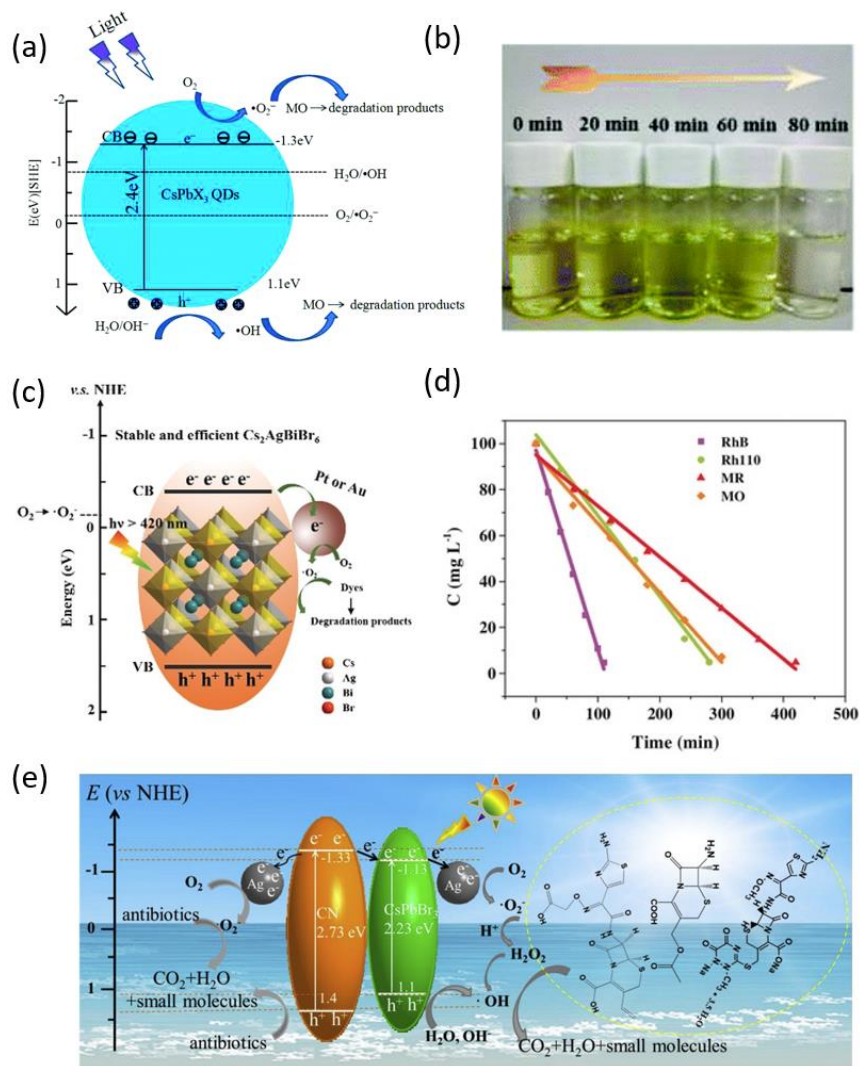


Figure 10. (a) Schematic illustration of the mechanism for the photocatalytic reaction of methyl orange (MO) over CsPbX₃ QDs and (b) Image of MO degradation for 80 min.¹⁰² Reproduced with permission from ref 102, Copyright 2017 Royal Society of Chemistry. (c) Scheme of photocatalytic degradation of Rhodamine B (RhB) on Cs₂AgBiBr₆/Pt(Au) composites and (d) Kinetic curves of the Rhodamine B (RhB), Rhodamine 110 (Rh110), Methyl red (MR), and Methyl orange (MO) degradation.¹⁰³ Reproduced with permission from 103, Copyright 2019 Wiley. (e) Schematic illustration of the mechanism for cephalosporin antibiotics degradation with CsPbBr₃/C₃N₄-Ag composite.¹⁰⁵ Reproduced with permission from 105, Copyright 2019 Elsevier.

To sum up, the above studies have shown the great potential for MHP-based photocatalysts to degrade organic pollutants, converting them into CO₂ and H₂O. However, more attention still needs to go towards addressing some

challenges with these materials. First of all, most MHPs are not stable under practical reaction conditions, especially in the presence of water or other polar solvents, therefore the design of stable MHP photocatalysts or the development of feasible strategies to keep these materials stable under reaction conditions are of great importance.^{2,12} On the other hand, the heavy metal, Pb, contained in MHPs is another concern, which may generate new environmental issues.¹² Therefore, efficient Pb-free MHPs should be developed for photocatalytic pollutant degradation.

Table 4. Summary of photocatalytic organic degradation using MHP-based composites.

Photocatalyst	light source	Pollutant	Degradation percent %	Ref.
		tetracycline hydrochloride/ethanol	76	107
CsPbBr ₃	300 W Xe, $\lambda \geq 420$ nm	methyl orange dye/ethanol	70	
		tetracycline hydrochloride/isopropanol	53	
		tetracycline hydrochloride/water	18	
Cs ₃ Bi ₂ I ₉ /Ag ₂ S			89	108
Cs ₃ Bi ₂ I ₉ /TiO ₂			84	
Cs ₃ Bi ₂ I ₉			62	
Cs ₃ Bi ₂ Br ₉ /Ag ₂ S	$\lambda \geq 420$ nm	methylene blue/ water	40	
Cs ₃ Bi ₂ Br ₉ /TiO ₂			28	
Cs ₃ Bi ₂ Br ₉			27	
Cs ₃ Bi ₂ Br ₉		methylene blue	66	
Cs ₃ Bi ₂ Br ₉ NCs		/isopropanol	59	
CsPbBr ₃ -IO	AM 1.5G	rhodamine 6G	95	109
CsPbBr ₃			75	
CsSnBr ₃	$\lambda \geq 420$ nm	crystal violet dye	73	
CsSnBr ₃	500 W Xe,	methyl orange dye	90	102
CsPbCl ₃	$\lambda \geq 420$ nm		82	
Cs ₂ AgBiBr ₆		Rhodamine B	98	110

1.5 Motivation and objectives

1.5.1 Motivation

Besides the more traditional photovoltaic applications, the utilization of MHP semiconductors for solar-to-chemical energy conversion has recently attracted considerable attention. Currently, MHP materials have become one of most the promising photocatalyst materials.¹² Their defect tolerant properties allow for novel processing methodologies.² So far, MHPs have successfully been used for solar fuel generation through photocatalytic CO₂ reduction and H₂ evolution,^{62,66,80,86} and their applications in organic synthesis and pollutant degradation are equally promising.^{92,93,102,106}

Despite their great potential, single MHPs generally possess modest photocatalytic performance due to their inefficient charge separation.¹² To date, great efforts have been made to promote the separation of photogenerated electrons and holes in MHPs. Nevertheless, the photocatalytic performance of MHP-based photocatalysts still does not meet the requirements for practical applications. Therefore, developing more powerful strategies to improve the photoactivity of MHP photocatalysts is necessary.

Besides the photocatalytic activity, the poor stability of MHPs is considered the main bottleneck for their further development.^{2,12} Most MHPs are reported to suffer from limited long-term operational stability due to their ionic nature and moisture sensitivity properties. When exposed to water, MHPs will degrade quickly into precipitates and dissolved ions.¹² Thus, exploring useful approaches to improve the stability of MHP-based photocatalyst is of great importance.

So far, although much progress has been made, an efficient and stable MHP-based system in practical reaction conditions (polar solvent, in-situ generated water reaction systems, etc.) is still challenging.¹² MHP photocatalysis research has been facing issues in simultaneously achieving higher photocatalytic activity and long-term stability.

1.5.2 Research objectives

This thesis aims to use MHP-based photocatalysts for solar-to-chemical energy conversion, focusing on enhancing the photocatalytic conversion efficiency and stability of the MHP photocatalysts.

The first objective is to construct a Schottky junction, i.e., loading Pd NCs on the surface of CsPbBr₃, to improve the catalytic performance of the Suzuki reaction, and investigate the exact photo and thermal contribution and the mechanism of the photocatalytic Suzuki reaction. The second objective is to focus on the cocatalyst, by synthesizing a phase-engineered crystalline/amorphous core@shell Pd (APd) as the cocatalyst, to further improve the photocatalytic performance of simultaneous H₂ evolution and organic synthesis over Cs₃Bi₂Br₉/APd photocatalysts. Although metal cocatalysts are an effective strategy to improve the photocatalytic activity of MHPs, the stability of MHPs during photocatalytic reactions is still challenging. To address this issue, a planar heterojunction solar photocatalyst cell, with a configuration of NiO_x/CsPbBr₃/TiO₂, was constructed to simultaneously boost the solar-driven photocatalytic performance and the stability of the MHPs.

1.6 References

1. The BP Energy Outlook. <https://www.bp.com/en/global/corporate/energy-economics/energy-outlook.html>.
2. Wang, J.; Liu, J.; Du, Z.; Li, Z., Recent advances in metal halide perovskite photocatalysts: Properties, synthesis and applications. *J. Energy Chem.* **2021**, *54*, 770-785.
3. Crabtree, G. W.; Lewis, N. S., Solar energy conversion. *Phys. Today* **2007**, *60*, 37-42.
4. Fujishima, A.; Honda, K., Electrochemical photolysis of water at a semiconductor electrode. *Nature* **1972**, *238*, 37-38.
5. Ameta, R.; Ameta, S. C., *Photocatalysis: principles and applications*. Crc Press: 2016.
6. Wang, J.; Shi, Y.Y.; Wang, Y.H.; Li, Z.Q., Rational design of metal halide perovskite nanocrystals for photocatalytic CO₂ reduction: Recent advances, challenges, and prospects. *ACS Energy Lett.* **2022**, *7*, 2043–2059.

7. Bai, S.; Gao, C.; Low, J.; Xiong, Y., Crystal phase engineering on photocatalytic materials for energy and environmental applications. *Nano Res.* **2019**, *12*, 2031-2054.
8. Akkerman, Q.A.; Rainò, G.; Kovalenko, M.V.; Manna, L., Genesis, challenges and opportunities for colloidal lead halide perovskite nanocrystals. *Nat. Mater.*, **2018**, *17*, 394-405.
9. Feng, C.; Tang, L.; Deng, Y.; Wang, J.; Liu, Y.; Ouyang, X.; Yang, H.; Yu, J.; Wang, J., A novel sulfur-assisted annealing method of g-C₃N₄ nanosheet compensates for the loss of light absorption with further promoted charge transfer for photocatalytic production of H₂ and H₂O₂. *Appl. Catal. B: Environ.* **2021**, *281*, 119539.
10. Ye, J.Z.; Byranvand, M.M.; Martinez, C.O; Hoye, R.L.Z.; Saliba, M.; Polavarapu, L., Defect passivation in lead-halide perovskite nanocrystals and thin films: Toward efficient LEDs and solar cells. *Angew. Chem. Int. Ed.* **2021**, *60*, 21636–21660.
11. Huang, H.; Zhao, J.; Du, Y.; Zhou, C.; Zhang, M.; Wang, Z.; Weng, Y.; Long, J.; Hofkens, J.; Steele, J. A., Direct Z-Scheme Heterojunction of Semicoherent FAPbBr₃/Bi₂WO₆ Interface for Photoredox Reaction with Large Driving Force. *ACS Nano* **2020**, *14*, 16689-16697.
12. Huang, H.; Pradhan, B.; Hofkens, J.; Roeffaers, M. B.; Steele, J. A., Solar-driven metal halide perovskite photocatalysis: Design, stability, and performance. *ACS Energy Lett.* **2020**, *5*, 1107-1123.
13. Schneider, J.; Matsuoka, M.; Takeuchi, M.; Zhang, J.; Horiuchi, Y.; Anpo, M.; Bahnemann, D. W., Understanding TiO₂ photocatalysis: mechanisms and materials. *Chem. Rev.* **2014**, *114*, 9919-86.
14. Weng, B.; Qi, M.-Y.; Han, C.; Tang, Z.-R.; Xu, Y.-J., Photocorrosion Inhibition of Semiconductor-Based Photocatalysts: Basic Principle, Current Development, and Future Perspective. *ACS Catal.* **2019**, *9*, 4642-4687.
15. Wang, J.C.; Li, N.Y.; Idris, A.M.; Wang, J.; Du, X.Y.; Pan, Z.X.; Li, Z.Q., Surface defect engineering of CsPbBr₃ nanocrystals for high efficient photocatalytic CO₂ reduction. *Sol. RRL* **2021**, *5*, 2100154.
16. Ou, M.; Tu, W.G.; Yin, S.M.; Xing, W.N.; Wu, S.Y.; Wang, H.J.; Wan, S.P.; Zhong, Q.; Xu, R., Amino-assisted anchoring of CsPbBr₃ perovskite quantum

dots on porous g-C₃N₄ for enhanced photocatalytic CO₂ reduction. *Angew. Chem.* **2018**, *130*, 13758-13762.

17. Liu, X.-K.; Xu, W.; Bai, S.; Jin, Y.; Wang, J.; Friend, R. H.; Gao, F., Metal halide perovskites for light-emitting diodes. *Nat. Mater.* **2021**, *20*, 10-21.

18. Jin, H.D.; Debroye, E.; Keshavarz, M.; Scheblykin, I.G; Roeffaers, M.B.J.; Hofkens, J.; Steele, J.A., It's a trap! On the nature of localised states and charge trapping in lead halide perovskites. *Mater. Horiz.* **2020**, *7*, 397-410.

19. Zhou, J.; Huang, J., Photodetectors based on organic–inorganic hybrid lead halide perovskites. *Adv. Sci.* **2018**, *5*, 1700256.

20. Steele, J. A.; Prakasam, V.; Huang, H.; Solano, E.; Chernyshov, D.; Hofkens, J.; Roeffaers, M. B., Trojans That Flip the Black Phase: Impurity-Driven Stabilization and Spontaneous Strain Suppression in γ -CsPbI₃ Perovskite. *J. Am. Chem. Soc.* **2021**, *143*, 10500-10508.

21. Chen, W.; Li, X.; Li, Y.; Li, Y., A review: crystal growth for high-performance all-inorganic perovskite solar cells. *Energy Environ. Sci.* **2020**, *13*, 1971-1996.

22. Duan, J.; Xu, H.; Sha, W. E. I.; Zhao, Y.; Wang, Y.; Yang, X.; Tang, Q., Inorganic perovskite solar cells: an emerging member of the photovoltaic community. *J. Mater. Chem. A* **2019**, *7*, 21036-21068.

23. Shi, M.; Li, G.; Tian, W.; Jin, S.; Tao, X.; Jiang, Y.; Pidko, E. A.; Li, R.; Li, C., Understanding the Effect of Crystalline Structural Transformation for Lead-Free Inorganic Halide Perovskites. *Adv. Mater.* **2020**, *32*, 2002137.

24. Zhang, J.; Hodes, G.; Jin, Z.; Liu, S. F., All-Inorganic CsPbX₃ Perovskite Solar Cells: Progress and Prospects. *Angew. Chem. Int. Ed.* **2019**, *58*, 15596-15618.

25. Li, B.; Fu, L.; Li, S.; Li, H.; Pan, L.; Wang, L.; Chang, B.; Yin, L., Pathways toward high-performance inorganic perovskite solar cells: challenges and strategies. *J. Mater. Chem. A* **2019**, *7*, 20494-20518.

26. Montecucco, R.; Quadrivi, E.; Po, R.; Grancini, G., All-Inorganic Cesium-Based Hybrid Perovskites for Efficient and Stable Solar Cells and Modules. *Adv. Energy Mater.* **2021**, *11*, 2100672.

27. Liang, J.; Wang, C.; Wang, Y.; Xu, Z.; Lu, Z.; Ma, Y.; Zhu, H.; Hu, Y.; Xiao, C.; Yi, X.; Zhu, G.; Lv, H.; Ma, L.; Chen, T.; Tie, Z.; Jin, Z.; Liu, J., All-Inorganic Perovskite Solar Cells. *J. Am. Chem. Soc.* **2016**, *138*, 15829-15832.

28. Zhou, Y.; Zhao, Y., Chemical stability and instability of inorganic halide perovskites. *Energy Environ. Sci.* **2019**, *12*, 1495-1511.
29. Chen, P.F.; Huang, Y.; Shi, Z.H.; Chen, X.Z.; Li, N., Improving the catalytic CO₂ reduction on Cs₂AgBiBr₆ by halide defect engineering: A DFT study. *Materials* **2021**, *14*, 2469.
30. Ito, S.; Tanaka, S.; Manabe, K.; Nishino, H., Effects of surface blocking layer of Sb₂S₃ on nanocrystalline TiO₂ for CH₃NH₃PbI₃ perovskite solar cells. *J. Phys. Chem. C* **2014**, *118*, 16995-17000.
31. Aristidou, N.; Eames, C.; Sanchez-Molina, I.; Bu, X.; Kosco, J.; Islam, M. S.; Haque, S. A., Fast oxygen diffusion and iodide defects mediate oxygen-induced degradation of perovskite solar cells. *Nat. Commun.* **2017**, *8*, 1-10.
32. Hoke, E. T.; Slotcavage, D. J.; Dohner, E. R.; Bowring, A. R.; Karunadasa, H. I.; McGehee, M. D., Reversible photo-induced trap formation in mixed-halide hybrid perovskites for photovoltaics. *Chem. Sci.* **2015**, *6*, 613-617.
33. Li, X.-H.; Baar, M.; Blechert, S.; Antonietti, M., Facilitating room-temperature Suzuki coupling reaction with light: Mott-Schottky photocatalyst for C-C-coupling. *Sci. Rep.* **2013**, *3*, 1-6.
34. Murdoch, M.; Waterhouse, G.; Nadeem, M.; Metson, J.; Keane, M.; Howe, R.; Llorca, J.; Idriss, H., The effect of gold loading and particle size on photocatalytic hydrogen production from ethanol over Au/TiO₂ nanoparticles. *Nat. Chem.* **2011**, *3*, 489-492.
35. Weng, B.; Quan, Q.; Xu, Y.-J., Decorating geometry- and size-controlled sub-20 nm Pd nanocubes onto 2D TiO₂ nanosheets for simultaneous H₂ evolution and 1,1-diethoxyethane production. *J. Mater. Chem. A* **2016**, *4*, 18366-18377.
36. Li, Q.; Guo, B.; Yu, J.; Ran, J.; Zhang, B.; Yan, H.; Gong, J. R., Highly efficient visible-light-driven photocatalytic hydrogen production of CdS-cluster-decorated graphene nanosheets. *J. Am. Chem. Soc.* **2011**, *133*, 10878-10884.
37. Onsuratoom, S.; Puangpetch, T.; Chavadej, S., Comparative investigation of hydrogen production over Ag-, Ni-, and Cu-loaded mesoporous-assembled TiO₂-ZrO₂ mixed oxide nanocrystal photocatalysts. *Chem. Eng. J.* **2011**, *173*, 667-675.

38. Hara, M.; Nunoshige, J.; Takata, T.; Kondo, J. N.; Domen, K., Unusual enhancement of H₂ evolution by Ru on TaON photocatalyst under visible light irradiation. *Chem. Commun.* **2003**, 24, 3000-3001.
39. Sasaki, Y.; Iwase, A.; Kato, H.; Kudo, A., The effect of co-catalyst for Z-scheme photocatalysis systems with an Fe³⁺/Fe²⁺ electron mediator on overall water splitting under visible light irradiation. *J. Catal.* **2008**, 259, 133-137.
40. Sato, J.; Saito, N.; Yamada, Y.; Maeda, K.; Takata, T.; Kondo, J. N.; Hara, M.; Kobayashi, H.; Domen, K.; Inoue, Y., RuO₂-loaded β-Ge₃N₄ as a non-oxide photocatalyst for overall water splitting. *J. Am. Chem. Soc.* **2005**, 127, 4150-4151.
41. Youngblood, W. J.; Lee, S.-H. A.; Kobayashi, Y.; Hernandez-Pagan, E. A.; Hoertz, P. G.; Moore, T. A.; Moore, A. L.; Gust, D.; Mallouk, T. E., Photoassisted overall water splitting in a visible light-absorbing dye-sensitized photoelectrochemical cell. *J. Am. Chem. Soc.* **2009**, 131, 926-927.
42. Han, Z.; Qiu, F.; Eisenberg, R.; Holland, P. L.; Krauss, T. D., Robust photogeneration of H₂ in water using semiconductor nanocrystals and a nickel catalyst. *Science* **2012**, 338, 1321-1324.
43. Li, Z. J.; Wang, J. J.; Li, X. B.; Fan, X. B.; Meng, Q. Y.; Feng, K.; Chen, B.; Tung, C. H.; Wu, L. Z., An Exceptional Artificial Photocatalyst, Ni-CdSe/CdS Core/Shell Hybrid, Made In Situ from CdSe Quantum Dots and Nickel Salts for Efficient Hydrogen Evolution. *Adv. Mater.* **2013**, 25, 6613-6618.
44. Huang, J.; Mulfort, K. L.; Du, P.; Chen, L. X., Photodriven charge separation dynamics in CdSe/ZnS core/shell quantum dot/cobaloxime hybrid for efficient hydrogen production. *J. Am. Chem. Soc.* **2012**, 134, 16472-16475.
45. Wang, F.; Wang, W. G.; Wang, X. J.; Wang, H. Y.; Tung, C. H.; Wu, L. Z., A highly efficient photocatalytic system for hydrogen production by a robust hydrogenase mimic in an aqueous solution. *Angew. Chem. Int. Ed.* **2011**, 50, 3193-3197.
46. Yu, J.; Yang, B.; Cheng, B., Noble-metal-free carbon nanotube-Cd_{0.1}Zn_{0.9}S composites for high visible-light photocatalytic H₂-production performance. *Nanoscale* **2012**, 4, 2670-2677.

47. Zhang, J.; Yu, J.; Jaroniec, M.; Gong, J. R., Noble metal-free reduced graphene oxide-Zn_xCd_{1-x}S nanocomposite with enhanced solar photocatalytic H₂-production performance. *Nano Lett.* **2012**, *12*, 4584-4589.
48. Xie, Y. P.; Liu, G.; Lu, G. Q. M.; Cheng, H.-M., Boron oxynitride nanoclusters on tungsten trioxide as a metal-free cocatalyst for photocatalytic oxygen evolution from water splitting. *Nanoscale* **2012**, *4*, 1267-1270.
49. Xiang, Q.; Yu, J.; Jaroniec, M., Synergetic effect of MoS₂ and graphene as cocatalysts for enhanced photocatalytic H₂ production activity of TiO₂ nanoparticles. *J. Am. Chem. Soc.* **2012**, *134*, 6575-6578.
50. Zhao, H.; Wang, J.; Dong, Y.; Jiang, P., Noble-metal-free iron phosphide cocatalyst loaded graphitic carbon nitride as an efficient and robust photocatalyst for hydrogen evolution under visible light irradiation. *ACS Sustain. Chem. Eng.* **2017**, *5*, 8053-8060.
51. Ran, J.; Zhang, J.; Yu, J.; Jaroniec, M.; Qiao, S. Z., Earth-abundant cocatalysts for semiconductor-based photocatalytic water splitting. *Chem. Soc. Rev.* **2014**, *43*, 7787-7812.
52. Xiao, N.; Li, S.; Li, X.; Ge, L.; Gao, Y.; Li, N., The roles and mechanism of cocatalysts in photocatalytic water splitting to produce hydrogen. *Chin. J. Catal.* **2020**, *41*, 642-671.
53. Chen, Q.; Mo, W.; Yang, G.; Zhong, S.; Lin, H.; Chen, J.; Bai, S., Significantly Enhanced Photocatalytic CO₂ Reduction by Surface Amorphization of Cocatalysts. *Small* **2021**, *17*, 2102105.
54. Chen, Q.; Wu, S.; Zhong, S.; Gao, B.; Wang, W.; Mo, W.; Lin, H.; Wei, X.; Bai, S.; Chen, J., What is the better choice for Pd cocatalysts for photocatalytic reduction of CO₂ to renewable fuels: high-crystallinity or amorphous? *J. Mater. Chem. A* **2020**, *8*, 21208-21218.
55. H. Huang, D. Verhaeghe, B. Weng, B. Ghosh, H. Zhang, J. Hofkens, J.A. Steel and M.B. Roeffaers, *Angew. Chem.* **2022**, *134*, e202203261.
56. Low, J.; Yu, J.; Jaroniec, M.; Wageh, S.; Al-Ghamdi, A. A., Heterojunction photocatalysts. *Adv. Mater.* **2017**, *29*, 1601694.
57. Lee, J.; Tan, L.-L.; Chai, S.-P., Heterojunction photocatalysts for artificial nitrogen fixation: fundamentals, latest advances and future perspectives. *Nanoscale* **2021**, *13*, 7011-7033.

58. Su, Q.; Li, Y.; Hu, R.; Song, F.; Liu, S.; Guo, C.; Zhu, S.; Liu, W.; Pan, J., Heterojunction photocatalysts based on 2D materials: the role of configuration. *Adv.Sustain.Syst.* **2020**, *4*, 2000130.
59. Yu, J.; Wang, S.; Low, J.; Xiao, W., Enhanced photocatalytic performance of direct Z-scheme g-C₃N₄-TiO₂ photocatalysts for the decomposition of formaldehyde in air. *Phys. Chem. Chem. Phys.* **2013**, *15*, 16883-16890.
60. Hisatomi, T.; Domen, K., Reaction systems for solar hydrogen production via water splitting with particulate semiconductor photocatalysts. *Nat. Catal.* **2019**, *2*, 387-399.
61. Park, S.; Choi, S.; Kim, S.; Nam, K. T., Metal Halide Perovskites for Solar Fuel Production and Photoreactions. *J. Phys. Chem. Lett.* **2021**, *12*, 8292-8301.
62. Park, S.; Chang, W. J.; Lee, C. W.; Park, S.; Ahn, H.-Y.; Nam, K. T., Photocatalytic hydrogen generation from hydriodic acid using methylammonium lead iodide in dynamic equilibrium with aqueous solution. *Nat. Energy* **2016**, *2*, 1-8.
63. Wu, Y.; Wang, P.; Zhu, X.; Zhang, Q.; Wang, Z.; Liu, Y.; Zou, G.; Dai, Y.; Whangbo, M. H.; Huang, B., Composite of CH₃NH₃PbI₃ with Reduced Graphene Oxide as a Highly Efficient and Stable Visible-Light Photocatalyst for Hydrogen Evolution in Aqueous HI Solution. *Adv. Mater.* **2018**, *30*, 1704342.
64. Wu, Y.; Wang, P.; Guan, Z.; Liu, J.; Wang, Z.; Zheng, Z.; Jin, S.; Dai, Y.; Whangbo, M.-H.; Huang, B., Enhancing the Photocatalytic Hydrogen Evolution Activity of Mixed-Halide Perovskite CH₃NH₃PbBr_{3-x}I_x Achieved by Bandgap Funneling of Charge Carriers. *ACS Catal.* **2018**, *8*, 10349-10357.
65. Wang, X.; Wang, H.; Zhang, H.; Yu, W.; Wang, X.; Zhao, Y.; Zong, X.; Li, C., Dynamic interaction between methylammonium lead iodide and TiO₂ nanocrystals leads to enhanced photocatalytic H₂ evolution from HI splitting. *ACS Energy Lett.* **2018**, *3*, 1159-1164.
66. Zhao, Z.; Wu, J.; Zheng, Y.-Z.; Li, N.; Li, X.; Tao, X., Ni₃C-decorated MAPbI₃ as visible-light photocatalyst for H₂ evolution from HI splitting. *ACS Catal.* **2019**, *9*, 8144-8152.
67. Wang, H.; Wang, X.; Chen, R.; Zhang, H.; Wang, X.; Wang, J.; Zhang, J.; Mu, L.; Wu, K.; Fan, F., Promoting photocatalytic H₂ evolution on organic-

inorganic hybrid perovskite nanocrystals by simultaneous dual-charge transportation modulation. *ACS Energy Lett.* **2018**, *4*, 40-47.

68. Wang, T.; Yue, D.; Li, X.; Zhao, Y., Lead-free double perovskite Cs₂AgBiBr₆/RGO composite for efficient visible light photocatalytic H₂ evolution. *Appl. Catal. B: Environ.* **2020**, *268*, 118399.

69. Pavliuk, M. V.; Abdellah, M.; Sa, J., Hydrogen evolution with CsPbBr₃ perovskite nanocrystals under visible light in solution. *Mater. Today Commun.* **2018**, *16*, 90-96.

70. Cai, C.; Teng, Y.; Wu, J. H.; Li, J. Y.; Chen, H. Y.; Chen, J. H.; Kuang, D. B., In situ photosynthesis of an MAPbI₃/CoP hybrid heterojunction for efficient photocatalytic hydrogen evolution. *Adv. Funct. Mater.* **2020**, *30*, 2001478.

71. Speltini, A.; Romani, L.; Dondi, D.; Malavasi, L.; Profumo, A., Carbon nitride-perovskite composites: Evaluation and optimization of photocatalytic hydrogen evolution in saccharides aqueous solution. *Catalysts* **2020**, *10*, 1259.

72. Romani, L.; Bala, A.; Kumar, V.; Speltini, A.; Milella, A.; Fracassi, F.; Listorti, A.; Profumo, A.; Malavasi, L., PEA₂SnBr₄: a water-stable lead-free two-dimensional perovskite and demonstration of its use as a co-catalyst in hydrogen photogeneration and organic-dye degradation. *J. Mater. Chem. C* **2020**, *8*, 9189-9194.

73. Li, R.; Li, X.; Wu, J.; Lv, X.; Zheng, Y.-Z.; Zhao, Z.; Ding, X.; Tao, X.; Chen, J.-F., Few-layer black phosphorus-on-MAPbI₃ for superb visible-light photocatalytic hydrogen evolution from HI splitting. *Appl. Catal. B: Environ.* **2019**, *259*, 118075.

74. Shyamal, S.; Pradhan, N., Halide perovskite nanocrystal photocatalysts for CO₂ reduction: successes and challenges. *J. Phys. Chem. Lett.* **2020**, *11*, 6921-6934.

75. Bresolin, B.-M.; Park, Y.; Bahnemann, D. W., Recent progresses on metal halide perovskite-based material as potential photocatalyst. *Catalysts* **2020**, *10*, 709.

76. Xu, Y. F.; Yang, M. Z.; Chen, B. X.; Wang, X. D.; Chen, H. Y.; Kuang, D. B.; Su, C. Y., A CsPbBr₃ Perovskite Quantum Dot/Graphene Oxide Composite for Photocatalytic CO₂ Reduction. *J. Am. Chem. Soc.* **2017**, *139*, 5660-5663.

77. Xu, Y.-F.; Yang, M.-Z.; Chen, H.-Y.; Liao, J.-F.; Wang, X.-D.; Kuang, D.-B., Enhanced Solar-Driven Gaseous CO₂ Conversion by CsPbBr₃ Nanocrystal/Pd Nanosheet Schottky-Junction Photocatalyst. *ACS Appl. Energy Mater.* **2018**, *1*, 5083-5089.
78. Ou, M.; Tu, W.; Yin, S.; Xing, W.; Wu, S.; Wang, H.; Wan, S.; Zhong, Q.; Xu, R., Amino-assisted anchoring of CsPbBr₃ perovskite quantum dots on porous g-C₃N₄ for enhanced photocatalytic CO₂ reduction. *Angew. Chem.* **2018**, *130*, 13758-13762.
79. Jiang, Y.; Liao, J.-F.; Xu, Y.-F.; Chen, H.-Y.; Wang, X.-D.; Kuang, D.-B., Hierarchical CsPbBr₃ nanocrystal-decorated ZnO nanowire/macroporous graphene hybrids for enhancing charge separation and photocatalytic CO₂ reduction. *J. Mater. Chem. A* **2019**, *7*, 13762-13769.
80. Wu, L. Y.; Mu, Y. F.; Guo, X. X.; Zhang, W.; Zhang, Z. M.; Zhang, M.; Lu, T. B., Encapsulating perovskite quantum dots in iron-based metal-organic frameworks (MOFs) for efficient photocatalytic CO₂ reduction. *Angew. Chem. Int. Ed.* **2019**, *58*, 9491-9495.
81. Jiang, Y.; Liao, J.-F.; Chen, H.-Y.; Zhang, H.-H.; Li, J.-Y.; Wang, X.-D.; Kuang, D.-B., All-solid-state Z-scheme α-Fe₂O₃/amine-RGO/CsPbBr₃ hybrids for visible-light-driven photocatalytic CO₂ reduction. *Chem* **2020**, *6*, 766-780.
82. Hou, J.; Cao, S.; Wu, Y.; Gao, Z.; Liang, F.; Sun, Y.; Lin, Z.; Sun, L., Inorganic colloidal perovskite quantum dots for robust solar CO₂ reduction. *Chem. Eur. J.* **2017**, *23*, 9481-9485.
83. Kong, Z.-C.; Liao, J.-F.; Dong, Y.-J.; Xu, Y.-F.; Chen, H.-Y.; Kuang, D.-B.; Su, C.-Y., Core@ shell CsPbBr₃@zeolitic imidazolate framework nanocomposite for efficient photocatalytic CO₂ reduction. *ACS Energy Lett.* **2018**, *3*, 2656-2662.
84. Zhou, L.; Xu, Y. F.; Chen, B. X.; Kuang, D. B.; Su, C. Y., Synthesis and Photocatalytic Application of Stable Lead-Free Cs₂AgBiBr₆ Perovskite Nanocrystals. *Small* **2018**, *14*, 1703762.
85. Xu, Y. F.; Wang, X. D.; Liao, J. F.; Chen, B. X.; Chen, H. Y.; Kuang, D. B., Amorphous-TiO₂-Encapsulated CsPbBr₃ Nanocrystal Composite Photocatalyst with Enhanced Charge Separation and CO₂ Fixation. *Adv. Mater. Interfaces* **2018**, *5*, 1801015.

86. Bhosale, S. S.; Kharade, A. K.; Jokar, E.; Fathi, A.; Chang, S.-m.; Diao, E. W.-G., Mechanism of photocatalytic CO₂ reduction by bismuth-based perovskite nanocrystals at the gas–solid interface. *J. Am. Chem. Soc.* **2019**, *141*, 20434-20442.
87. Mu, Y.-F.; Zhang, W.; Guo, X.-X.; Dong, G.-X.; Zhang, M.; Lu, T.-B., Water-tolerant lead halide perovskite nanocrystals as efficient photocatalysts for visible-light-driven CO₂ reduction in pure water. *ChemSusChem* **2019**, *12*, 4769-4774.
88. Guo, X.-X.; Tang, S.-F.; Mu, Y.-F.; Wu, L.-Y.; Dong, G.-X.; Zhang, M., Engineering a CsPbBr₃-based nanocomposite for efficient photocatalytic CO₂ reduction: improved charge separation concomitant with increased activity sites. *RSC Adv.* **2019**, *9*, 34342-34348.
89. Pan, A.; Ma, X.; Huang, S.; Wu, Y.; Jia, M.; Shi, Y.; Liu, Y.; Wangyang, P.; He, L.; Liu, Y., CsPbBr₃ perovskite nanocrystal grown on MXene nanosheets for enhanced photoelectric detection and photocatalytic CO₂ reduction. *J. Phys. Chem. Lett.* **2019**, *10*, 6590-6597.
90. Guo, S.-H.; Zhou, J.; Zhao, X.; Sun, C.-Y.; You, S.-Q.; Wang, X.-L.; Su, Z.-M., Enhanced CO₂ photoreduction via tuning halides in perovskites. *J. Catal.* **2019**, *369*, 201-208.
91. Wang, X.-D.; Huang, Y.-H.; Liao, J.-F.; Jiang, Y.; Zhou, L.; Zhang, X.-Y.; Chen, H.-Y.; Kuang, D.-B., In situ construction of a Cs₂SnI₆ perovskite nanocrystal/SnS₂ nanosheet heterojunction with boosted interfacial charge transfer. *J. Am. Chem. Soc.* **2019**, *141*, 13434-13441.
92. Chen, K.; Deng, X.; Dodekatos, G.; Tüysüz, H., Photocatalytic polymerization of 3, 4-ethylenedioxythiophene over cesium lead iodide perovskite quantum dots. *J. Am. Chem. Soc.* **2017**, *139*, 12267-12273.
93. Zhu, X.; Lin, Y.; San Martin, J.; Sun, Y.; Zhu, D.; Yan, Y., Lead halide perovskites for photocatalytic organic synthesis. *Nat. Commun.* **2019**, *10*, 1-10.
94. Wang, K.; Lu, H.; Zhu X.; Lin, Y.; Beard, M.; Yan, Y.; Chen X., Ultrafast reaction mechanisms in perovskite doped photocatalytic C–C coupling. *ACS Energy Lett.* **2020**, *5*, 566–571.

95. Zhu, X.; Lin, Y.; Sun, Y.; Beard, M. C.; Yan, Y., Lead-halide perovskites for photocatalytic α -alkylation of aldehydes. *J. Am. Chem. Soc.* **2019**, *141*, 733-738.
96. Huang, H.; Yuan, H.; Janssen, K. P. F.; Solís-Fernández, G.; Wang, Y.; Tan, C. Y. X.; Jonckheere, D.; Debroye, E.; Long, J.; Hendrix, J.; Hofkens, J.; Steele, J. A.; Roeffaers, M. B. J., Efficient and Selective Photocatalytic Oxidation of Benzylic Alcohols with Hybrid Organic–Inorganic Perovskite Materials. *ACS Energy Lett.* **2018**, *3*, 755-759.
97. Schunemann, S.; van Gastel, M.; Tuysuz, H., A CsPbBr₃/TiO₂ Composite for Visible-Light-Driven Photocatalytic Benzyl Alcohol Oxidation. *ChemSusChem* **2018**, *11*, 2057-2061.
98. Cheng, R.; Steele, J. A.; Roeffaers, M. B.; Hofkens, J.; Debroye, E., Dual-Channel Charge Carrier Transfer in CsPbX₃ Perovskite/W₁₈O₄₉ Composites for Selective Photocatalytic Benzyl Alcohol Oxidation. *ACS Appl. Energy Mater.* **2021**, *4*, 3460-3468.
99. Wu, W.-B.; Wong, Y.-C.; Tan, Z.-K.; Wu, J., Photo-induced thiol coupling and C–H activation using nanocrystalline lead-halide perovskite catalysts. *Catal. Sci. Technol.* **2018**, *8*, 4257-4263.
100. Dai, Y.; Tüysüz, H., Lead-free Cs₃Bi₂Br₉ perovskite as photocatalyst for ring-opening reactions of epoxides. *ChemSusChem* **2019**, *12*, 2587-2592.
101. Sharma, D.; Sinha, A.; Dhayal, V. In *Fabrication of graphitic carbon nitride-based nanocomposites photocatalyst for degradation of organic pollutants: A Review*, IOP Conference Series: Earth and Environmental Science, IOP Publishing: 2021; p 012010.
102. Gao, G.; Xi, Q.; Zhou, H.; Zhao, Y.; Wu, C.; Wang, L.; Guo, P.; Xu, J., Novel inorganic perovskite quantum dots for photocatalysis. *Nanoscale* **2017**, *9*, 12032-12038.
103. Zhang, Z.; Liang, Y.; Huang, H.; Liu, X.; Li, Q.; Chen, L.; Xu, D., Stable and highly efficient photocatalysis with lead-free double-perovskite of Cs₂AgBiBr₆. *Angew. Chem. Int. Ed.* **2019**, *58*, 7263-7267.
104. Pu, Y.-C.; Fan, H.-C.; Liu, T.-W.; Chen, J.-W., Methylamine lead bromide perovskite/protonated graphitic carbon nitride nanocomposites: interfacial

- charge carrier dynamics and photocatalysis. *J. Mater. Chem. A* **2017**, *5*, 25438-25449.
105. Paul, T.; Das, D.; Das, B. K.; Sarkar, S.; Maiti, S.; Chattopadhyay, K. K., CsPbBrCl₂/g-C₃N₄ type II heterojunction as efficient visible range photocatalyst. *J. Hazard. Mater.* **2019**, *380*, 120855.
106. Zhao, Y.; Shi, H.; Hu, X.; Liu, E.; Fan, J., Fabricating CsPbX₃/CN heterostructures with enhanced photocatalytic activity for penicillins 6-APA degradation. *Chem. Eng. J.* **2020**, *381*, 122692.
107. Qian, X.; Chen, Z.; Yang, X.; Zhao, W.; Liu, C.; Sun, T.; Zhou, D.; Yang, Q.; Wei, G.; Fan, M., Perovskite cesium lead bromide quantum dots: A new efficient photocatalyst for degrading antibiotic residues in organic system. *J. Clean. Prod.* **2020**, *249*, 119335.
108. Bhattacharjee, S.; Chaudhary, S. P.; Bhattacharyya, S., Lead-Free Metal Halide Perovskite Nanocrystals for Photocatalysis in Water. **2019**.
109. Huynh, K. A.; Nguyen, D. L. T.; Nguyen, V. H.; Vo, D. V. N.; Trinh, Q. T.; Nguyen, T. P.; Kim, S. Y.; Le, Q. V., Halide perovskite photocatalysis: progress and perspectives. *J. Chem. Technol. Biotechnol.* **2020**, *95*, 2579-2596.
110. Zhang, Z.; Liang, Y.; Huang, H.; Liu, X.; Li, Q.; Chen, L.; Xu, D., Stable and Highly Efficient Photocatalysis with Lead-Free Double-Perovskite of Cs₂AgBiBr₆. *Angew. Chem. Int. Ed.* **2019**, *58*, 7263-7267

Chapter 2. Photothermal Suzuki coupling over a metal halide perovskite/Pd nanocube composite catalyst

Chunhua Wang, Bo Weng,* Masoumeh Keshavarz, Min-Quan Yang, Haowei Huang, Yang Ding, Feili Lai, Imran Aslam, Handong Jin, Giacomo Romolini, Bao-Lian Su, Julian A. Steele, Johan Hofkens* and Maarten B. J. Roefsaers*

Adapted with permission from *ACS Appl. Mater. Interfaces* **2022**, 14, 17185–17194.

Contributions

C.W., B.W., J. H. and M.B.J.R. designed the project; C.W. conducted the most experiments, including sample preparation, SEM, DRS, PL, Raman, GC, GC-MS, and activity tests; M.K., M.Q., H.H., Y.D., I.A., H.J. and G.R. performed part of the experiments; B.W., F.L., B.S., and J.A. S. supported the experiments and helped to analyze the results; Y. J. (Xiamen University) carried out the theoretical calculations; C.W. analyzed all results and wrote the draft; C.W., B.W., J.H. and M.B.J.R. together revised the manuscript with input from all the authors.

Abstract

The development of improved catalysts capable of performing the Suzuki coupling reaction has attracted considerable attention. Recent findings have shown that the use of photoactive catalysts improves the performance, while the reaction mechanism and temperature-dependence performance of such systems are still under debate. Herein, we report Pd nanocubes/CsPbBr₃ as an efficient catalyst for the photothermal Suzuki reaction. The photo-induced and thermal contribution to the overall catalytic performance has been investigated. At temperatures around and below 30 °C light controls the activity, while thermal catalysis determines the reactivity at higher temperature. The Pd/CsPbBr₃ catalyst exhibits 11 times higher activity than pure CsPbBr₃ at 30 °C due to reduced activation barrier and facilitated charge carrier dynamics. Furthermore, the alkoxide radicals (R-O[•]) for Suzuki reaction are experimentally and theoretically confirmed, and photogenerated holes are proven to be crucial for cleaving C-B bonds of phenylboronic acids to drive the reaction. This work prescribes a general strategy to study photothermal catalysis and offers a mechanistic guideline for photothermal Suzuki reactions.

2.1 Introduction

The Suzuki coupling reaction is one of the most important organic synthetic methods for C-C bond formation.^{1, 2} While the reactions were initially performed using Pd complexes as homogeneous catalyst, a lot of research has been focused on the fabrication of solid catalysts using Pd nanoparticles (NPs).³⁻⁵ Pd is the preferred catalyst for thermally driven Suzuki coupling reactions and temperature significantly influences the performance. The catalytic activity of Pd NPs is reported to be associated with the particle morphology, i.e., exposing different facets; cubic Pd has been found to present an improved reactivity due to the presence of the (100) crystal facets.⁶ Recent research has shown the possibility to enhance the Suzuki coupling reaction under light irradiation through the use of photocatalytic supports, such as TiO₂, C₃N₄, SiC, WS₂, in combination with Pd NPs.^{3, 5, 7} Yet, the temperature-dependent photocatalytic activity of Pd-photocatalytic support hybrids is seldomly investigated. Bai et al. reported photocatalytic Suzuki coupling reactions with Pd and TiO₂ decorated carbon nanofibers, and they showed that the performance increased from 30 to 50 °C.⁸ However, the precise contribution of photo- and thermal catalysis at different temperatures has not been clarified since the photoactivity of TiO₂ also improves with the increased temperature.⁹ Recently, metal halide perovskites (MHPs) have emerged as promising photocatalysts exploiting their excellent opto-electronic properties such as tunable bandgap, strong light absorption coefficient, long carrier diffusion length, small exciton binding energy, and low-cost solution-processing.¹⁰ Although MHPs-based photocatalysts have been explored for various chemical processes, their performance in driving Suzuki coupling reactions has not yet been explored.

On the other hand, the underlying reaction mechanisms of photocatalytic Suzuki couplings are still under debate. For instance, the exact role of photogenerated holes is controversial. Antonietti et al. proposed that the photoexcited holes can assist in cleaving C-B bond in phenylboronic acids,⁴ while Kim and coworkers claimed that the holes will be trapped by the solvent but not participate in the coupling reaction.⁵ Moreover, the reaction intermediates generated from the phenylboronic acids remain uncertain. Specifically, both OH⁻ and CO₃²⁻ anions have been reported to activate

phenylboronic acids to form intermediates.^{3, 4} Additionally, the alkoxide ion (EtO⁻) is also speculated to activate the phenylboronic acids,¹¹ while direct experimental evidence is lacking. Summarizing, there is no consensus on the photocatalytic Suzuki reaction mechanism.

Herein, we report Pd nanocubes (NCs) deposited on the photoactive CsPbBr₃ MHP as efficient photothermal Suzuki coupling catalyst using solar irradiation (AM 1.5G) at near ambient temperature conditions. The precise contribution of the photo-induced and thermal catalysis to the overall performance is resolved. At mild conditions, below 30 °C, the photocatalytic reaction is responsible for the majority of the conversions, while thermally driven catalysis determines the reactivity at higher temperature. Benefiting from the synergistic photothermal effect leading to a reduced activation barrier, the Pd/CsPbBr₃ catalyst exhibits 11 times higher activity than pure CsPbBr₃ and 4 times for Pd. Through advanced characterization it is shown that the CsPbBr₃ metal halide perovskite (MHP) efficiently collects the solar irradiation and the presence of Pd NPs mediates in the efficient charge extraction through Schottky barrier formation and surface defect passivation. Further, through a set of control experiments and theoretical calculations, the reaction radicals, *i.e.*, alkoxides (R-O⁻), are confirmed and the photogenerated holes are revealed to be crucial for the cleavage of the C-B bonds of phenylboronic acids to boost the Suzuki coupling reaction.

2.2 Results and discussion

To prepare the CsPbBr₃ and Pd/CsPbBr₃ hybrid catalysts, a room-temperature antisolvent precipitation method was adopted,¹² in which the Pd NCs were synthesized based on reported methods.¹³ X-ray diffraction (XRD) patterns (Figure S1) reveal that the pure CsPbBr₃ possesses an orthorhombic (*Pnma*) phase and the pure Pd has a cube morphology.^{13, 14} Due to the low Pd loading no typical diffraction peaks assigned to Pd are detected in the hybrids.¹³ Raman spectroscopy further confirms that CsPbBr₃ is the predominant material in the hybrids and Pd has no influence on the CsPbBr₃ structure (Figure S2). Scanning electron micrographs (Figure S3) show that the CsPbBr₃ and 3 wt% Pd/CsPbBr₃ composites have similar surface morphologies. Energy-dispersive

X-ray spectroscopy proves the presence of Pd, Cs, Pb and Br elements in the samples (Figure S3e). Transmission electron microscopy (TEM) (Figure S4) shows the successful deposition of Pd NCs on the surface of CsPbBr₃ in which the average size of Pd is around 17.2 ± 0.7 nm. From high-resolution TEM images, the lattice spacings of CsPbBr₃ ((110)=0.42 nm) and Pd ((200)=0.20 nm) were identified.^{13, 15} Nitrogen physisorption data (Figure S5) shows that the surface area of CsPbBr₃ is similar with that of Pd/CsPbBr₃ (Table S1), suggesting the Pd deposition has a negligible effect on the materials surface. Through inductively coupled plasma-mass spectrometry (ICP-MS) the precise amount of Pd was determined to be 2.72 wt% in the 3 wt% Pd/CsPbBr₃ composite.

Next, the photocatalytic Suzuki coupling reaction of iodobenzene with phenylboronic acid as a model reaction was performed. Without catalyst, no Suzuki coupling product was detected (Figure 1a), and the pure CsPbBr₃ shows a 11% conversion and moderate selectivity (81%) with benzene as the main side product (Figure S6) after 4 h under 1-sun solar light irradiation at 30 °C. Notably, the catalytic activity shows an impressive enhancement in the presence of Pd. The optimal 3 wt% Pd/CsPbBr₃ catalyst exhibits the highest conversion (96.5 %) with nearly 100% selectivity, an 11-fold improvement compared to pure CsPbBr₃. Further increasing Pd loading beyond 3% resulted in a reduced conversion, which could be attributed to competitive light absorption and enhanced charge recombination caused by Pd.¹⁶ Table S2 compares the catalytic performance of 3 wt% Pd/CsPbBr₃ catalyst from this work to other reported photocatalytic Suzuki coupling catalysts. The reaction protocol was further extended to the coupling of different aryl halides and phenylboronic acids (Table 1). All aryl iodides were converted into the corresponding products in high yields (entries 1-4), while the compound with electron-withdrawing substitutions (entries 1-3) show higher activity than that with electron-donating substitutions (entry 4). This can be explained by the fact that electron-withdrawing substituents result in an electron-deficient aromatic ring which facilitates the nucleophilic attack *via* the photogenerated electrons on the electron-rich Pd NPs.⁷ Besides, no steric hindrance effect was observed (entries 2 and 3). Also, phenylboronic acids with electron-donating or electron-

withdrawing substituents can easily convert into their desired products (entries 5-8), without an obvious steric hindrance effect (entries 7 and 8). Moreover, the applicability of the Pd/CsPbBr₃ catalyst for bromobenzene derivatives and aryl chlorides was also investigated (entries 9-14), and excellent performance was achieved. The results of photocatalytic coupling with different aryl halides and phenylboronic acids suggest the versatility of 3 wt% Pd/CsPbBr₃ hybrid catalyst. The effect of the light intensity on catalytic activity was investigated (Figure 1b). The purely thermal conversion was measured in the dark and the photo-induced contribution was obtained by subtracting this thermal activity from the overall photothermal conversion.³ This shows that there is an almost linear relation between the photo-induced activity and light intensity, indicating that light irradiation plays a key role in driving the Suzuki reaction in this system.^{3, 4}

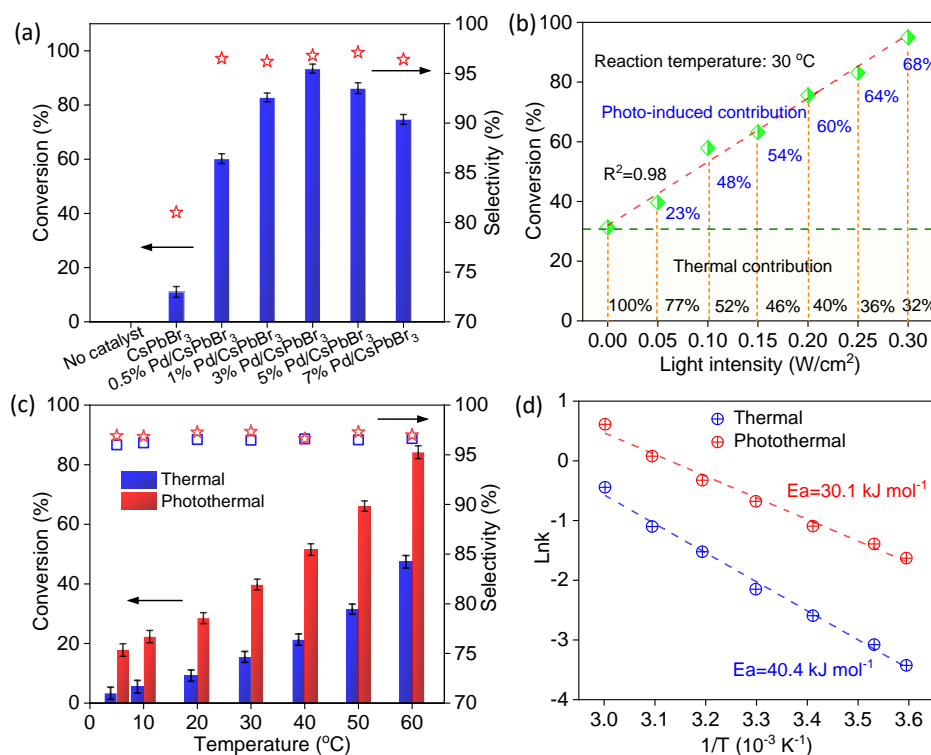
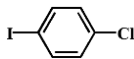
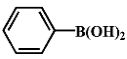
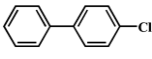
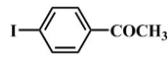
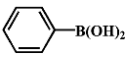
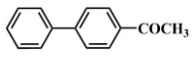
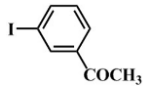
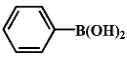
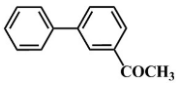
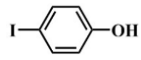
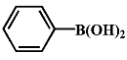
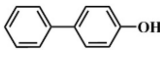
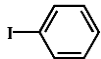
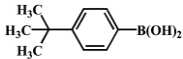
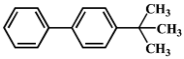
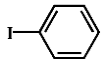
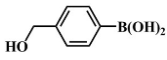
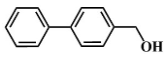
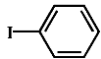
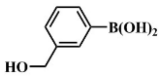
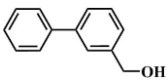
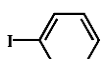
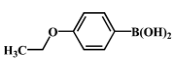
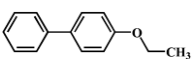
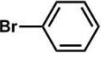
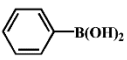
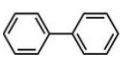
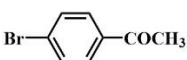
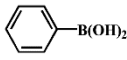

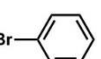
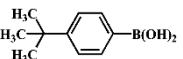
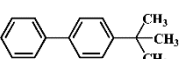
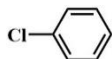
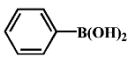
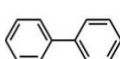
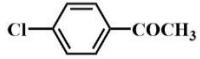
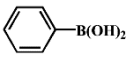
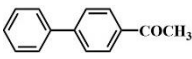
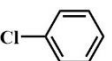
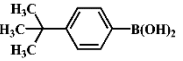
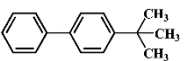


Figure 1. (a) The photocatalytic performance of Suzuki coupling reaction over CsPbBr₃ and Pd/CsPbBr₃ hybrids at 30 °C for 4 h under 1-sun irradiation. (b) The dependence of the catalytic activity of 3 wt% Pd/CsPbBr₃ on the solar light intensity at 30 °C for 4 h. (c) Thermal and photothermal Suzuki reactions under different temperatures (5-60 °C) for 1 h with 1-sun light irradiation. (d) Apparent activation energy derived *via* Arrhenius equation, where k represents the rate constant. Reaction conditions: 0.1 mmol iodobenzene, 0.12 mmol

phenylboronic acid, 15 mg catalyst, 0.4 mmol Cs₂CO₃, 3 mL ethanol, simulated solar light (150 W Xe lamp, AM 1.5G), reaction time (4 h for a-b and 1 h for c).

Table 1. The catalytic performances of 3 wt% Pd/CsPbBr₃ catalyst for Suzuki reaction with different aryl halides and phenylboronic acids.^[a]

Entry	Reactant 1	Reactant 2	Main product	Conversion (%)	Selectivity (%)
1 ^a				99.6	99.5
2 ^a				99.2	99.6
3 ^a				99.5	99.4
4 ^a				90.8	98.7
5 ^a				96.5	99.2
6 ^a				93.7	99.3
7 ^a				92.6	99.6
8 ^a				92.0	99.1
9 ^a				88.3	99.3
10 ^a				86.7	99.0
11 ^a				87.0	98.9
12 ^b				65.8	98.3
13 ^b				64.3	99.1
14 ^b				65.1	98.6

[a]Reaction conditions: 0.1 mmol aryl halides, 0.12 mmol phenylboronic acids, 15 mg catalyst, 0.4 mmol Cs₂CO₃, 3 mL ethanol, simulated solar light (150 W Xe lamp, AM 1.5G), reaction time (4 h, 30 °C). [b]Reaction conditions: 0.05 mmol aryl chlorides, 0.06 mmol phenylboronic acids, 20 mg catalyst, 0.2 mmol Cs₂CO₃, 3 mL ethanol, simulated solar light (150 W Xe lamp, AM 1.5G), reaction time (6 h, 30 °C).

To evaluate the contribution of thermal and photo-induced effect on the overall catalytic performance of the Pd/CsPbBr₃ composites, the Suzuki reaction was performed at controlled temperatures between 5 and 60 °C, while keeping the light irradiation constant at 1-sun. As shown in Figure 1c, with the increase of temperature, the catalytic performance of 3 wt% Pd/CsPbBr₃ increases gradually. Notably, below 30 °C, the photo-induced activity exceeds the thermal contribution of Pd. When using the pure constituents, for CsPbBr₃ only photo-induced activity was observed, while for Pd only thermal activity was measured. Additionally, it is worth noting that the activity of 3 wt% Pd/CsPbBr₃ is about double that of the sum of the conversions obtained by pure CsPbBr₃ and Pd (Figure S7), indicating the synergetic effect of photo and thermal.^{17, 18} By increasing reaction temperature to 60 °C, the contribution of photo-induced activity in total conversion clearly decreases. This may be attributed to the fact that thermally most of the reaction sites in Pd for Suzuki reaction are already activated and thus the effect of light on the performance is reduced accordingly. Using the temperature dependent activity data, the apparent activation energy, derived *via* the Arrhenius equation (see Supporting Information and Figure S8),¹⁸ was calculated to be 40.4 and 30.1 kJ mol⁻¹ (Figure 1d) for thermal and photothermal catalysis, respectively. To explain this favourable contribution of the photogenerated charge carriers on the Suzuki reaction, theoretical calculations indicate that the photogenerated electron can weaken the C-I in iodobenzene thus simplifying the cleavage.¹⁹ The stability tests (Figure S9a) show no significant loss in activity even after six reaction cycles with a total of 24 hours. XRD patterns do not show changes in crystal structure of the catalyst after recycling (Figure S9b), while ICP-MS tests show no Pd has leached during the reaction processes, and without changes in activity after catalytic separation

(Figure S10). *In situ* temperature dependent XRD and Raman tests (Figures S11 and S12) confirm that the stability of the material under the applied reaction conditions. Both optical (absorbance and PL) characterization and XPS show that there is no observable halide exchange during the catalytic reaction process at higher temperature (60 °C) (Figure S13).

To understand the origin of the activity enhancement in Pd/CsPbBr₃ hybrids, the photophysical properties of these materials were studied. X-ray photoelectron spectroscopy (XPS) was first performed to investigate/determine the chemical structure and valence state of the materials. Figure S14a shows the two typical Cs 3d peaks located at 724.1 and 738.2 eV, which are assigned Cs 3d_{5/2} and Cs 3d_{3/2}, respectively.²⁰ After loading the Pd NCs, these peaks shift 0.15 eV toward higher binding energy, indicating that electrons transfer from CsPbBr₃ to Pd due to the formation of a Schottky junction.²¹ As a result, the presence of Pd can mediate in the efficient charge extraction in CsPbBr₃ (vide infra). A similar shift is also found in Pb 4f and Br 3d (Figures S14b and c). Additionally, the Pd 3d peaks with binding energies of 334.6 and 339.9 eV in 3wt% Pd/CsPbBr₃ (Figure S14d) correspond to Pd 3d_{5/2} and Pd 3d_{3/2}, respectively, showing a lower binding energy as compared to metallic Pd originating from electron enrichment on the Pd NCs.³

Photoelectrochemical characterizations were used to confirm the beneficial effect of Pd in charge transfer and separation in CsPbBr₃ materials. Transient on-off photocurrent measurements (Figure 2a) show that the 3 wt% Pd/CsPbBr₃ composite displays a higher photocurrent than pure CsPbBr₃. A similar trend is found in the photocurrent response versus monochromatic light test, where an elevated current density for the Pd/CsPbBr₃ composite is observed (Figure 2b), indicating that the Pd incorporation can effectively promote the transfer and migration of photogenerated charge carriers.²² Moreover, the photocurrent density of 3 wt% Pd/CsPbBr₃ sample derived from cathodic polarization curves (Figure S15) also presents an obvious enhancement compared to pure CsPbBr₃ at the same potential range, agreeing well with bespoke observations.¹³ To understand this enhancement in photocurrent, electrochemical impedance spectroscopy (EIS) was carried out to examine the charge transfer properties of the samples.²² The charge-transfer

resistance for 3 wt% Pd/CsPbBr₃ (227 Ω) is much lower than that of CsPbBr₃ (353 Ω) (Figure 2c), indicating better efficiency in charge transfer within the Pd/CsPbBr₃, which is in agreement with its improved photocurrent.²³ Furthermore, the surface charge transfer efficiency (η_t) was calculated to be 36.5 % for CsPbBr₃ (Figure 2d); while in the presence of Pd, the η_t of Pd/CsPbBr₃ composite as high as 58.4 %, 1.6-fold higher than that of pure CsPbBr₃ (Figure S16), further confirming the faster transfer efficiency of photogenerated charge carriers.²⁴ Based on the above analyses, a schematic view representing the charge dynamics is depicted (Figure S17). Under light irradiation, the photogenerated electrons in CsPbBr₃ transfer to Pd, and the as-formed Schottky barrier at the interface will block the back-flow of electrons from Pd to CsPbBr₃, leading to efficient separation of photogenerated charge carriers.^{3, 4}

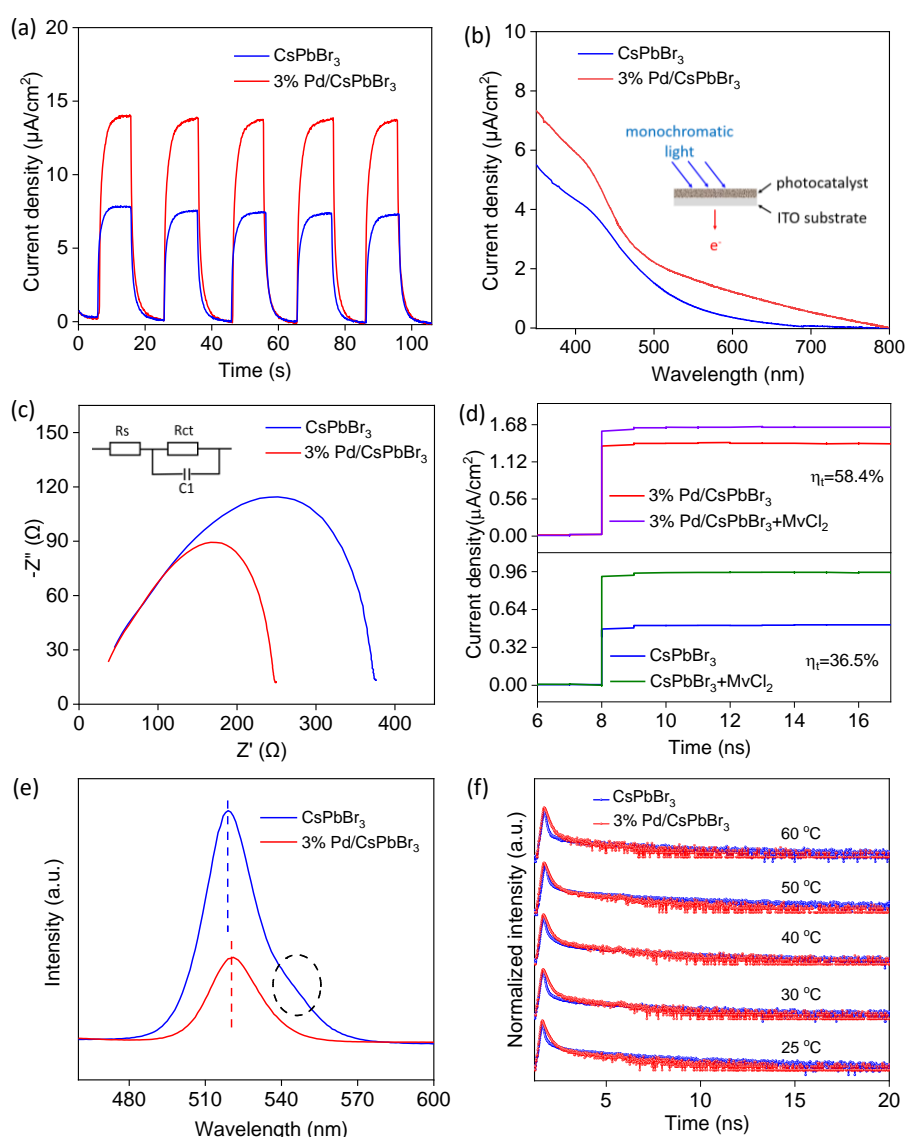


Figure 2. (a) Transient photocurrent, (b) Photocurrent response versus monochromatic light, (c) EIS Nyquist plots, (d) Surface charge transfer efficiency (η_t), (e) Steady-state PL spectra and (f) *In situ* temperature-dependent transient luminescence decays of CsPbBr₃ and 3 wt % Pd/CsPbBr₃ materials.

The optical absorption properties of the samples were characterized through UV-Vis diffuse reflection spectroscopy (DRS). The absorption spectrum of CsPbBr₃ (Figure S18a) reveals an absorption band edge at 551 nm, with a bandgap of 2.25 eV (Figure S18b).²⁵ No changes in bandgap after loading the Pd are observed, while the samples exhibit an enhanced absorption intensity at longer wavelengths, with color changing from orange-yellow to dark black (Figure S19). This can be ascribed to the light scattering of Pd and thus promoting the light absorption of CsPbBr₃ therefore contributing to catalytic activity enhancement.¹³

The photophysical processes in the CsPbBr₃ and Pd/CsPbBr₃ materials were examined through steady-state photoluminescence (PL) spectroscopy. The PL spectrum of CsPbBr₃ (Figure 2e) shows an emission peak at around 525 nm,²⁶ with a small shoulder located at ~550 nm which can be attributed to either surface defect or self-absorption.^{27, 28} A lower PL intensity in Pd/CsPbBr₃ hybrids was observed compared to CsPbBr₃ due to the suppressed radiative recombination.²¹ The small shoulder in the PL spectrum disappeared after the incorporation of Pd (Figures 2e and S20), which can be attributed to the surface passivation by Pd originating by reducing the amount of Pb defects at the surface similar to ligand-capped surfaces, and thus reducing an unwanted recombination pathway for the photogenerated charge carriers.^{29, 30} Additionally, a red shift of the PL peak of the 3 wt% Pd/CsPbBr₃ sample is observed, which is further investigated by temperature-dependent (4.2-300 K) steady-state PL (Figure S21). Note that the PL peak of CsPbBr₃ maxima exhibit a blue-shift with increasing temperature (Figure S21c), originating from the temperature induced lattice expansion and its competition with the electron-phonon coupling.³¹ The electron-phonon coupling constants of these two systems, extracted from the temperature-dependence of the emission line

width,³² are similar (Figure S21d), indicating no fundamental changes in the electron-phonon interactions in these two samples. Additionally, low temperature (77 K) absorption measurements show that both CsPbBr₃ and the Pd/CsPbBr₃ composite have similar absorption band edges (Figure S22), further confirming that the Pd does not affect the intrinsic properties of CsPbBr₃. To better understand the charge dynamics behind the temperature dependent activity behaviour, *in situ* temperature-dependent transient PL was performed (Figure 2f). The PL decays of the samples are analyzed using a sum of two exponential decays, where the extracted two decay constants τ_1 and τ_2 are associated with the bound exciton and free exciton recombination, respectively.³³ The lifetime of the 3 wt% Pd/CsPbBr₃ slightly increases as a function of temperature from 25 to 60 °C as compared to CsPbBr₃ (Figure S23), which can be attributed to the CsPbBr₃ surface defect passivation by Pd.¹⁹ To sum up, the above analyses revealed that the nature of the enhanced catalytic performance in Pd/CsPbBr₃ hybrids originating from the improved photoelectric properties. Moreover, the Pd nanoparticles in the catalyst composites not only serve as an electron reservoir enhancing the photogenerated charge separation in CsPbBr₃ (Figures 2 and S16) but also as source of catalytic sites for Suzuki couplings (Figure 1c and S7).

Next, the Suzuki coupling reaction mechanism was then systematically investigated. For the initiation of Suzuki reactions, anions like OH⁻ and CO₃²⁻ are generally reported to activate the phenylboronic acid to form C₆H₅-B(OH)₃⁻ and C₆H₅-B(OH)₂CO₃²⁻ intermediates to facilitate the C-B bond cleavage.^{5, 34} However, these speculated intermediates and their final products have not been experimentally demonstrated.^{5,7} To elucidate this issue, gas chromatography-mass spectrometry (GC-MS) was employed. When using ethanol as the solvent, besides the desired biphenyl product, the triethyl borate compound was also detected (Figure S24). Besides, the reaction can also be driven by the EtONa compound (Figure S25). Thus, we deduce that the ethoxide (EtO⁻) may interact with phenylboronic acid to form a boronate complex C₆H₅-B(OH)₂EtO⁻. This hypothesis was theoretically confirmed by DFT calculation, where the bond dissociation energy of C-B bond of various phenylboronic acid compounds was calculated (Table S3). The results show

that the C-B bond dissociation energy of $\text{C}_6\text{H}_5\text{-B(OH)}_2\text{EtO}^-$ radicals is $317.48 \text{ kJ mol}^{-1}$, which is lower than that of $\text{C}_6\text{H}_5\text{-B(OH)}_2$ ($468.78 \text{ kJ mol}^{-1}$), and $\text{C}_6\text{H}_5\text{-B(OH)}_2\text{CO}_3^{2-}$ ($325.56 \text{ kJ mol}^{-1}$) and $\text{C}_6\text{H}_5\text{-B(OH)}_3^-$ ($320.79 \text{ kJ mol}^{-1}$), indicating that the EtO^- is more conducive to boost the C-B bond cleavage of phenylboronic acid. Similarly, when using isopropanol and butanol solvents, both biphenyl and boron-alcohol compounds (triisopropyl borate and tributyl borate, Figures S26-29) can be detected. Tributyl borate cannot be detected by GC-MS (Figure S27), even for the pure compound (Figure S28). Instead, Raman measurements confirm the existence of this product in the reaction (Figure S29). These experimental and theoretical results confirmed the key role of alkoxide (R-O^-) like EtO^- in triggering the Suzuki reaction.

To further confirm the proposed reaction mechanism, the catalytic performance in protic solvents (ethanol, isopropanol and butanol) and aprotic solvents (acetonitrile, acetone and dichloromethane) was compared. Figure 3a shows that protic solvents exhibit high activities, while no biphenyl product is detected in aprotic solvents (Figures S30 and S31). However, when ethanol was added to acetonitrile, a measurable conversion was measured (Figure 3b), suggesting the critical role of alkoxide in the Suzuki reaction.^{5, 34} Subsequently, the effects of different bases were examined. Figure 3c shows the reaction could not proceed without a base, as it is necessary to dissociate the alcohols. All carbonate bases are effective, while hydroxide bases yield moderate conversion. This can be attributed to the fact that abundant free and reactive hydroxides interact strongly with Pd, thus covering active sites, leading to the lower catalytic performance.³⁵

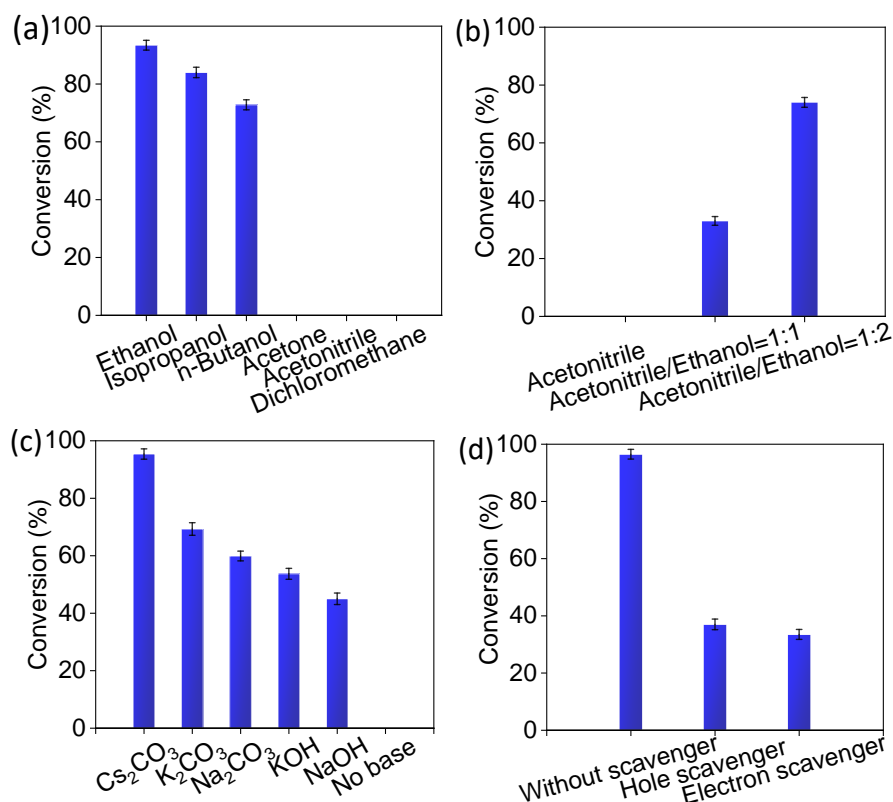


Figure 3. Effects of (a, b) solvents, (c) bases and (d) scavengers on the catalytic activity over 3 wt% Pd/CsPbBr₃. Reaction conditions: 0.1 mmol iodobenzene, 0.12 mmol phenylboronic acid, 15 mg catalyst, 0.4 mmol base, 3 mL solvent, simulated solar light (150 W Xe lamp, AM 1.5G), reaction time (4 h).

Finally, the influence of photoexcited charge carriers on the Suzuki coupling was studied by using scavengers. With electron scavenger 5,5-Dimethyl-1-pyrroline N-oxide,^{3, 7} the conversion is decreased to the same level as no-light conditions (Figure 3d), suggesting that the photon-mediated reaction is quenched. Since ethanol is considered as a holes scavenger, triethanolamine possessing lower oxidation potential than ethanol,³⁶ was employed to trap the holes. A dramatic decrease in the conversion is observed. These results show that the coupling reaction cannot proceed smoothly without photogenerated electrons and holes. Moreover, no oxidation products of solvents and reduction products (such as H₂) were detected *via* GC and GC-MS measurements (Figures S24, S26-27), indicating that holes were not transferred to the solvent and oxidize it during the reaction process.

Based on above results, we propose a plausible mechanism that is responsible for photothermal catalytic Suzuki couplings over the Pd/CsPbBr₃ catalyst (Figure 4, Equation S1). Under light irradiation, CsPbBr₃ absorbs solar light to produce electron-hole pairs. Electrons transfer to Pd through the Schottky contact,^{3, 4} and the electron-rich Pd can activate the C-X bond of aryl halides and produce Pd-adsorbed aryl.^{19, 37} Meanwhile, phenylboronic acids and alkoxide form a boron-alkoxide complex, where holes assist in the activation of this molecule by weakening the C-B bonds.^{4, 7} These reactions can be more effective due to the reduced activation barrier originating from the photo-thermal synergistic effect. When the activated phenylboronic acids complex transfers to the redox-activated aryl halides, the coupling reaction occurs easily to produce the desired biphenyl products.

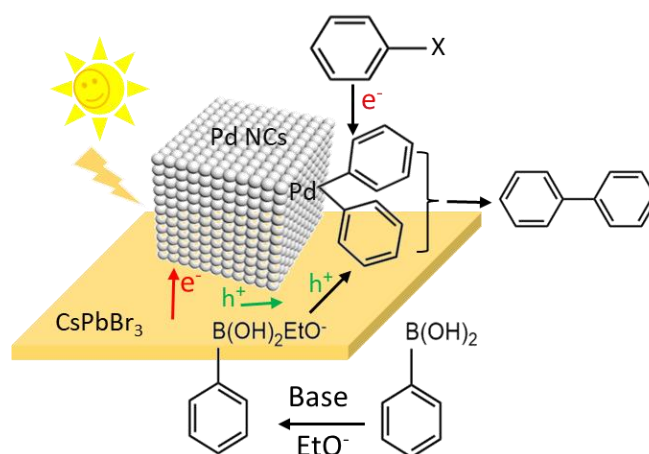


Figure 4. A Proposed mechanism for the Suzuki coupling reactions over Pd/CsPbBr₃ catalyst.

2.3 Conclusions

In summary, the photothermal and thermal contribution to the catalytic activity and the mechanism of the Suzuki reaction were investigated using a Pd NCs-decorated MHP (Pd/CsPbBr₃) photothermal catalyst. Photo and thermal contributions were derived from the temperature-dependent experiments, showing that light plays a key role at mild conditions (< 30 °C) while thermal catalysis component takes over at higher temperatures. At room temperature, the reduced activation energy of the photothermal processes, results in an over 11 times higher activity for Pd/CsPbBr₃ than for pure CsPbBr₃. Detailed optical

and photoelectrochemical studies showed that Pd deposition not only promotes the separation of photogenerated charge carriers, but it also passivates CsPbBr₃ surface defects. Furthermore, the reaction mechanism of the photocatalytic Suzuki process was experimentally and theoretically demonstrated. This work provides a new perspective to study photothermal catalysis and offers mechanistic insights in the photocatalytic Suzuki reaction.

2.4 Experimental section

Materials

Lead(II) bromide ($\geq 98\%$), potassium bromide ($\geq 99\%$), L-ascorbic acid (99%), poly(vinyl pyrrolidone) (PVP, M.W. z 55 000), cesium carbonate (99.9%), sodium carbonate ($\geq 99.5\%$) potassium carbonate ($\geq 99\%$), sodium hydroxide(98%), potassium hydroxide (pellets for analysis), iodobenzene (98%), phenylboronic acid (95%), acetonitrile ($\geq 99.8\%$), dichloromethane ($\geq 99.8\%$), 4-chlorobiphenyl (99%), 1-chloro-4-iodobenzene (99%), acetaldehyde diethyl acetal (99%), 3-iodoacetophenone (97%), 4-ethoxyphenylboronic acid (99%), 4-tert-butylphenylboronic acid ($\geq 95\%$), 4-iodoacetophenone ($\geq 97\%$), 1-butanol (99.8%) and tributyl borate ($\geq 99\%$) were purchased from Sigma-Aldrich. Ethanol (absolute, $\geq 99.8\%$) and acetone ($\geq 99.8\%$) were purchased from Fisher Chemical. 3-(hydroxymethyl)phenylboronic acid and 1-propanol ($\geq 99.5\%$) were bought from Honeywell. Dimethyl sulfoxide (DMSO, anhydrous, Max. 0.005% water), 2-propanol (99.9%) and toluene (99%) were supplied by VWR chemicals. Cesium bromide (99.9%), potassium palladium(II) chloride (99.9%), 4-(hydromethyl)benzeneboronic acid (98%) and trifluorotoluene (99%) were purchased from Alfa Aesar. The Milli-Q water was obtained from the Milli-Q System. All chemicals were used without further purification.

Photocatalyst preparation

Preparation of CsPbBr₃ catalyst

CsPbBr₃ was synthesized at room temperature by the anti-solvent precipitation method.¹² First, lead(II) bromide (PbBr₂) and cesium bromide (CsBr) were dissolved in dimethyl sulfoxide (DMSO) at a precursor concentration of 0.3 M

with a molar ratio of 1:1. After the PbBr_2 and CsBr precursors were fully dissolved, the precursor solution was added into toluene solution to get the CsPbBr_3 suspension. After washing twice, the suspension was dried in a vacuum oven at 70 °C overnight.

Synthesis of palladium nanocubes (Pd NCs)

Palladium nanocubes (Pd NCs) were synthesized according to previous method.¹³ First of all, 105 mg poly(vinyl pyrrolidone) (PVP), 60 mg L-ascorbic acid (AA) and 600 mg of KBr were put in an 8 mL aqueous solution, and pre-heated under magnetic stirring at 80 °C for 10 min. Secondly, 63 mg potassium palladium(II) chloride (K_2PdCl_4) was dissolved in 3.0 mL aqueous solution, then the K_2PdCl_4 solution was added into the above solution and kept stirring at 80 °C for 3 h, where PVP, AA and KBr acted as a stabilizer, reductant, capping agent, respectively. Finally, the Pd NCs product was collected by centrifugation and washed with ethanol, and re-dispersed in ethanol at a concentration of 1 mg/mL.

Fabrication of Pd/CsPbBr₃ composites

A series of x wt% Pd/CsPbBr₃ catalysts were synthesized at room temperature by the similar precipitation method mentioned above. In a typical experiment (3 wt% Pd/CsPbBr₃), 100 mg CsPbBr₃ powder was first added to 15 mL ethanol solution and kept stirring for 30 min. After that, 20 mL of ethanol solution containing 3 mg Pd NCs was added dropwise into the vigorously stirred CsPbBr₃ suspension. Then the mixture was kept stirring at room temperature for 12 h. Finally, the Pd/CsPbBr₃ suspension was washed twice, and collected by centrifugation and dried in a vacuum oven at 70 °C.

Characterization

X-ray diffraction (XRD) patterns of the samples were recorded with a Malvern PANalytical Empyrean diffractometer with Bragg-Brentano geometry, using a PIXcel3D solid-state detector and a Cu anode, and the diffractogram was recorded in the 2θ ranging from 10 to 70 degrees with a step size of 0.0131° and an integration time of 150 s/step. For the temperature-dependent XRD

patterns, the diffractometer was equipped with an Anton Paar TTK 600 low-temperature chamber with a CCU 100 control unit as the heating stage. The temperature was varied from 30 °C up to 60 °C. Each diffractogram was recorded every 10 °C where the chosen temperature was kept for 5 min before the measurement. The sample was deposited as a powder bed and heated at 10°C/min in N₂. Ultraviolet-visible spectrophotometer (UV-Vis, Lambda-950) was employed to obtain the optical properties of the samples by UV-vis diffuse reflectance spectroscopy (DRS) in the wavelength 300-800 nm with 1 nm increment, where BaSO₄ and black carbon were used as the references. Scanning electron micrographs of samples were recorded by scanning electron microscopy (SEM, FEI-Q FEG250). Transmission electron microscopy (TEM) and high-resolution transmission electron microscopy (HRTEM) were analysed using a JEOL model JEM 2010 EX instrument at an acceleration voltage of 200 kV. X-ray photoelectron spectroscopy (XPS, Al K α X-ray source, 1486.6 eV) was employed to investigate the chemical structure and valence state of the elements of the catalysts, and the C 1s signal was set to a position of 284.6 eV. Electrochemical impedance spectroscopy, cathodic polarization curves and photocurrent response, were made using a standard three-electrode setup. Ag/AgCl electrode was employed as the reference electrode, and a platinum sheet was used as the counter electrode. The working electrode was deposited on a cleaned indium tin oxide (ITO) substrate. More specifically, firstly, 10 mg powder photocatalyst was fully dispersed in 1 mL toluene by sonication. Then 20 μ L slurry solution was dropped onto the ITO substrate where the exposed area of the working electrode was fixed at 0.25 cm² by using Scotch tape to protect the boundary of the ITO substrate, and dried at 80 °C for 2 h to improve adhesion. After that, the Scotch tape was unstuck, followed by isolating the uncoated electrode with epoxy resin. Connection to the CsPbBr₃ working electrode was immersed in the electrolyte solution. 0.1 M tetrabutylammonium hexafluorophosphate (TBAPF₆) dissolved in dichloromethane (DCM) solution was used as the electrolyte. Electrochemical impedance spectra were obtained on an electrochemical workstation by applying an alternating current (AC) voltage (5 mV amplitude) in a frequency range from 10 KHz to 5 MHz with the open circuit potential of 0.2 V under simulated solar light. Photocurrent

response measurements were performed as that of impedance spectra. Cathodic polarization curves were achieved via linear sweep voltammetry technique with a scan rate of 0.2 mV/s. Raman measurements were performed using an upright optical microscope (BX53, Olympus, Japan) equipped with a motorized stage (Märzhäuser Wetzlar GmbH, Germany) on a commercial Raman setup (MonoVista CRS+, S&I GmbH, Germany). Continuous-wave laser light from 785 nm laser (IPS, USA) with an average power of 5 mW was focused onto the sample with a 50x objective (MPLN, Olympus, Japan). After collecting light by the same objective, the Raman scattered light from the sample was filtered using a long-pass edge filter (LP02-785RE-25, Semrock, USA) and passed through a 100 μm confocal pinhole. Afterwards, the signal is sent to a monochromator (SpectraPro HRS-500, Princeton Instruments, USA) equipped with a grating of 1200 grooves/mm. The signal is then directed to a CCD camera (Newton 920, Andor, UK) for recording. The measurements at different temperatures were performed using a temperature-controlled stage (Linkam Scientific Instruments, UK). The acquisition time was set to 1 s with averages of 5 acquisitions to increase the signal-to-noise ratio. For the temperature-dependent photoluminescence (PL) measurements, a He flow cryostat in which the temperature can be varied from 4.2 to 300 K was used. The sample was excited with a solid-state laser (Thorlabs M365LP1 with driver DC2200) operating at 365 nm *via* a 550 μm core optical fiber. The PL spectra were collected in an increment of 5 K through 11 optical fibers surrounding the excitation fiber. The fibers were coupled to a LOT-QD Shamrock F/4 spectrometer with an electron-multiplying charge-coupled detector iXon DV887. Time-resolved PL spectra were recorded on a Leica DMI8 system. As an excitation source, a pulsed white light laser (SuperK Extreme EXW-12, NKT Photonics) operating at 405 nm and set at a repetition rate of 20 MHz and a fluence of 2 $\mu\text{J mm}^{-2}$ was employed. The samples were mounted on a Linkam stage where the temperature can be varied between room temperature and 500 K. The samples were illuminated through an air objective of an inverted microscope system (Leica DMI8). The fluorescence photons were detected by an avalanche photodiode (SPCM-AQR-14, Perkin–Elmer) *via* the same objective passing through dichroic and cut-off filters. Photon counting and time

tagging were performed within a TimeHarp 200 module (PicoQuant), with a time resolution of 29 ps per channel. The fluorescence lifetime images were analyzed using SymphoTime 32 software (PicoQuant). All calculations were carried out with the Gaussian 16 program. The B3LYP/6-311+G(3df,2p) was used for all geometry optimizations, vibrational frequency and single-point energy calculations.

(Photo)thermal catalytic coupling reaction

All Suzuki cross-coupling reactions were conducted in a 25 mL quartz reactor. In a typical experiment, 0.1 mmol iodobenzene, 0.12 mmol phenylboronic acid, 0.4 mmol Cs₂CO₃ and 15 mg catalyst were mixed in 3 mL ethanol, then the reactant mixture and solvent were evacuated by a mechanical pump to remove air completely and protected by an Ar atmosphere before irradiation. The mixture was stirred continuously under 1-sun solar irradiation (AM 1.5G) with a 150 W Xe lamp for 4 h. The temperature of the reaction system was accurately controlled within the temperature window 5-60 °C and kept 1-sun solar light intensity. After the reaction, the mixture was centrifuged, and the filtrates were analyzed by GC to obtain the conversion of iodobenzene. The conversion and selectivity of iodobenzene were defined as follows:

$$\text{Conversion (\%)} = [(C_0 - C_A)/C_0] \times 100\%$$

$$\text{Selectivity (\%)} = [C_B/(C_0 - C_A)] \times 100\%$$

Where C₀ is the initial concentration of iodobenzene, C_A and C_B are the concentrations of the iodobenzene and corresponding product of the reaction, respectively.

2.5 References

- (1) Beletskaya, I. P.; Alonso, F.; Tyurin, V., The Suzuki-Miyaura Reaction after the Nobel Prize. *Coord. Chem. Rev.* **2019**, *385*, 137-173.
- (2) Gu, Q.; Jia, Q.; Long, J.; Gao, Z., Heterogeneous Photocatalyzed C–C Cross-coupling Reactions Under Visible-light and Near-infrared Light Irradiation. *ChemCatChem* **2019**, *11*, 669-683.

- (3) Jiao, Z.; Zhai, Z.; Guo, X.; Guo, X.-Y., Visible-Light-Driven Photocatalytic Suzuki–Miyaura Coupling Reaction on Mott–Schottky-Type Pd/SiC Catalyst. *J. Phys. Chem. C* **2015**, *119*, 3238-3243.
- (4) Li, X.-H.; Baar, M.; Blechert, S.; Antonietti, M., Facilitating Room-Temperature Suzuki Coupling Reaction with Light: Mott-Schottky Photocatalyst for C-C-coupling. *Sci. Rep.* **2013**, *3*, 1-6.
- (5) Raza, F.; Yim, D.; Park, J. H.; Kim, H. I.; Jeon, S. J.; Kim, J. H., Structuring Pd Nanoparticles on 2H-WS₂ Nanosheets Induces Excellent Photocatalytic Activity for Cross-Coupling Reactions under Visible Light. *J. Am. Chem. Soc.* **2017**, *139*, 14767-14774.
- (6) Collins, G.; Schmidt, M.; O'Dwyer, C.; Holmes, J. D.; McGlacken, G. P., The Origin of Shape Sensitivity in Palladium-catalyzed Suzuki–Miyaura Cross Coupling Reactions. *Angew. Chem. Int. Ed.* **2014**, *53*, 4142-4145.
- (7) Rohani, S.; Ziarati, A.; Ziarani, G. M.; Badiei, A.; Burgi, T., Engineering of Highly Active Au/Pd Supported on Hydrogenated Urchin-Like Yolk@Shell TiO₂ for Visible Light Photocatalytic Suzuki Coupling. *Catal. Sci. Technol.* **2019**, *9*, 3820-3827.
- (8) Wang, J.; Bai, J.; Liang, H.; Li, C., Photothermal Catalytic Effect of Pd-TiO₂/CNFs Composite Catalyst in Suzuki Coupling Reaction. *Colloids Surf. A Physicochem. Eng. Asp.* **2019**, *572*, 283-289.
- (9) Meng, F.; Liu, Y.; Wang, J.; Tan, X.; Sun, H.; Liu, S.; Wang, S., Temperature Dependent Photocatalysis of g-C₃N₄, TiO₂ and ZnO: Differences in Photoactive Mechanism. *J. Colloid Interface Sci.* **2018**, *532*, 321-330.
- (10) Huang, H.; Pradhan, B.; Hofkens, J.; Roeloffs, M. B.; Steele, J. A., Solar-Driven Metal Halide Perovskite Photocatalysis: Design, Stability, and Performance. *ACS Energy Lett.* **2020**, *5*, 1107-1123.
- (11) Li, W.; Zhang, B.; Li, X.; Zhang, H.; Zhang, Q., Preparation and Characterization of Novel Immobilized Fe₃O₄@SiO₂@mSiO₂-Pd(0) Catalyst with Large Pore-size Mesoporous for Suzuki Coupling Reaction. *Appl. Catal. A: Gen.* **2013**, *459*, 65-72.
- (12) Huang, H.; Yuan, H.; Janssen, K. P.; Solís-Fernández, G.; Wang, Y.; Tan, C. Y.; Jonckheere, D.; Debroye, E.; Long, J.; Hendrix, J., Efficient and Selective

Photocatalytic Oxidation of Benzylic Alcohols with Hybrid Organic–inorganic Perovskite Materials. *ACS Energy Lett.* **2018**, *3*, 755-759.

(13) Weng, B.; Quan, Q.; Xu, Y.-J., Decorating Geometry- and Size-controlled sub-20 nm Pd Nanocubes onto 2D TiO₂ Nanosheets for Simultaneous H₂ Evolution and 1,1-diethoxyethane Production. *J. Mater. Chem. A* **2016**, *4*, 18366-18377.

(14) Zhang, M.; Zheng, Z.; Fu, Q.; Chen, Z.; He, J.; Zhang, S.; Yan, L.; Hu, Y.; Luo, W., Growth and Characterization of All-inorganic Lead Halide Perovskite Semiconductor CsPbBr₃ Single Crystals. *CrystEngComm* **2017**, *19*, 6797-6803.

(15) Chen, M.; Hu, H.; Tan, Y.; Yao, N.; Zhong, Q.; Sun, B.; Cao, M.; Zhang, Q.; Yin, Y., Controlled Growth of Dodecapod-branched CsPbBr₃ Nanocrystals and Their Application in White Light Emitting Diodes. *Nano Energy* **2018**, *53*, 559-566.

(16) Huang, H.; Yuan, H.; Zhao, J.; Solis-Fernandez, G.; Zhou, C.; Seo, J. W.; Hendrix, J.; Debroye, E.; Steele, J. A.; Hofkens, J., C (sp³)–H Bond Activation by Perovskite Solar Photocatalyst Cell. *ACS Energy Lett.* **2018**, *4*, 203-208.

(17) Zhu, L.; Gao, M.; Peh, C. K. N.; Ho, G. W., Solar-driven Photothermal Nanostructured Materials Designs and Prerequisites for Evaporation and Catalysis Applications. *Mater. Horiz.* **2018**, *5*, 323-343.

(18) Kang, L.; Liu, X. Y.; Wang, A.; Li, L.; Ren, Y.; Li, X.; Pan, X.; Li, Y.; Zong, X.; Liu, H.; Frenkel, A. I.; Zhang, T., Photo–Thermo Catalytic Oxidation over a TiO₂-WO₃-Supported Platinum Catalyst. *Angew. Chem. Int. Ed.* **2020**, *59*, 12909-12916.

(19) Xiao, Q.; Sarina, S.; Jaatinen, E.; Jia, J.; Arnold, D. P.; Liu, H.; Zhu, H., Efficient Photocatalytic Suzuki Cross-coupling Reactions on Au–Pd Alloy Nanoparticles under Visible Light Irradiation. *Green Chem.* **2014**, *16*, 4272.

(20) Chang, Y.; Yoon, Y. J.; Li, G.; Xu, E.; Yu, S.; Lu, C.-H.; Wang, Z.; He, Y.; Lin, C. H.; Wagner, B. K.; Tsukruk, V. V.; Kang, Z.; Thadhani, N.; Jiang, Y.; Lin, Z., All-Inorganic Perovskite Nanocrystals with a Stellar Set of Stabilities and Their Use in White Light-Emitting Diodes. *ACS Appl. Mater. Interfaces* **2018**, *10*, 37267-37276.

(21) Lu, S.; Weng, B.; Chen, A.; Li, X.; Huang, H.; Sun, X.; Feng, W.; Lei, Y.; Qian, Q.; Yang, M.-Q., Facet Engineering of Pd Nanocrystals for Enhancing

Photocatalytic Hydrogenation: Modulation of the Schottky Barrier Height and Enrichment of Surface Reactants. *ACS Appl. Mater. Interfaces* **2021**, *13*, 13044-13054.

(22) Yan, M.; Hua, Y.; Zhu, F.; Gu, W.; Jiang, J.; Shen, H.; Shi, W., Fabrication of Nitrogen Doped Graphene Quantum Dots-BiOI/MnNb₂O₆ pn Junction Photocatalysts with Enhanced Visible Light Efficiency in Photocatalytic Degradation of Antibiotics. *Appl. Catal. B: Environ.* **2017**, *202*, 518-527.

(23) Huang, H.; Zhou, C.; Jiao, X.; Yuan, H.; Zhao, J.; He, C.; Hofkens, J.; Roeffaers, M. B.; Long, J.; Steele, J. A., Subsurface Defect Engineering in Single-unit-cell Bi₂WO₆ Monolayers Boosts Solar-driven Photocatalytic Performance. *ACS Catal.* **2019**, *10*, 1439-1443.

(24) Feng, C.; Tang, L.; Deng, Y.; Wang, J.; Liu, Y.; Ouyang, X.; Yang, H.; Yu, J.; Wang, J., A Novel Sulfur-assisted Annealing Method of g-C₃N₄ Nanosheet Compensates for the Loss of Light Absorption with Further Promoted Charge Transfer for Photocatalytic Production of H₂ and H₂O₂. *Appl. Catal. B: Environm.* **2021**, *281*, 119539.

(25) Liang, J.; Wang, C.; Wang, Y.; Xu, Z.; Lu, Z.; Ma, Y.; Zhu, H.; Hu, Y.; Xiao, C.; Yi, X., All-inorganic Perovskite Solar Cells. *J. Am. Chem. Soc.* **2016**, *138*, 15829-15832.

(26) Xu, Y. F.; Yang, M. Z.; Chen, B. X.; Wang, X. D.; Chen, H. Y.; Kuang, D. B.; Su, C. Y., A CsPbBr₃ Perovskite Quantum Dot/Graphene Oxide Composite for Photocatalytic CO₂ Reduction. *J. Am. Chem. Soc.* **2017**, *139*, 5660-5663.

(27) Lee, S. M.; Moon, C. J.; Lim, H.; Lee, Y.; Choi, M. Y.; Bang, J., Temperature-Dependent Photoluminescence of Cesium Lead Halide Perovskite Quantum Dots: Splitting of the Photoluminescence Peaks of CsPbBr₃ and CsPb(Br/I)₃ Quantum Dots at Low Temperature. *J. Phys. Chem. C* **2017**, *121*, 26054-26062.

(28) Schötz, K.; Askar, A. M.; Peng, W.; Seeberger, D.; Gujar, T. P.; Thelakkat, M.; Köhler, A.; Huettner, S.; Bakr, O. M.; Shankar, K., Double Peak Emission in Lead Halide Perovskites by Self-absorption. *J. Mater. Chem. C* **2020**, *8*, 2289-2300.

- (29) Wang, L.; Zhou, H.; Hu, J.; Huang, B.; Sun, M.; Dong, B.; Zheng, G.; Huang, Y.; Chen, Y.; Li, L., A Eu^{3+} - Eu^{2+} Ion Redox Shuttle Imparts Operational Durability to Pb-I Perovskite Solar Cells. *Science* **2019**, *363*, 265-270.
- (30) Guo, D.; Bartesaghi, D.; Wei, H.; Hutter, E. M.; Huang, J.; Savenije, T. J., Photoluminescence from Radiative Surface States and Excitons in Methylammonium Lead Bromide Perovskites. *J. Phys. Chem. Lett.* **2017**, *8*, 4258-4263.
- (31) Zhang, D.; Eaton, S. W.; Yu, Y.; Dou, L.; Yang, P., Solution-phase Synthesis of Cesium Lead Halide Perovskite Nanowires. *J. Am. Chem. Soc.* **2015**, *137*, 9230-9233.
- (32) Wright, A. D.; Verdi, C.; Milot, R. L.; Eperon, G. E.; Pérez-Osorio, M. A.; Snaith, H. J.; Giustino, F.; Johnston, M. B.; Herz, L. M., Electron-phonon Coupling in Hybrid Lead Halide Perovskites. *Nat. Commun.* **2016**, *7*, 1-9.
- (33) Wang, C.; Huang, H.; Weng, B.; Verhaeghe, D.; Keshavarz, M.; Jin, H.; Liu, B.; Xie, H.; Ding, Y.; Gao, Y.; Yuan, H.; Steele, J. A.; Hofkens, J.; Roeffaers, M. B., Planar Heterojunction Boosts Solar-driven Photocatalytic Performance and Stability of Halide Perovskite Solar Photocatalyst cell. *Appl. Catal. B: Environ.* **2022**, *301*, 120760.
- (34) Yim, D.; Raza, F.; Park, J. H.; Lee, J. H.; Kim, H. I.; Yang, J. K.; Hwang, I. J.; Kim, J. H., Ultrathin WO_3 Nanosheets Converted from Metallic WS_2 Sheets by Spontaneous Formation and Deposition of PdO Nanoclusters for Visible Light-Driven C-C Coupling Reactions. *ACS Appl. Mater. Interfaces* **2019**, *11*, 36960-36969.
- (35) Briggs, B. D.; Pekarek, R. T.; Knecht, M. R., Examination of Transmetalation Pathways and Effects in Aqueous Suzuki Coupling Using Biomimetic Pd Nanocatalysts. *J. Phys. Chem. C* **2014**, *118*, 18543-18553.
- (36) Wang, M.; Shen, S.; Li, L.; Tang, Z.; Yang, J., Effects of Sacrificial Reagents on Photocatalytic Hydrogen Evolution over Different Photocatalysts. *J. Mater. Sci.* **2017**, *52*, 5155-5164.
- (37) Wang, Z. J.; Ghasimi, S.; Landfester, K.; Zhang, K. A. I., Photocatalytic Suzuki Coupling Reaction Using Conjugated Microporous Polymer with Immobilized Palladium Nanoparticles under Visible Light. *Chem. Mater.* **2015**, *27*, 1921-1924.

2.6 Appendix to Chapter 2

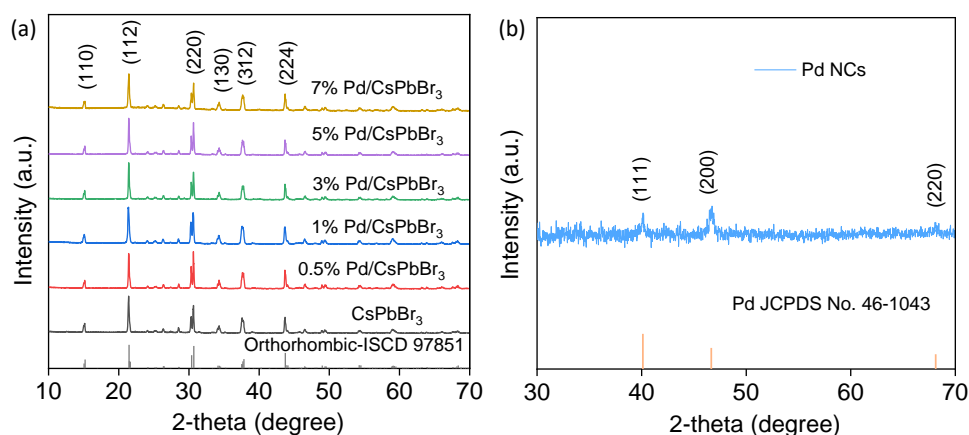


Figure S1. XRD patterns of (a) CsPbBr₃ and Pd/CsPbBr₃ composites and (b) Pd NCs.

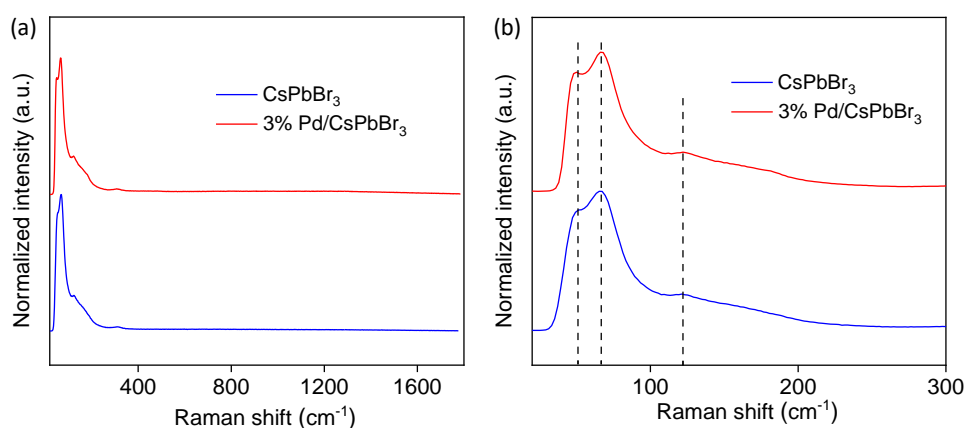


Figure S2. (a) Raman spectra and (b) magnified view of Raman spectra of CsPbBr₃ and 3% Pd/CsPbBr₃ in the range of 20-300 cm⁻¹ materials, respectively. The vibration peaks located at 52 and 67 cm⁻¹ are assigned to the vibrational mode of the [CsBr₆]⁴⁻ octahedron, and the peak at 120 cm⁻¹ is assigned to the motion of Cs⁺ cations.¹⁻³ This result confirms that CsPbBr₃ is the predominant species in the 3% Pd/CsPbBr₃ samples.

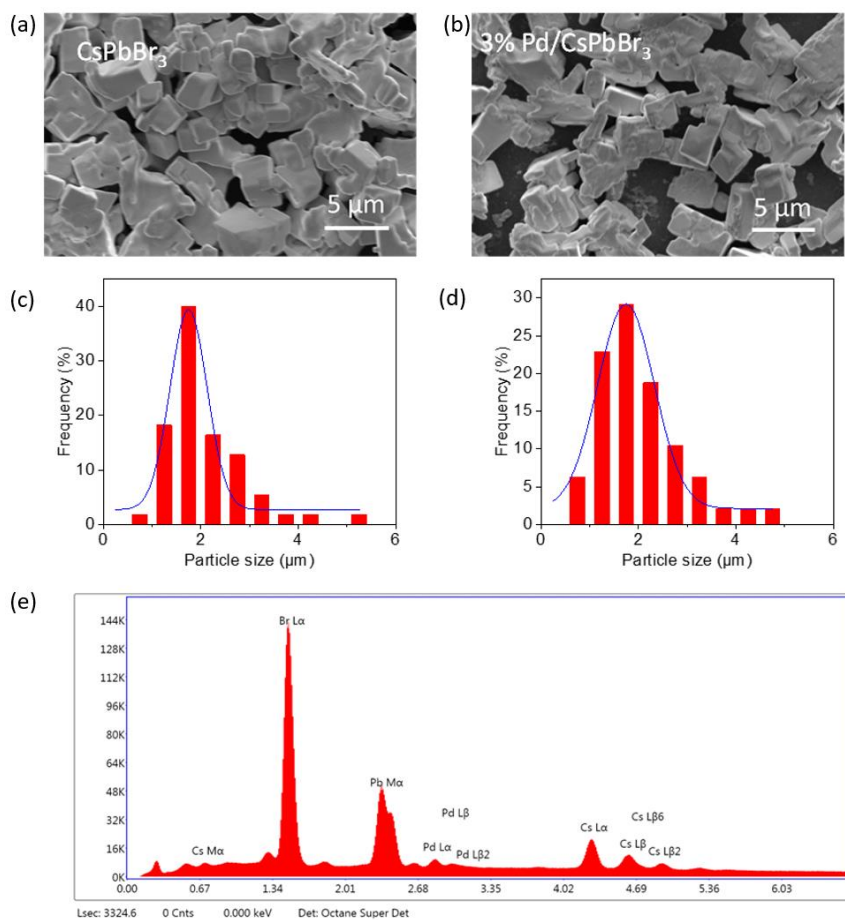


Figure S3. (a-b) SEM images of (a) pure CsPbBr₃ and (b) 3% Pd/CsPbBr₃ materials. (c-d) particle size distribution of (c) CsPbBr₃ and (d) 3% Pd/CsPbBr₃. (e) EDS spectrum recorded for 3% Pd/CsPbBr₃ catalyst.

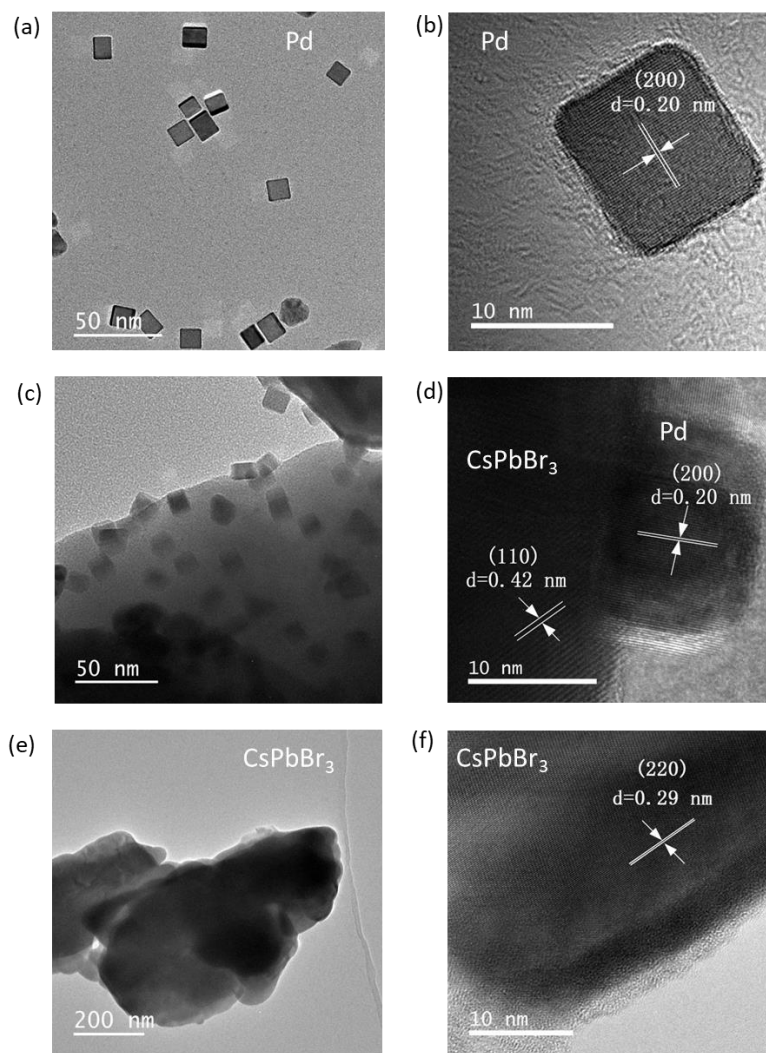


Figure S4. TEM and HRTEM images of (a-b) Pd NCs, (c-d) 3%Pd/CsPbBr₃ and (e-f) CsPbBr₃, respectively.

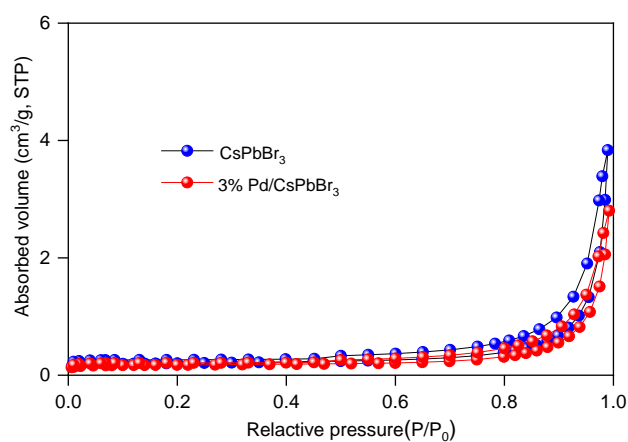


Figure S5. Nitrogen adsorption-desorption isotherms of the CsPbBr₃ and 3% Pd/CsPbBr₃ samples.

Table S1. BET surface areas, pore size and pore volume the as-synthesized CsPbBr₃ and 3% Pd/CsPbBr₃ samples.

Sample	S _{BET} (m ² g ⁻¹)	Pore size (nm)	Pore volume (cm ³ g ⁻¹)
CsPbBr ₃	1.49	1.45	0.0083
3% Pd/CsPbBr ₃	1.34	1.49	0.009

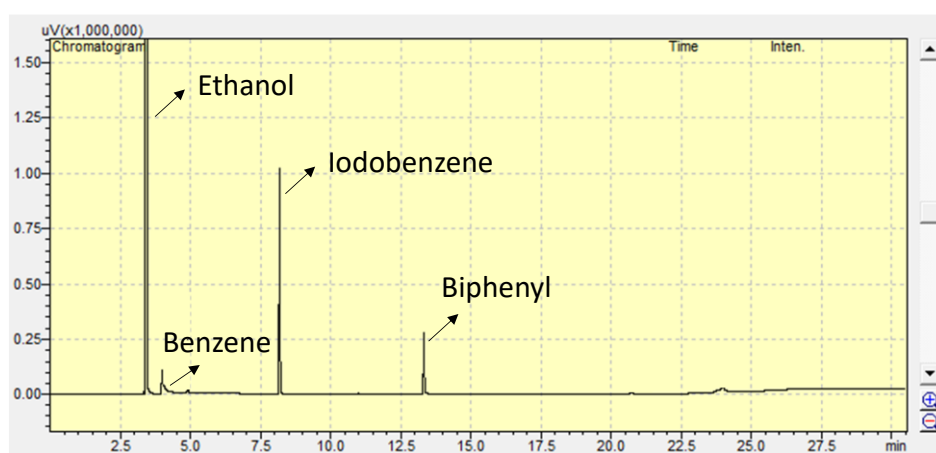


Figure S6. Gas chromatogram of the reaction mixture after Suzuki coupling reaction.

Table S2. Comparison of 3 wt% Pd/CsPbBr₃ catalyst with reported photocatalytic Suzuki couplings photocatalysts.

Catalyst	Light Source	Reaction conditions	TOF (h ⁻¹)	Ref.
Pd/CsPbBr ₃	Xe lamp (150 W)	15 mg of catalyst (3 wt% Pd), 25 °C, 1h	23.7 (Iodobenzene)	This work
Supramolecular ensemble 2:Cu ₂ O	Tungsten filament bulb (100 W)	H ₂ O/EtOH (1:1), K ₂ CO ₃ (1.5 eq.), 0.02 mM catalyst, RT, 8 h	1.45 (bromobenzene)	4
Cu ₇ S ₄ @Pd	Laser power (0.45 W cm ⁻²)	H ₂ O/NaOH, 50 mg of catalyst (5.4 mg Pd), 58.8 °C, 0.5h	3.05 (Iodophenol)	5
Pd/Au/PN-CeO ₂	Xe lamp (150 W)	H ₂ O/DMF (1:1), K ₂ CO ₃ (3 eq.), 15 mg of catalyst (2.95 wt% Au, 0.41 wt% Pd), 25°C, 5h	6.3 (Iodobenzene)	6
Au-Pd alloy NPs	White LED lamp (0.5 W cm ⁻²)	DMF/H ₂ O (3:1), K ₂ CO ₃ (3 eq.), 50 mg catalyst (containing 3% of metals), Ar atmosphere, 30 °C, 6 h	14.5 (bromobenzene)	7
Pd/WO _{3-x} nanowires	Xe lamp (300 W)	EtOH, K ₂ CO ₃ , 20 mg of catalyst (2 wt% Pd), 25/60 °C, 1.67 h	28.64 (Iodobenzene)	8
Nano Pd/TiO ₂	white LED strips (15 W)	H ₂ O-PEG (1:1), NaOC(CH ₃) ₃ (3 eq.), 15 mg of catalyst (7.04×10 ⁻³ mmol of Pd), 28 °C, 4 h	33 (Iodobenzene)	9
m-CNR-Pd	Xe lamp (150 W)	H ₂ O/EtOH (1:1), K ₂ CO ₃ , 10 mg of catalyst (3 wt% Pd), 1h, RT	51.6 (Iodobenzene)	10
Pd@PDA-CL	Two white LED lamps (12 W)	DMF/H ₂ O (1:1), K ₂ CO ₃ , Pd@PDA-CL (containing 0.6 mg of Pd), RT, 2h	85 (Iodotoluene)	11

Pd@B-BO3	white LED lamp (1.2 W/cm ²)	DMF/H ₂ O (1:1), K ₂ CO ₃ , 10 mg of catalyst (3 wt% Pd), RT, 2h	86.9 (Iodotoluene)	12
Au-Pd/TiO ₂	Blue LED lamp (5 W)	H ₂ O/EtOH (1:1), K ₂ CO ₃ , catalyst containing 0.002 mmol Pd, RT (25 ± 5 °C), 5h	98 (Iodobenzene)	13
Pd-NiFe ₂ O ₄ /rGO	Xe lamp (300 W)	H ₂ O/EtOH (1:9), K ₂ CO ₃ , catalyst (0.5 mmol% Pd), 25 °C, 0.5 h	130.6 (Bromotoluene)	14
Au-Pd NPs	laser power (1.68 W)	H ₂ O, NaOH, 0.49 μmol of catalyst, 25 °C, 1 h	162 (Iodobenzene)	15
Pd/SiC	Xe lamp (300 W)	DMF/H ₂ O (3:1), Cs ₂ CO ₃ (3 eq.), 10 mg of catalyst (3 wt% Pd), 30 °C, 1.33 h	1053 (Iodobenzene)	16
2H-WS ₂ /Pd NPs	white LED lamp (60W)	EtOH/H ₂ O (2:1), K ₂ CO ₃ (5 eq.), 2H-WS ₂ /PdNPs (Pd 2.85 μg), RT, 3 h	1244 (Iodotoluene)	17
PdO@WO ₃	white LED lamp (60W)	MeOH/H ₂ O (2:1), Cs ₂ CO ₃ , PdO@WO ₃ (7.27 μg, 68wt%Pd:5 μg of Pd), RT, 4 h	1438.62 (Iodotoluene)	18

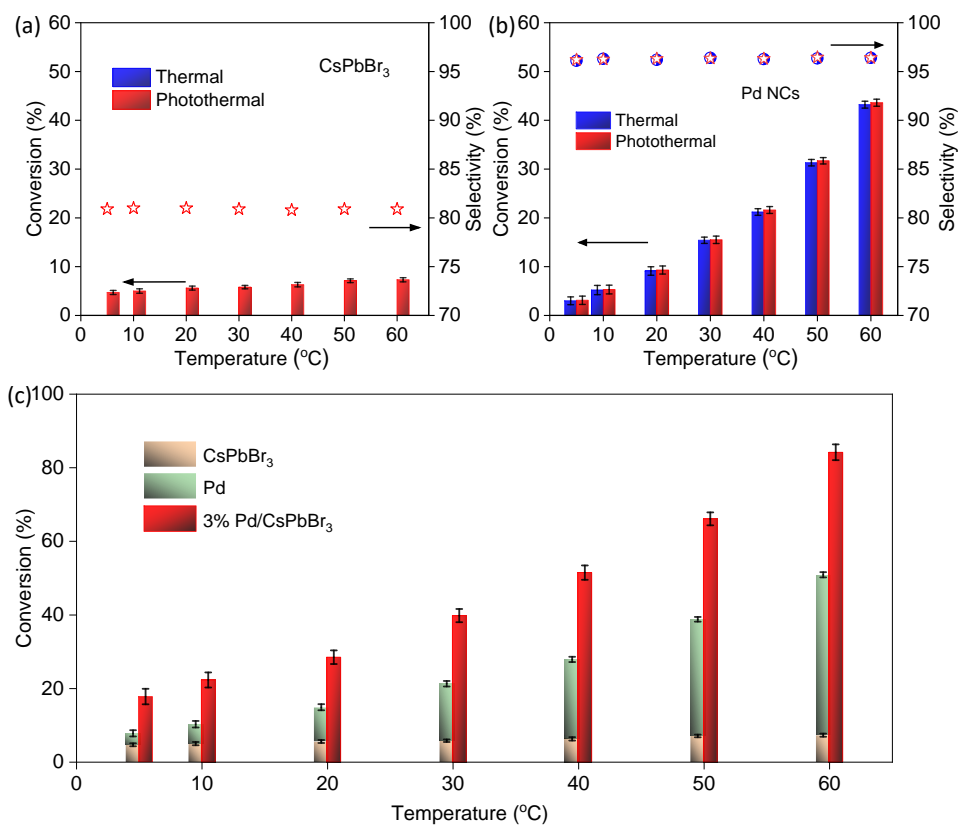


Figure S7. (a-b) Thermal and photothermal Suzuki reactions over (a) CsPbBr₃ and (b) Pd catalysts under controlled temperature in the range of 5-60 °C. (c) Comparison of the activity of 3% Pd/CsPbBr₃ to the sum of the individual components. Reaction conditions: 0.1 mmol iodobenzene, 0.12 mmol phenylboronic acid, 15 mg catalyst, 0.4 mmol Cs₂CO₃, 3 mL ethanol, simulated solar light (150 W Xe lamp, AM 1.5G), reaction time (1h).

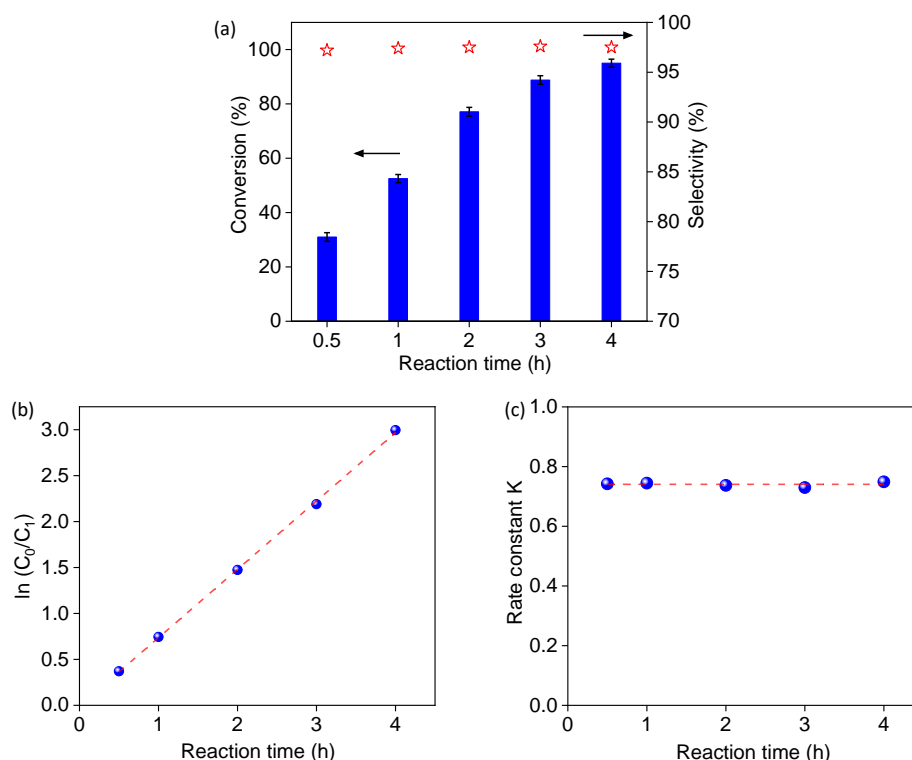


Figure S8. (a) Time-dependent Suzuki coupling reaction over 3% Pd/CsPbBr₃ catalyst. (b) The plot of $\ln(C_0/C_1)$ -T at different periods of reaction time in 4 h. (c) The extracted rate constant. Reaction conditions: 0.1 mmol iodobenzene, 0.12 mmol phenylboronic acid, 15 mg catalyst, 0.4 mmol Cs₂CO₃, 3 mL ethanol, simulated solar light (150 W Xe lamp), reaction time (0.5-4 h, 30 °C).

At different periods of reaction time in 4 h, the conversions were calculated, and a first-order dependence of the reaction rate on the concentration of biphenyl was found. According to the first-order reaction rate equation: $k = \frac{1}{t} \ln \frac{C_0}{C_1}$, where t is the reaction time, C_0 and C_1 are the concentration of iodobenzene before and after reaction, thus the values of the rate constants k were calculated.

For thermal catalytic processes, the calculated k values at different temperatures are: $k_{278.15K} = 9.03 \times 10^{-6} \text{ s}^{-1}$, $k_{283.15K} = 1.28 \times 10^{-5} \text{ s}^{-1}$, $k_{293.15K} = 2.08 \times 10^{-5} \text{ s}^{-1}$, $k_{303.15K} = 3.24 \times 10^{-5} \text{ s}^{-1}$, $k_{313.15K} = 6.06 \times 10^{-5} \text{ s}^{-1}$, $k_{323.15K} = 9.24 \times 10^{-5} \text{ s}^{-1}$, $k_{333.15K} = 1.78 \times 10^{-4} \text{ s}^{-1}$. For photothermal catalytic processes, the k values at different temperatures are: $k_{278.15K} = 5.44 \times 10^{-5} \text{ s}^{-1}$, $k_{283.15K} = 6.90 \times 10^{-5} \text{ s}^{-1}$, $k_{293.15K} = 9.32 \times 10^{-5} \text{ s}^{-1}$, $k_{303.15K} = 1.41 \times 10^{-4} \text{ s}^{-1}$, $k_{313.15K} = 2.01 \times 10^{-4} \text{ s}^{-1}$, $k_{323.15K} = 3.00 \times 10^{-4} \text{ s}^{-1}$, $k_{333.15K} = 5.12 \times 10^{-4} \text{ s}^{-1}$.

The dependence of the rate constant k of the reaction on the temperature can be describe via the Arrhenius equation as:

$$k = Ae^{\frac{-E_a}{RT}}$$

where k is the rate constant, T is the temperature in kelvins, A is the pre-exponential factor (a constant for each chemical reaction), E_a is the activation energy, R is the universal gas constant ($8.314 \text{ J K}^{-1} \text{ mol}^{-1}$). Taking the natural logarithm of Arrhenius equation yields:

$$\ln k = \frac{-E_a}{R} \left(\frac{1}{T} \right) + \ln A$$

Therefore, a plot of $\ln k$ versus T^{-1} gives a straight line, whose gradient and intercept can be used to determine the E_a and preexponential factor A , respectively.

Based on reaction kinetics, the slop ($\frac{-E_a}{R}$) of thermal and photothermal catalytic processes is -4.86 and -3.625 , respectively. Thus, the E_a for thermal and photothermal reaction is calculated to be 40.4 kJ mol^{-1} and 30.1 kJ mol^{-1} , respectively.

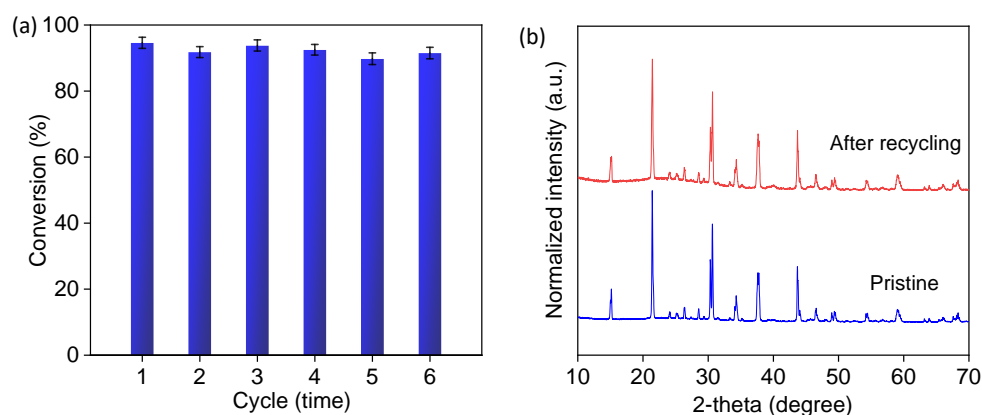


Figure S9. (a) The stability test of 3% Pd/CsPbBr₃ catalyst and (b) XRD pattern before and after recycling. Reaction conditions: 0.1 mmol iodobenzene, 0.12 mmol phenylboronic acid, 15 mg catalyst, 0.4 mmol Cs₂CO₃, 3 mL ethanol, simulated solar light (150 W Xe lamp, AM 1.5G), reaction time (4 h, 30 °C).

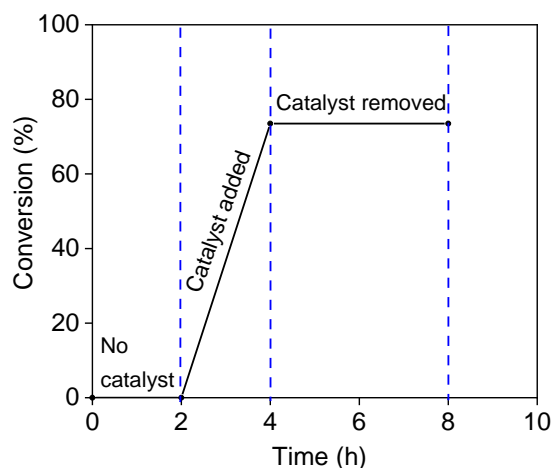


Figure S10. Suzuki coupling reaction over 3% Pd/CsPbBr₃ catalyst. After the irradiation of 2 h, the catalyst was removed *via* centrifugation and the reaction was continued under irradiation for 4 h using the supernatant liquid. Reaction conditions: 0.1 mmol iodobenzene, 0.12 mmol phenylboronic acid, 15 mg catalyst, 0.4 mmol Cs₂CO₃, 3 mL ethanol, simulated solar light (150 W Xe lamp, AM 1.5G), reaction time (2 h, 30 °C).

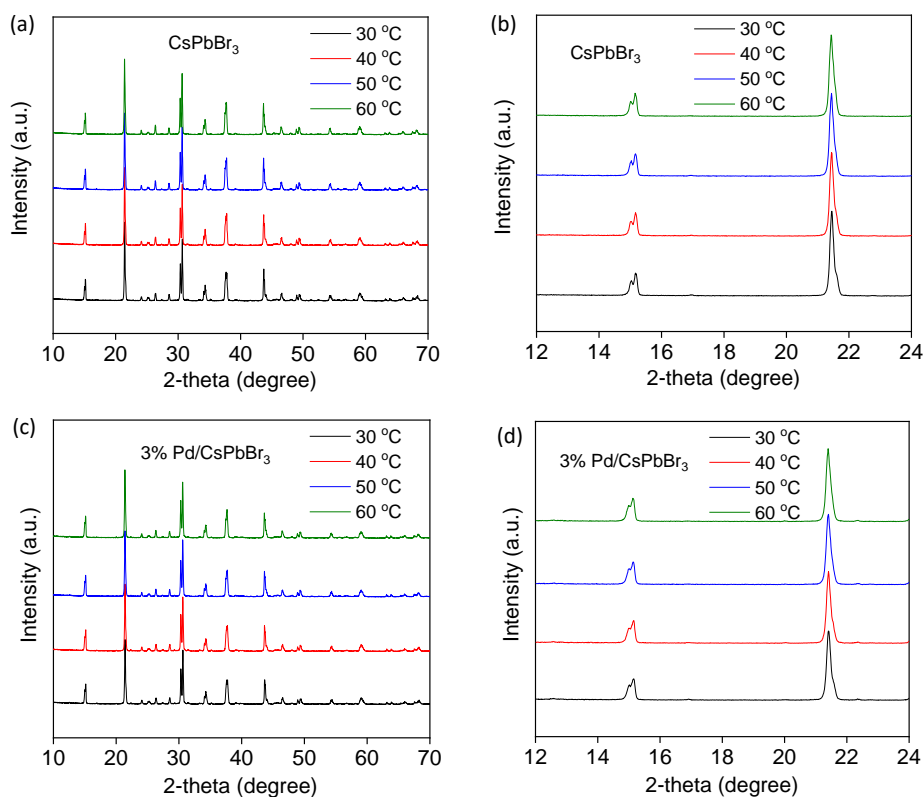


Figure S11. *In situ* temperature-dependent XRD patterns of (a-b) CsPbBr₃ and (c-d) 3% Pd/CsPbBr₃ material measured in the range of 30-60 °C. The XRD

patterns show the same diffraction peaks for both CsPbBr₃ and 3% Pd/CsPbBr₃ under different temperatures, indicating that there are negligible structural changes over these materials.

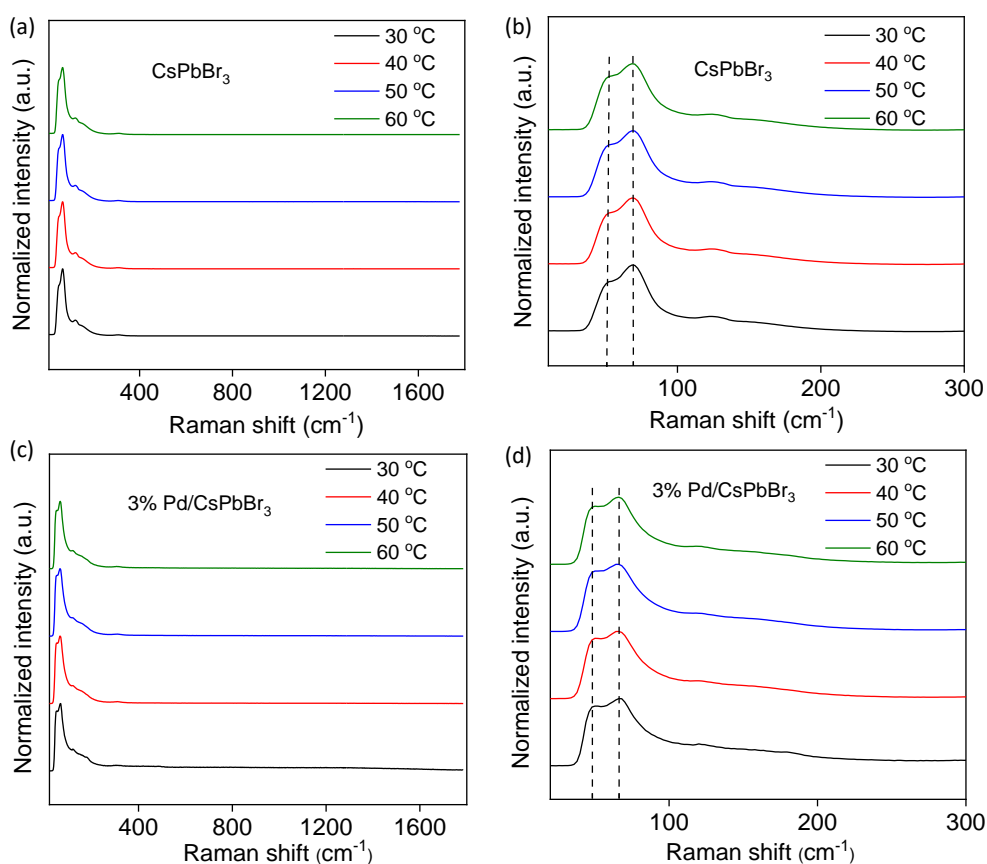


Figure S12. *In situ* temperature-dependent Raman spectra of (a-b) CsPbBr₃ and (c-d) 3% Pd/CsPbBr₃ material measured in the range of 30-60 °C. Three Raman active modes belonging to CsPbBr₃ for both CsPbBr₃ and 3% Pd/CsPbBr₃ were detected, and all Raman peaks and the profile of the spectra remain unchanged versus temperatures, indicating that these materials exhibit high stability and no phase transition occurs during these reaction conditions.

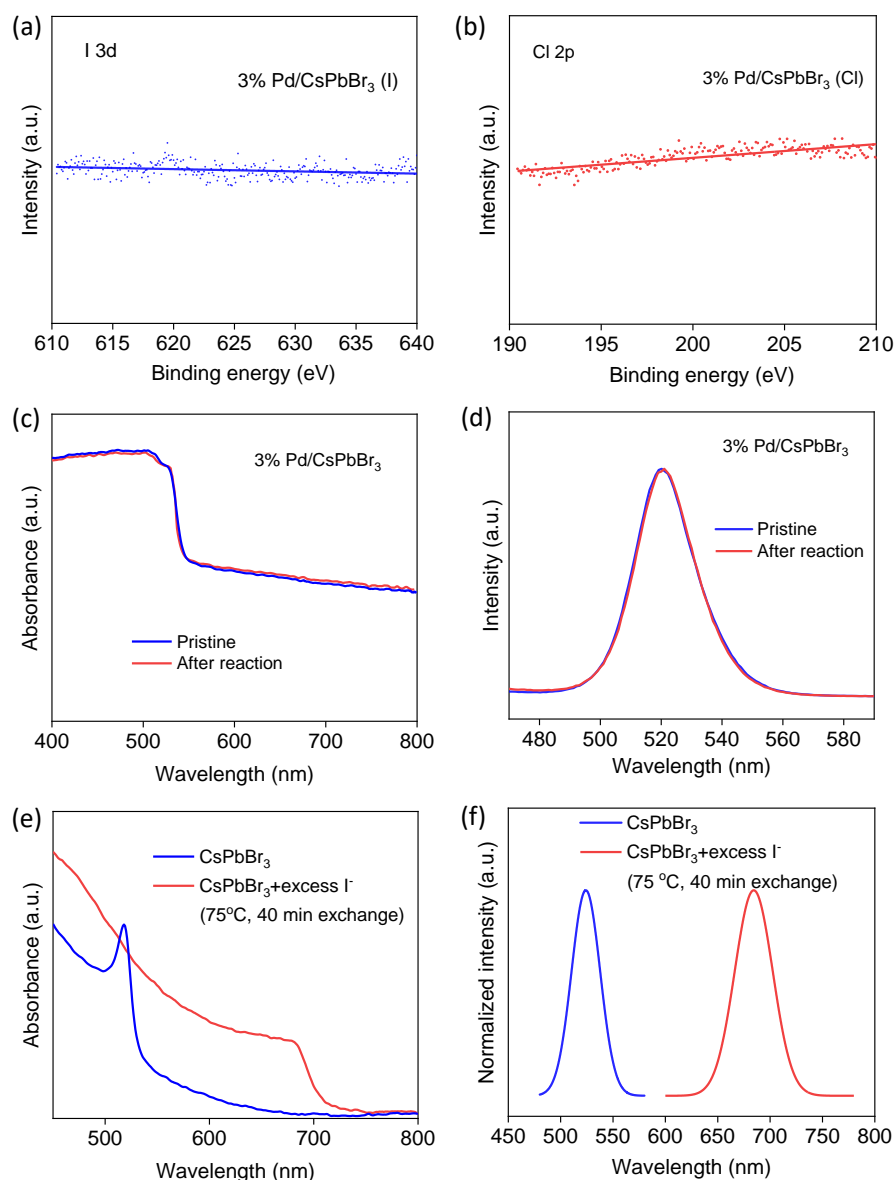


Figure S13. (a-b) High-resolution XPS spectra of (a) I 3d and (b) Cl 2p core levels of 3% Pd/CsPbBr₃ after catalytic Suzuki reaction, where 3% Pd/CsPbBr₃ (I) and 3% Pd/CsPbBr₃ (Cl) represent the catalyst after catalytic reaction under 60 °C together with 1-sun light irradiation with iodobenzene and chlorobenzene reactant, respectively. (c) Absorption and (d) PL spectra of 3% Pd/CsPbBr₃ before and after catalytic Suzuki reaction at 60 °C. (e) Absorption and (f) PL spectra of a typical halide exchange experiments for CsPbBr₃ according to a reported method. Suzuki reaction conditions: 0.1 mmol iodobenzene, 0.12 mmol phenylboronic acid, 15 mg catalyst, 0.4 mmol Cs₂CO₃, 3 mL ethanol, simulated solar light (150 W Xe lamp, AM 1.5G), reaction time (1h, 60 °C). Halide exchange reaction conditions: halide exchange was performed by

soaking CsPbBr₃ film in a PbI₂ solution at temperature of 75 °C for 40 min. The solution was made by dissolving PbI₂ into a mixture solution of 1-octadecene, oleylamine, and oleic acid at 170 °C.¹⁹

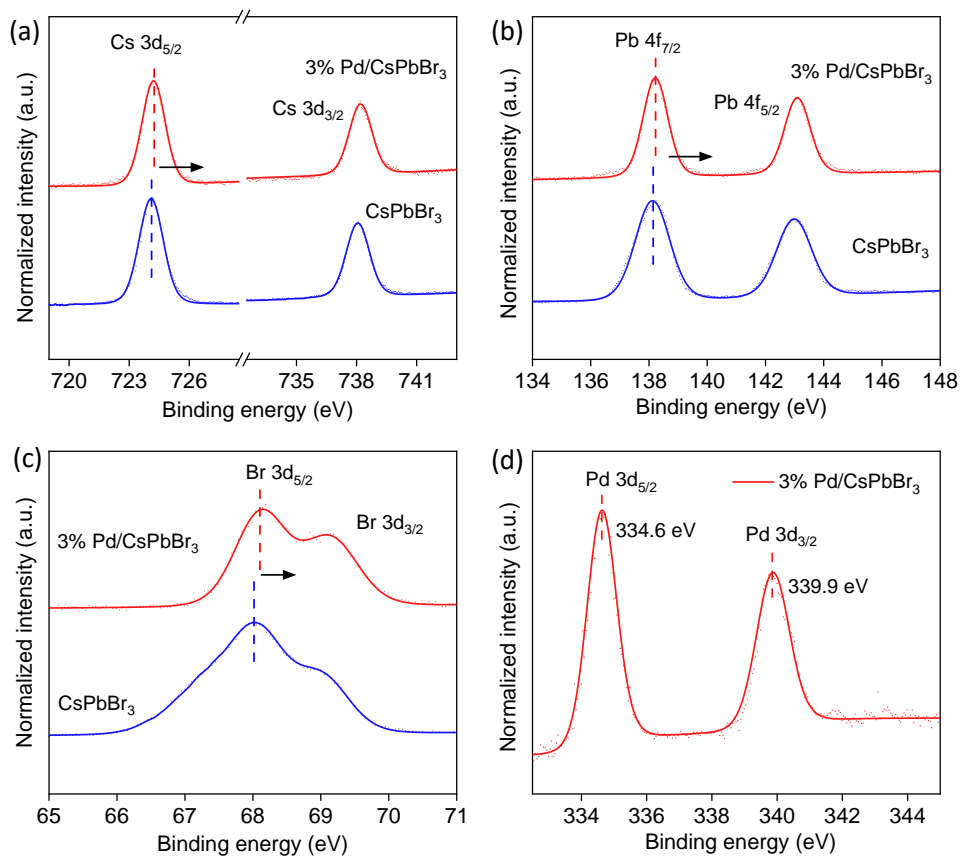


Figure S14. The XPS spectra of (a) Cs 3d, (b) Pb 4f, (c) Br 3d and (d) Pd 3d core levels of CsPbBr₃ and 3% Pd/CsPbBr₃ materials, respectively.

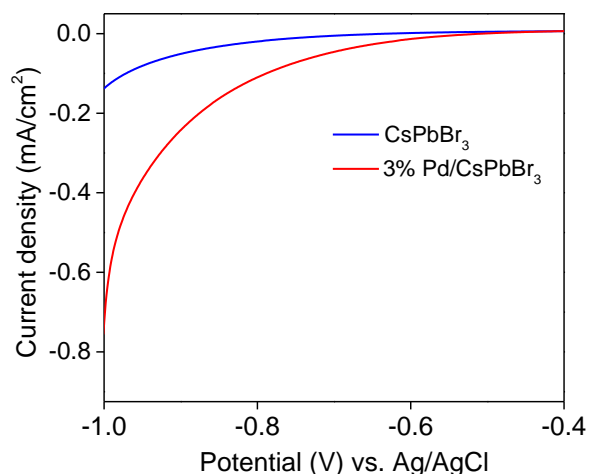


Figure S15. The cathodic polarization curves of CsPbBr₃ and 3% Pd/CsPbBr₃ using the linear sweep voltammetry technique with a scan rate of 0.2 mV s⁻¹.

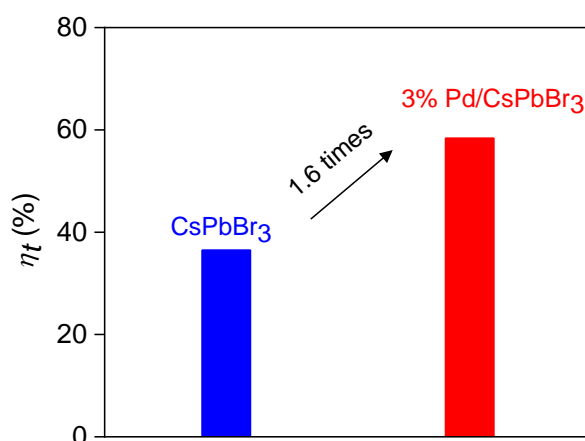


Figure S16. Comparison the surface charge transfer efficiency (η_t) of CsPbBr₃ and 3% Pd/CsPbBr₃.

The surface charge transfer efficiency (η_t) of CsPbBr₃ and 3% Pd/CsPbBr₃ was evaluated (under solar light irradiation without and with MVCl₂ under the potential of 0.06 V). (Figures 1d). Generally, the photocatalytic rate of a photocatalyst is mainly determined by optical absorption (η_a), charge carrier separation (η_s), and η_t .^{20, 21} The photocurrent density (J_1) is given by the theoretical formula:²⁰

$$J_1 = J_m \times \eta_a \times \eta_s \times \eta_t \quad (1)$$

Where J_m is the theoretical maximum photocurrent density. When adding a fast electron scavenger methyl viologen dichloride ($MVCl_2$), the surface charge transfer can be greatly promoted and reached almost 100 %, ²⁰ thus the current density in this case can be calculated as follows:²⁰

$$J_2 = J_m \times \eta_a \times \eta_s \quad (2)$$

Hence, the η_t can be obtained by combining Eq.s (1) and (2)

$$\eta_t = J_1/J_2$$

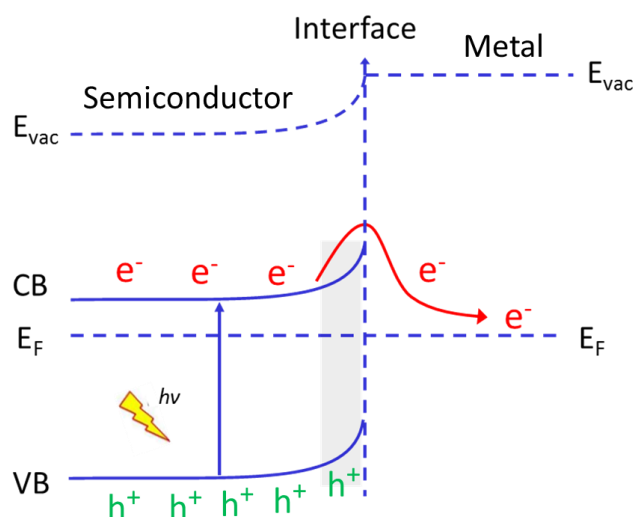


Figure S17. Schematic band diagram of Pd/CsPbBr₃ composites illustrating the charge transfer driven by the Schottky junction, where E_{vac} , E_F , CB, and VB represent vacuum level, Fermi level, conduction band and valence band, respectively.

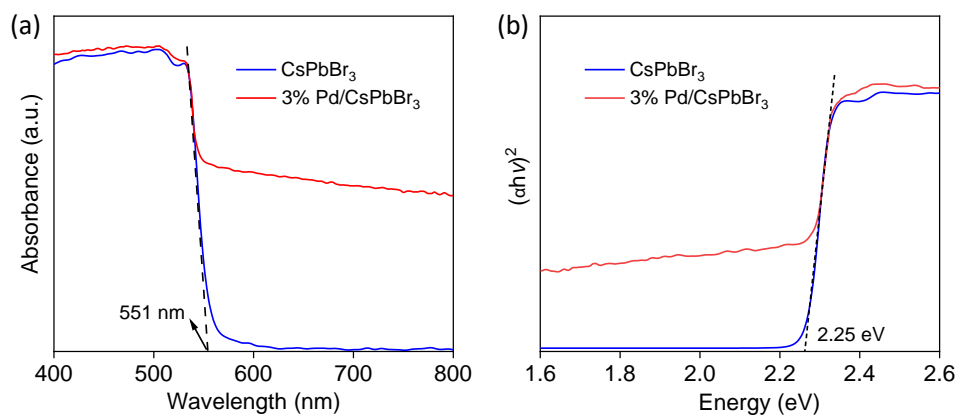


Figure S18. (a) Absorption spectra and (b) Tauc plots of CsPbBr₃ and 3% Pd/CsPbBr₃ materials.

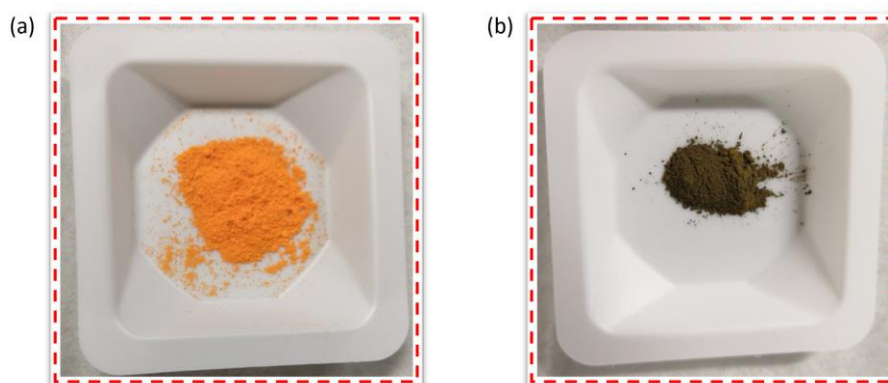


Figure S19. The digital photographs of (a) CsPbBr₃ and (b) 3% Pd/CsPbBr₃, respectively.

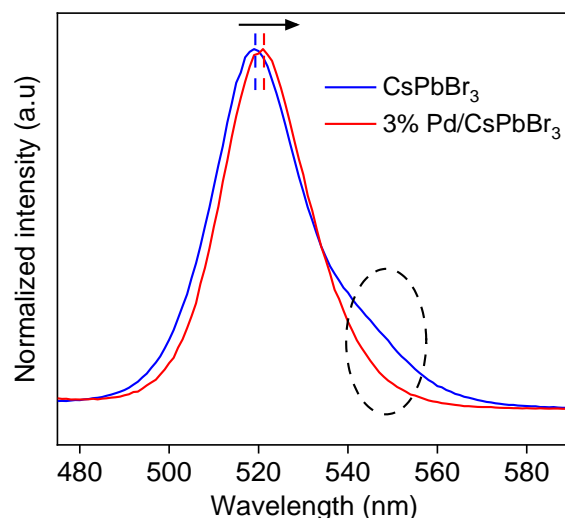


Figure S20. Normalized steady-state PL spectra of CsPbBr₃ and 3% Pd/CsPbBr₃ measured at room temperature.

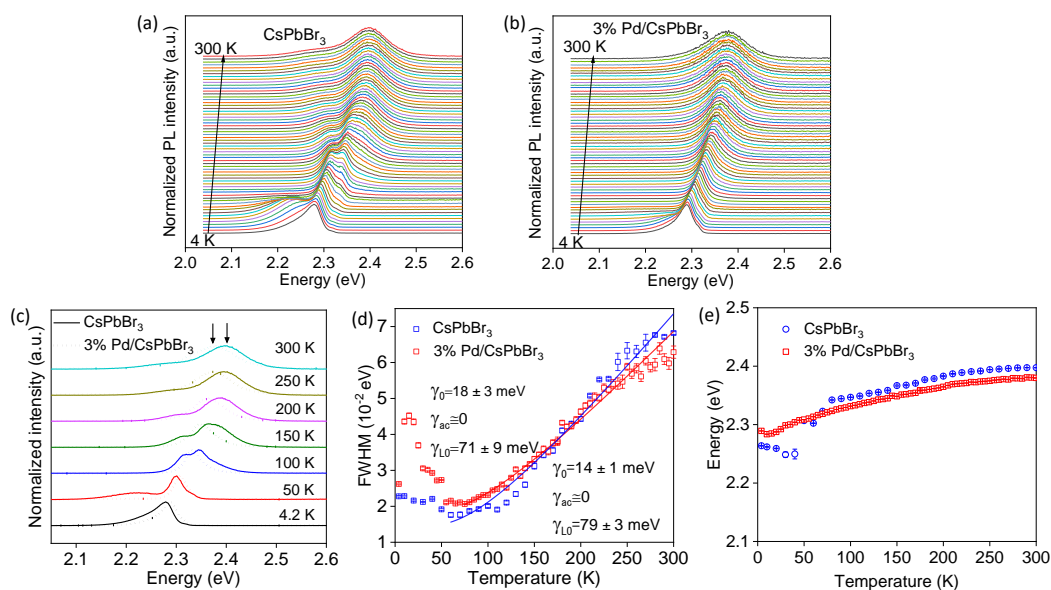


Figure S21. Normalized PL spectra measurement under low temperature ranging from 4.2-300 K of (a) pure CsPbBr₃, (b) 3% Pd/CsPbBr₃ hybrid at 5 K increment and (c) at selected temperatures. (d) FWHM of the temperature-dependent PL spectra as a function of temperature for CsPbBr₃ and 3% Pd/CsPbBr₃. (e) PL (main) peak centers vs temperature for both systems.

To obtain the information on electron-phonon coupling constants in these two systems, all the PL spectra are fitted with Gaussians, and the PL peak centers, full width at half-maximum (FWHM) and integrated intensity are extracted (Figure S15). The emission line width is described as following described as follows:^{22, 23}

$$\begin{aligned}\Gamma(T) &= \Gamma_0 + \Gamma_{ac} + \Gamma_{LO} \\ &= \Gamma_0 + \gamma_{ac}T + \gamma_{LO}n\end{aligned}$$

where Γ_0 is a constant and represents the temperature-independent inhomogeneous broadening parameter. Γ_{ac} and Γ_{LO} are the acoustic and optical phonon (Fröhlich) interactions with carrier-phonon coupling constants γ_{ac} and γ_{LO} , respectively.²² The electron-phonon coupling constants, extracted from both systems are similar with negligible changes, indicating no fundamental changes in the electron-phonon interactions in the CsPbBr₃ and 3% Pd/CsPbBr₃ samples.

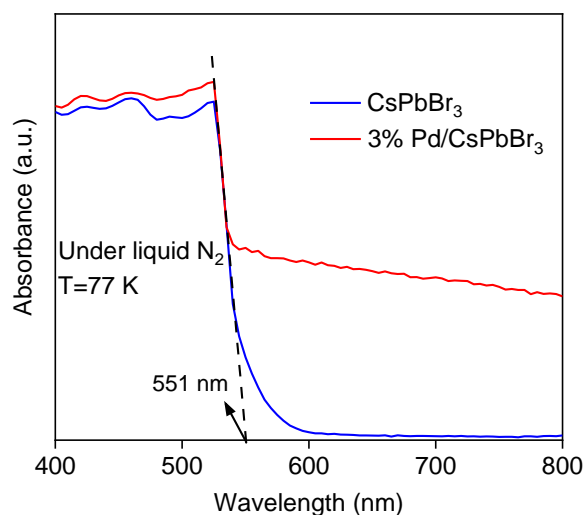


Figure S22. Absorption spectra of CsPbBr₃ and 3% Pd/CsPbBr₃ measured under low temperature (77 K).

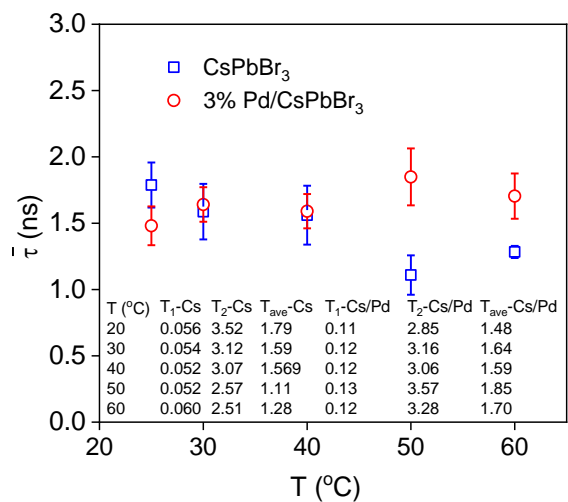


Figure S23. Temperature-dependent PL lifetime of CsPbBr₃ and 3% Pd/CsPbBr₃ materials.

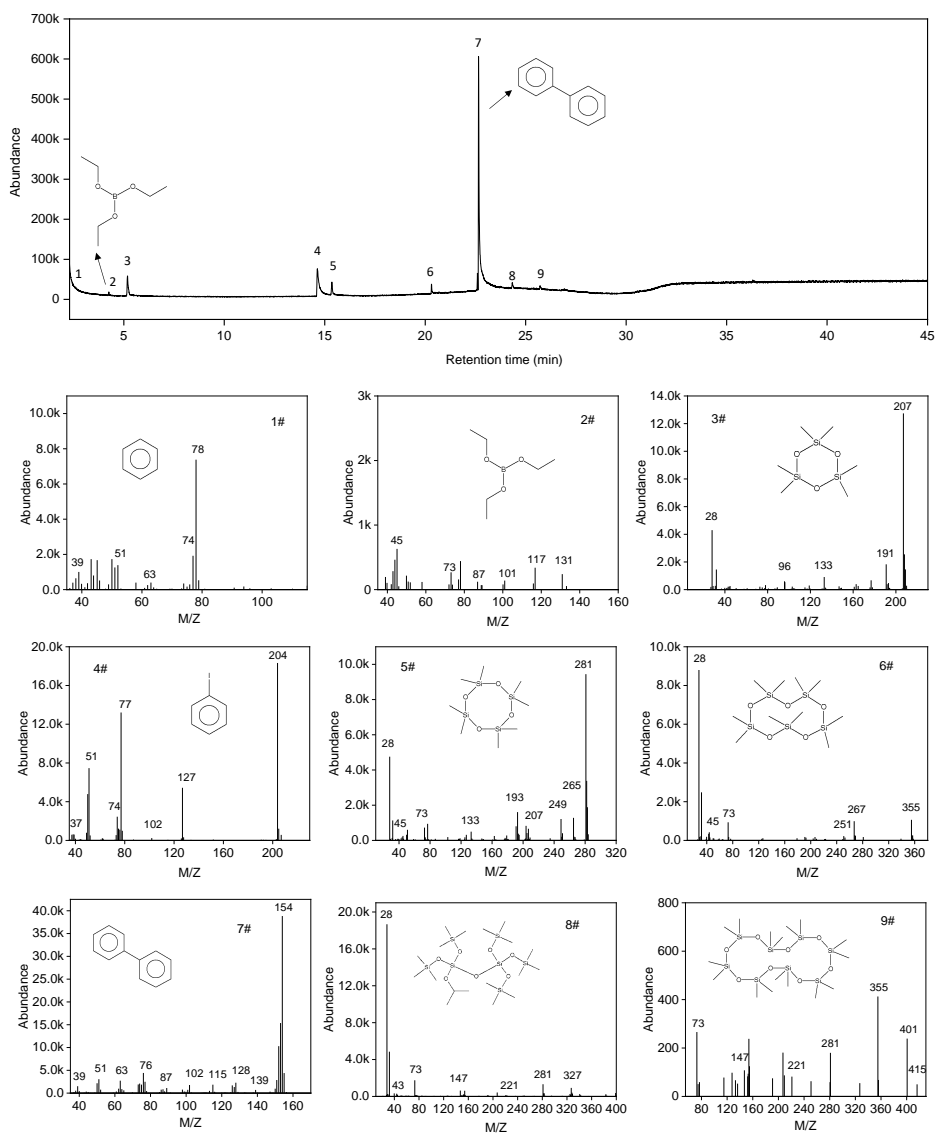


Figure S24. GC-MS analysis of the products of the Suzuki reaction using ethanol solvent over 3% Pd/CsPbBr₃ composite. Reaction conditions: 0.1 mmol iodobenzene, 0.12 mmol phenylboronic acid, 15 mg catalyst, 0.4 mmol Cs₂CO₃, 3 mL ethanol, simulated solar light (150 W Xe lamp, AM 1.5G), reaction time (4 h, 30 °C).

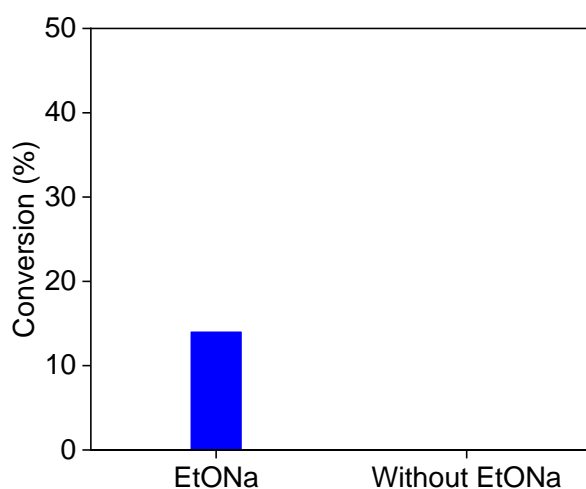


Figure S25. The catalytic performance of Suzuki coupling reaction over 3% Pd/CsPbBr₃ hybrids with or without EtONa compound. Reaction conditions: 0.1 mmol iodobenzene, 0.12 mmol phenylboronic acid, 15 mg catalyst, 0.4 mmol EtONa, 3 mL ethanol, simulated solar light (150 W Xe lamp, AM 1.5G), reaction time (4 h, 30 °C).

Table S3. The bond dissociation energy of the C-B bond for the various phenylboronic acid compounds.

Compound	C-B bond dissociation energy (kJ/mol)
$\text{C}_6\text{H}_5\text{-B(OH)}_2$	468.78
$\text{C}_6\text{H}_5\text{-B(OH)}_3^-$	320.79
$\text{C}_6\text{H}_5\text{-B(OH)}_2\text{CO}_3^{2-}$	325.56
$\text{C}_6\text{H}_5\text{-B(OH)}_2\text{EtO}^-$	317.48
$\text{C}_6\text{H}_5\text{-B(OH)(EtO)}_2^-$	341.25
$\text{C}_6\text{H}_5\text{-B(EtO)}_3^-$	360.45

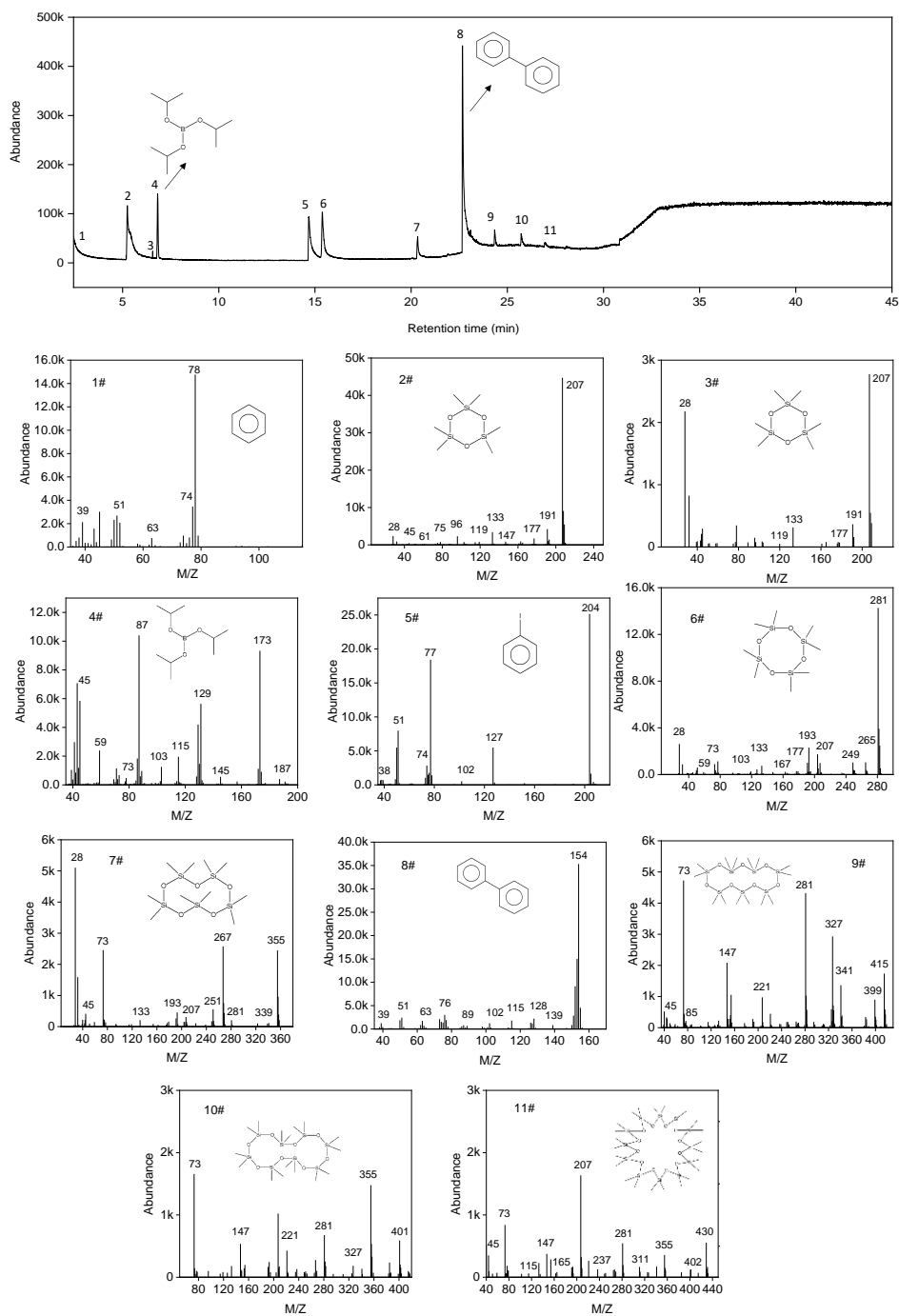


Figure S26. GC-MS analysis of the products of the Suzuki reaction using isopropanol solvent over 3% Pd/CsPbBr₃ composite. Reaction conditions: 0.1 mmol iodobenzene, 0.12 mmol phenylboronic acid, 15 mg catalyst, 0.4 mmol Cs₂CO₃, 3 mL isopropanol, simulated solar light (150 W Xe lamp, AM 1.5G), reaction time (4 h, 30 °C).

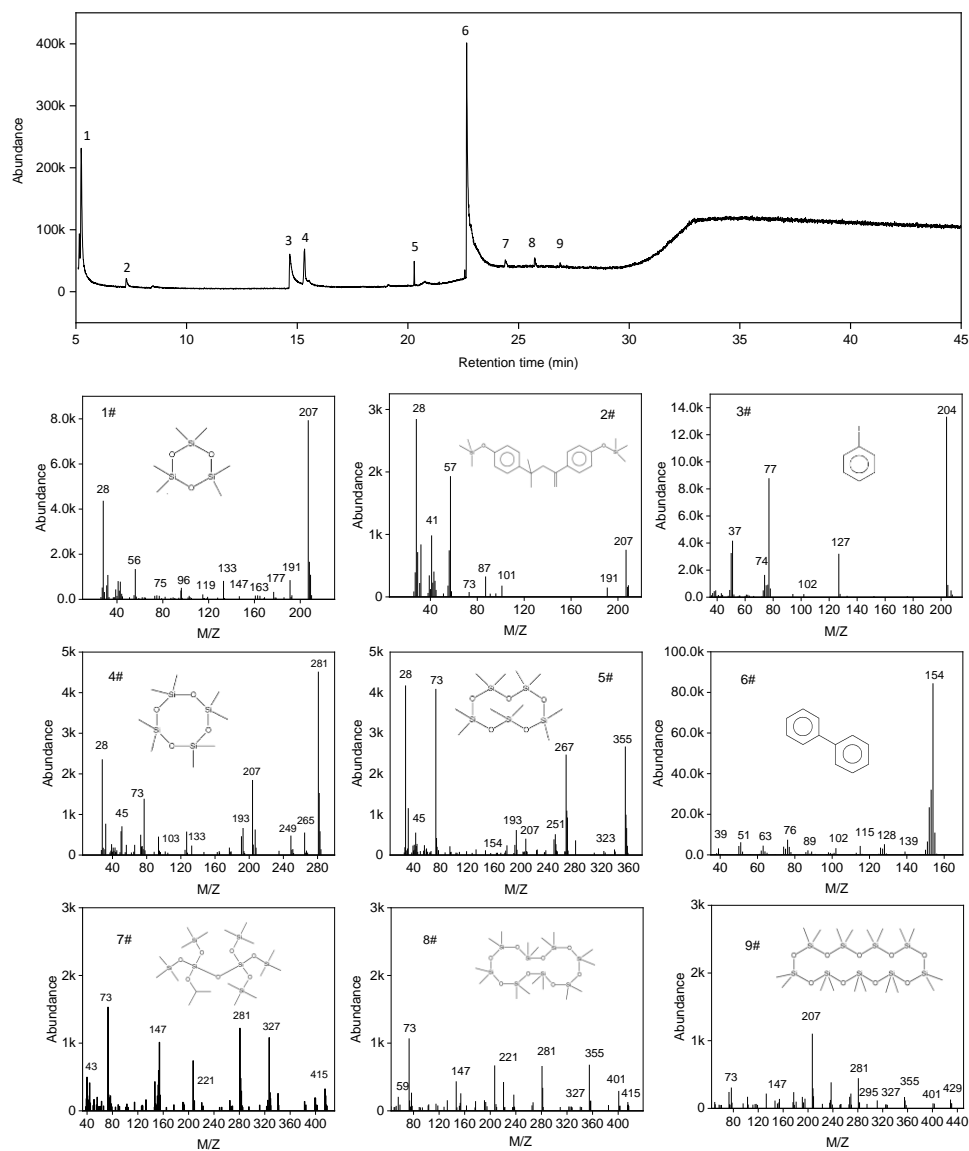


Figure S27. GC-MS analysis of the products of the Suzuki reaction using n-butanol solvent over 3% Pd/CsPbBr₃ composite. Reaction conditions: 0.1 mmol iodobenzene, 0.12 mmol phenylboronic acid, 15 mg catalyst, 0.4 mmol Cs₂CO₃, 3 mL n-butanol, simulated solar light (150 W Xe lamp, AM 1.5G), reaction time (4 h, 30 °C).

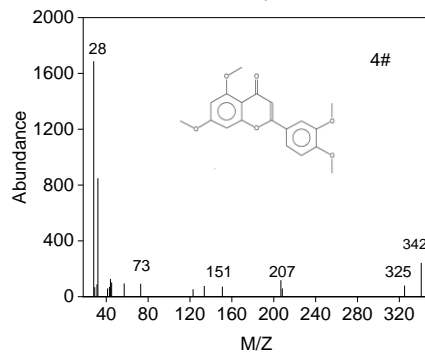
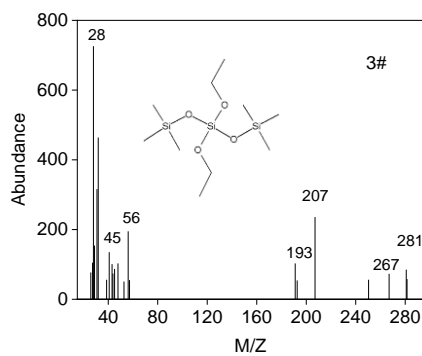
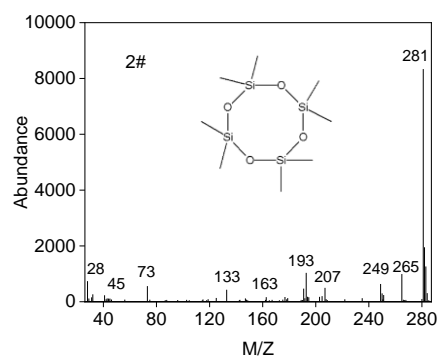
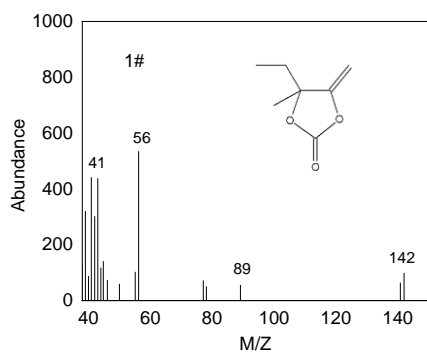
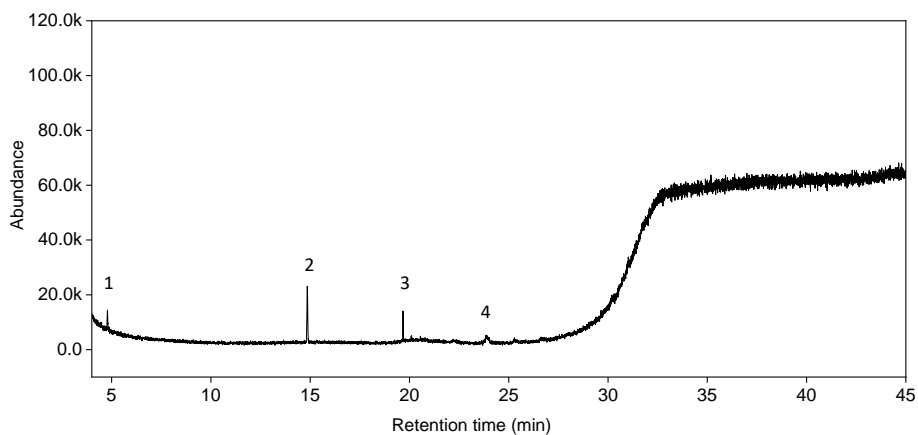


Figure S28. GC-MS analysis of the products of the pure tributyl borate compound.

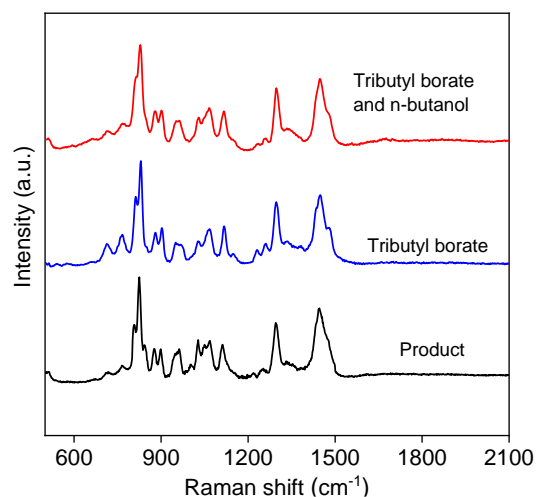


Figure S29. Raman spectra of the product of the Suzuki reaction using n-butanol solvent over 3% Pd/CsPbBr₃ composite (black), the pure tributyl borate compound (blue) and the mixture of tributyl borate and n-butanol (red). Reaction conditions: 0.1 mmol iodobenzene, 0.12 mmol phenylboronic acid, 15 mg catalyst, 0.4 mmol Cs₂CO₃, 3 mL n-butanol, simulated solar light (150 W Xe lamp, AM 1.5G), reaction time (4 h, 30 °C).

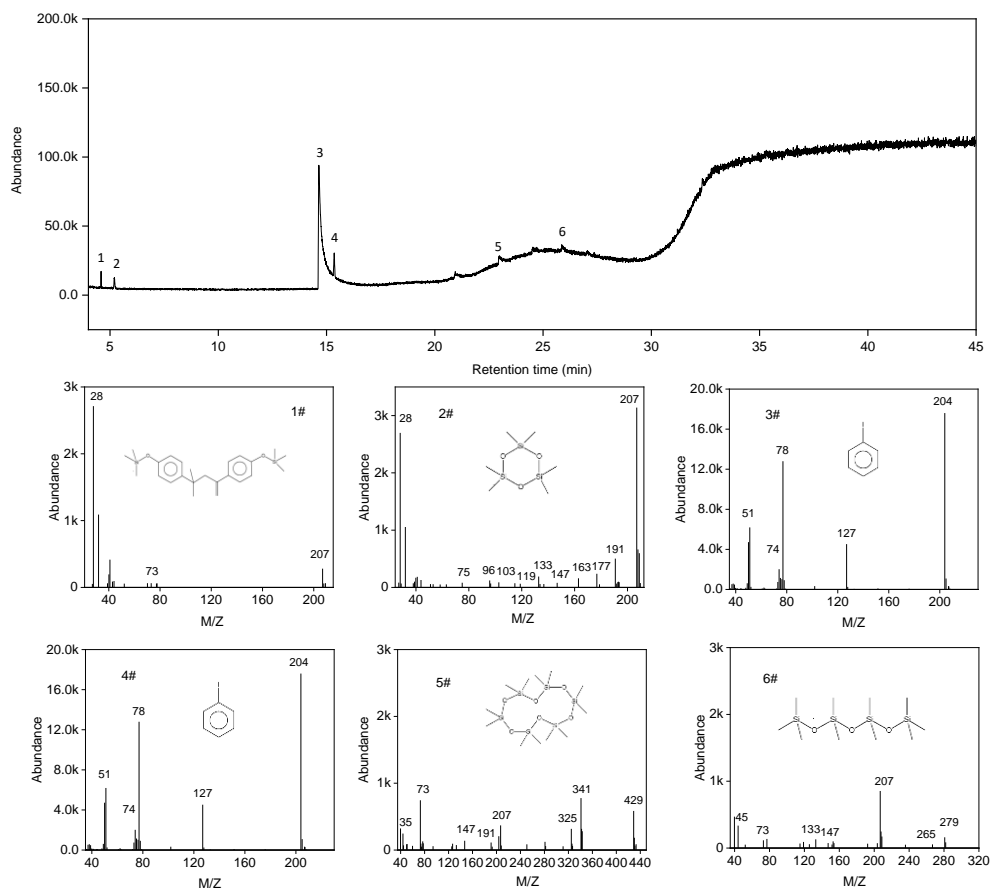


Figure S30. (a) GC-MS analysis of the products of the Suzuki reaction using acetonitrile solvent with Cs_2CO_3 base over 3% Pd/CsPbBr₃ composite. Reaction conditions: 0.1 mmol iodobenzene, 0.12 mmol phenylboronic acid, 15 mg catalyst, 0.4 mmol Cs_2CO_3 , 3 mL acetonitrile, simulated solar light (150 W Xe lamp, AM 1.5G), reaction time (4 h, 30 °C).

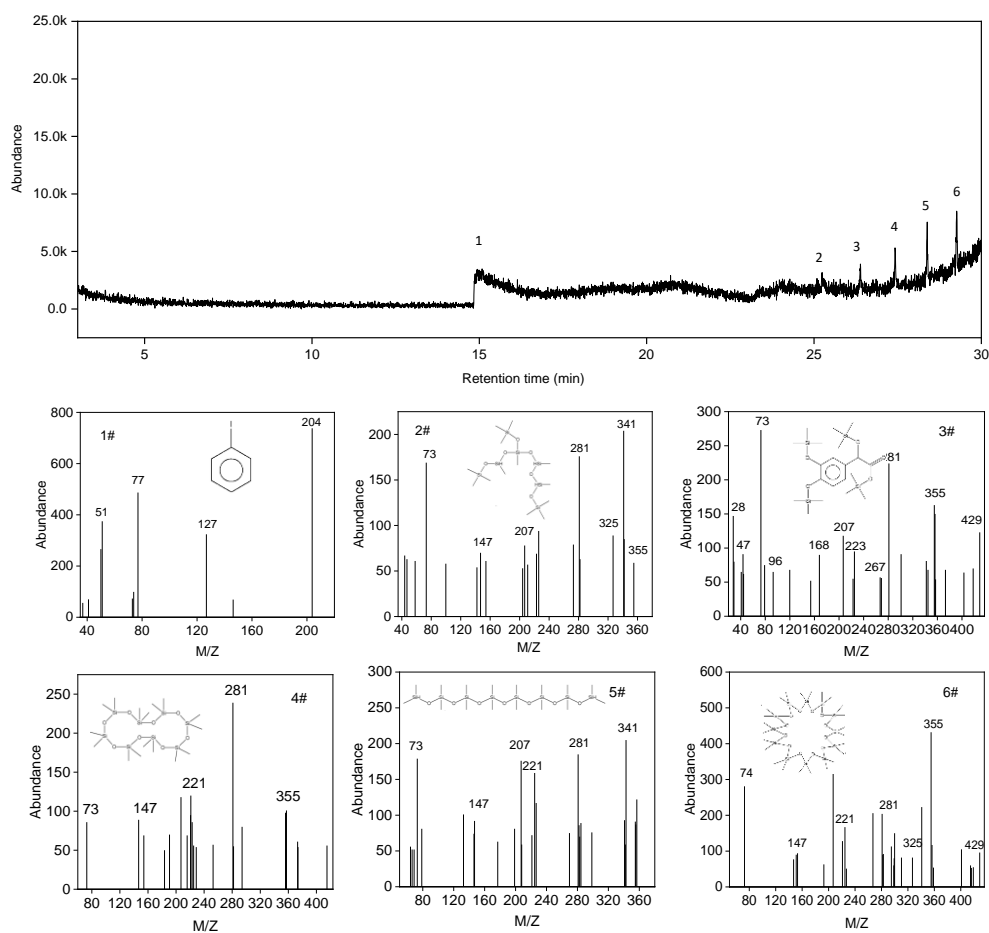
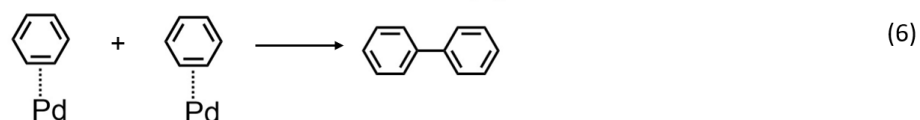
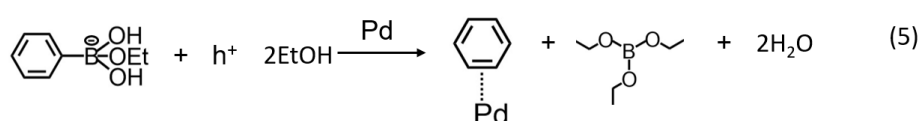
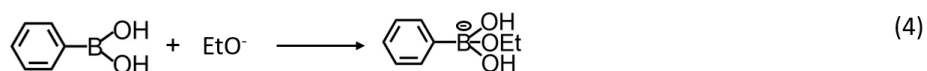
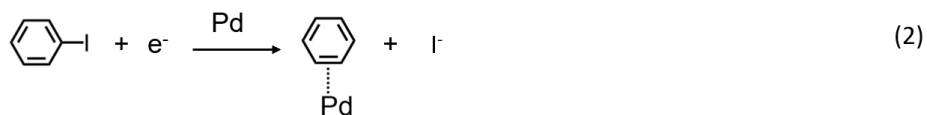


Figure S31. (a) GC-MS analysis of the products of the Suzuki reaction using acetonitrile solvent with NaOH base over 3% Pd/CsPbBr₃ composite. Reaction conditions: 0.1 mmol iodobenzene, 0.12 mmol phenylboronic acid, 15 mg catalyst, 0.4 mmol NaOH, 3 mL acetonitrile, simulated solar light (150 W Xe lamp, AM 1.5G), reaction time (4 h, 30 °C).

Equation S1. The detailed reaction equations for Suzuki coupling reaction over Pd/Cs₃Bi₂Br₉ catalyst.



References

- (1) Cha, J.-H.; Han, J. H.; Yin, W.; Park, C.; Park, Y.; Ahn, T. K.; Cho, J. H.; Jung, D.-Y., Photoresponse of CsPbBr₃ and Cs₄PbBr₆ Perovskite Single Crystals. *J. Phys. Chem. Lett.* **2017**, *8*, 565-570.
- (2) Zhang, L.; Zeng, Q.; Wang, K., Pressure-Induced Structural and Optical Properties of Inorganic Halide Perovskite CsPbBr₃. *J. Phys. Chem. Lett.* **2017**, *8*, 3752-3758.
- (3) Akbali, B.; Topcu, G.; Guner, T.; Ozcan, M.; Demir, M. M.; Sahin, H., CsPbBr₃ perovskites: Theoretical and experimental investigation on water-assisted transition from nanowire formation to degradation. *Phys. Rev. Mater.* **2018**, *2*, 034601.
- (4) Singh, G.; Kumar, M.; Sharma, K.; Bhalla, V., A supramolecular ensemble of a PBI derivative and Cu₂O NPs: potential photocatalysts for the Suzuki and Suzuki type coupling reactions. *Green Chem.* **2016**, *18*, 3278-3285.
- (5) Cui, J.; Li, Y.; Liu, L.; Chen, L.; Xu, J.; Ma, J.; Fang, G.; Zhu, E.; Wu, H.; Zhao, L.; Wang, L.; Huang, Y., Near-Infrared Plasmonic-Enhanced Solar Energy Harvest for Highly Efficient Photocatalytic Reactions. *Nano Lett* **2015**, *15*, 6295-301.

- (6) Zhang, S.; Chang, C.; Huang, Z.; Ma, Y.; Gao, W.; Li, J.; Qu, Y., Visible-Light-Activated Suzuki–Miyaura Coupling Reactions of Aryl Chlorides over the Multifunctional Pd/Au/Porous Nanorods of CeO₂ Catalysts. *ACS Catal.* **2015**, *5*, 6481-6488.
- (7) Xiao, Q.; Sarina, S.; Jaatinen, E.; Jia, J.; Arnold, D. P.; Liu, H.; Zhu, H., Efficient photocatalytic Suzuki cross-coupling reactions on Au–Pd alloy nanoparticles under visible light irradiation. *Green Chem.* **2014**, *16*, 4272.
- (8) Lou, Z.; Gu, Q.; Liao, Y.; Yu, S.; Xue, C., Promoting Pd-catalyzed Suzuki coupling reactions through near-infrared plasmon excitation of WO₃–nanowires. *Appl. Catal. B: Environ.* **2016**, *184*, 258-263.
- (9) Koohgard, M.; Hosseini-Sarvari, M., Enhancement of Suzuki–Miyaura coupling reaction by photocatalytic palladium nanoparticles anchored to TiO₂ under visible light irradiation. *Catal. Commun.* **2018**, *111*, 10-15.
- (10) Li, X.-H.; Baar, M.; Blechert, S.; Antonietti, M., Facilitating room-temperature Suzuki coupling reaction with light: Mott-Schottky photocatalyst for C-C-coupling. *Sci. Rep.* **2013**, *3*, 1-6.
- (11) Xie, A.; Zhang, K.; Wu, F.; Wang, N.; Wang, Y.; Wang, M., Polydopamine nanofilms as visible light-harvesting interfaces for palladium nanocrystal catalyzed coupling reactions. *Catal. Sci. Technol.* **2016**, *6*, 1764-1771.
- (12) Wang, Z. J.; Ghasimi, S.; Landfester, K.; Zhang, K. A. I., Photocatalytic Suzuki Coupling Reaction Using Conjugated Microporous Polymer with Immobilized Palladium Nanoparticles under Visible Light. *Chem. Mater.* **2015**, *27*, 1921-1924.
- (13) Han, D.; Bao, Z.; Xing, H.; Yang, Y.; Ren, Q.; Zhang, Z., Fabrication of plasmonic Au-Pd alloy nanoparticles for photocatalytic Suzuki-Miyaura reactions under ambient conditions. *Nanoscale* **2017**, *9*, 6026-6032.
- (14) Li, Y.; Zhang, Z.; Pei, L.; Li, X.; Fan, T.; Ji, J.; Shen, J.; Ye, M., Multifunctional photocatalytic performances of recyclable Pd-NiFe₂O₄/reduced graphene oxide nanocomposites via different co-catalyst strategy. *Appl. Catal. B: Environ.* **2016**, *190*, 1-11.
- (15) Wang, F.; Li, C.; Chen, H.; Jiang, R.; Sun, L. D.; Li, Q.; Wang, J.; Yu, J. C.; Yan, C. H., Plasmonic harvesting of light energy for Suzuki coupling reactions. *J. Am. Chem. Soc.* **2013**, *135*, 5588-601.

- (16) Jiao, Z.; Zhai, Z.; Guo, X.; Guo, X.-Y., Visible-Light-Driven Photocatalytic Suzuki–Miyaura Coupling Reaction on Mott–Schottky-type Pd/SiC Catalyst. *J. Phys. Chem. C* **2015**, *119*, 3238-3243.
- (17) Raza, F.; Yim, D.; Park, J. H.; Kim, H. I.; Jeon, S. J.; Kim, J. H., Structuring Pd Nanoparticles on 2H-WS₂ Nanosheets Induces Excellent Photocatalytic Activity for Cross-Coupling Reactions under Visible Light. *J. Am. Chem. Soc.* **2017**, *139*, 14767-14774.
- (18) Yim, D.; Raza, F.; Park, J. H.; Lee, J. H.; Kim, H. I.; Yang, J. K.; Hwang, I. J.; Kim, J. H., Ultrathin WO₃ Nanosheets Converted from Metallic WS₂ Sheets by Spontaneous Formation and Deposition of PdO Nanoclusters for Visible Light-Driven C-C Coupling Reactions. *ACS Appl. Mater. Interfaces* **2019**, *11*, 36960-36969.
- (19) Hoffman, J. B.; Schleper, A. L.; Prashant, V. K., Transformation of Sintered CsPbBr₃ Nanocrystals to Cubic CsPbI₃ and Gradient CsPbBr_xI_{3-x} through Halide Exchange. *J. Am. Chem. Soc.* **2016**, *138*, 8603–8611.
- (20) Feng, C.; Tang, L.; Deng, Y.; Wang, J.; Liu, Y.; Ouyang, X.; Yang, H.; Yu, J.; Wang, J., A novel sulfur-assisted annealing method of g-C₃N₄ nanosheet compensates for the loss of light absorption with further promoted charge transfer for photocatalytic production of H₂ and H₂O₂. *Appl. Catal. B: Environm.* **2021**, *281*, 119539.
- (21) Feng, C.; Tang, L.; Deng, Y.; Wang, J.; Luo, J.; Liu, Y.; Ouyang, X.; Yang, H.; Yu, J.; Wang, J., Synthesis of Leaf-Vein-Like g-C₃N₄ with Tunable Band Structures and Charge Transfer Properties for Selective Photocatalytic H₂O₂ Evolution. *Adv. Funct. Mater.* **2020**, *30*, 2001922.
- (22) Steele, J. A.; Puech, P.; Keshavarz, M.; Yang, R.; Banerjee, S.; Debroye, E.; Kim, C. W.; Yuan, H.; Heo, N. H.; Vanacken, J.; Walsh, A.; Hofkens, J.; Roeffaers, M. B. J., Giant Electron-Phonon Coupling and Deep Conduction Band Resonance in Metal Halide Double Perovskite. *ACS Nano* **2018**, *12*, 8081-8090.
- (23) Wright, A. D.; Verdi, C.; Milot, R. L.; Eperon, G. E.; Pérez-Osorio, M. A.; Snaith, H. J.; Giustino, F.; Johnston, M. B.; Herz, L. M., Electron–phonon coupling in hybrid lead halide perovskites. *Nat. Commun.* **2016**, *7*, 1-9.

Chapter 3. Simultaneous photocatalytic H₂ generation and organic synthesis over crystalline-amorphous Pd nanocube decorated Cs₃Bi₂Br₉

Chunhua Wang, Bo Weng,* Yuhe Liao, Biao Liu, Masoumeh Keshavarz, Yang Ding, Haowei Huang, Davy Verhaeghe, Julian A. Steele, Wenhui Feng, Bao-Lian Su, Johan Hofkens* and Maarten B. J. Roeffaers*

Adapted with permission from *Chem. Commun.*, 2022, Accepted.

Contributions

C.W., B.W., J. H. and M.B.J.R. designed the project; C.W. conducted the most experiments, including sample preparation, SEM, DRS, PL, Raman, GC, GC-MS, and activity tests; Y.L., M.K., Y.D., H.H., and W.F. performed part of the experiments; B.W., Y.D., D.V., J.A.S., and B.S. supported the experiments and helped to analyze the results; B.L. carried out the theoretical calculations; C.W. analyzed all results and wrote the draft; C.W., B.W., J.H. and M.B.J.R. together revised the manuscript with input from all the authors.

Abstract

A Cs₃Bi₂Br₉ photocatalyst decorated with crystalline-amorphous Pd nanocube cocatalyst is reported to simultaneously produce 1400 μmol h⁻¹ g⁻¹ of H₂ and benzaldehyde from the selective benzyl alcohol oxidation. This route offers an alternative for photocatalytic H₂ generation using metal halide perovskites under mild conditions.

3.1 Introduction

Photocatalytic H₂ generation is considered a promising strategy for the sustainable production of energy.¹⁻⁵ Recently, metal halide perovskites (MHPs) have emerged as efficient H₂ evolution photocatalysts.⁶⁻⁸ However, most of the H₂ evolution reaction (HER) experiments are performed in saturated aqueous hydrohalic acid HX (X = Br and I) solutions using the dynamic dissolution-precipitation equilibrium to keep the MHP stable.^{9, 10} During the photocatalytic process, the halide anion, X⁻, will be oxidized to X₃⁻, which requires additional reducing agents (such as H₃PO₂) to regenerate X⁻.^{11, 12} This limits the real-world large-scale applicability and the overall sustainability. Moreover, the strong acidity and corrosive ability of the hydrohalic acid solution make the operational conditions harsher and put limitations to the selection of cocatalysts based on their stability.¹¹ Therefore, it is important to explore alternative photocatalytic HER routes using MHPs.

Dual-functional photocatalytic processes that couple HER with industrially relevant organic reactions, such as simultaneous H₂ evolution and value-added aldehyde generation from alcohols, have recently received extensive attention.^{13, 14} Such a dual-purpose photocatalytic reaction offers an excellent alternative for H₂ evolution over MHP photocatalysts avoiding concentrated hydrohalic acid solutions. Additionally, compared to the traditional photocatalytic conversion of alcohols to aldehydes, both the photogenerated electrons and holes in dual-functional systems can be used effectively, to produce value-added products.¹²

On the other hand, despite MHPs having been used for various photocatalytic applications, pure MHP materials generally exhibit modest photocatalytic performance.¹¹ To improve the photoactivity, the decoration of the MHP surface with a metal cocatalyst has been shown to be effective.¹¹ Pd for example has been demonstrated to efficiently improve the photocatalytic performance by promoting the photogenerated charge carrier separation.^{13, 15} Moreover, controlling the nanoparticle morphology of Pd further improves the photoactivity of Pd-nanocube cocatalyst.¹⁵ In addition, recent studies indicate that surface amorphization is an effective route to increase the number of active sites, while

partially amorphization Pd can favor charge separation and surface reactions, thus improving the overall photocatalytic activity.^{15, 16}

In this work, we report the successful application of Cs₃Bi₂Br₉ MHP decorated with crystalline-amorphous core@shell Pd (APd) nanocubes, as cocatalyst, to efficiently coproduce H₂ and benzaldehyde (BAD) from benzyl alcohol (BA). Benefiting from the formation of a Schottky junction between Cs₃Bi₂Br₉ and Pd, photogenerated charges in Cs₃Bi₂Br₉ are efficiently separated. Through targeted amorphization of the Pd nanoparticle surface, more active sites are formed, which enhances the HER over APd/Cs₃Bi₂Br₉. As a result, excellent production rates of 1421 $\mu\text{mol h}^{-1} \text{g}^{-1}$ for H₂ and 1457 $\mu\text{mol h}^{-1} \text{g}^{-1}$ for BAD are achieved with 1% APd/Cs₃Bi₂Br₉, which is 4-fold higher than that of pure Cs₃Bi₂Br₉, and superior to most reported photocatalysts so far. Through a set of control experiments, a plausible reaction mechanism was proposed.

3.2 Results and discussion

Fig. S1 describes the synthetic procedure of these materials. X-ray diffraction experiments (Fig. S2A) confirm the formation of Cs₃Bi₂Br₉ (trigonal phase). Compared to crystalline Pd, the intensity of the diffraction peaks of the APd sample is decreased.¹⁷ Raman spectroscopy (Fig. S3) and scanning electron microscopy (Fig. S4) confirm that the deposition of APd nanoparticles in the employed relative amounts, between 0.25 and 2 wt%, does not compromise the perovskite structure and morphology of the material. Inductively coupled plasma-mass spectrometry shows the efficient deposition of APd with the exact amount of APd in the composite matching well the target amount added to the synthesis mixture (Table S1). Transmission electron microscopy (TEM) confirms the synthesized Pd has a cube morphology (Fig. S5A), and the amorphization of the surface of APd is shown by high-resolution TEM (Fig. S5D), leading to a crystalline-amorphous core@shell structure. Lattice spacings of 0.33 nm and 0.20 nm (Fig. S5F) in APd/Cs₃Bi₂Br₉ hybrids are ascribed to Cs₃Bi₂Br₉ (003)¹⁸ and Pd (200),¹³ respectively.

The photocatalytic performance of these MHP-based samples was evaluated by simultaneous H₂ evolution and BAD generation from BA (See ESI for details). No reaction products are detected in absence of a photocatalyst (Fig. 1A). After

14 h of solar illumination (AM 1.5G), the pure $\text{Cs}_3\text{Bi}_2\text{Br}_9$ sample displayed an average H_2 production rate of $341 \pm 36 \mu\text{mol h}^{-1} \text{g}^{-1}$, together with $368 \pm 30 \mu\text{mol h}^{-1} \text{g}^{-1}$ of BAD with $> 99\%$ selectivity. As expected, the photoactivity is improved dramatically after introducing APd cocatalyst. The best production rates of $1421 \pm 91 \mu\text{mol h}^{-1} \text{g}^{-1}$ and $1457 \pm 78 \mu\text{mol h}^{-1} \text{g}^{-1}$ for H_2 and BAD, respectively, are obtained with 1% APd/ $\text{Cs}_3\text{Bi}_2\text{Br}_9$; this is a 4-fold enhancement over the pure $\text{Cs}_3\text{Bi}_2\text{Br}_9$; the apparent quantum efficiency at 400 nm is 0.33%. APd loading beyond 1% leads to reduced performance, which could be explained by the effect that excessive amounts of metal, APd, can also serve as a charge recombination center.¹⁹ The material with optimal loading, 1% APd/ $\text{Cs}_3\text{Bi}_2\text{Br}_9$, displays a multifold improved photoactivity compared to $\text{Cs}_3\text{Bi}_2\text{Br}_9$ functionalized with the fully crystalline or fully amorphous Pd analogues (Fig. S6), as well as other reported MHP-based photocatalysts (Tables S2 and S3). Recycle tests show the 1% APd/ $\text{Cs}_3\text{Bi}_2\text{Br}_9$ photocatalyst remains stable for at least 70 h of use (Fig. 1B). Morphology, structure and optical properties characterizations achieved through XRD, SEM, PL and absorbance spectra (Fig. S7) further confirm the excellent stability of the photocatalysts.

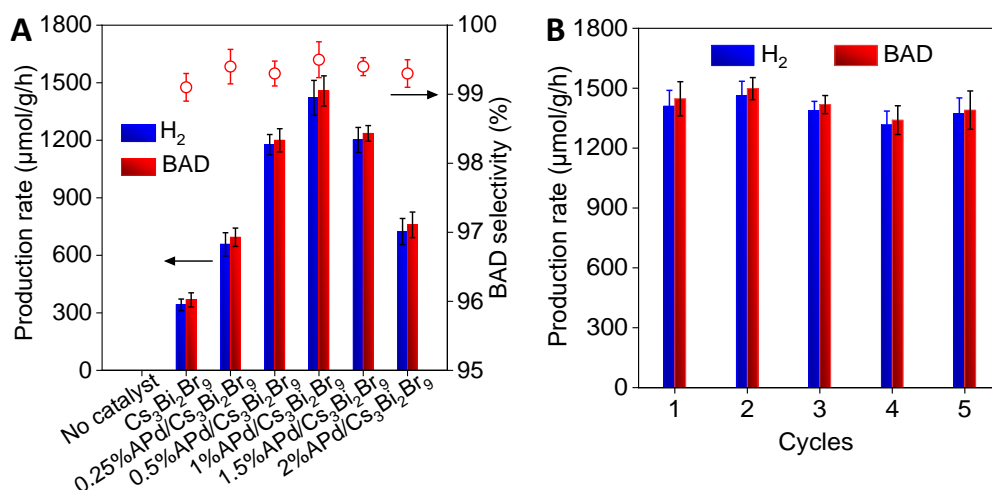


Fig. 1. (A) Simultaneous photocatalytic H_2 evolution and BAD production from BA over $\text{Cs}_3\text{Bi}_2\text{Br}_9$ loaded with $x\%$ APd/ $\text{Cs}_3\text{Bi}_2\text{Br}_9$ hybrids ($x=0.25, 0.5, 1, 1.5,$ and 2). (B) Recycle tests for 1% APd/ $\text{Cs}_3\text{Bi}_2\text{Br}_9$ composite. Reaction conditions: 1 mmol BA, 15 mg catalyst, 2.5 mL benzotrifluoride, simulated solar light (AM 1.5G, 150 W Xe lamp, light intensity: 100 mW/cm^2), reaction time (14 h).

To understand the exact origin of the photoactivity enhancement by APd loading, experimental and theoretical analyses were carried out. UV-vis diffuse reflectance spectroscopy (DRS) was employed to investigate the optical properties of $\text{Cs}_3\text{Bi}_2\text{Br}_9$ and 1% APd/ $\text{Cs}_3\text{Bi}_2\text{Br}_9$, showing that both materials exhibit similar visible light absorption properties with an absorption maximum around 470 nm (2.64 eV, Fig. S8), in agreement with previous reports.²⁰ The introduction of APd increases the light absorption beyond 475 nm, paralleled by the color change (Fig. S9), which is attributed to the APd because of its: (i) enhanced scattering and (ii) enhanced light absorption due to interband transition of bound electrons.^{19, 21} The photoluminescence (PL) spectra of both materials are similar (Fig. S10A), while there is a very strong intensity drop (35 %) after APd addition leading to reduced radiative recombination of electron-hole pairs.^{13, 19} Time-resolved PL was further performed to study the photophysical processes involved, with the PL decays analyzed using a summed bi-exponential, yielding two distinct decay constants (τ_i) and amplitudes (A_j). Here τ_1 and τ_2 are associated with the bound exciton and free exciton recombination, respectively.⁷ Compared to pure $\text{Cs}_3\text{Bi}_2\text{Br}_9$, the APd/ $\text{Cs}_3\text{Bi}_2\text{Br}_9$ sample displays longer photogenerated charge carrier lifetimes (Fig. S10B), with τ_1 and τ_2 increasing significantly, suggesting the effective migration of photogenerated charge carriers in $\text{Cs}_3\text{Bi}_2\text{Br}_9$.²²

X-ray photoelectron spectroscopy (XPS) was used to explore the chemical structure and valence state of these two materials. Fig. S11A shows that two typical Cs 3d peaks of $\text{Cs}_3\text{Bi}_2\text{Br}_9$ located at 724.1 and 738.2 eV are assigned to Cs 3d_{5/2} and Cs 3d_{3/2},⁷ respectively. These peaks shift to higher binding energies (BE) after APd loading can be attributed to a shift in electron density from $\text{Cs}_3\text{Bi}_2\text{Br}_9$ to APd.¹⁹ A similar phenomenon was observed for Bi 4f and Br 3d (Figs. S11B and S11C). Meanwhile, the Pd 3d XPS peaks (Fig. S11D) in 1% APd/ $\text{Cs}_3\text{Bi}_2\text{Br}_9$ move slightly towards lower BE than that of metallic Pd,¹⁹ originating from the enrichment of electrons on APd.

Photoelectrochemical measurements were performed to investigate the charge-transfer properties. Polarization curves (Fig. S12A) show that the presence of APd enhances the current density of $\text{Cs}_3\text{Bi}_2\text{Br}_9$, indicating the efficient charge transfer in 1% APd/ $\text{Cs}_3\text{Bi}_2\text{Br}_9$.^{19, 23} This is consistent with

transient photocurrent response measurements, where a higher photocurrent is observed for 1% APd/Cs₃Bi₂Br₉ (Fig. 2A). Photocurrent response versus monochromatic light test also verified the photocurrent density over 1% APd/Cs₃Bi₂Br₉ higher than that of pure Cs₃Bi₂Br₉ (Fig. S12B). To better understand the charge-transfer resistance, electrochemical impedance spectroscopy (EIS) was performed. The 1% APd/Cs₃Bi₂Br₉ hybrid presents a smaller semicircle in the Nyquist plots (Fig. 2B), indicating the improved charge carrier migration efficiency.¹³ This is supported by surface charge transfer efficiency (η_t) measurements (Fig. 2C). The η_t of 1% APd/Cs₃Bi₂Br₉ is calculated to be 62%, much higher than that of Cs₃Bi₂Br₉ (29%). These results uncover that the 1% APd/Cs₃Bi₂Br₉ sample possesses elevated charge separation efficiency, empowering faster surface photoredox reactions.²⁴

To reveal the underlying mechanism of charge transfer in the hybrid materials, the band structure of these samples was evaluated. Mott-Schottky measurements (Fig. S13), combined with bandgap data, show the conduction band (CB) and valence band (VB) edge potential of Cs₃Bi₂Br₉ are -0.57 and 2.07 eV (vs. NHE), respectively, confirming the suitable redox potentials (+ 0.68 eV) for the performed reaction.²⁵ Besides, The calculated density of charge carriers (N_D) of 1% APd/Cs₃Bi₂Br₉ slightly larger than that of pure Cs₃Bi₂Br₉, suggesting an enhanced carrier density of 1% APd/Cs₃Bi₂Br₉ due to the decoration of APd NCs. Moreover, theoretical calculations show that the work function (WF) of Cs₃Bi₂Br₉ is 4.82 eV, and the WF of APd is 5.61 eV (Figs. S14 A and B). Driven by the different WF of Cs₃Bi₂Br₉ and APd, electrons migrate across the interface forming a Schottky barrier (Fig. S14D).²⁶ Band bending induces a built-in electric field, driving the electrons in Cs₃Bi₂Br₉ to move to APd.¹⁹ Moreover, the role of APd in charge separation was then assessed by analysing the charge density difference ($\Delta\rho$). Fig. S15A illustrates the obvious charge transfer at the interface in APd/Cs₃Bi₂Br₉, confirmed by the plane-averaged $\Delta\rho$ data (Fig. S15B), suggesting the efficiency in charge separation in Cs₃Bi₂Br₉ in the presence of APd.

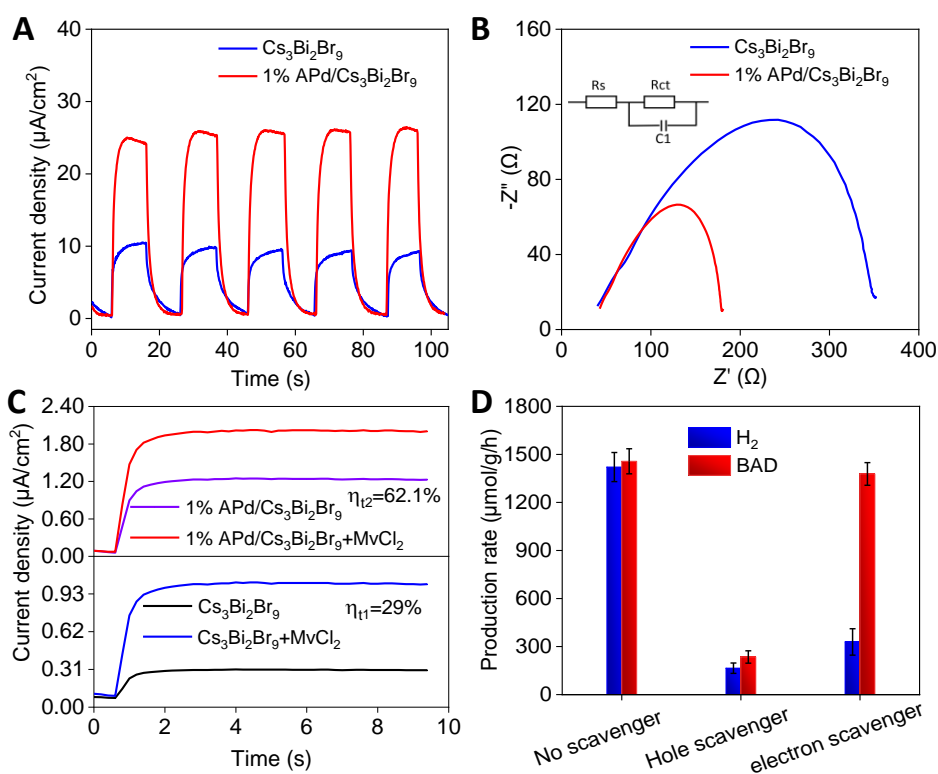
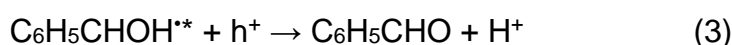
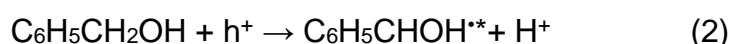
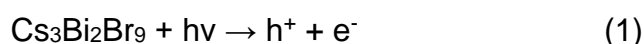


Fig. 2. (A) Transient photocurrents, (B) EIS spectra and (C) Surface charge transfer efficiency (η_t) of $\text{Cs}_3\text{Bi}_2\text{Br}_9$ and 1% APd/ $\text{Cs}_3\text{Bi}_2\text{Br}_9$ photocatalysts. (D) The effect of electron and hole scavengers on the photocatalytic performance of H_2 evolution and BAD generation over 1% APd/ $\text{Cs}_3\text{Bi}_2\text{Br}_9$. Reaction conditions: 1 mmol BA, 15 mg catalyst, 2.5 mL benzotrifluoride, simulated solar light (AM 1.5G, 150 W Xe lamp, light intensity: $100 \text{ mW}/\text{cm}^2$), reaction time (14 h).

To understand the mechanism of the targeted reaction, control experiments with scavengers were conducted. The addition of a hole scavenger (sodium sulfite, 1mM) largely diminished both BAD and H_2 formation (Fig. 2D), suggesting the photogenerated holes are the major oxidative species for triggering the overall reaction.⁷ When an electron scavenger (potassium persulfate, 1mM) was added into the system, the BAD formation was not influenced, while the H_2 production decreased sharply, revealing that the photogenerated electrons are major reductive species for H_2 generation.^{27, 28} In situ electron spin resonance (ESR) using 5,5-dimethyl-1-pyrroline N-oxide (DMPO) as the trapping reagent was conducted to monitor reaction intermediates.²⁹ Fig. S16 shows six ESR peaks indexed as DMPO-carbon-

centred radical (DMPO- \cdot C) and additional nitroxide-like radical signals formed by the light-induced cleavage of the N–C bond and the ring-opening of DMPO- \cdot C adduct,^{29, 30} while no ESR signals are detected in the dark, indicating the generation of C₆H₅CH(OH) \cdot free radicals during the photocatalytic reaction process.¹⁰

Based on these experiments, we propose a mechanism for the dehydrogenation of BA with simultaneous H₂ and BAD production over APd/Cs₃Bi₂Br₉ catalysts (Fig. S17), and the reaction equations are as follows:



Under solar light illumination, Cs₃Bi₂Br₉ absorbs photons with energy larger than the bandgap to generate electron-hole pairs. The photogenerated electrons transfer from the CB of Cs₃Bi₂Br₉ to the APd due to the formation of a Schottky junction, leaving the holes in the VB of Cs₃Bi₂Br₉.¹⁹ Two holes are required to oxidize adsorbed BA molecules to produce BAD via C₆H₅CH(OH) \cdot while releasing two protons (H⁺).²⁹ These protons are reduced by the electrons in APd to generate H₂.²⁹

3.3 Conclusions

In summary, we have developed a dual-functional photocatalytic system for simultaneous H₂ evolution and BAD production over MHP-based photocatalysts. Phase-engineered crystalline-amorphous core@shell APd cocatalyst was used to promote charge transfer and surface redox reaction. As a result, an excellent photocatalytic performance of H₂ and BAD products over APd/Cs₃Bi₂Br₉ was achieved. Based on a set of control experiments, a possible reaction mechanism was proposed. This work offers an alternative for MHP-based solar-to-fuel conversion through dual-functional photocatalytic systems. On the other hand, from the perspective of green solvents, exploring low-toxic solvents such as isopropanol alcohol, ethyl acetate, etc., to replace the benzotrifluoride while keeping MHP stable, is promising.

3.4 References

1. H. Lin, J. Wang, J. Zhao, Y. Zhuang, B. Liu, Y. Zhu, H. Jia, K. Wu, J. Shen and X. Fu, *Angew. Chem.*, 2022, **134**, e202117645.
2. H. Lin, Z. Ma, J. Zhao, Y. Liu, J. Chen, J. Wang, K. Wu, H. Jia, X. Zhang and X. Cao, *Angew. Chem.*, 2021, **133**, 1255-1263.
3. S. Wu, Y. Pan, H. Lin, L. Li, X. Fu and J. Long, *ChemSusChem*, 2021, **14**, 4958-4972.
4. Y. Chen, C. Gao, T. Yang, W. Li, H. Xu and Z. Sun, *Chinese J. Struct. Chem*, 2022, **41**, 2204001-2204011.
5. R. Chen, J. Chen, H. Che, G. Zhou, Y. Ao and Bin Liu, *Chinese J. Struct. Chem*, 2022, **41**, 2201014-2201018.
6. X. Zhu, Y. Lin, J. San Martin, Y. Sun, D. Zhu and Y. Yan, *Nat. Commun.*, 2019, **10**, 1-10.
7. C. Wang, H. Huang, B. Weng, D. Verhaeghe, M. Keshavarz, H. Jin, B. Liu, H. Xie, Y. Ding and Y. Gao, *Appl. Catal. B: Environ.*, 2022, **301**, 120760.
8. H. Huang, D. Verhaeghe, B. Weng, B. Ghosh, H. Zhang, J. Hofkens, J. A. Steele and M. B. Roeffaers, *Angew. Chem.*, 2022, **134**, e202203261.
9. S. Park, W. J. Chang, C. W. Lee, S. Park, H.-Y. Ahn and K. T. Nam, *Nat. Energy*, 2016, **2**, 1-8.
10. T. Wang, D. Yue, X. Li and Y. Zhao, *Appl. Catal. B: Environ.*, 2020, **268**, 118399.
11. H. Huang, B. Pradhan, J. Hofkens, M. B. Roeffaers and J. A. Steele, *ACS Energy Lett.*, 2020, **5**, 1107-1123.
12. W. Shang, Y. Li, H. Huang, F. Lai, M. B. Roeffaers and B. Weng, *ACS Catal.*, 2021, **11**, 4613-4632.
13. B. Weng, Q. Quan and Y.-J. Xu, *J. Mater. Chem. A*, 2016, **4**, 18366-18377.
14. H. Wang, P. Hu, J. Zhou, M. B. Roeffaers, B. Weng, Y. Wang and H. Ji, *J. Mater. Chem. A*, 2021, **9**, 19984-19993.
15. Q. Chen, S. Wu, S. Zhong, B. Gao, W. Wang, W. Mo, H. Lin, X. Wei, S. Bai and J. Chen, *J. Mater. Chem. A*, 2020, **8**, 21208-21218.
16. Q. Chen, W. Mo, G. Yang, S. Zhong, H. Lin, J. Chen and S. Bai, *Small*, 2021, **17**, 2102105.

17. H. Cheng, N. Yang, G. Liu, Y. Ge, J. Huang, Q. Yun, Y. Du, C. J. Sun, B. Chen, J. Liu and H. Zhang, *Adv. Mater.*, 2020, **32**, e1902964.
18. B. Yang, J. Chen, F. Hong, X. Mao, K. Zheng, S. Yang, Y. Li, T. Pullerits, W. Deng and K. Han, *Angew. Chem. Int. Ed.*, 2017, **56**, 12471-12475.
19. S. Lu, B. Weng, A. Chen, X. Li, H. Huang, X. Sun, W. Feng, Y. Lei, Q. Qian and M.-Q. Yang, *ACS Appl. Mater. Interfaces*, 2021, **13**, 13044-13054.
20. M. Shi, G. Li, W. Tian, S. Jin, X. Tao, Y. Jiang, E. A. Pidko, R. Li and C. Li, *Adv. Mater.*, 2020, **32**, e2002137.
21. S. Sarina, H. Y. Zhu, Q. Xiao, E. Jaatinen, J. Jia, Y. Huang, Z. Zheng and H. Wu, *Angew. Chem. Int. Ed.*, 2014, **53**, 2935-2940.
22. H. Huang, H. Yuan, J. Zhao, G. Solís-Fernández, C. Zhou, J. W. Seo, J. Hendrix, E. Debroye, J. A. Steele, J. Hofkens, J. Long and M. B. J. Roeffaers, *ACS Energy Lett.*, 2018, **4**, 203-208.
23. S. Liu, W. Qi, S. Adimi, H. Guo, B. Weng, J. P. Attfield and M. Yang, *ACS Appl. Mater. Interfaces*, 2021, **13**, 7238-7247.
24. C. Wang, B. Weng, M. Keshavarz, M.-Q. Yang, H. Huang, Y. Ding, F. Lai, I. Aslam, H. Jin and G. Romolini, *ACS Appl. Mater. Interfaces*, 2022, **14**, 17185-17194.
25. Y. Wu, X. Ye, S. Zhang, S. Meng, X. Fu, X. Wang, X. Zhang and S. Chen, *J. Catal.*, 2018, **359**, 151-160.
26. X.-H. Li, M. Baar, S. Blechert and M. Antonietti, *Sci. Rep.*, 2013, **3**, 1-6.
27. X. Xiao, J. Jiang and L. Zhang, *Appl. Catal. B: Environ.*, 2013, **142**, 487-493.
28. H. Huang, C. Zhou, X. Jiao, H. Yuan, J. Zhao, C. He, J. Hofkens, M. B. Roeffaers, J. Long and J. A. Steele, *ACS Catal.*, 2019, **10**, 1439-1443.
29. Q. Lin, Y.-H. Li, M.-Y. Qi, J.-Y. Li, Z.-R. Tang, M. Anpo, Y. M. Yamada and Y.-J. Xu, *Appl. Catal. B: Environ.*, 2020, **271**, 118946.
30. D. Jiang, X. Chen, Z. Zhang, L. Zhang, Y. Wang, Z. Sun, R. M. Irfan and P. Du, *J. Catal.*, 2018, **357**, 147-153.

3.5 Appendix to Chapter 3

Experimental section

Materials and reagents

Bismuth(III) bromide (BiBr_3 , $\geq 98\%$), potassium palladium(II) chloride (K_2PdCl_4 , 99%), potassium bromide (KBr , 99%), L-ascorbic acid ($\text{C}_6\text{H}_8\text{O}_6$, 99%), poly(vinyl pyrrolidone) (PVP, M.W. $\approx 55\,000$), benzyl alcohol (anhydrous, 99.8 %) were purchased from Sigma-Aldrich. Cesium bromide (CsBr , 99%) and benzotrifluoride ($\geq 98\%$) were purchased from Alfa Aesar. Dimethyl sulfoxide (DMSO, anhydrous, Max. 0.005% water) was supplied by VWR chemicals. Ethanol (absolute, $\geq 99.8\%$) was purchased from Fisher Chemical. Bismuthiol I (1,3,4-thiadiazole-2,5-dithiol ($\text{C}_2\text{H}_2\text{N}_2\text{S}_3$), $\geq 99.0\%$) was purchased from Fluka. The Milli-Q water was obtained from the Milli-Q System. All chemicals were used without further purification.

Photocatalyst preparation

Preparation of $\text{Cs}_3\text{Bi}_2\text{Br}_9$ catalyst

$\text{Cs}_3\text{Bi}_2\text{Br}_9$ material was synthesized at room temperature using an anti-solvent precipitation method. Firstly, the $\text{Cs}_3\text{Bi}_2\text{Br}_9$ perovskite precursor solution was prepared by dissolving CsBr and BiBr_3 ($\text{CsBr}/\text{BiBr}_3=3:2$) in dimethyl sulfoxide (DMSO) at a precursor concentration of 0.4 M. Secondly, the fully dissolved $\text{Cs}_3\text{Bi}_2\text{Br}_9$ precursor solution was added to isopropanol to get the $\text{Cs}_3\text{Bi}_2\text{Br}_9$ suspension. After washing twice, the $\text{Cs}_3\text{Bi}_2\text{Br}_9$ suspension was collected by centrifugation. Finally, the $\text{Cs}_3\text{Bi}_2\text{Br}_9$ material was dried in a vacuum oven at 60 °C overnight.^[a]

^[a]Note: this was added as a footnote to Chapter 3 (which is based on a published article) based on the discussion during the preliminary PhD defence.

Synthesis of palladium nanocubes (Pd NCs)

The Pd NCs were synthesized according to the previously reported method.¹ First, PVP, KBr and AA with the amount of 105 mg, 600 mg, and 60 mg, respectively, were added in an 8 mL Milli-Q water under magnetic stirring at 80 °C for 10 min. Second, 3 mL Milli-Q water solution containing 63 mg K₂PdCl₄ was added to the above mixture under magnetic stirring at 80 °C for 3 h, Finally, the synthesized black Pd NCs were collected by centrifugation and washed with isopropanol, and then dispersed in isopropanol or methanol at a concentration of 1 mg/mL.

Synthesis of amorphous palladium (APd)

The APd was synthesized by a previously reported method with slight modification.² In a typical experiment, 1 mL of the as-synthesized Pd NCs with a concentration 1 mg/mL in methanol was mixed with 9 mL of a methanol solution containing 50 mg of bismuthiol I. The mixed solution was sealed in a closed vial under magnetic stirring at 25 °C for 8 h. After that, the APd products were collected by centrifugation and washed with isopropanol.

Synthesis of APd/Cs₃Bi₂Br₉ composite

A series of x wt% APd/Cs₃Bi₂Br₉ photocatalysts were synthesized at room temperature through the similar precipitation method mentioned above. In a typical experiment (1% APd/Cs₃Bi₂Br₉), 15 mL isopropanol containing 100 mg Cs₃Bi₂Br₉ powder was first kept stirring for 30 min, and then 20 mL of isopropanol solution containing 1 mg APd was added dropwise into the vigorously stirred Cs₃Bi₂Br₉ suspension. Then the mixture was kept stirring at room temperature for 12 h. Finally, the APd/Cs₃Bi₂Br₉ suspension was collected by centrifugation after washing twice and dried in a vacuum oven at 60 °C.

Characterization

Instrumentations and methods

X-ray diffraction (XRD) patterns of the catalysts were achieved using an X-ray diffractometer (Cu K α 1 radiation, $\lambda=1.5406$ Å) in the 2 θ ranging from 10 to 70 degrees at a scan rate of 0.02°/s. Scanning electron micrographs of samples

were recorded by scanning electron microscopy (SEM, FEI-Q FEG250). Transmission electron microscopy (TEM) and high-resolution transmission electron microscopy (HRTEM) were analysed using a JEOL model JEM 2010 EX instrument at an acceleration voltage of 200 kV. Ultraviolet-visible spectrophotometer (UV-vis, Lambda-950) was employed to obtain the optical properties of the samples by UV-vis diffuse reflectance spectroscopy (DRS) in the wavelength of 300-800 nm, where BaSO₄ and black carbon were used as the references. Steady-state photoluminescence spectra were recorded on an Edinburgh FLS980 with an excitation wavelength of 365 nm in the wavelength of 425-575 nm. Time-resolved PL spectra were recorded on a Leica DMI8 system with a pulsed white light laser (SuperK Extreme EXW-12, NKT Photonics) operating at 405 nm and set at a repetition rate of 20 MHz and a fluence of 2 μJ mm⁻². X-ray photoelectron spectroscopy (XPS, Al Kα X-ray source, 1486.6 eV) was employed to study the chemical structure and valence state information of the materials, and the C 1s signal was set to a position of 284.6 eV. Photoelectrochemical measurements were carried out using a standard three-electrode setup. Ag/AgCl electrode was employed as the reference electrode, a platinum sheet was used as the counter electrode. The working electrode was deposited on a cleaned indium tin oxide (ITO) substrate and immersed in the electrolyte solution. Tetrabutylammonium hexafluorophosphate (TBAPF₆, 0.1 M) dissolved in dichloromethane (DCM) solution was used as the electrolyte. Electrochemical impedance spectroscopy (EIS) was obtained on an electrochemical workstation under an alternating current (AC) voltage (5 mV amplitude) in a frequency range from 10 kHz to 5 MHz with the open circuit potential of 0.2 V. Photocurrent response measurements were performed under simulated solar light irradiation. Cathodic polarization curves were achieved via linear sweep voltammetry technique with a scan rate of 0.2 mV/s. Mott–Schottky plots were measured in dark at a frequency of 1 kHz.

The surface charge transfer efficiency (η_t) was measured by adding methylviologen dichloride (MVCl₂) into the electrolyte as a fast electron scavenger.^{3, 4} The photocurrent can be described by the following Equation.⁴

$$J_1 = J_m \times \eta_a \times \eta_s \times \eta_t \quad (1)$$

When adding $MVCl_2$ to the electrolyte, the surface charge transfer is very fast and the η_t approximately reaches 100%. The photocurrent can be written as Equation.³

$$J_2 = J_m \times \eta_a \times \eta_s \quad (2)$$

Due to J_m , η_a , η_s are unchanged before and after adding the $MVCl_2$, the surface transfer efficiency (η_t) can be given as:^{3, 4}

$$\eta_t = J_1/J_2 \quad (3)$$

Density functional theory (DFT) calculation

The present calculations have been performed with the Vienna ab initio simulation package (VASP) code, based on density functional theory (DFT). Projector-augmented wave method is used to describe the interaction between ion cores and valence electrons. Atomic structures are optimized using the exchange-correlation functional of Perdew, Burke, and Ernzerhof. A plane-wave cutoff of 400 eV is used in the calculation. Monkhorst-Pack $5 \times 5 \times 1$ k-point grid is used to sample the Brillouin zone. All atoms are allowed to be fully relaxed till the atomic Hellmann-Feynman forces are less than 0.02 eV/\AA . The convergence criterion of energy in the self-consistency process is set at about $1 \times 10^{-4} \text{ eV}$. The plane-averaged charge density difference can be written as $\Delta\rho(z) = \rho_{\text{tot}} - \rho_{\text{Cs}_3\text{Bi}_2\text{Br}_9} - \rho_{\text{APd}}$. Here, ρ_{tot} is the plane-averaged density of the combined APd/ $\text{Cs}_3\text{Bi}_2\text{Br}_9$ system. $\rho_{\text{Cs}_3\text{Bi}_2\text{Br}_9}$ and ρ_{APd} are the plane-averaged densities of the free-standing $\text{Cs}_3\text{Bi}_2\text{Br}_9$ interface and APd interface, respectively, which are calculated by freezing the atomic positions of the respective components in the combined system.

Photocatalytic activity evaluation

The photocatalytic reactions were conducted in a 25 mL quartz reactor. In a typical experiment, 15 mg catalyst (1% APd/ $\text{Cs}_3\text{Bi}_2\text{Br}_9$) and 1 mmol benzyl alcohol (BA) were added to 2.5 mL benzotrifluoride. Then, the mixture was evacuated by a mechanical pump to completely remove air, and under simulated solar light illumination (150 W Xe lamp) for 14 h. After the illumination, the amount of H_2 evolved was detected using a gas chromatograph (GC, Shimadzu 2014) equipped with a thermal conductivity detector (TCD). Then,

the mixture was centrifuged, and the filtrates were analyzed by GC (Shimadzu 2010) to obtain the amount of the generated benzaldehyde (BAD). The conversion and selectivity of BA were defined as follows:

$$\text{Conversion (\%)} = [(C_0 - C_A)/C_0] \times 100\%$$

$$\text{Selectivity (\%)} = [C_B/(C_0 - C_A)] \times 100\%$$

Where C_0 is the initial concentration of BA, C_A and C_B are the concentrations of the BA substrate and corresponding BAD product, respectively. The apparent quantum efficiency (AQE) for H_2 generation measured at 400 nm (light intensity: 9.02 mW/cm^2) is calculated according to the following equations:

$$\begin{aligned} \text{AQE} &= (\text{number of reacted electrons}/\text{number of incident electrons}) \times 100\% \\ &= (2 \times \text{number of evolved } H_2 \text{ electrons}/\text{number of incident electrons}) \times 100\% \\ &= (2 \times 6.02 \times 10^{23} \times 0.0025) / \{ (14 \times 3600 \times 9.02) / [(6.6261 \times 10^{-34}) \times (3 \times 10^8)] / (4 \times 10^{-7}) \} \\ &= 0.33\% \end{aligned}$$

Main text supporting characterization

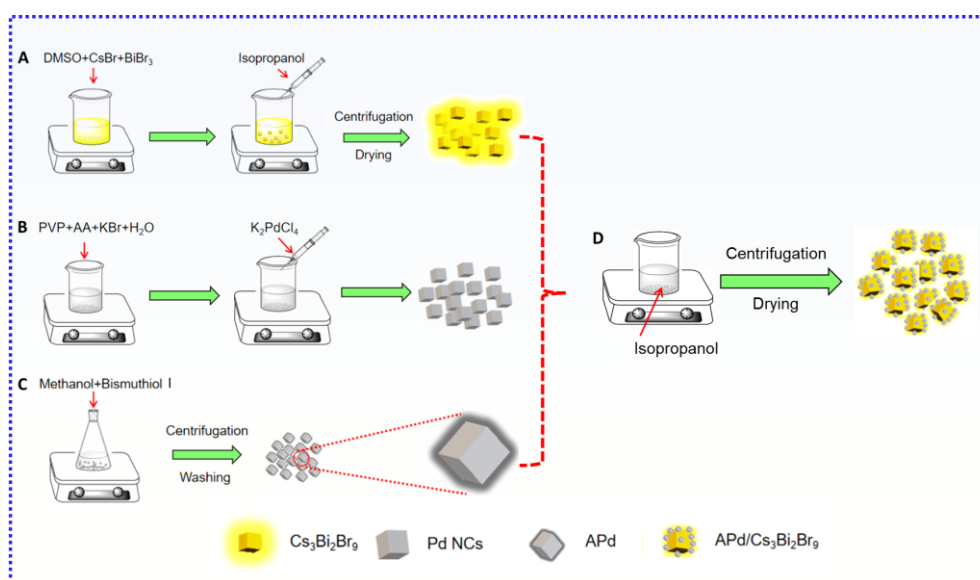


Fig. S1. The synthetic procedure of $Cs_3Bi_2Br_9$, Pd, APd, and APd/ $Cs_3Bi_2Br_9$ materials.

Note: The $Cs_3Bi_2Br_9$ powder was synthesized by an antisolvent precipitation method using the $Cs_3Bi_2Br_9$ precursor solution with fully dissolved CsBr and

BiBr₃ (CsBr/BiBr₃=3:2 in DMSO); Pd nanocubes (NCs) were synthesized according to the previous method,¹ and crystalline-amorphous Pd (APd) component was synthesized through modifying Pd NCs via a thiol molecule (bismuthiol I).² In the following, a series of APd/Cs₃Bi₂Br₉ hybrids with various Pd contents were synthesized by the decoration of the APd on the surface of Cs₃Bi₂Br₉ at room temperature, where the well-anchored APd NCs provide a crucial platform for charge transfer and interfacial redox reaction.

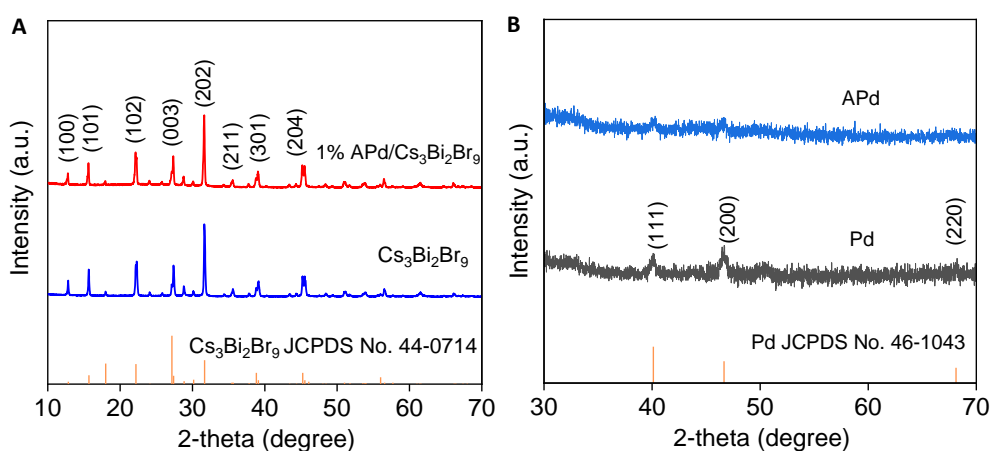


Fig. S2. XRD patterns of (A) Cs₃Bi₂Br₉ and 1% APd/Cs₃Bi₂Br₉ materials and (B) Pd and APd samples.

Note: This result reveals that the Cs₃Bi₂Br₉ in these hybrids is indexed to the trigonal phase (JCPDS No. 44-0714).⁵ No typical diffraction peaks assigned to Pd in APd/Cs₃Bi₂Br₉ were detected due to the low content of APd (1%).¹ XRD patterns in Fig. S2B show the as-prepared crystalline Pd NCs possess obvious diffraction peaks, while the intensity of the peaks of APd decreased significantly, indicating the formation of crystalline-amorphous structure.² This can be attributed to the replacement of PVP by thiol molecules because thiol-metal bond is enthalpically more favourable than pyrrolidone oxygen/nitrogen metal coordination.⁶ Meanwhile, the attached hydrophilic or amphiphilic thiol ligands will be dissolved in an alcohol solution to some extent, which leads to the displacement of Pd, thus forming this crystalline-amorphous structure.⁷

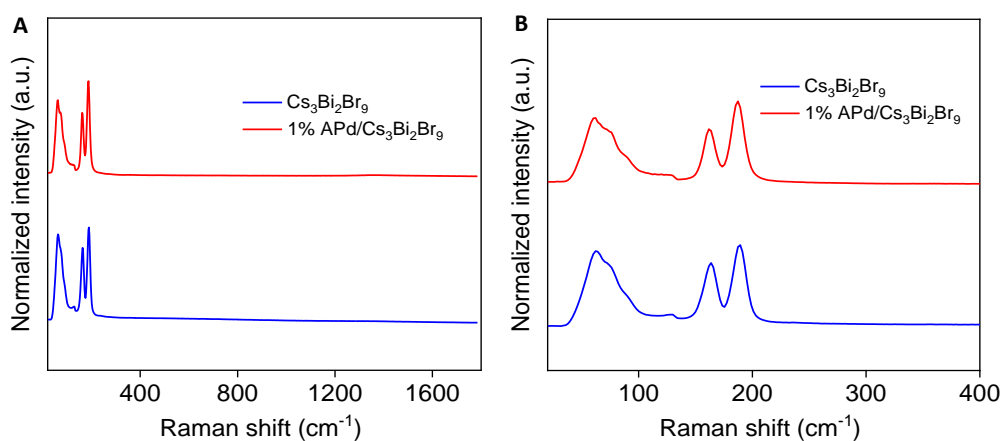


Fig. S3. Raman spectra of $\text{Cs}_3\text{Bi}_2\text{Br}_9$ and 1% APd/ $\text{Cs}_3\text{Bi}_2\text{Br}_9$ materials in the range of (A) 20-1800 cm^{-1} and (B) 20-400 cm^{-1} .

Note: Raman spectroscopy further confirmed that $\text{Cs}_3\text{Bi}_2\text{Br}_9$ is the predominant species and APd deposition does not affect the structure of $\text{Cs}_3\text{Bi}_2\text{Br}_9$. The modes at 167 and 192 cm^{-1} are attributed to the stretching vibrations of Bi-Br bonds in BiBr_6 octahedra.⁸ The other two peaks located at 63.9 and 74.6 cm^{-1} are due to vibrations of Br atoms only.^{8,9} The two samples decorated with APd correspond to the $\text{Cs}_3\text{Bi}_2\text{Br}_9$ vibrational mode, suggesting that $\text{Cs}_3\text{Bi}_2\text{Br}_9$ are the predominant species, agreeing with the XRD results.

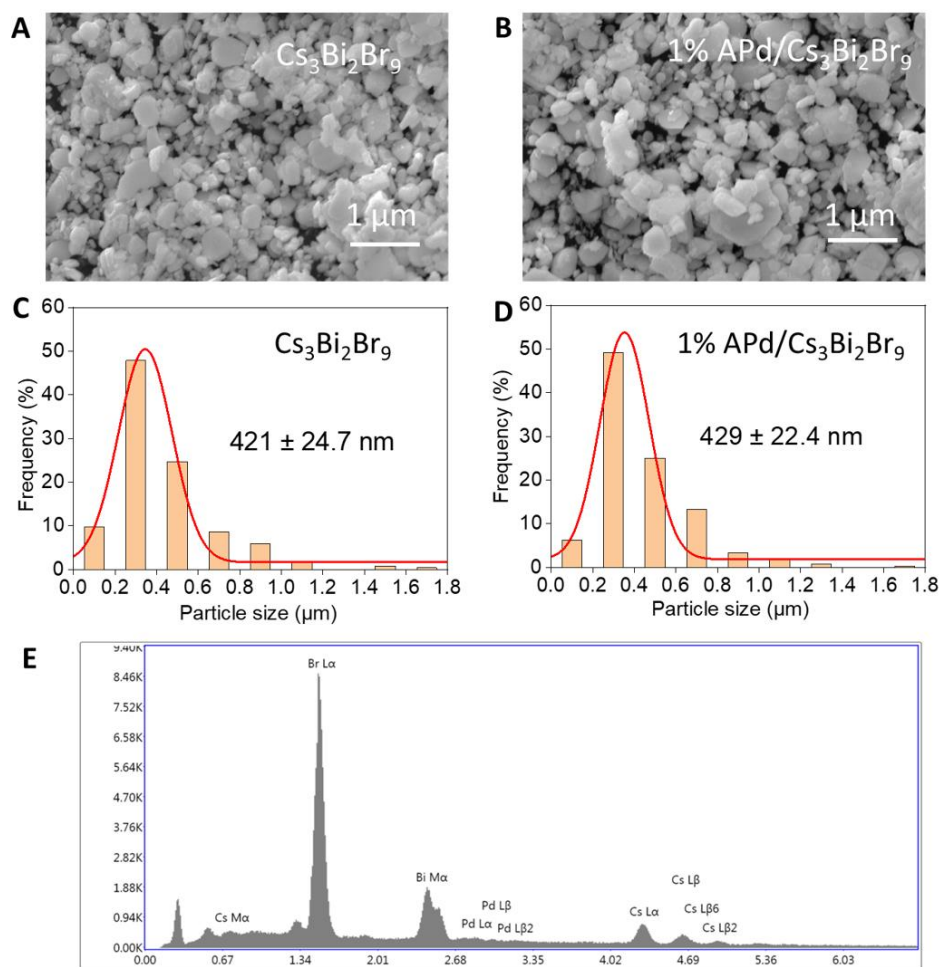


Fig. S4. (A-C) SEM images of (A) $\text{Cs}_3\text{Bi}_2\text{Br}_9$ and (B) 1% APd/ $\text{Cs}_3\text{Bi}_2\text{Br}_9$ materials. (C-D) Particle size distribution of (C) $\text{Cs}_3\text{Bi}_2\text{Br}_9$ and (D) 1% APd/ $\text{Cs}_3\text{Bi}_2\text{Br}_9$. (E) EDS spectra recorded for 1% APd/ $\text{Cs}_3\text{Bi}_2\text{Br}_9$.

Note: The surface morphology of materials recorded through the scanning electron microscope (SEM) reveals the average size of $\text{Cs}_3\text{Bi}_2\text{Br}_9$ is around 550 nm; after loading APd, the resultant samples show a similar morphology relative to the blank $\text{Cs}_3\text{Bi}_2\text{Br}_9$. Energy-dispersive X-ray spectroscopy (EDS) spectrum confirmed the Cs, Bi, Br and Pd elements in the hybrid materials.

Table S1. The inductively coupled plasma-mass spectrometry (ICP-MS) result of Pd content in 1% APd/Cs₃Bi₂Br₉ sample.

Sample	Theoretical value (Pd content)	ICP-MS (Pd content)
1% APd/Cs ₃ Bi ₂ Br ₉	1%	0.96%

Note: Inductively coupled plasma-mass spectrometry (ICP-MS) confirmed the amount of Pd in 1% APd/Cs₃Bi₂Br₉ sample is 0.96 wt%, which matches the theoretical value.

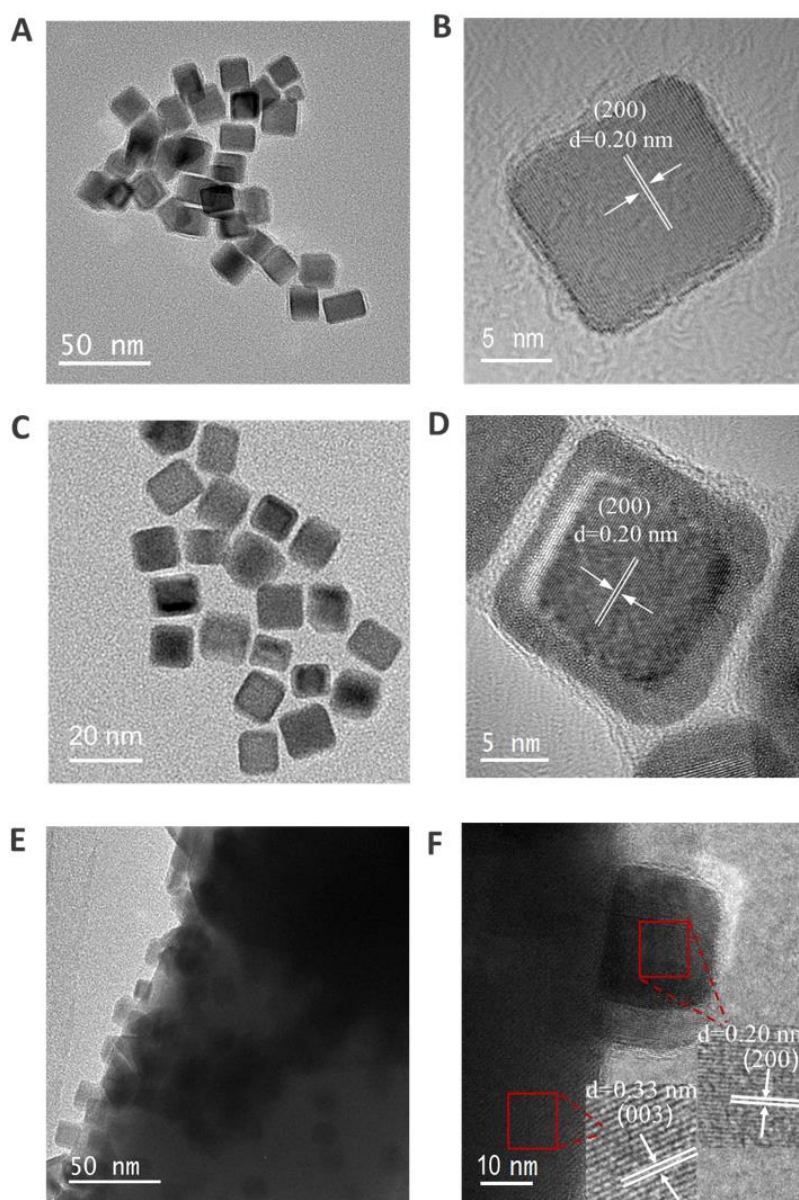


Fig. S5. Transmission electron microscopy (TEM) and high-resolution TEM (HRTEM) images of (A and B) Pd NCs, (C and D) APd NCs and (E and F) 1% APd/Cs₃Bi₂Br₉ material, respectively.

Note: TEM confirms the synthesized Pd has a cube morphology (Fig. S5A), HRTEM image shows that the lattice fringe of 0.20 nm corresponds to Pd (200)¹ crystal facet (Fig. S5B). The amorphization of the surface of APd leading to a crystalline-amorphous core@shell structure (Fig. S5D), and the lattice fringes of 0.33 nm and 0.20 nm in 1% APd/Cs₃Bi₂Br₉ (Fig. S5F) corresponding to Cs₃Bi₂Br₉ (003)⁵ and Pd (200),¹ respectively.

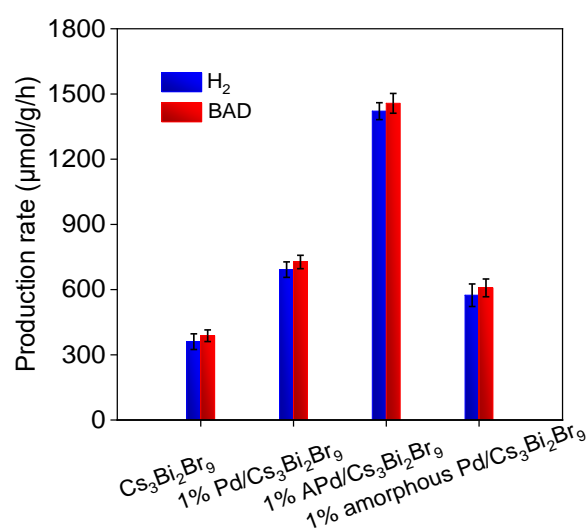


Fig. S6. Comparison of the photocatalytic performance of pure Cs₃Bi₂Br₉, and Cs₃Bi₂Br₉ coupled with crystalline Pd (1% Pd/Cs₃Bi₂Br₉), crystalline-amorphous Pd (1% APd/Cs₃Bi₂Br₉) and fully amorphous Pd (1% amorphous Pd/Cs₃Bi₂Br₉) composites. Reaction conditions: 1 mmol BA, 15 mg catalyst, 2.5 mL benzonitrilfluoride, simulated solar light (AM 1.5G, 150 W Xe lamp, light intensity: 100 mW/cm²), reaction time (14 h).

Note: This result shows that the photoactivity of photocatalysts with crystalline-amorphous Pd cocatalyst is superior to that of pure crystalline and fully amorphous Pd, confirming the beneficial effect of partially surface amorphization of Pd.

Table S2. Comparison of photocatalytic H₂ evolution over various MHP-based photocatalysts.

Photocatalyst	Light source	Medium	H ₂ production rate (μmol g ⁻¹ h ⁻¹)	Ref.
Cs ₃ Bi ₂ Br ₉ /APd	AM 1.5G, 150 W	BA/BTF	1421	This Work
MAPbBr ₃	λ ≥ 420 nm	HI/HBr acid mix solution	11.20	10
MAPbBr ₃	λ ≥ 420 nm	HI acid	11.31	11
MAPbBr ₃	λ ≥ 420 nm, 300 W Xe	HI solution	14.00	12
DMF-MAPbBr ₃	λ ≥ 420 nm	HI acid	22.62	11
DMSO-MAPbBr ₃	λ ≥ 420 nm	HI acid	31.67	11
MAPbI ₃	λ ≥ 475 nm	HI solution	33	11
MAPbBr ₃ /Pt	λ ≥ 420 nm	HI/HBr solution	33.60	10
MAPbBr ₃	λ ≥ 420 nm	Saturated HI solution	38.00	13
MAPbBr ₃ /Pt	λ ≥ 420 nm, 300 W Xe	HI solution	40.00	12
CsAgBiBr ₄ /rGO	λ ≥ 420 nm, 300 W Xe	HBr acid	50	14
MAPbBr ₃ /Pt	λ ≥ 420 nm	Saturated HI solution	90	13
CsPbBr ₃ /Ru@TiO ₂	445 nm, 50 mW laser	Triethanolamine	160	15
MA ₃ Bi ₂ I ₉ /Pt	λ ≥ 400 nm, 300 W	HI solution	170	16
MAPbI ₃ /TiO ₂	AM 1.5G	HI acid	436.6	13
PEDOT:PSS/MA PbBr ₃ /Ta ₂ O ₅	λ ≥ 420 nm), 150 mW/cm ²	HBr solution	650	17
DMASnBr ₃ /g-C ₃ N ₄	500 W cm ⁻² Xe	Glucose solution	925	18
MAPbBr _{3-x} I _x /Pt	λ ≥ 420 nm), 300 W	HBr/HI solution	2604.80	10

BP/MAPbI₃ $\lambda \geq 420$ nm), 300 HI solution 3742 19
mW/cm²

BA: benzyl alcohol. BTF: benzotrifluoride

Table S3. Comparison of selective photocatalytic oxidation of benzyl alcohol (BA) to benzaldehyde (BAD) over various MHP-based photocatalysts.

Photocatalyst	Light source	Medium	BAD production rate ($\mu\text{mol g}^{-1} \text{h}^{-1}$)	Ref.
Cs ₃ Bi ₂ Br ₉ /APd	AM 1.5G, 150 W	BA/BTF	1457	This work
FAPbBr ₃	AM1.5 G	Trifluorotoluene	18	20
FAPbBr ₃ /Bi ₂ WO ₆	AM 1.5G	Trifluorotoluene	250	20
CsPbBr ₃ /TiO ₂	$\lambda > 420$ nm, 300W	Toluene	500	21
FAPbBr ₃ /Bi ₂ WO ₆	AM1.5 G, 150W	Trifluorotoluene	580	20
FAPbBr ₃ /TiO ₂	AM1.5G, 150W	Toluene	800	22
CsPbX ₃ /W ₁₈ O ₄₉	AM1.5G, 150W	Hexane	1000	23
Cs ₃ Bi ₂ Br ₉ /TiO ₂	$\lambda > 420$ nm, 300W	Toluene	1465	24

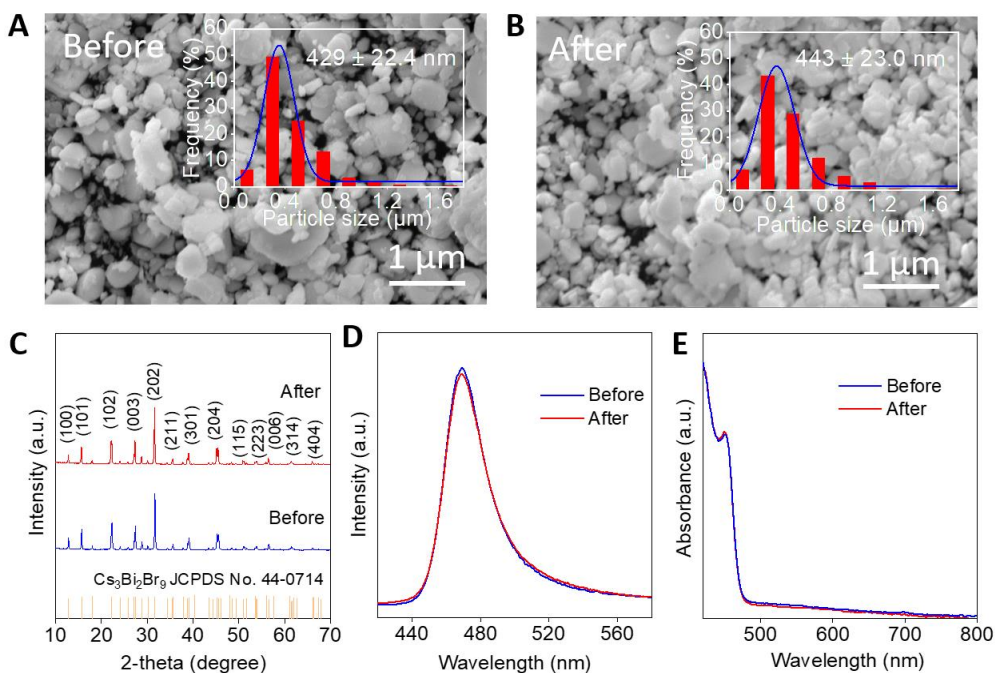


Fig. S7. (A-B) SEM images of 1% APd/Cs₃Bi₂Br₉ material (A) before and after five reaction cycles. (C) XRD, (D) PL and (E) Absorption spectra of 1% APd/Cs₃Bi₂Br₉ before and after recycling measurements, respectively.

Note: This result shows that there are negligible changes in morphology, structure and optical properties of the material after the recycling test.

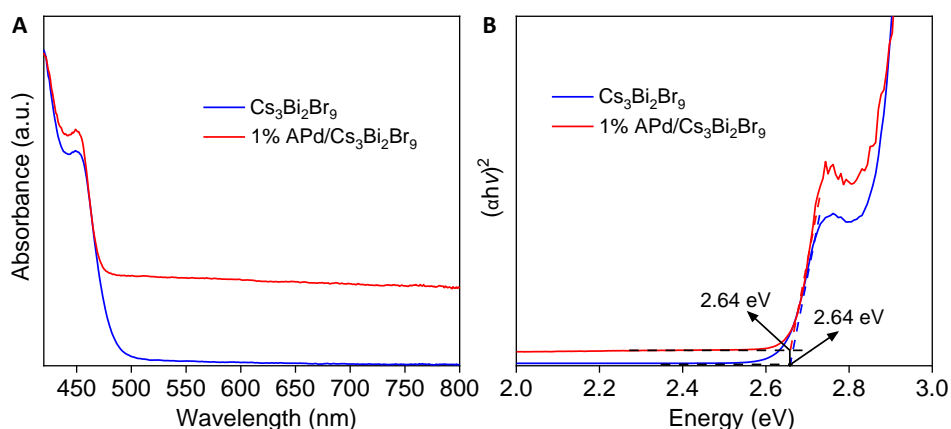


Fig. 8. (A) DRS spectra and (B) Tauc plots of Cs₃Bi₂Br₉ and 1% APd/Cs₃Bi₂Br₉ materials.

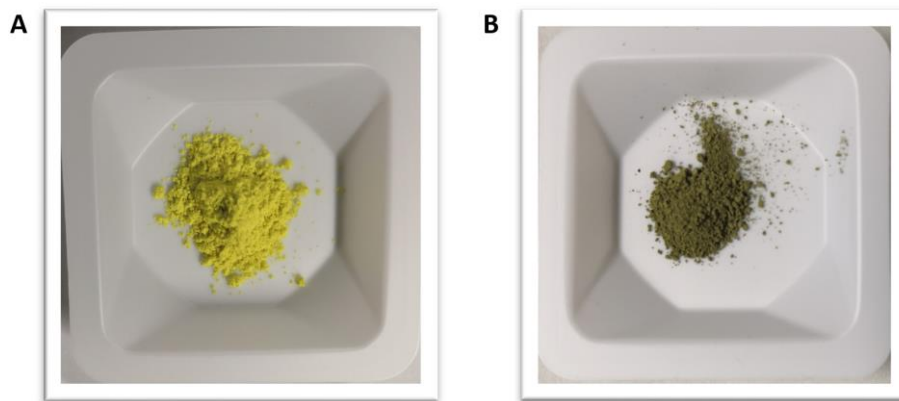


Fig. S9. The digital photographs of (A) $\text{Cs}_3\text{Bi}_2\text{Br}_9$ and (B) 1% APd/ $\text{Cs}_3\text{Bi}_2\text{Br}_9$ materials.

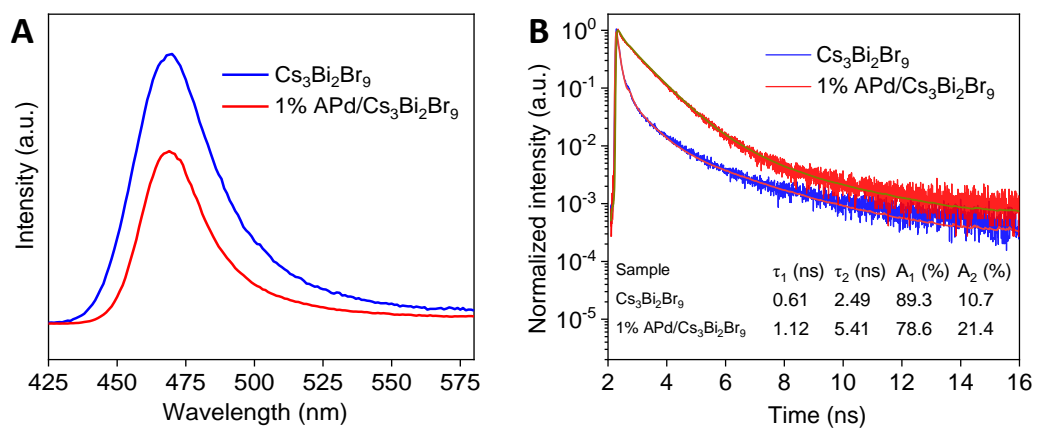


Fig. S10. (A) Steady-state PL spectra and (B) time-resolved PL decays of $\text{Cs}_3\text{Bi}_2\text{Br}_9$ and 1% APd/ $\text{Cs}_3\text{Bi}_2\text{Br}_9$ materials.

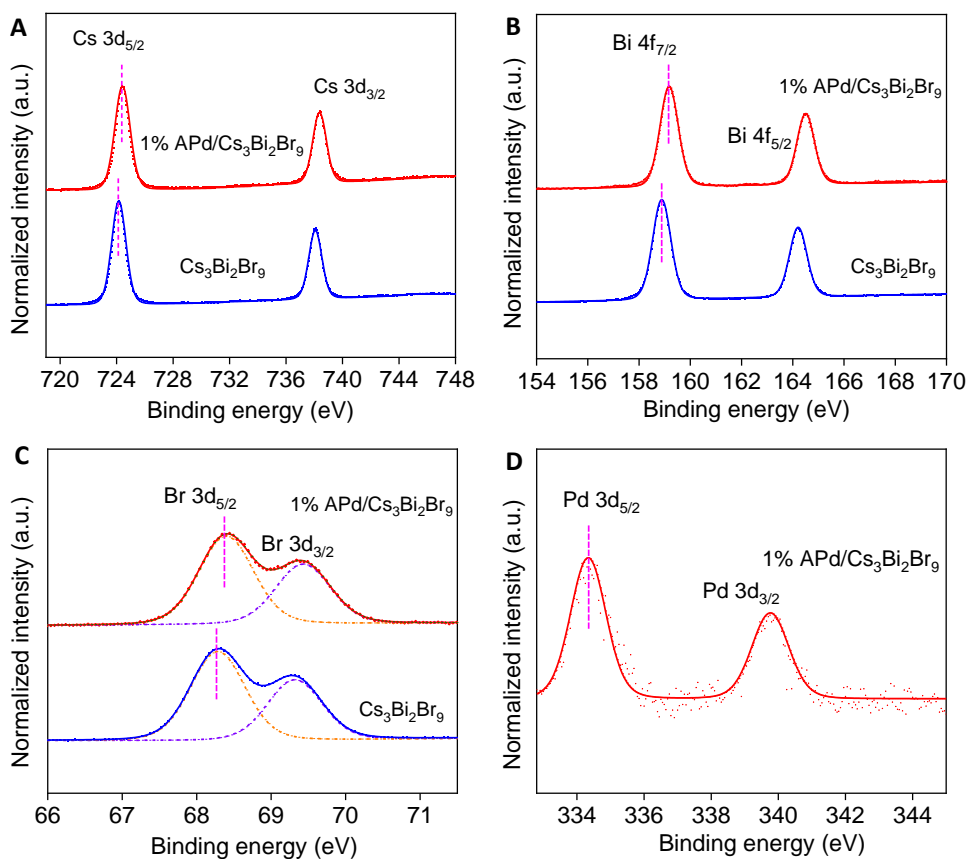


Fig. S11. High-resolution XPS spectra of (A) Cs 3d, (B) Bi 4f, (C) Br 3d core levels of Cs₃Bi₂Br₉ and 1% APd/Cs₃Bi₂Br₉ and (D) Pd 3d core level of 1% APd/Cs₃Bi₂Br₉.

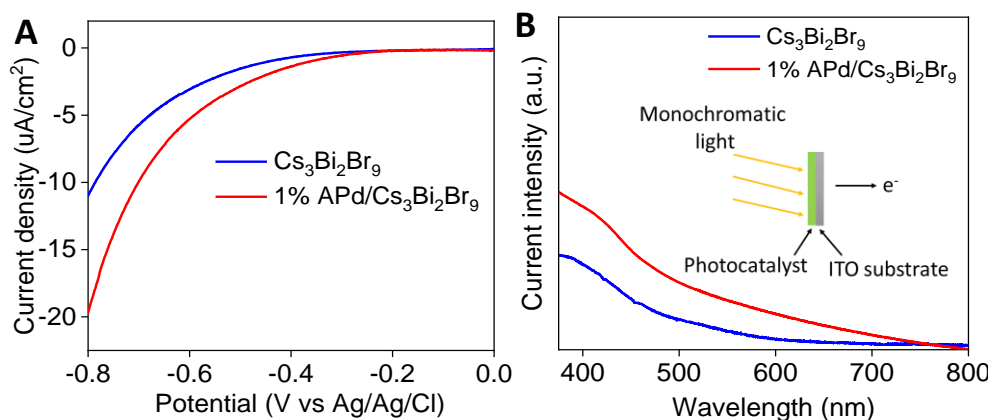


Fig. S12. (A) Polarization curves measured in dark and (B) Photocurrent response versus monochromatic light under the potential of 0.06 V of Cs₃Bi₂Br₉ and 1% APd/Cs₃Bi₂Br₉ materials.

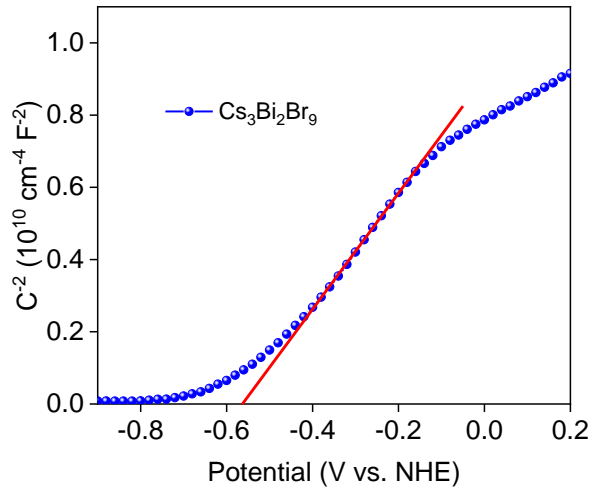


Fig. S13. Mott-Schottky plots of $\text{Cs}_3\text{Bi}_2\text{Br}_9$ measured in dark at the frequency of 1 kHz.

Note: Based on the slopes of the Mott-Schottky plots, the flat band potentials of $\text{Cs}_3\text{Bi}_2\text{Br}_9$ and 1% APd/ $\text{Cs}_3\text{Bi}_2\text{Br}_9$ are concluded to be -0.57 V and -0.59 V, respectively, and the density of the charge carrier (N_D) of pure $\text{Cs}_3\text{Bi}_2\text{Br}_9$ and 1% APd/ $\text{Cs}_3\text{Bi}_2\text{Br}_9$ can be calculated according to the following equation:²⁵⁻²⁷

$$N_D = \frac{2}{q\varepsilon\varepsilon_0} \frac{dE}{d\frac{1}{C^2}} = \frac{2}{q\varepsilon\varepsilon_0} \frac{1}{\text{slope}}$$

where N_D is the density of charge carriers, C is the space charge capacitance, E denotes the applied potential, q is the electric charge (1.602×10^{-19} C), ε and ε_0 refer to the dielectric constant of the semiconductor (13.8)²⁸ and permittivity in a vacuum (8.85×10^{-12} F m^{-1}). The calculated N_D of 1% APd/ $\text{Cs}_3\text{Bi}_2\text{Br}_9$ is 8.28×10^{19} cm^{-3} , slightly larger than that of pure $\text{Cs}_3\text{Bi}_2\text{Br}_9$ (6.43×10^{19} cm^{-3}), showing that an enhanced carrier densities after the decoration of APd NCs.

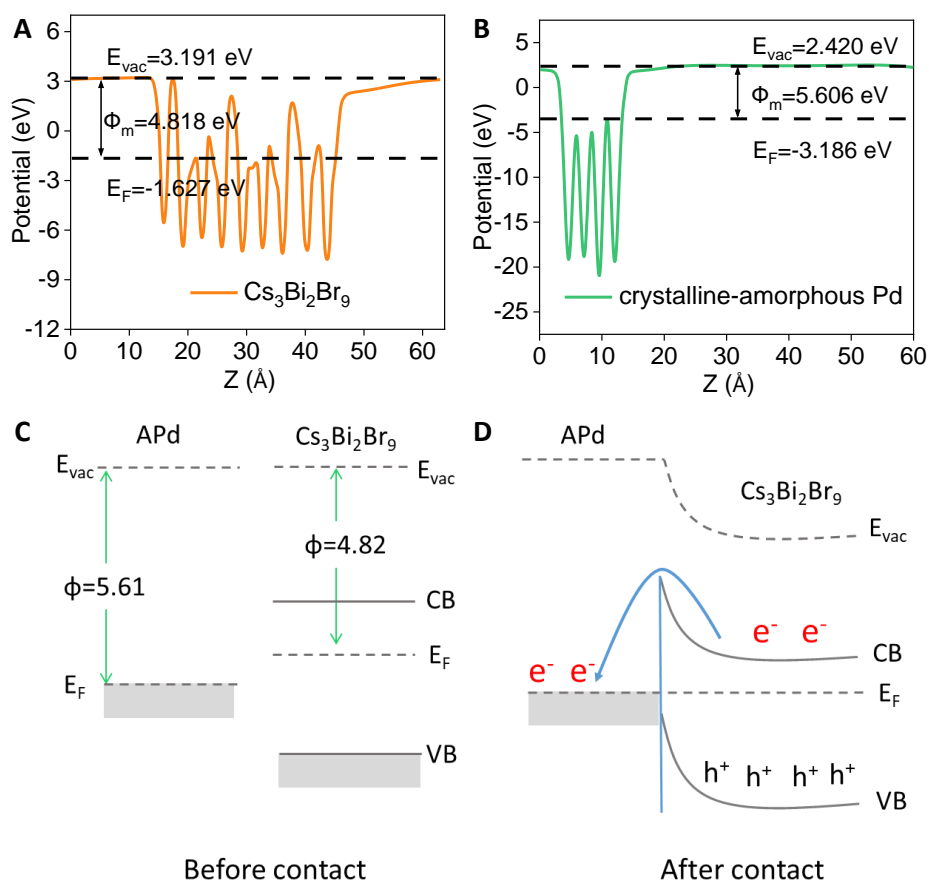


Fig. S14. The work function of (A) $\text{Cs}_3\text{Bi}_2\text{Br}_9$ and (B) APd materials. (C) Schematic energy diagram of APd and $\text{Cs}_3\text{Bi}_2\text{Br}_9$. (D) Schematic band diagram of APd/ $\text{Cs}_3\text{Bi}_2\text{Br}_9$ composites illustrating the charge transfer driven by a Schottky junction, where E_{vac} , E_F , CB, and VB represent vacuum level, Fermi level, conduction band and valence band, respectively. Orange and green curves present the potential line.

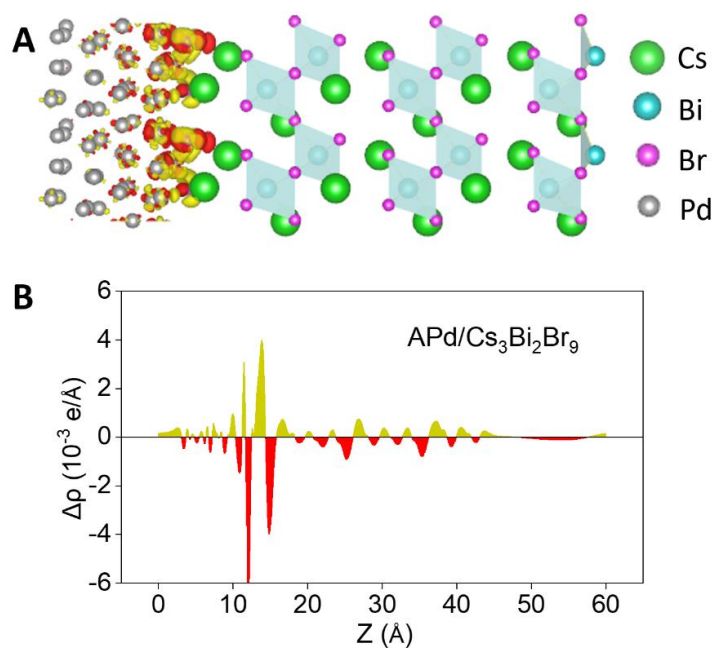


Fig. S15. (A) Charge density difference and (B) planar-averaged differential charge density of APd/Cs₃Bi₂Br₉ interface. The yellow and red areas represent electron accumulation and depletion, respectively.

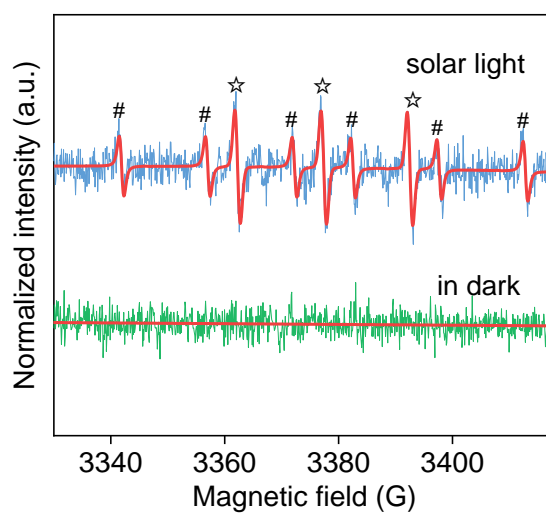


Fig. S16. ESR spectra of DMPO-carbon centered radical (#) and nitroxide-like radical (☆) over APd/Cs₃Bi₂Br₉ samples in BA and benzotrifluoride mixture.

Note: This result indicates the generation of C₆H₅CH(OH)[•] free radicals during the photocatalytic reaction process. Namely, photocatalytic selective BA oxidation occurs *via* carbon-centered radicals.

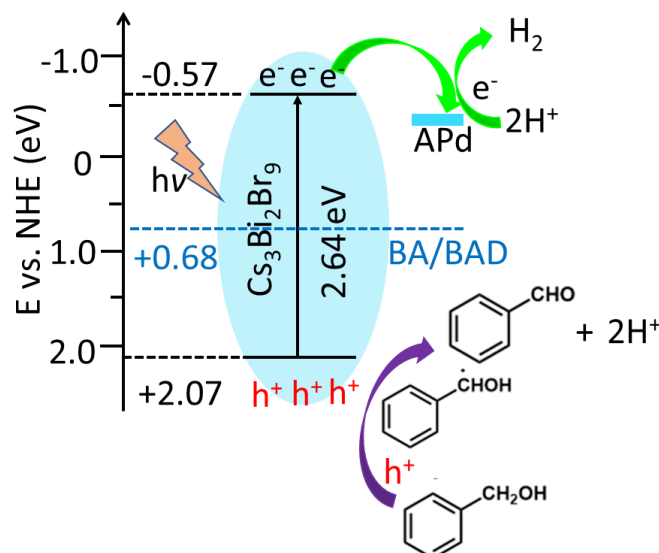


Fig. S17. Proposed reaction mechanism for the dual-functional photocatalytic system for dehydrogenation of BA with simultaneous H₂ and BAD production over APd/Cs₃Bi₂Br₉ photocatalyst.

References

1. B. Weng, Q. Quan and Y.-J. Xu, *J. Mater. Chem. A*, 2016, **4**, 18366-18377.
2. H. Cheng, N. Yang, G. Liu, Y. Ge, J. Huang, Q. Yun, Y. Du, C. J. Sun, B. Chen, J. Liu and H. Zhang, *Adv. Mater.*, 2020, **32**, e1902964.
3. C. Feng, L. Tang, Y. Deng, J. Wang, Y. Liu, X. Ouyang, H. Yang, J. Yu and J. Wang, *Appl. Catal. B: Environ.*, 2021, **281**, 119539.
4. C. Feng, L. Tang, Y. Deng, J. Wang, J. Luo, Y. Liu, X. Ouyang, H. Yang, J. Yu and J. Wang, *Adv. Funct. Mater.*, 2020, **30**, 2001922.
5. B. Yang, J. Chen, F. Hong, X. Mao, K. Zheng, S. Yang, Y. Li, T. Pullerits, W. Deng and K. Han, *Angew. Chem. Int. Ed.*, 2017, **56**, 12471-12475.
6. S. Zhang, S. Kim and V. V. Tsukruk, *Langmuir*, 2017, **33**, 3576-3587.
7. C. Vericat, M. E. Vela, G. Benitez, P. Carro and R. C. Salvarezza, *Chem. Soc Rev.*, 2010, **39**, 1805-1834.
8. G. Bator, J. Baran, R. Jakubas and M. Karbowski, *Vib. Spectr.*, 1998, **16**, 11-20.
9. M. Y. Valakh, M. Lisitsa, E. Y. Peresh, O. Trylis and A. Yaremko, *J. Mol. Struct.* 1997, **436**, 309-313.

10. Y. Wu, P. Wang, Z. Guan, J. Liu, Z. Wang, Z. Zheng, S. Jin, Y. Dai, M.-H. Whangbo and B. Huang, *ACS Catal.*, 2018, **8**, 10349-10357.
11. S. Park, W. J. Chang, C. W. Lee, S. Park, H.-Y. Ahn and K. T. Nam, *Nat. Energy*, 2016, **2**, 1-6.
12. Y. Wu, P. Wang, X. Zhu, Q. Zhang, Z. Wang, Y. Liu, G. Zou, Y. Dai, M. H. Whangbo and B. Huang, *Adv. Mater.*, 2018, **30**, 1704342.
13. X. Wang, H. Wang, H. Zhang, W. Yu, X. Wang, Y. Zhao, X. Zong and C. Li, *ACS Energy Lett.*, 2018, **3**, 1159-1164.
14. T. Wang, D. Yue, X. Li and Y. Zhao, *Appl. Catal. B: Environ.*, 2020, **268**, 118399.
15. M. V. Pavliuk, M. Abdellah and J. Sá, *Mater. Today Commun.*, 2018, **16**, 90-96.
16. Y. Guo, G. Liu, Z. Li, Y. Lou, J. Chen and Y. Zhao, *ACS Sustain. Chem. Eng.*, 2019, **7**, 15080-15085.
17. H. Wang, X. Wang, R. Chen, H. Zhang, X. Wang, J. Wang, J. Zhang, L. Mu, K. Wu and F. Fan, *ACS Energy Lett.*, 2018, **4**, 40-47.
18. A. Speltini, L. Romani, D. Dondi, L. Malavasi and A. Profumo, *Catalysts*, 2020, **10**, 1259.
19. R. Li, X. Li, J. Wu, X. Lv, Y.-Z. Zheng, Z. Zhao, X. Ding, X. Tao and J.-F. Chen, *Appl. Catal. B: Environ.*, 2019, **259**, 118075.
20. H. Huang, J. Zhao, Y. Du, C. Zhou, M. Zhang, Z. Wang, Y. Weng, J. Long, J. Hofkens and J. A. Steele, *ACS Nano*, 2020, **14**, 16689-16697.
21. S. Schunemann, M. van Gastel and H. Tuysuz, *ChemSusChem*, 2018, **11**, 2057-2061.
22. H. Huang, H. Yuan, K. P. F. Janssen, G. Solís-Fernández, Y. Wang, C. Y. X. Tan, D. Jonckheere, E. Debroye, J. Long, J. Hendrix, J. Hofkens, J. A. Steele and M. B. J. Roeffaers, *ACS Energy Lett.*, 2018, **3**, 755-759.
23. R. Cheng, J. A. Steele, M. B. Roeffaers, J. Hofkens and E. Debroye, *ACS Appl. Energy Mater.*, 2021, **4**, 3460-3468.
24. Q. Sun, W. Ye, J. Wei, L. Li, J. Wang, J.-H. He and J.-M. Lu, *J. Alloys Compd*, 2022, **893**, 162326.
25. I. A. Digdaya, L. Han, T. W. Buijs, M. Zeman, B. Dam, A. H. Smets and W. A. Smith, *Energy Environ. Sci.*, 2015, **8**, 1585-1593.

26. Q. Wang, S. Yu, W. Qin and X. Wu, *Nanoscale Adv.*, 2020, **2**, 274-285.
27. H. Zhang, L. Ma, J. Ming, B. Liu, Y. Zhao, Y. Hou, Z. Ding, C. Xu, Z. Zhang and J. Long, *Appl. Catal. B: Environ.*, 2019, **243**, 481-489.
28. X. Li, P. Zhang, Y. Hua, F. Cui, X. Sun, L. Liu, Y. Bi, Z. Yue, G. Zhang and X. Tao, *ACS Appl. Mater. Interfaces*, 2022, **14**, 9340-9351.

Chapter 4. Planar heterojunction boosts solar-driven photocatalytic performance and stability of halide perovskite solar photocatalyst cell

Chunhua Wang, Haowei Huang,* Bo Weng, Davy Verhaeghe, Masoumeh Keshavarz, Handong Jin, Biao Liu, Haipeng Xie, Yang Ding, Yujie Gao, Haifeng Yuan, Julian A. Steele, Johan Hofkens,* Maarten B. J. Roeffaers*

Adapted with permission from *Appl. Catal. B: Environ.*, **2022**, *301*, 120760.

Contributions

C.W., H.H., J. H. and M.B.J.R. designed the project; C.W. conducted the most experiments, including sample preparation, SEM, DRS, PL, GC, GC-MS, and activity tests; H.J., H.X., and Y.D., performed part of the experiments; B.W., D.V., M.K., Y.G., H.Y., and J.A.S. supported the experiments and helped to analyze the results; B.L. carried out the theoretical calculations; C.W. analyzed all results and wrote the draft; C.W., H.H., J.H. and M.B.J.R. together revised the manuscript with input from all the authors.

Abstract

The excellent optoelectronic properties of metal halide perovskites (MHPs) have been employed in various photocatalytic applications, but their poor water stability is considered as the main bottleneck for further development. Herein, we protect the light-absorbing CsPbBr₃ MHP with a NiO_x and TiO₂ hole and electron extracting layer. This planar NiO_x/CsPbBr₃/TiO₂ architecture can easily be fabricated through solution-processing. When applied to selective photocatalytic oxidation of benzyl alcohol, this system presents a 7-fold enhancement of photoactivity and an improved stability for over 90 h compared to CsPbBr₃ counterpart. Interestingly, we find that trace amounts of water improve photoactivity. Through experimental and theoretical analyses, this improvement could be attributed to water-induced structural reorganization of MHP, leading to improved crystal quality and decreased effective masses of charge carriers. This work indicates planar heterojunction helps improve the photoactivity and stability of MHP photocatalyst, and our findings provide insights into the effect of water on MHPs.

4.1 Introduction

Solar energy conversion and utilization by artificial photosynthesis are among the most promising strategies to address current environmental issues and provide an energy source not suffering from fluctuating availability. So far, much effort has been devoted to exploring various photocatalysts, such as inorganic oxides, nitrides, and sulfides [1, 2], carbon-based materials [3] and metal-coordination compounds [4]. However, most reported photocatalysts suffer from a limited light absorption range and rapid charge carrier recombination. Future practical applications require addressing these challenges. Recently, the excellent light absorption properties of metal-halide perovskites (MHPs) have triggered a breakthrough in various solar harvesting applications [5, 6]. MHPs have excellent optical and electronic properties such as a high absorption coefficient, low exciton binding energy, and long carrier diffusion length. Furthermore, their structure seems very defect tolerant allowing various low-cost processing methodologies [7-10]. Recently, MHP photocatalysts successfully generated solar fuels through CO₂ reduction [11] and H₂ evolution [12], and their performance for light-driven organic synthesis [13] and pollutant degradation [14] is equally promising.

Despite the excellent photocatalytic performance, most reported MHP photocatalysts have limited long-term stability due to their moisture sensitivity [15-18]. In the presence of large quantities of water, MHPs tend to decompose relatively quickly into a PbX₂ (X = I, Br, Cl) precipitate, and dissolved ions (Cs⁺/MA⁺/FA⁺ cation, and halide anion) [16, 17]. In aqueous environments, saturated halo acid solutions can be used to keep the MHP from decomposing [19]. Alternatively, apolar solvents provide a practical photocatalytic environment for MHPs [13, 20-22]. However, the generation of water and polar reaction products during the photocatalytic processes lead to a deterioration of the performance after several hours of operation [13, 21]. In short, MHP photocatalysis research has been facing issues to achieve long-term stability due to the presence or generation of polar molecules such as water. To slow down the deactivation of MHP, a core-shell structure is a straightforward stabilization method [23]. Also, the addition of drying agents such as anhydrous Na₂SO₄, to absorb the produced water in the reaction system, is an effective

way of stabilization [22]. Further, planar heterojunction structure using inorganic oxides as protecting layers to cover the MHP has been demonstrated to improve the stability of MHP solar cells or photoelectrodes [24-26]. On the other hand, selective oxidations of alcohols into aldehydes are important reactions in organic industry [27]. Among them, the selective benzyl alcohol (BA) oxidation has attracted much attention since benzaldehyde (BAD) is one of the essential intermediates for fine chemicals, fragrances and flavouring additives [28]. Compared to the hydrolysis of benzal chloride, the selective oxidation of BA into BAD using O₂ as the oxidant is a highly desired sustainable for industrial application.

Here, we show the construction of a stable solar photocatalyst cell (NiO_x/CsPbBr₃/TiO₂), with a planar heterojunction structure, where the NiO_x and TiO₂ serve not only as charge carrier transportation layers but also as MHP protecting layers. When applying to selective oxidation of benzyl alcohol under simulated solar light irradiation, this solar photocatalyst cell displays improved photoactivity (a 7-fold enhancement) and stability (23 versus 18 successive cycles before the activity is lower than the first cycle) compared to the pure CsPbBr₃, with an average of production rate 16.3 μmol cm⁻² h⁻¹ for over 90 h, or 23 successive cycles of 4 h each. Interestingly, the solar photocatalyst cell displays a significant increase (80.4 %) in performance during the first 56 h or 14 operation cycles. Detailed control experiments reveal that this activity enhancement is related to the water molecules generated during the reaction. This *in-situ* generated water improves the crystal symmetry of CsPbBr₃, a result confirmed by density functional theory (DFT) calculations. Through a combination of complementary techniques, we show that this water-induced structural reorganization reduces the charge carrier effective mass, thus enhancing the charge carrier separation and transfer.

4.2 Experimental section

Materials

Nickel(II) nitrate hexahydrate (Ni(NO₃)₂·6H₂O), lead(II) bromide (PbBr₂), titanium(IV) oxide (TiO₂), benzyl alcohol (BA), 2-phenylethanol, dimethyl sulfoxide (DMSO), 1-phenylethanol, 4-fluorobenzyl alcohol, ethylene glycol,

ethylenediamine and ethanol were purchased from Sigma-Aldrich. Cesium bromide (CsBr) and trifluorotoluene were purchased from Alfa Aesar. All chemicals were used without further purification.

Photocatalyst fabrication

Prior to the fabrication of photocatalysts, ITO coated glasses were cleaned using an ultrasonic cleaner in detergent, Milli-Q water, acetone and isopropanol for 30 min in sequence [29, 30]. After that, the cleaned ITO glasses were dried by nitrogen and then immediately illuminated by a UV-ozone machine for 30 min.

CsPbBr₃ photocatalysts were deposited onto ITO coated glasses through a low-temperature solution process by spin-coating. In a typical experiment, 74.5 mg CsBr and 128.5 mg PbBr₂ were first dissolved in 1 mL anhydrous DMSO to prepare 0.35 M CsPbBr₃ precursor solution. Then, the as-prepared solution was spin-coated onto ITO glass at 1000 rpm for 15 s, followed by 3000 rpm for 75 s. The prepared films were kept on a hot plate immediately at 70 °C for 30 min. NiO_x/CsPbBr₃/TiO₂ solar cell photocatalysts were fabricated by a three-step solution-processed technology. Specifically, the prepared 1.0 M Ni(NO₃)₂·6H₂O ethylenediamine solution was dropped onto glass ITO substrate, followed by spin-coating at 4000 rpm for 40 s, and then annealed in the air environment at 300 °C for 60 min, to form the NiO_x hole extracting layer. Secondly, CsPbBr₃ layer was deposited onto NiO_x layer through the same low-temperature solution process by spin-coating as mentioned above. Finally, a pre-prepared TiO₂ precursor solution (50 mg mL⁻¹ in ethanol, where the particle size of the TiO₂ is 21 nm, and the TiO₂ power was suspended in the ethanol solution for 1h *via* ultrasonication without using any ligands) was spin-coated onto CsPbBr₃ at 4000 rpm for 40 s, then annealed at 70 °C for 2 min. Pure NiO_x, TiO₂, NiO_x/CsPbBr₃ and CsPbBr₃/TiO₂ samples were used as reference, and the preparation process was the same as above. All processes were conducted in a glovebox.

Characterization

Absorption spectra were obtained by ultraviolet-visible spectrophotometer (UV-vis, Lambda-950) and the absorption coefficient (α) of the thin films was calculated using the following expression: $\alpha = 2.303 A/t$, where A is absorbance and t is the thickness of thin film. X-ray diffractometer (XRD, Cu K α 1 radiation, $\lambda = 1.5406 \text{ \AA}$) was used to obtain the crystallographic properties of the samples. Scanning electron microscopy (SEM) images of samples were taken with a FEI-Q FEG250 system and cross-sectional SEM images were obtained using FEI Helios Nanolab 600i SEM. The steady-state photoluminescence was recorded on an Edinburgh FLS980, from 490 to 580 nm with 5 nm increments and 1 s integration time, under an excitation wavelength of 480 nm. Fluorescence lifetime data was recorded on a home-built confocal FLIM microscope. Emission from a pulsed 480-nm laser diode (LDH-D-C-485, Picoquant, Berlin, Germany) was cleaned up (Chroma ET485/20x, F49-482, AHF Analysentechnik, Tübingen, Germany) and the laser pulsing was set to 1 MHz (PDL 828 Sepia2, Picoquant). X-ray photoelectron spectroscopy (XPS, Al K α X-ray source, 1486.6 eV) was employed to investigate the detailed effect of water on perovskite with different cycle times, and the C 1s signal was set to a position of 284.6 eV. Electrochemical measurements were made using a standard three-electrode setup. The reference electrode was Ag/AgCl electrode, and a platinum sheet was used as the counter electrode. Connection to the CsPbBr₃ working electrode was immersed in the electrolyte solution. The absorption coefficient (α) of NiO_x, CsPbBr₃ and TiO₂ thin films in this region was calculated via equation: $\alpha = 2.303 A/t$, where A is absorbance and t is the thickness of thin film. The calculated α value of NiO_x, CsPbBr₃ and TiO₂ is 2.4×10^4 , 4.1×10^4 and $2.5 \times 10^4 \text{ cm}^{-1}$ at 400 nm, respectively.

Photocatalytic activity evaluation

The activity of CsPbBr₃ and CsPbBr₃-based solar cell photocatalysts were evaluated using selective photocatalytic oxidation of benzylic alcohols. The specific operation procedure for the photocatalytic activity measurements is described as follows: trifluorotoluene solution was first being saturated in a sealed bottle with molecular oxygen for 1 hour. After that, CsPbBr₃

photocatalysts with an illumination area of $1.0 \times 1.2 \text{ cm}^2$ were put into a 20 mL quartz reactor with 2.5 mL saturated trifluorotoluene and 0.5 mmol BA, and the whole reaction system was kept sealing up and under light illumination using a 150 W Xe lamp with AM 1.5G filter to simulate the solar light spectrum. After irradiation of 4 h, the liquid was analyzed by Shimadzu GC-2010. The conversion of BA, and selectivity of BA/BAD are defined as follows [13]:

$$\text{Conversion (\%)} = C_0 - C_{BA} / C_0 \times 100\%$$

$$\text{Selectivity (\%)} = C_{BAD} / (C_0 - C_{BA}) \times 100\%$$

where C_0 is the initial concentration of BA; C_{BA} and C_{BAD} are the concentrations of the reaction substrate and corresponding product of the photocatalytic reaction, respectively.

Interband absorption by excitons using Elliot model

We have applied a semi-empirical relation suggested by Manoogian and Woolley [31] to the experimentally obtained absorption coefficient near the band edge for all materials under study. This model has been obtained from Elliot's theory of Wannier excitons [32] where the contributions of discrete exciton transitions are added to the continuum transitions and are convoluted with a Lorentzian with a broadening of Γ . The expression is given by [33, 34]:

$$\alpha(h\nu) = \alpha_0 \sum_n^{\infty} \left(\frac{1}{n^3} \right) \left(\frac{\Gamma_n}{2} \right)^2 / \left[\left(\frac{\Gamma_n}{2} \right)^2 + \left(h\nu - E_g + \frac{R_x}{n} \right)^2 \right] + \alpha_1 \left\{ \frac{\pi}{2} + \arctan \left[\left(h\nu - E_g \right) / \left(\frac{\Gamma_c}{2} \right) \right] \right\}$$

Here α_0 and α_1 represent the absorption peak at the ground state exciton energy and bandgap, respectively. Γ_n is the full width at half maximum of the Lorentzian and Γ_c accounts for the full width of the continuum excitons. R_x is the exciton binding energy and E_g represents the bandgap. n is an integer and referred to as exciton quantum number. Higher values of n can be neglected due to the n^{-3} dependence of the intensity of the excitons peaks. This equation can be used for bulk semiconductors with exciton binding energies much smaller than the bandgap (Wannier excitons) and describe optical transitions to bound and ionized excitonic states. This theory has been applied to model the band edge of halide perovskites as well [35, 36]. The extracted bandgaps

are summarized in Figure S3, Figure S10 and Figure S11, and Table S1. The high energy side of the curves cannot be well described with this model either due to a non-parabolicity band effect which is not taken into consideration [33] or the presence of other bands that accounts for carrier absorption. Yet, it fits well to the data at the band edges and the obtained bandgaps are in agreement with the other studies [25].

XRD structural refinement using Le Bail method

We modelled the scattering patterns using the Le Bail method in Fullprof [37], *i.e.*, refining the unit cell (a, b, c), the scattering offset, the profile parameters (U, V, W), and the peak intensities to match the measured diffraction pattern. Thus, this simple model was robust for determining the relative volume change in the unit cell (Figure 5d), as it was not necessary to know the structural factor and associated structural parameters (*i.e.*, internal tilting), since they are not considered in this type of analysis. All patterns were indexed to an orthorhombic (Pbnm) γ -phase perovskite and a preferential orientation (*i.e.*, perovskite thin film texture; direction and distribution of the grains) was taken into account.

Density functional theory calculation

The present calculations have been performed with the Vienna ab initio simulation package (VASP) code, based on density functional theory (DFT). The projector-augmented wave method is used to describe the interaction between ion cores and valence electrons. Atomic structures are optimized using the exchange-correlation functional of Perdew, Burke, and Ernzerhof (PBE). A plane-wave cutoff of 450 eV is used in the calculation. A Monkhorst-Pack 6x6x1 k-point grid is used to sample the Brillouin zone (BZ). All atoms are allowed to be fully relaxed till the atomic Hellmann-Feynman forces are less than 0.01 eV/Å. The convergence criterion of energy in the self-consistency process is set at about 1×10^{-4} eV.

The effective mass (m^*) is calculated as the following equation:

$$m^* = \hbar^2 \left[\frac{\partial^2 \varepsilon(k)}{\partial k^2} \right]^{-1}$$

Where the k is the wave vector along different directions and the $\varepsilon(k)$ represents the eigenvalues of energy band.

4.3 Results and discussion

Characterization of the photocatalysts

A series of CsPbBr₃ films and CsPbBr₃-based planar heterojunction solar photocatalyst cells (NiO_x/CsPbBr₃/TiO₂) deposited on ITO glass substrates were fabricated *via* simple low-temperature solution-processing starting from different CsPbBr₃ precursor solution concentrations (the detailed process is described in Experimental section). The crystal structure of CsPbBr₃ films and solar photocatalyst cells was determined by X-ray diffraction (XRD). Figure 1a shows the XRD patterns of these CsPbBr₃ films, the characteristic diffraction peaks of the orthorhombic (*Pnma*) space group were found and confirmed by structural refinement using the Le Bail method (Figure S1) [37]. The XRD pattern of solar photocatalyst cell (Figure 1b) consists of diffraction peaks from NiO_x, CsPbBr₃ and TiO₂, indicating successful synthesis of these three components. The CsPbBr₃ films adopt an orthorhombic crystal phase in the constructed solar photocatalyst cells. The surface morphology of CsPbBr₃ perovskite films was characterized by SEM. Scanning electron micrographs of CsPbBr₃ films with different precursor solution concentrations (0.05 M-0.45 M) are shown in Figures S2a-e, in which the surface coverage of CsPbBr₃ film improves gradually from 40.7% to 78.5% with increasing precursor solution concentration (Figure S2f). Besides, cross-sectional SEM images of CsPbBr₃ film and solar photocatalyst cell in Figures 1c and d confirmed this layer-by-layer structure.

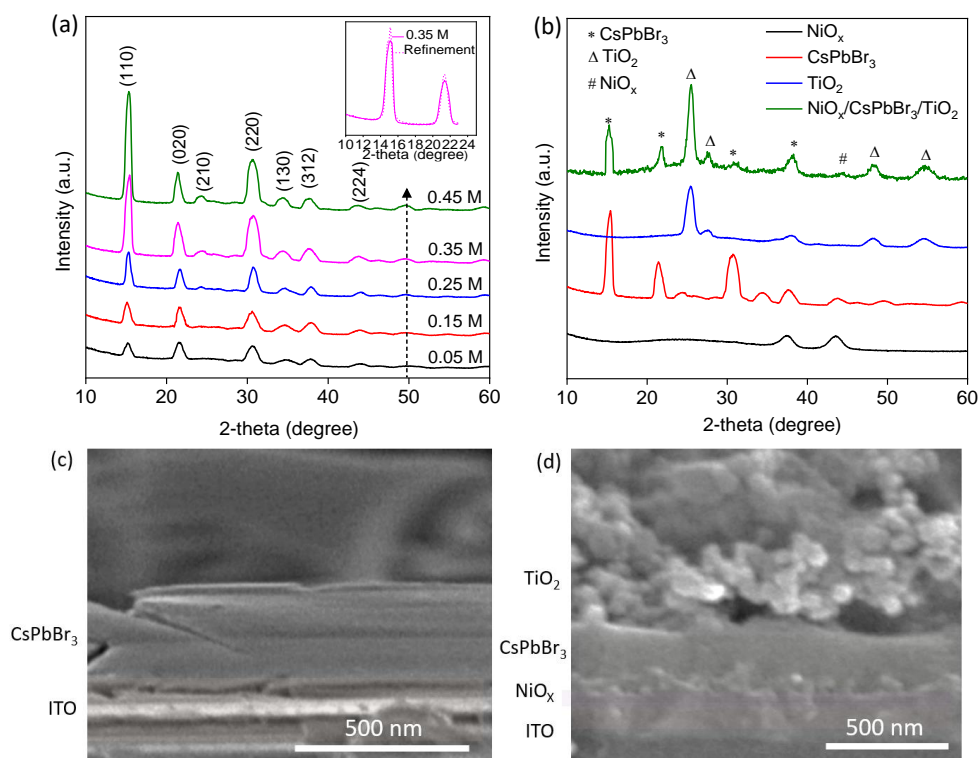


Figure 1. XRD patterns of (a) CsPbBr₃ thin films spin-coated with different precursor concentrations (0.05 M-0.45 M) and (b) NiO_x/CsPbBr₃/TiO₂ solar photocatalyst cell consists of NiO_x, CsPbBr₃ and TiO₂. (c-d) Cross-sectional SEM of CsPbBr₃ thin films and CsPbBr₃-based solar photocatalyst cell, respectively, where the precursor concentration of CsPbBr₃ is 0.35 M.

Figures 2a and b represent the UV-Vis absorption spectra of all as-prepared CsPbBr₃ films and solar photocatalyst cells possessing strong visible-light absorption. While an excitonic peak is visible around 520 nm, excitons only make up a small fraction of photogenerated species (approx. 1%) with the majority of absorbed photons leading to free charge carriers [7, 38]. The bandgap of these CsPbBr₃ films, extracted using Elliott's model [32, 35, 36] (Experimental section), agrees well with the reported 2.3 eV (Figure S3) [25]. The NiO_x/CsPbBr₃/TiO₂ solar photocatalyst cell processes strong light absorption in the visible range due to the good absorption coefficient of NiO_x, CsPbBr₃, TiO₂ component (2.4×10^4 , 4.1×10^4 and 2.5×10^4 cm⁻¹ at 400 nm, respectively) (see Experimental section).

Steady-state and time-resolved photoluminescence (PL) measurements were performed to reveal the photophysical processes in these materials. As shown

in Figure 2c, both CsPbBr₃ and NiO_x/CsPbBr₃/TiO₂ display an emission peak at around 525 nm, while the PL intensity of NiO_x/CsPbBr₃/TiO₂ was strongly quenched after the deposition of NiO_x and TiO₂ as compared to the uncoated CsPbBr₃ film, indicative of improved charge separation and reduced radiative recombination [20]. This is further corroborated by time-resolved PL decay measurements, that revealed significant changes in charge dynamics in the NiO_x/CsPbBr₃/TiO₂ solar photocatalyst cell (Figure 2d). The luminescence decays of the CsPbBr₃ film and NiO_x/CsPbBr₃/TiO₂ are analyzed using a sum of two exponential decays, with two distinct decay constants (τ_j) and amplitudes (A_j). The two extracted decay times, τ_1 and τ_2 are associated with the bound exciton and free exciton recombination, respectively [39-41]. The solar photocatalyst cell NiO_x/CsPbBr₃/TiO₂ showed a longer lifetime than the pure CsPbBr₃ film, with τ_1 and τ_2 increasing significantly (see Figure 2d), hinting to the effective extraction of the photogenerated charge carriers in CsPbBr₃ by NiO_x and TiO₂ layers (vide infra) [20, 24].

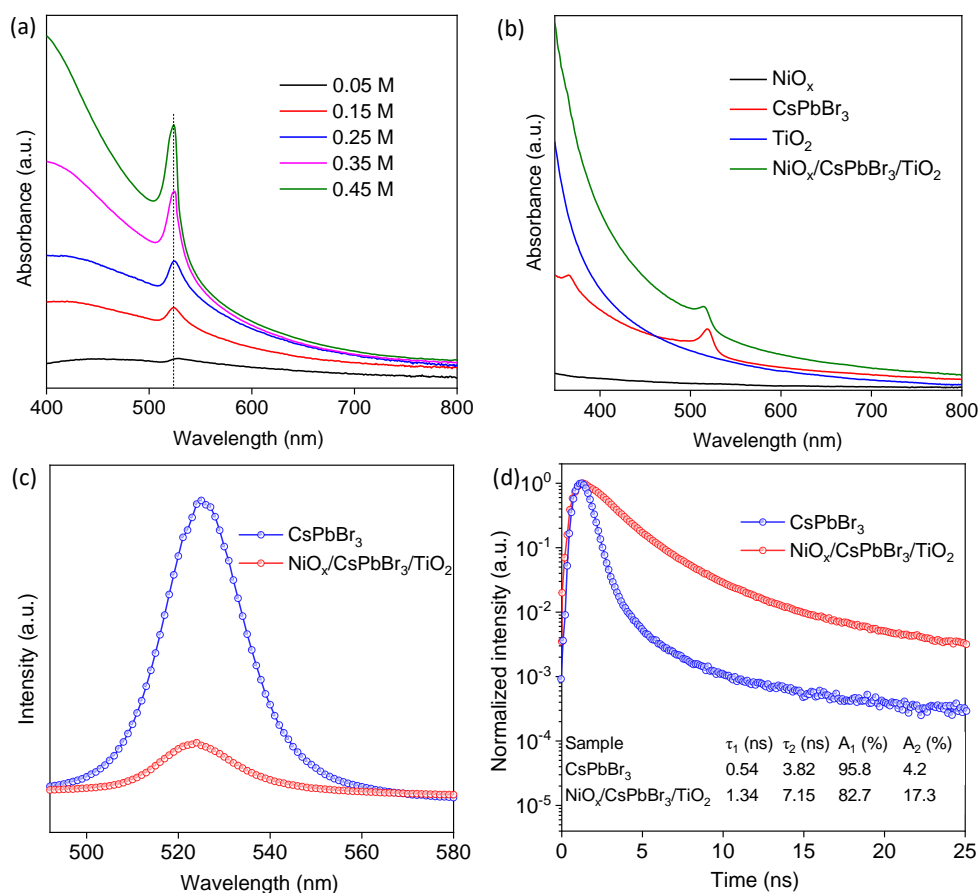


Figure 2. Absorption spectra of (a) CsPbBr₃ thin films with different precursor concentrations and (b) NiO_x/CsPbBr₃/TiO₂ with three components, i.e., NiO_x,

CsPbBr₃ and TiO₂. (c) Steady-state PL spectra and (d) PL lifetime decay traces of CsPbBr₃ thin film and NiO_x/CsPbBr₃/TiO₂ solar photocatalyst cell.

Photocatalytic performance and stability tests

The photocatalytic performance of the CsPbBr₃ films and solar photocatalyst cells (1.0×1.2 cm²) was evaluated under simulated solar light (AM 1.5G) by studying the selective oxidation of benzyl alcohol (BA, 0.5 mmol) in a nonpolar solvent (trifluorotoluene, 2.5 mL) with saturated molecular oxygen under simulated solar light illumination (BA + O₂ → BAD + H₂O). As shown in Figure S4, all CsPbBr₃ films converted at least 1.1 μmol cm⁻² h⁻¹ BA toward BAD based on the per illumination area [42, 43], with an excellent selectivity of over 99%. After the introduction of NiO_x and TiO₂, the NiO_x/CsPbBr₃/TiO₂ solar photocatalyst cells presented a significant increase in photoactivity of at least 5.8 μmol cm⁻² h⁻¹ (Figure 3a) while maintaining over 99% selectivity, in which the optimal photocatalyst cell (NiO_x/CsPbBr₃/TiO₂-4) presented a BAD generation rate of 12.1 μmol cm⁻² h⁻¹ after 4 h of irradiation, a 7-fold enhancement compared to pure CsPbBr₃. Gas chromatography–mass spectrometry (GC-MS) was employed to check these products (Figure S5). In comparison to other reference photocatalysts (Figure S6a), this planar heterojunction layered system displayed the highest photoactivity. Note that the activity of NiO_x/CsPbBr₃/TiO₂-4 was around 2-fold higher than the sum of the individual components CsPbBr₃, NiO_x and TiO₂ (Figure S6b), which can be attributed to the synergistic effect of the charge extraction by NiO_x and TiO₂ [20]. Comparison of this solar photocatalyst cell with reported MHP-based catalysts for organic synthesis (Table S2) and selective photocatalytic oxidation BA to BAD over various photocatalysts (Table S3) showed the excellent photocatalytic performance of this solar photocatalyst cell. The production rate of the NiO_x/CsPbBr₃/TiO₂ photocatalyst cell is also comparable to other thin film based photoelectrochemical (PEC) or PEC-photovoltaic (PEC-PV) systems (Table S4). Besides the benzyl alcohol, the efficient conversion of benzylic alcohols, such as 2-phenylethanol, 1-phenylethanol and 4-fluorobenzyl alcohol, confirmed the general applicability of the solar photocatalyst cell, as summarized in Table S5. Further, to confirm the photocatalytic performance of

the proposed photocatalyst cell architecture, we tested the CsPbBr₃ films and photocatalyst cells for the selective oxidation of toluene to BAD with saturated molecular oxygen under simulated solar light illumination. The photocatalytic activity is summarized in Figure S7a, and GC-MS was employed to check the generated products (Figures S7b-d). Similarly, both CsPbBr₃ thin film and photocatalyst cell were effective for photocatalytic oxidation toluene to BAD, with BA as the main side product. Also, the NiO_x/CsPbBr₃/TiO₂ photocatalyst cells presented a significant increase in photoactivity (an 8.7-fold enhancement), compared to the CsPbBr₃ counterpart. These results confirmed the versatility of the MHP-based planar heterojunction structure for photocatalytic organic transformation.

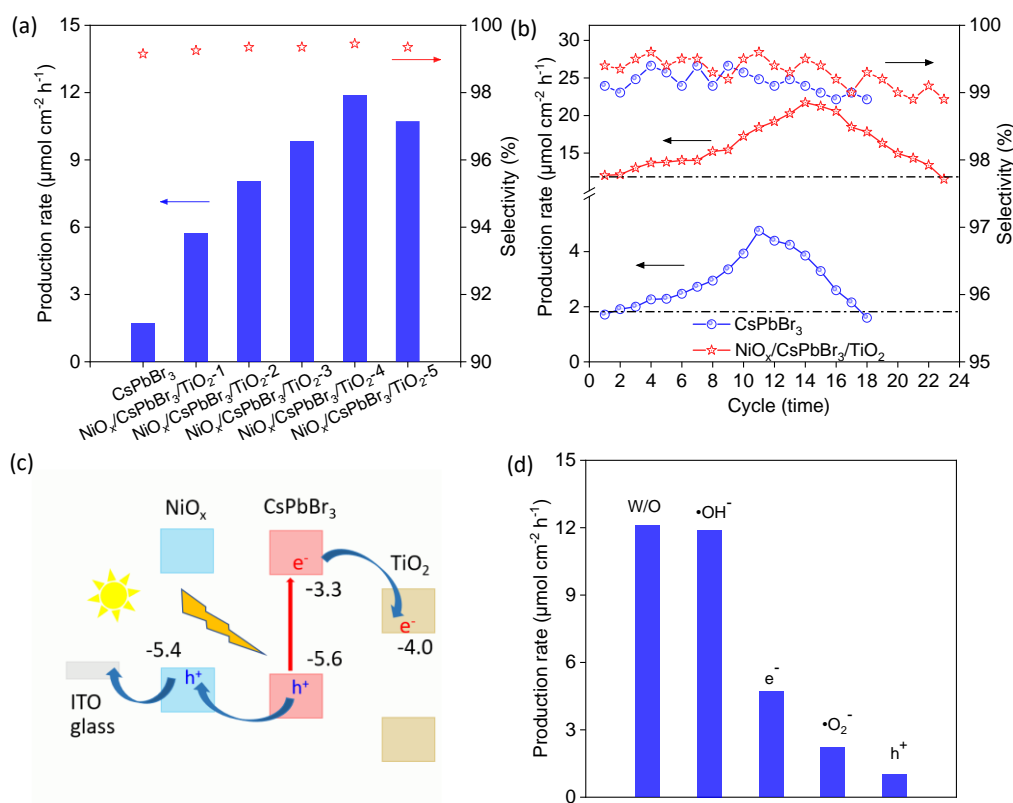


Figure 3. (a) Selective photocatalytic oxidation of BA to BAD over films of CsPbBr₃ and NiO_x/CsPbBr₃/TiO₂ photocatalysts, where NiO_x/CsPbBr₃/TiO₂-n (n=1, 2, 3, 4 and 5) represents the precursor solution concentration of CsPbBr₃ is 0.05 M, 0.15 M, 0.25 M, 0.35 M and 0.45 M, respectively. (b) Recycling test of NiO_x/CsPbBr₃/TiO₂ solar photocatalyst cell and pure CsPbBr₃ thin film photocatalyst. (c) The energy band diagram of the photocatalytic cell. (d) The effects of various radical scavengers on the photocatalytic performance of BA

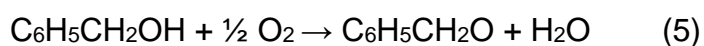
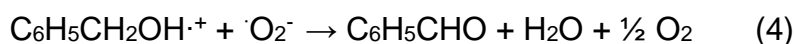
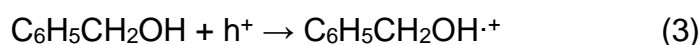
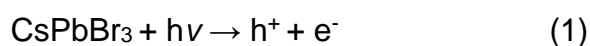
oxidation over photocatalyst cell, where W/O represents without scavengers, $\cdot\text{OH}^-$, e^- , $\cdot\text{O}_2^-$, and h^+ represents the radical that is targeted by the addition of t-butanol, potassium persulfate, 1,4-benzoquinone and ammonium oxalate additives, respectively. Reaction conditions: photocatalytic cell or CsPbBr_3 thin film photocatalysts ($1.0 \times 1.2 \text{ cm}^2$), 0.5 mmol BA in 2.5 ml trifluorotoluene with saturated molecular oxygen, AM 1.5G simulated solar light (150 W Xe lamp), reaction time (4 h).

The stability of the best solar photocatalyst cell, $\text{NiO}_x/\text{CsPbBr}_3/\text{TiO}_2$ -4, was evaluated by a recycling test in which after 4h the reaction solution was removed, analysed and fresh solution was added. As shown in Figure 3b, the photocatalyst cell showed no activity drops in comparison to the initial one in 23 successive cycles. An average BAD production rate of $16.3 \mu\text{mol cm}^{-2} \text{ h}^{-1}$ was achieved for over 90 h of testing. Meanwhile, a selectivity of around 99% was maintained for 23 cycles. The turnover number (TON) is 45300 and turnover frequency (TOF) is $492.4 \text{ (h}^{-1}\text{)}$ for the first 23 cycles. Furthermore, the recycle test revealed an interesting behaviour with an initially improving photocatalytic performance. The highest BAD production rate of $21.7 \mu\text{mol cm}^{-2} \text{ h}^{-1}$ was achieved after 14 cycles (56 h in total), a 1.8-fold improvement compared to the initial one ($12.1 \mu\text{mol cm}^{-2} \text{ h}^{-1}$). With further reaction cycles, however, the photocatalytic efficiency gradually decreases. After 23 cycles, the activity of the solar photocatalyst cell is lower than the first cycle testing. The recycle test of the pure CsPbBr_3 film photocatalyst also showed a similar tendency as the CsPbBr_3 -based solar photocatalyst cell, *i.e.*, the photoactivity increases with increasing reaction cycle (Figure 3b), indicating the CsPbBr_3 film itself is the key factor that causes this interesting behavior in photoactivity. The highest production rate of BAD ($4.8 \mu\text{mol cm}^{-2} \text{ h}^{-1}$) of CsPbBr_3 film photocatalyst was achieved after 11 cycles of 4 h testing (44 h in total). This represents a 3-fold improvement to the first 4 h run, while maintaining a selectivity of around 99%. Note that after the 11th cycle the activity of the CsPbBr_3 films is worse than the first cycle. These results indicate that the durability of CsPbBr_3 film is inferior to that of solar photocatalyst cell in which NiO_x and TiO_2 were deposited on the bottom and top of CsPbBr_3 , respectively, as the protecting layers. More

importantly, to the best of our knowledge, this is the first report on perovskite photocatalysis that the photoactivity increases with reaction time instead of decrease.

Mechanism study

To elucidate the pathways of photogenerated charge carriers, the energy band structure of the NiO_x/CsPbBr₃/TiO₂ photocatalytic cell was investigated. As shown in Figure 3c, the valence maximum (VBM) and conduction band minimum (CBM) of CsPbBr₃ are -5.6 eV and -3.3 eV, respectively. The VBM of NiO_x is -5.4 eV, and the CBM of TiO₂ is -4.0 eV. Therefore, the photogenerated electrons and holes can be easily extracted and transfer to TiO₂ and NiO_x, respectively [20], to participate in the reaction. Furthermore, to understand the mechanism of photocatalytic selective BA oxidation reaction over the photocatalyst cell, different radical scavengers, *i.e.*, ammonium oxalate, potassium persulfate, 1,4-benzoquinone and t-butanol for holes (h⁺), electrons (e⁻), superoxide radicals ($\cdot\text{O}_2^-$), and for hydroxyl radicals ($\cdot\text{OH}^-$), respectively [20], were employed to examine the role of various redox-active species. Figure 3c shows the effects of these radical scavengers on the photocatalytic performance, and the detailed parameters are listed in Table S6. Scavenging the holes with ammonium oxalate almost completely stops the reaction, and in the presence of potassium persulfate as electron scavenger also resulted in a sharp drop in the photoactivity; a similar effect is observed when adding 1,4-benzoquinone to the reaction system, while t-butanol has negligible effect on the photoactivity. These results suggest that both holes and electrons actually participate in the BA oxidation reaction. Based on these experiments, we propose following mechanism that responsible for the photocatalytic oxidation of BA over the photocatalyst cell, and the reaction mechanism is as follows [13, 21]:



Under solar light illumination, CsPbBr₃ absorbs solar light to produce electron-hole pairs. Electrons transfer to TiO₂ to reduce the molecular oxygen adsorbed on TiO₂ into $\cdot\text{O}_2^-$ species. Meanwhile, the photogenerated holes transfer to NiO_x and oxidize the benzyl alcohol substrates to carbocations. It is well known that dense and uniform thin films are important for efficient charge separation and transfer in solar cells. While for photocatalysis, besides considering charge separation and transfer, molecules need to directly interact with the photocatalyst to be able to participate in the redox reactions. For the standalone photocatalyst cell-based photocatalysis, different from solar cells, discontinuities in the thin film can serve as the active sites, thus promoting the benzyl alcohol oxidation reaction. Therefore, it is important to establish a balance between the efficient charge separation and sufficient adsorption area. Since both TiO₂ and NiO_x are not fully dense and continuous (Figure S8), BA substrates and molecular oxygen can be easily adsorbed on non-covered, accessible area and border of NiO_x and TiO₂, respectively. Finally, the BA radical carbocations react with $\cdot\text{O}_2^-$ species to produce the BAD product. On the other hand, some previous studies with g-C₃N₄ as the photocatalyst have shown that the H₂O₂ can be possible generated as an intermediate during the photocatalytic processes.²⁷ In our system H₂O₂ was however not detected using iodometry.^[a]

^[a]Note: this comment was added as a footnote to Chapter 4 (which is based on a published article) based on the discussion during the preliminary PhD defence.

Besides, to reveal the factors that cause the 3-fold improvement in photoactivity over CsPbBr₃ films, a series of control experiments were carried out. In these experiments, the role of the solvent (trifluorotoluene), the effect of extended illumination (AM 1.5G, simulated solar light), and molecular adsorption of BA and BAD were explored (Figure 4a). Solvent and photodegradation were ruled out, and the presence of BA or BAD only had a minute effect on the activity. Another factor that should be taken into consideration is the generation of water during the photocatalytic oxidation reaction of BA. To simulate experimental conditions, controlled amounts of water were added to the reaction system while keeping the sample in dark for 4 h, before starting the photocatalytic testing; the water amounts are in the same order of magnitude as those photocatalytically generated during the process. Figure 4b shows the significant effect of water on the measured photocatalytic performance. Specifically, the BAD generation steadily improved 2-fold, with 0.8 μL water incubation, before slowly decreasing again with large amounts of water. These results strongly suggest the beneficial effects of trace amounts of water on the catalytic performance, while excessive water has an adverse effect.

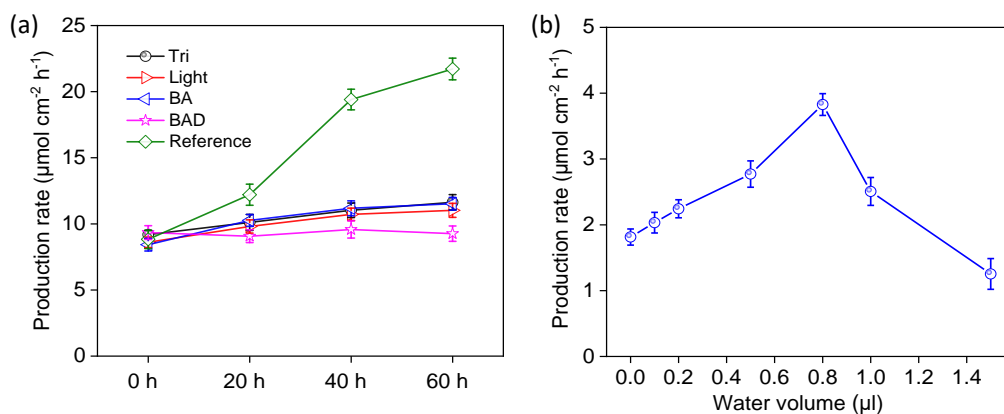


Figure 4. (a) The effect of solvent (trifluorotoluene), light irradiation (AM 1.5 G, simulated solar light), substrate (benzyl alcohol) and main product (benzaldehyde) on photocatalytic activity for 60 h with an interval of 20 h. (b) Photocatalytic activity (4 h) of CsPbBr₃ thin film photocatalyst as a function of the added amount of water to the reaction system. Reaction conditions: CsPbBr₃ photocatalyst ($1.0 \times 1.2 \text{ cm}^2$), 0.5 mmol benzyl alcohol in 2.5 ml trifluorotoluene solution with saturated molecular oxygen, AM 1.5 G simulated solar light irradiation (150 W Xe lamp), illumination time (4 h). With Tri, Light, BA, BAD and Reference referring to storage of the CsPbBr₃ thin film before

photocatalytic testing in: (1) Tri: 2.5 mL trifluorotoluene in dark. (2) Light: 2.5 mL trifluorotoluene solution under AM 1.5 G simulated solar light illumination. (3) BA: 2.5 mL trifluorotoluene solution with 0.5 mmol benzyl alcohol in dark. (4) BAD: 2.5 mL trifluorotoluene with 0.03 mmol benzaldehyde in dark. While Reference sample is the CsPbBr₃ thin film used for the cycling test, with the identical reaction conditions as above.

To determine the underlying mechanism of this beneficial effect, changes in the structural properties of CsPbBr₃ with increasing cycle times were studied. The XRD patterns in Figure 5a show similar diffraction peaks for the recycled MHP films. However, changes are visible when analyzing the peak position and peak width in detail, as shown in Figure 5b. Refining the data with the Le Bail method (Figure S9) [37] reveals the peak-width parameter U (a resolution function parameter used to quantify the peak width) declines substantially from 16.28 (cycle 0) to 8.02 (cycle 11) and then increases to 13.14 after the 14th cycle (Figure 5c); the normalized lattice parameters, as a function of cycles, are plotted in Figure 5d. Meanwhile, the normalized, pseudo-cubic unit cell volume (per unit formula, determined from the crystallographic data) reduced about 5% from 211.01 Å³ to 202.13 Å³ after cycle 11 and expanded to 206.14 Å³ with further increased cycling to 14 (Figure 5d, the detailed parameters are shown in Table S7). This indicates that the crystallinity of CsPbBr₃ first improves before decreasing [44-46].

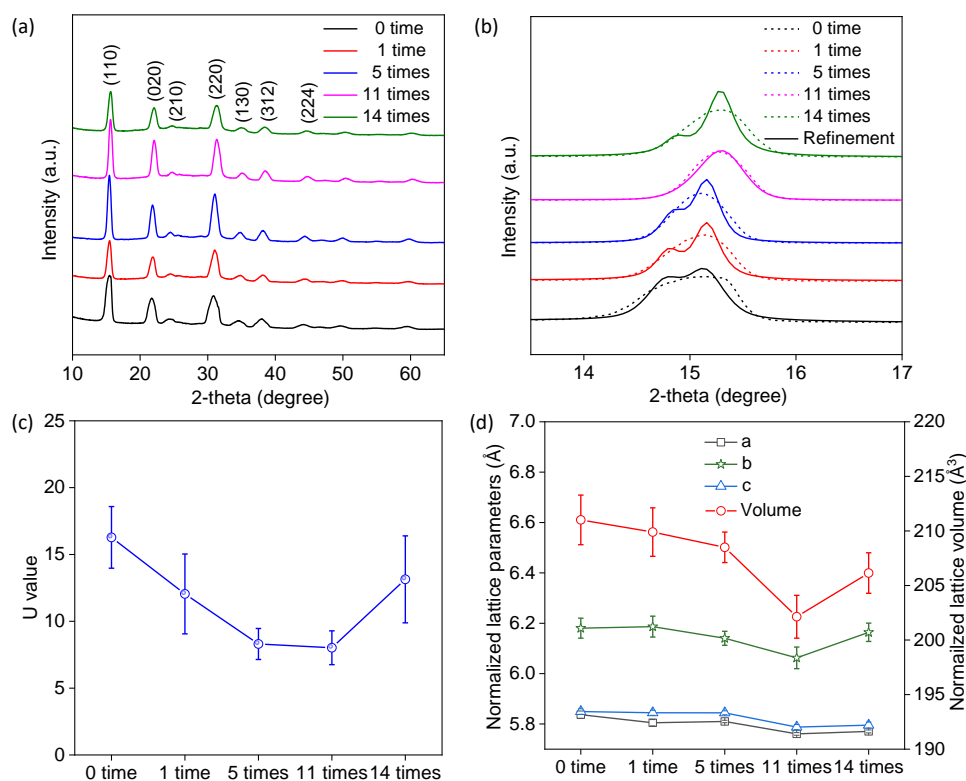


Figure 5. (a) XRD patterns of CsPbBr₃ films recorded before photocatalytic testing, after 1, 5, 11, and 14 testing cycles. (b) Magnified view of XRD patterns of CsPbBr₃ films before and after photocatalytic testing on the most prominent diffraction signal recorded around 15 degrees, with the structural refinement *via* Le Bail method. (c-d) Dependence of the recorded XRD peak broadening and lattice parameters, respectively, on the photocatalytic recycling (derived from the use of a dominant empirical broadening parameter U during the structural refinement (Le Bail method)). The other key experimental parameters, like layer thickness and instrumental geometry, are kept constant. Normalization of the γ -phase lattice is made *via* rescaling the orthorhombic unit cell by $(1/\sqrt{2}, 1/\sqrt{2}, 1/2)$, with the pseudo-cubic unit cell volume also being normalized by the same fractions.

To identify the underlying reason for this improved crystallinity, DFT-based simulations were performed. The model started from a clean CsPbBr₃ slab with H₂O adsorbed before relaxation; Vienna ab initio simulation package (VASP) codes (details see Experimental section) [47]. As shown in Figures 6a and b, the calculated bonding angles of Pb-Br-Pb are 172.8° and 166.9° in CsPbBr₃+H₂O and pure CsPbBr₃ slab, respectively. The result shows that the

PbBr₆ octahedrons in CsPbBr₃ become more symmetrical after surface adsorption of H₂O molecules, consistent with the experimental XRD data. In addition, DFT calculations revealed a significant drop in effective mass of the charge carriers in the CsPbBr₃+H₂O slab; calculated electron effective mass 0.385 *m*₀ (CsPbBr₃) vs. 0.366 *m*₀ (CsPbBr₃+H₂O) and the effective hole mass reduces from 0.515 *m*₀ to 0.489 *m*₀. This lower effective mass relates to higher mobility and lower recombination probability [48].

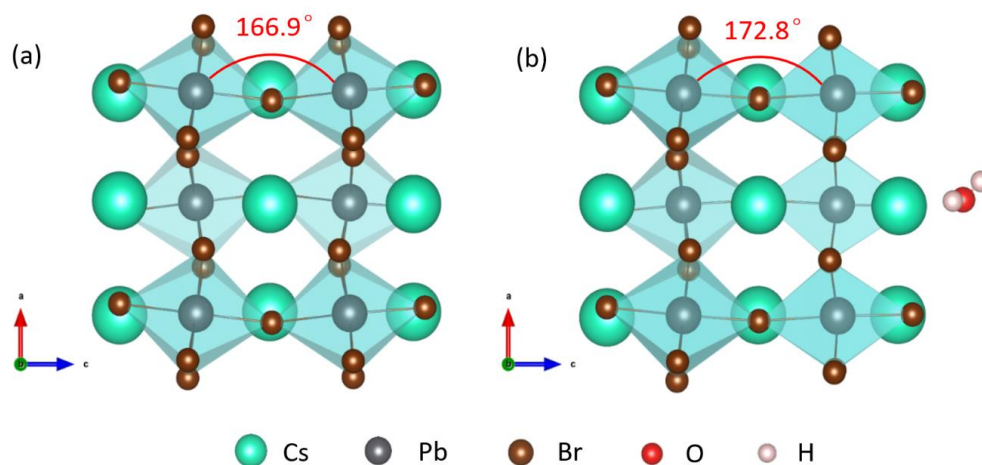


Figure 6. The models of (a) clean CsPbBr₃ slab and (b) CsPbBr₃ slab adsorbed H₂O molecules, the calculated bonding angles of Pb-Br-Pb are 166.9° and 172.8° in CsPbBr₃ and CsPbBr₃+H₂O slab, respectively.

Photophysical properties and electronic structures analyses

The transfer and recombination kinetics of charge carriers were experimentally validated with time-resolved PL measurements. Normalized steady-state PL spectra (Figure 7a) reveal a blue-shift of the emission maximum from 526 nm to 521 nm (0.023 eV) with increasing reaction cycles. This is in agreement with the absorption data (Figure S10a). While the absorption slightly decreases, the absorption edge shows a slight blue-shift of about 0.026 eV. With this information at hand, time-resolved PL was used to generate insight into the charge carrier dynamics and experimentally validate the observations from DFT. As shown in Figure 7b, an increase in PL lifetime is observed with increasing reaction cycles (the detailed parameters are shown in Table S8). The longest lifetime is obtained after 11 cycles, in which the contribution of τ_1 is reduced from 93.4% (0.58 ns) to 86.6% (1.16 ns). Meanwhile, the contribution of τ_2 is increased from 6.6% to 13.4% for the recycled one, with the τ_2 extended from

3.64 to 6.23 ns. Further increasing cycles beyond 11 times leads to a slightly decreased lifetime but still larger than the pristine one. The suppressed exciton recombination and enhanced carrier lifetime are linked to the separation of electron-hole pairs [49]. This result provides clear evidence for the better effective charge separation after water absorption on the surface of CsPbBr₃. The prolonged lifetime enhances the probability of photocatalytic surface reaction over unwanted recombination pathways [50, 51]. These findings show that the beneficial effect of trace amount of water can be linked to optimizing the crystal structure and improving the charge carrier migration to the CsPbBr₃ surface.

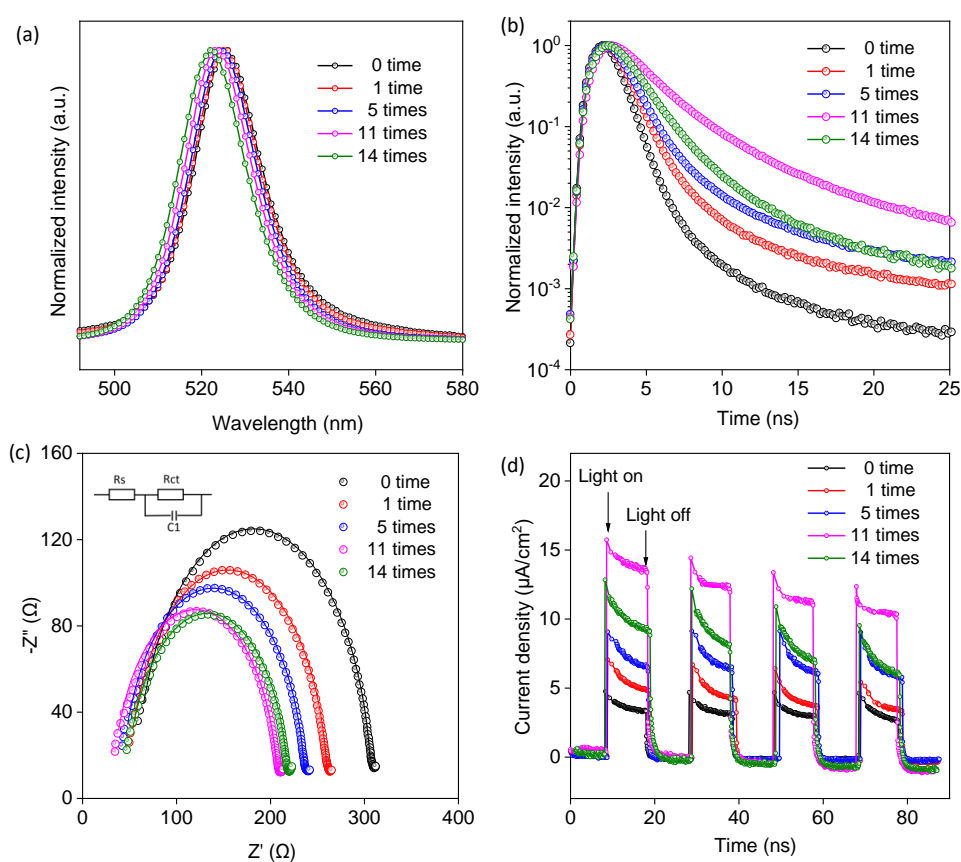


Figure 7. (a) Steady-state PL spectra, (b) PL lifetime decay traces, (c) Nyquist plots and (d) Photocurrent responses of CsPbBr₃ films under repeated reactions with the cycle time of 0 time, 1 time, 5 times, 11 times and 14 times, respectively. The inset in Figure 7c is the equivalent circuit used to fit the impedance spectra for EIS analysis.

To evaluate changes in the charge-transfer properties, electrochemical impedance spectroscopy (EIS) was performed. Figure 7c reveals that with

increasing cycles, the semicircle radius in the Nyquist plot becomes smaller, signifying a smaller charge-transfer resistance [51]. The details of these semicircles quantified with an equivalent circuit are summarized in Table S9. The resistance decreases from 259 Ohm (before cycle 1) to 172 Ohm (after cycle 11), indicating an improved electronic conductivity [11]. In addition, the photocurrent responses of CsPbBr₃ with different cycle times under solar light irradiation were tested to evaluate photogenerated charge carrier dynamics. As shown in Figure 7d, the photocurrent of CsPbBr₃ under repeated cycles, especially the 11th cycle, increases significantly compared to the original one, suggesting more efficiency in conductivity and charge generation [51].

The energy level transition on CsPbBr₃ during the cycling tests was explored by XPS. As shown in Figure 8a, the XPS spectra of the Cs 3d had no significant change in the spectral shape, while the peaks presented a shift of around 0.5 eV (11 times) to higher binding energy (BE). A similar shift was also found in the spectra of Pb 4f and Br 3d, as shown in Figures 8b and c. Previous research has revealed that the BE shift can be attributed to water (the water molecules acted as an *n*-dopant), which makes the Fermi level position closer to conduction band minimum (CBM) [52, 53]. Thus, the generated trace water would increase electron density and accordingly improve reduction ability.

To further investigate the effect of water on band structure of the CsPbBr₃ thin-film with different cycles, electrochemical flat band potential (E_{fb}) measurements (Mott–Schottky curves) were carried out as shown in Figure 8d. The positive slope is characteristic of an *n*-type semiconductor [54]. The calculated E_{fb} of CsPbBr₃ with repeated cycles was found to be more negative than that of CsPbBr₃ film without photocatalytic use, before cycle 1 $E_{fb} = -0.83$ V versus Ag/AgCl whereas after cycle 11 it is -1.07 V. Generally, flat-band potential lies very close to the bottom of the conduction band for *n*-type semiconductors [54, 55]. Using the band gap information from the UV-vis spectra (Figure S10c), the energy band structure of CsPbBr₃ is illustrated in Figure S11. This implies that the conduction band potential becomes more negative with increasing reaction time [54], which responds to the XPS results.

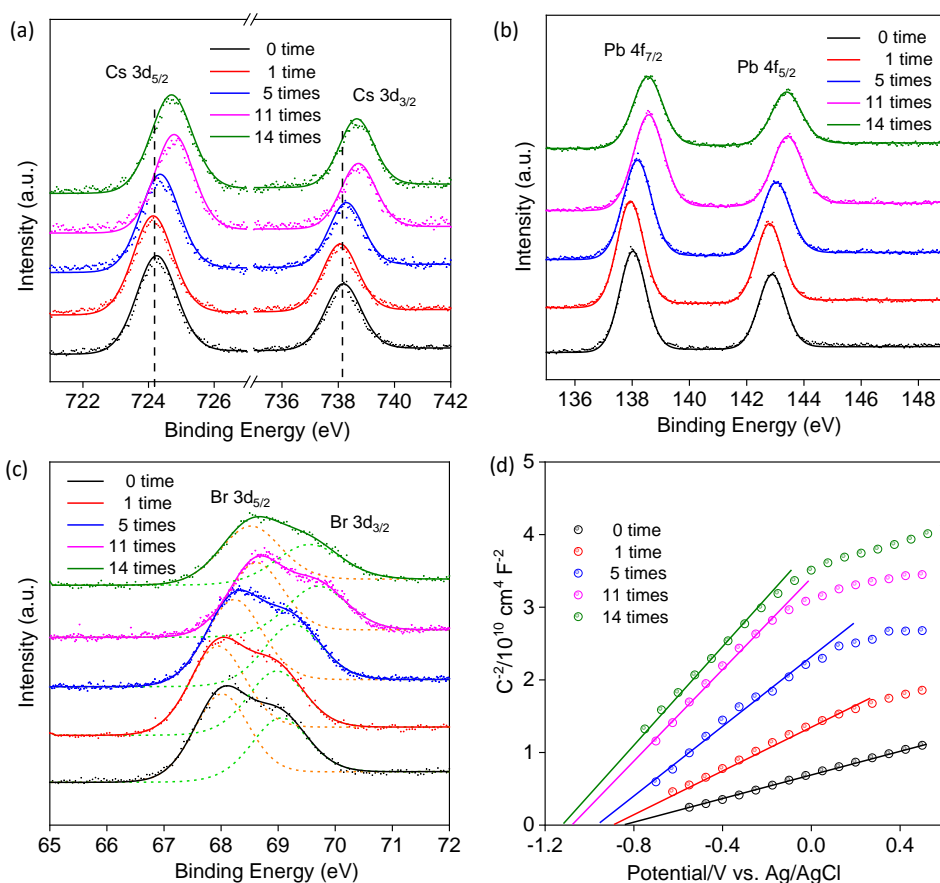


Figure 8. The XPS spectra of (a) Cs 3d, (b) Pb 4f and (c) Br 3d core levels, and (d) Mott–Schottky plots of CsPbBr₃ films under repeated reactions with the cycle time of 0 time, 1 time, 5 times, 11 times and 14 times, respectively.

4.4 Conclusions

In summary, a stable planar photocatalyst cell NiO_x/CsPbBr₃/TiO₂ is developed that yields on average 16.3 μmol cm⁻² h⁻¹ of BAD from the selective oxidation of BA, for over 90 h testing under simulated solar light illumination. A NiO_x and TiO₂ hole and electron extracting layer improve the photogenerated charge extraction from the light-absorbing CsPbBr₃ layer while simultaneously protecting it from the environment. Our experimental and theoretical results also indicate the trace amounts of H₂O can drastically enhance the photoactivity (a 3-fold improvement) of the as-generated CsPbBr₃ by improving the crystal symmetry and decreasing the effective mass of the charge carriers. This work offers an effective strategy for constructing stable metal halide based photocatalysts *via* simple solution-processing. Besides, our findings provide deeper insights into the effect of water on MHP material and shed light on the

beneficial effect of trace amounts of water to improve the photoactivity of perovskite solar catalyst cell.

4.5 References

- [1] J. Schneider, M. Matsuoka, M. Takeuchi, J. Zhang, Y. Horiuchi, M. Anpo, D.W. Bahnemann, Understanding TiO₂ photocatalysis: mechanisms and materials, *Chem. Rev.*, 114 (2014) 9919-9986.
- [2] B. Weng, M.-Y. Qi, C. Han, Z.-R. Tang, Y.-J. Xu, Photocorrosion Inhibition of Semiconductor-Based Photocatalysts: Basic Principle, Current Development, and Future Perspective, *ACS Catal.*, 9 (2019) 4642-4687.
- [3] S. Guo, Z. Deng, M. Li, B. Jiang, C. Tian, Q. Pan, H. Fu, Phosphorus-Doped Carbon Nitride Tubes with a Layered Micro-nanostructure for Enhanced Visible-Light Photocatalytic Hydrogen Evolution, *Angew. Chem. Int. Ed. Engl.*, 55 (2016) 1830-1834.
- [4] B. Weng, K.Q. Lu, Z. Tang, H.M. Chen, Y.J. Xu, Stabilizing ultrasmall Au clusters for enhanced photoredox catalysis, *Nat. Commun.*, 9 (2018) 1543.
- [5] H. Huang, B. Pradhan, J. Hofkens, M.B.J. Roeffaers, J.A. Steele, Solar-Driven Metal Halide Perovskite Photocatalysis: Design, Stability, and Performance, *ACS Energy Lett.*, 5 (2020) 1107-1123.
- [6] M.A. Green, A. Ho-Baillie, H.J. Snaith, The emergence of perovskite solar cells, *Nature Photonics*, 8 (2014) 506-514.
- [7] D. Luo, W. Yang, Z. Wang, A. Sadhanala, Q. Hu, R. Su, R. Shivanna, G.F. Trindade, J.F. Watts, Z. Xu, Enhanced photovoltage for inverted planar heterojunction perovskite solar cells, *Science*, 360 (2018) 1442-1446.
- [8] C. Wang, C. Zhang, S. Wang, G. Liu, H. Xia, S. Tong, J. He, D. Niu, C. Zhou, K. Ding, Y. Gao, J. Yang, Low-temperature processed, efficient, and highly reproducible cesium-doped triple cation perovskite planar heterojunction solar cells, *Solar RRL*, 2 (2018) 1700209.
- [9] Q. Jiang, L. Zhang, H. Wang, X. Yang, J. Meng, H. Liu, Z. Yin, J. Wu, X. Zhang, J. You, Enhanced electron extraction using SnO₂ for high-efficiency planar-structure HC(NH₂)₂PbI₃-based perovskite solar cells, *Nature Energy*, 2 (2016), 1-7.

- [10] H. Zhou, Q. Chen, G. Li, S. Luo, T.-b. Song, H.-S. Duan, Z. Hong, J. You, Y. Liu, Y. Yang, Interface engineering of highly efficient perovskite solar cells, *Science*, 345 (2014) 542-546.
- [11] G. Gao, Q. Xi, H. Zhou, Y. Zhao, C. Wu, L. Wang, P. Guo, J. Xu, Novel inorganic perovskite quantum dots for photocatalysis, *Nanoscale*, 9 (2017) 12032-12038.
- [12] Y. Wu, P. Wang, X. Zhu, Q. Zhang, Z. Wang, Y. Liu, G. Zou, Y. Dai, M.H. Whangbo, B. Huang, Composite of $\text{CH}_3\text{NH}_3\text{PbI}_3$ with Reduced Graphene Oxide as a Highly Efficient and Stable Visible-Light Photocatalyst for Hydrogen Evolution in Aqueous HI Solution, *Adv. Mater.*, 30 (2018) 1704342.
- [13] H. Huang, H. Yuan, K.P.F. Janssen, G. Solís-Fernández, Y. Wang, C.Y.X. Tan, D. Jonckheere, E. Debroye, J. Long, J. Hendrix, J. Hofkens, J.A. Steele, M.B.J. Roeffaers, Efficient and Selective Photocatalytic Oxidation of Benzylic Alcohols with Hybrid Organic–Inorganic Perovskite Materials, *ACS Energy Lett.*, 3 (2018) 755-759.
- [14] Z. Zhang, Y. Liang, H. Huang, X. Liu, Q. Li, L. Chen, D. Xu, Stable and Highly Efficient Photocatalysis with Lead-Free Double-Perovskite of $\text{Cs}_2\text{AgBiBr}_6$, *Angew. Chem. Int. Ed. Engl.*, 58 (2019) 7263-7267.
- [15] J. Huang, S. Tan, P.D. Lund, H. Zhou, Impact of H_2O on organic–inorganic hybrid perovskite solar cells, *Energy Environ. Sci.*, 10 (2017) 2284-2311.
- [16] B. Philippe, B.-W. Park, R. Lindblad, J. Oscarsson, S. Ahmadi, E.M.J. Johansson, H. Rensmo, Chemical and Electronic Structure Characterization of Lead Halide Perovskites and Stability Behavior under Different Exposures-A Photoelectron Spectroscopy Investigation, *Chem. Mater.*, 27 (2015) 1720-1731.
- [17] T.A. Berhe, W.-N. Su, C.-H. Chen, C.-J. Pan, J.-H. Cheng, H.-M. Chen, M.-C. Tsai, L.-Y. Chen, A.A. Dubale, B.-J. Hwang, Organometal halide perovskite solar cells: degradation and stability, *Energy Environ. Sci.*, 9 (2016) 323-356.
- [18] S. Yang, S. Chen, E. Mosconi, Y. Fang, X. Xiao, C. Wang, Y. Zhou, Z. Yu, J. Zhao, Y. Gao, Stabilizing halide perovskite surfaces for solar cell operation with wide-bandgap lead oxysalts, *Science*, 365 (2019) 473-478.
- [19] S. Park, W.J. Chang, C.W. Lee, S. Park, H.-Y. Ahn, K.T. Nam, Photocatalytic hydrogen generation from hydriodic acid using

methylammonium lead iodide in dynamic equilibrium with aqueous solution, *Nat. Energy*, 2 (2016), 1-8.

[20] H. Huang, H. Yuan, J. Zhao, G. Solis-Fernandez, C. Zhou, J.W. Seo, J. Hendrix, E. Debroye, J.A. Steele, J. Hofkens, C (sp³)–H Bond Activation by Perovskite Solar Photocatalyst Cell, *ACS Energy Lett.*, 4 (2018) 203-208.

[21] S. Schünemann, M. van Gastel, H. Tüysüz, A CsPbBr₃/TiO₂ Composite for Visible-Light-Driven Photocatalytic Benzyl Alcohol Oxidation, *ChemSusChem*, 11 (2018) 2057-2061.

[22] Y. Dai, C. Poidevin, C. Ochoa-Hernandez, A.A. Auer, H. Tuysuz, A Supported Bismuth Halide Perovskite Photocatalyst for Selective Aliphatic and Aromatic C-H Bond Activation, *Angew. Chem. Int. Ed.*, 59 (2020) 5788-5796.

[23] Z.J. Li, E. Hofman, J. Li, A.H. Davis, C.H. Tung, L.Z. Wu, W. Zheng, Photoelectrochemically active and environmentally stable CsPbBr₃/TiO₂ core/shell nanocrystals, *Adv. Funct. Mater.*, 28 (2018) 1704288.

[24] J. You, L. Meng, T.-B. Song, T.-F. Guo, Y. Yang, W.-H. Chang, Z. Hong, H. Chen, H. Zhou, Q. Chen, Y. Liu, N. De Marco, Y. Yang, Improved air stability of perovskite solar cells via solution-processed metal oxide transport layers, *Nat. Nanotechnol.*, 11 (2015) 75-81.

[25] J. Liang, C. Wang, Y. Wang, Z. Xu, Z. Lu, Y. Ma, H. Zhu, Y. Hu, C. Xiao, X. Yi, All-inorganic perovskite solar cells, *J. Am. Chem. Soc.*, 138 (2016) 15829-15832.

[26] L.-F. Gao, W.-J. Luo, Y.-F. Yao, Z.-G. Zou, An all-inorganic lead halide perovskite-based photocathode for stable water reduction, *Chem. Commun.*, 54 (2018) 11459-11462.

[27] J. Li, M. Li, H. Sun, Z. Ao, S. Wang, S. Liu, Understanding of the Oxidation Behavior of Benzyl Alcohol by Peroxymonosulfate via Carbon Nanotubes Activation, *ACS Catal.* 10 (2020) 3516-3525.

[28] Z. Zhao¹, M. M. Flores Espinosa¹, J. Zhou, W. Xue, X. Duan, J. Miao, Yu Huang, Synthesis of surface controlled nickel/palladium hydride nanodendrites with high performance in benzyl alcohol oxidation, *Nano Res.*, 12 (2019) 1467-1472.

[29] J. Huang, C. Wang, Z. Liu, X. Qiu, J. Yang, J. Chang, Simultaneously enhanced durability and performance by employing dopamine copolymerized

PEDOT with high work function and water-proofness for inverted perovskite solar cells, *J. Mater. Chem. C*, 6 (2018) 2311-2318,

[30] C. Wang, C. Zhang, S. Tong, H. Xia, L. Wang, H. Xie, Y. Gao, J. Yang, Energy level and thickness control on PEDOT:PSS layer for efficient planar heterojunction perovskite cells, *J. Phys. D: Appl. Phys.*, 51 (2018) 025110,

[31] A. Manoogian, J. Woolley, Temperature dependence of the energy gap in semiconductors, *Can. J. Phys.*, 62 (1984) 285-287.

[32] R. Elliott, Intensity of optical absorption by excitons, *Phys. Rev.*, 108 (1957) 1384.

[33] L. Roa, C. Rincon, J. Gonzalez, M. Quintero, Analysis of direct exciton transitions in $\text{CuGa}(\text{S}_x\text{Se}_{1-x})_2$ alloys, *J. Phys. Chem. Solids*, 51 (1990) 551-555.

[34] G. Marín, C. Rincon, S. Wasim, C. Power, G. Sanchez Perez, Temperature dependence of the fundamental absorption edge in CuInTe_2 , *J. Appl. Phys.*, 81 (1997) 7580-7583.

[35] M. Saba, M. Cadelano, D. Marongiu, F. Chen, V. Sarritzu, N. Sestu, C. Figus, M. Aresti, R. Piras, A.G. Lehmann, Correlated electron-hole plasma in organometal perovskites, *Nat. Commun.* 5 (2014) 1-10.

[36] N. Sestu, M. Cadelano, V. Sarritzu, F. Chen, D. Marongiu, R. Piras, M. Mainas, F. Quochi, M. Saba, A. Mura, Absorption F-sum rule for the exciton binding energy in methylammonium lead halide perovskites, *J. Phys. Chem. Lett.*, 6 (2015) 4566-4572.

[37] D. Balzar, X-ray diffraction line broadening: Modeling and applications to high-Tc superconductors, *J. Res. Natl. Inst. Stand. Technol.*, 98 (1993) 321.

[38] D. Marongiu, M. Saba, F. Quochi, A. Mura, G. Bongiovanni, The role of excitons in 3D and 2D lead halide perovskites, *J. Mater. Chem. C*, 7 (2019) 12006-12018.

[39] M. Anni, A. Cretì, Y. Zhang, M.L. De Giorgi, M. Lomascolo, Investigation of the role of the environment on the photoluminescence and the exciton relaxation of CsPbBr_3 nanocrystals thin films, *Appl. Sci.*, 10 (2020) 2148.

[40] J. Wang, R. Cao, P. Da, Y. Wang, T. Hu, L. Wu, J. Lu, X. Shen, F. Xu, G. Zheng, Purcell effect in an organic-inorganic halide perovskite semiconductor microcavity system, *Appl. Phys. Lett.*, 108 (2016) 022103.

- [41] Z. Zhang, Z. Chen, J. Zhang, W. Chen, J. Yang, X. Wen, B. Wang, N. Kobamoto, L. Yuan, J.A. Stride, Significant improvement in the performance of PbSe quantum dot solar cell by introducing a CsPbBr₃ perovskite colloidal nanocrystal back layer, *Adv. Energy Mater.*, 7 (2017) 1601773.
- [42] J. Luo, H. Yang, Z. Liu, F. Li, S. Liu, J. Ma, B. Liu, Organic-inorganic hybrid perovskite-TiO₂ nanorod arrays for efficient and stable photoelectrochemical hydrogen evolution from HI splitting, *Mater. Today Chem.*, 12 (2019) 1-6.
- [43] S. Lee, G.Y. Jang, J.K. Kim, J.H. Park, Solar-harvesting lead halide perovskite for artificial photosynthesis, *J. Energy Chem.* 62 (2021) 11-26.
- [44] Z. Li, X. Liu, J. Xu, Y. Liao, H. Zhao, B. Zhang, S.F. Liu, J. Yao, Moisture-Induced Crystallinity Improvement for Efficient CsPbI_{3-x}Br_x Perovskite Solar Cells with Excess Cesium Bromide, *J. Phys. Chem. Lett.*, 10 (2019) 4587-4595.
- [45] J.-W. Lee, S.-H. Bae, Y.-T. Hsieh, N. De Marco, M. Wang, P. Sun, Y. Yang, A Bifunctional Lewis Base Additive for Microscopic Homogeneity in Perovskite Solar Cells, *Chem*, 3 (2017) 290-302.
- [46] N. Adhikari, A. Dubey, E.A. Gaml, B. Vaagensmith, K.M. Reza, S.A. Mabrouk, S. Gu, J. Zai, X. Qian, Q. Qiao, Crystallization of a perovskite film for higher performance solar cells by controlling water concentration in methyl ammonium iodide precursor solution, *Nanoscale*, 8 (2016) 2693-2703.
- [47] B. Liu, M. Long, M. Cai, L. Ding, J. Yang, Interfacial charge behavior modulation in 2D/3D perovskite heterostructure for potential high-performance solar cells, *Nano Energy*, 59 (2019) 715-720.
- [48] J. Zhang, P. Zhou, J. Liu, J. Yu, New understanding of the difference of photocatalytic activity among anatase, rutile and brookite TiO₂, *Phys. Chem. Chem. Phys.*, 16 (2014) 20382-20386.
- [49] D. Shi, V. Adinolfi, R. Comin, M. Yuan, E. Alarousu, A. Buin, Y. Chen, S. Hoogland, A. Rothenberger, K. Katsiev, Low trap-state density and long carrier diffusion in organolead trihalide perovskite single crystals, *Science*, 347 (2015) 519-522.
- [50] P. Niu, L. Zhang, G. Liu, H.-M. Cheng, Graphene-Like Carbon Nitride Nanosheets for Improved Photocatalytic Activities, *Adv. Funct. Mater.*, 22 (2012) 4763-4770.

- [51] J. Oh, J.M. Lee, Y. Yoo, J. Kim, S.-J. Hwang, S. Park, New insight of the photocatalytic behaviors of graphitic carbon nitrides for hydrogen evolution and their associations with grain size, porosity, and photophysical properties, *Appl. Catal. B: Environ.*, 218 (2017) 349-358.
- [52] Y. Li, X. Xu, C. Wang, C. Wang, F. Xie, J. Yang, Y. Gao, Degradation by Exposure of Coevaporated $\text{CH}_3\text{NH}_3\text{PbI}_3$ Thin Films, *J. Phys. Chem. C*, 119 (2015) 23996-24002.
- [53] C. Wang, Y. Gao, Stability of perovskites at the surface analytic level, *J. Phys. Chem. Lett.*, 9 (2018) 4657-4666.
- [54] X. Xiao, J. Jiang, L. Zhang, Selective oxidation of benzyl alcohol into benzaldehyde over semiconductors under visible light: The case of $\text{Bi}_{12}\text{O}_{17}\text{Cl}_2$ nanobelts, *Appl. Catal. B: Environ.*, 142-143 (2013) 487-493.
- [55] Y. Su, Z. Han, L. Zhang, W. Wang, M. Duan, X. Li, Y. Zheng, Y. Wang, X. Lei, Surface hydrogen bonds assisted meso-porous WO_3 photocatalysts for high selective oxidation of benzylalcohol to benzylaldehyde, *Appl. Catal. B: Environ.*, 217 (2017) 108-114.

4.6 Appendix to Chapter 4

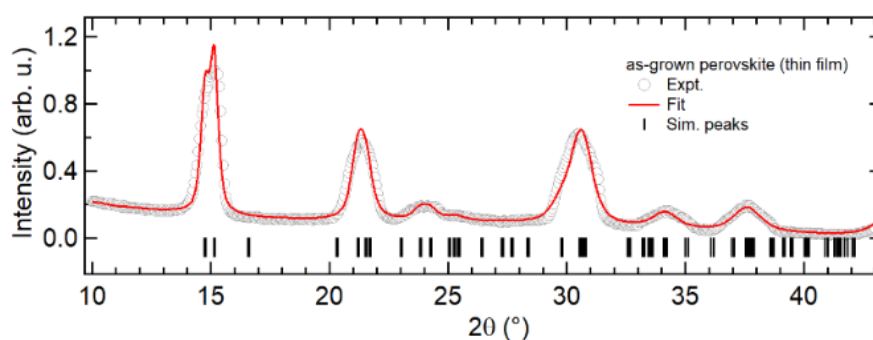


Fig. S1. XRD structural refinement of CsPbBr_3 thin film *via* Le Bail method.

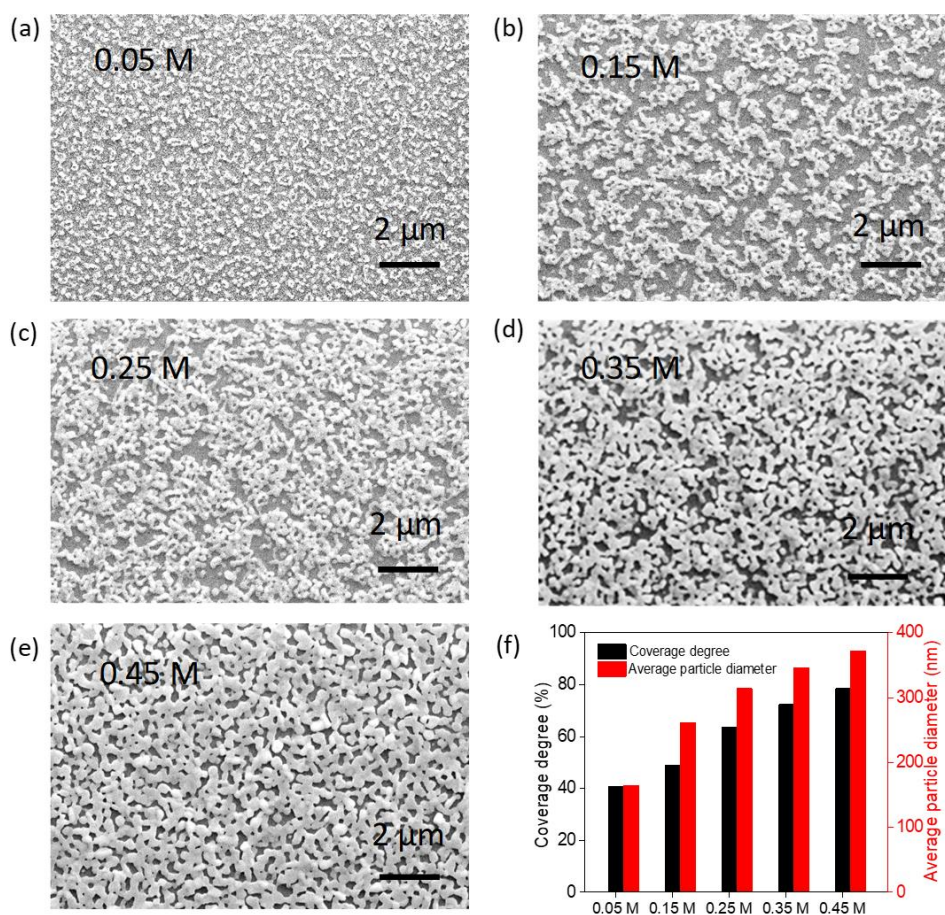


Fig. S2. SEM morphology images of CsPbBr₃ films fabricated with different precursor concentrations (a) 0.05 M, (b) 0.15 M, (c) 0.25 M, (d) 0.35 M and (e) 0.45 M, respectively. (f) The coverage degree and average particle diameter distribution of CsPbBr₃ films with precursor solution concentrations ranging from 0.05 to 0.45 M.

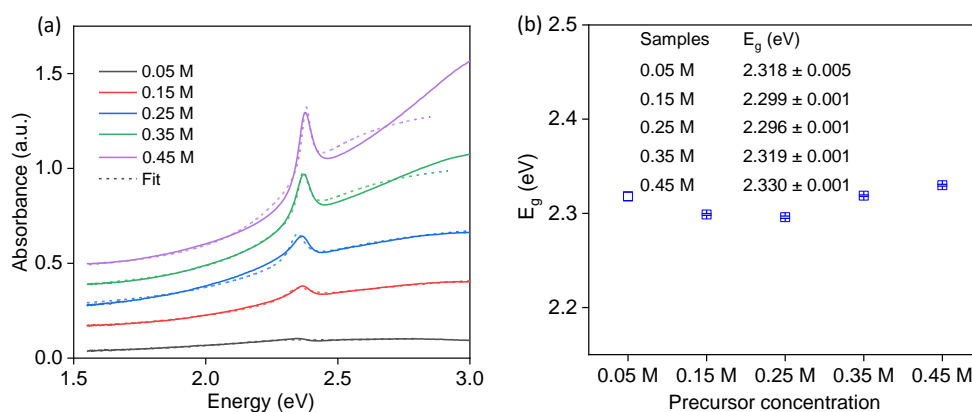


Fig. S3. (a) Simulation of the absorption spectra CsPbBr₃ thin films using the Elliot model with the precursor solution concentration of 0.05 M, 0.15 M, 0.25 M, 0.35 M and 0.45 M. full lines: experimental data, dashed line: fit to the Elliot model. (b) The bandgap energy values of CsPbBr₃ thin films extracted *via* the Elliot model.

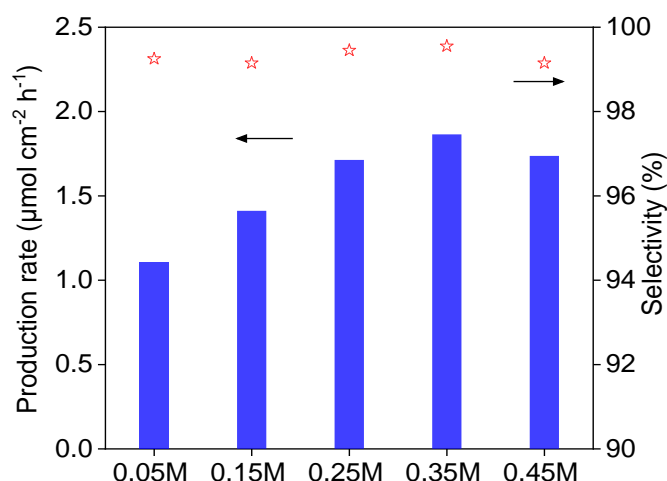


Fig. S4. Photocatalytic performance of benzyl alcohol oxidation over CsPbBr₃ thin film with the precursor solution concentration ranging from 0.05 M to 0.45 M. Reaction conditions: CsPbBr₃ thin film photocatalyst ($1.0 \times 1.2 \text{ cm}^2$), 0.5 mmol benzyl alcohol in 2.5 mL trifluorotoluene solution with saturated molecular oxygen, AM 1.5 G simulated solar light irradiation (150 W Xe lamp), illumination time (4 h).

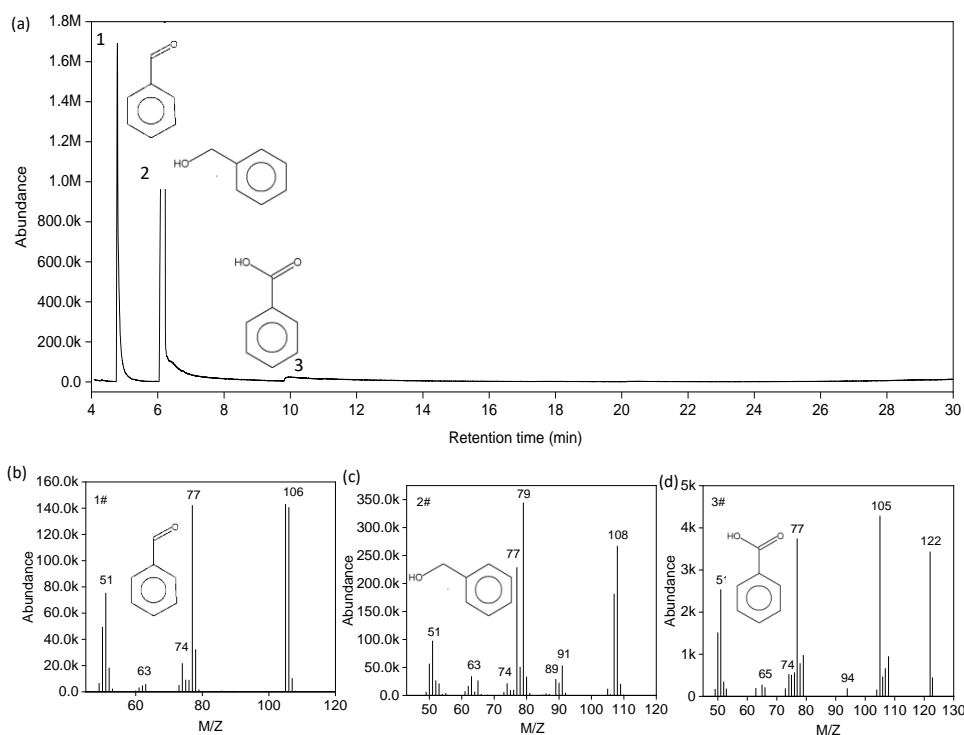


Fig. S5. (a) GC-MS spectra of the products over $\text{NiO}_x/\text{CsPbBr}_3/\text{TiO}_2$ photocatalyst cell. (b-c) The spectrum of (b) benzaldehyde, (c) benzyl alcohol and (d) benzoic acid, respectively. Reaction conditions: photocatalyst cell ($1.0 \times 1.2 \text{ cm}^2$), 0.5 mmol benzyl alcohol in 2.5 mL trifluorotoluene solution with saturated molecular oxygen, AM 1.5 G simulated solar light irradiation (150 W Xe lamp), illumination time (4 h).

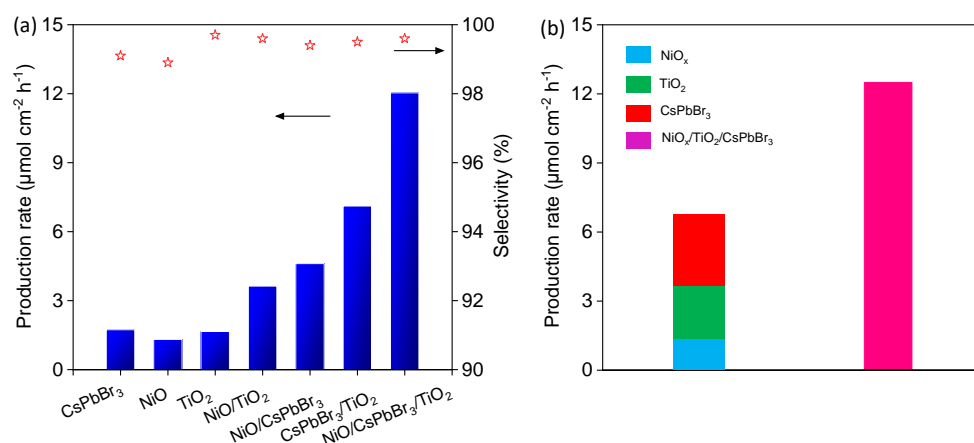


Fig. S6. (a) Selective photocatalytic oxidation of BA to BAD over CsPbBr_3 , $\text{NiO}_x/\text{CsPbBr}_3/\text{TiO}_2$ thin films and other reference photocatalysts. (b) Comparison of the photoactivity of solar photocatalyst cell and the sum of the individual components CsPbBr_3 , NiO_x and TiO_2 photocatalysts. Reaction conditions: various photocatalysts ($1.0 \times 1.2 \text{ cm}^2$), 0.5 mmol benzyl alcohol in

2.5 ml trifluorotoluene solution with saturated molecular oxygen, AM 1.5 G simulated solar light irradiation (150 W Xe lamp), reaction time (4 h).

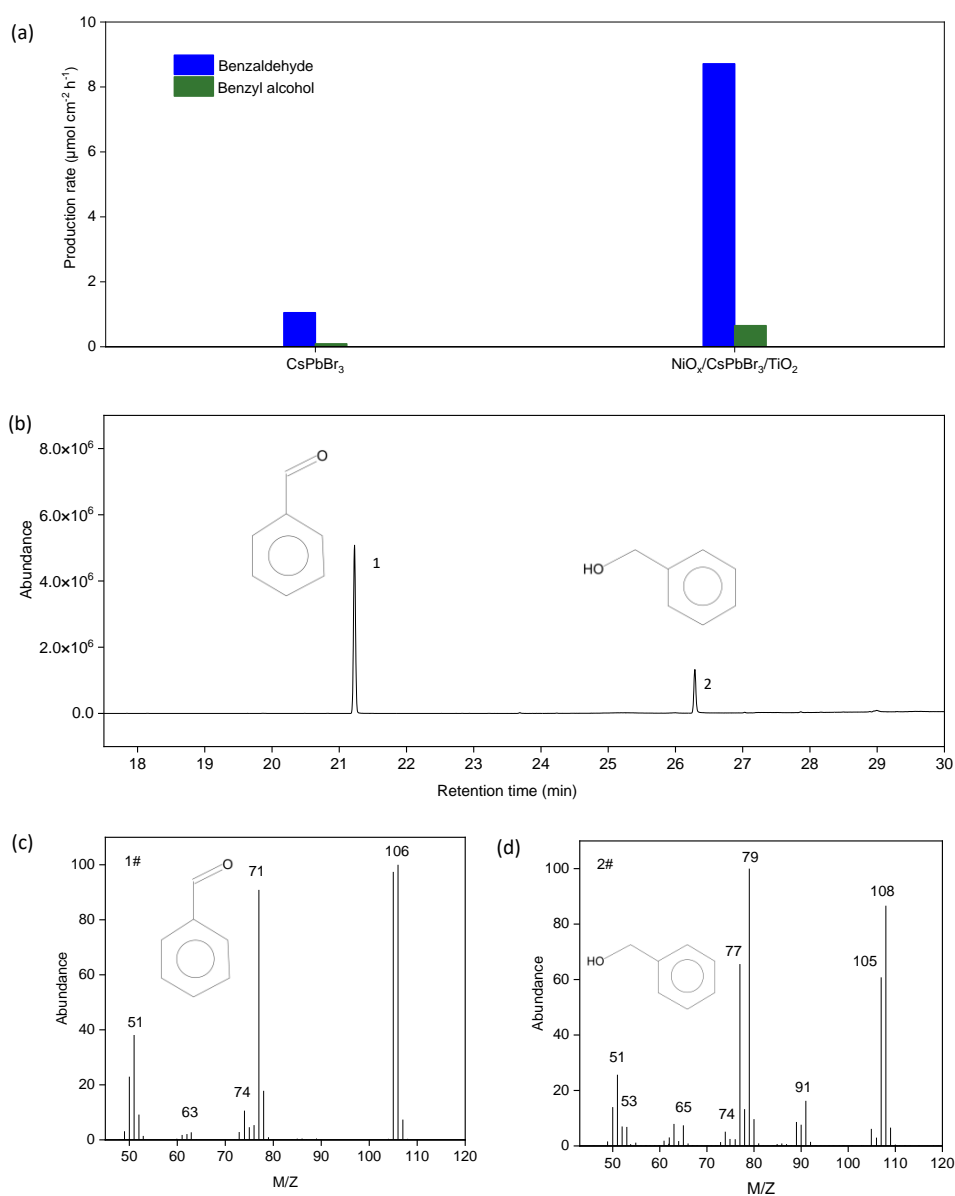


Fig. S7. (a) Photocatalytic oxidation of toluene to benzaldehyde over pure CsPbBr_3 thin film and $\text{NiO}_x/\text{CsPbBr}_3/\text{TiO}_2$ photocatalyst cell. (b-d) GC-MS spectra of the products over $\text{NiO}_x/\text{CsPbBr}_3/\text{TiO}_2$ photocatalyst cell after 8h of irradiation under simulated solar light, (b) the full spectrum of these products, *i.e.*, benzaldehyde and benzyl alcohol, and the corresponding spectra of (c) benzaldehyde and (d) benzyl alcohol, respectively. Reaction conditions: CsPbBr_3 film or $\text{NiO}_x/\text{CsPbBr}_3/\text{TiO}_2$ photocatalyst cell ($1.0 \times 1.2 \text{ cm}^2$), 2.5 ml toluene solution with saturated molecular oxygen, AM 1.5 G simulated solar light irradiation (150 W Xe lamp), illumination time (8 h, room temperature).

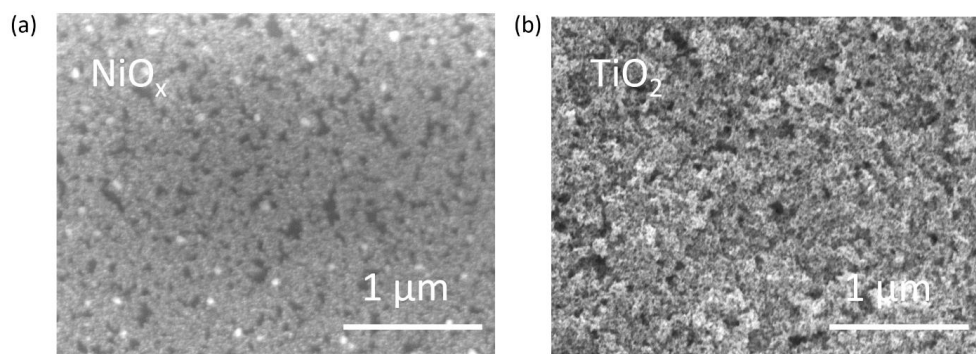


Fig. S8. SEM images of (a) NiO_x and (b) TiO₂ thin films, respectively.

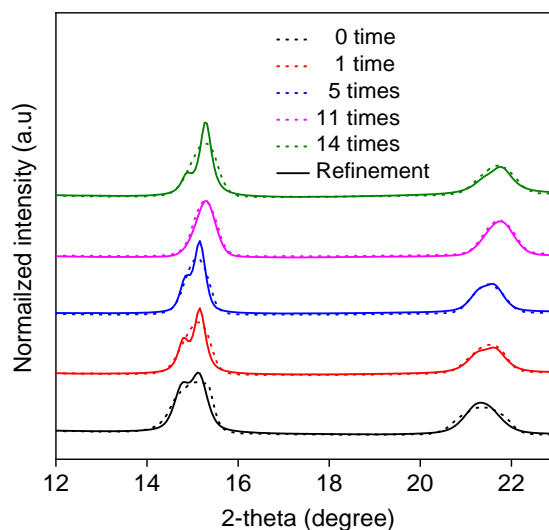


Fig. S9. XRD structural refinement of CsPbBr₃ with different cycle times using Le Bail method. The other key experimental parameters, like layer thickness and instrumental geometry, are kept constant. Normalization of the γ -phase lattice is made *via* rescaling the orthorhombic unit cell by $(1/\sqrt{2}, 1/\sqrt{2}, 1/2)$, with the pseudo-cubic unit cell volume also being normalized by the same fractions.

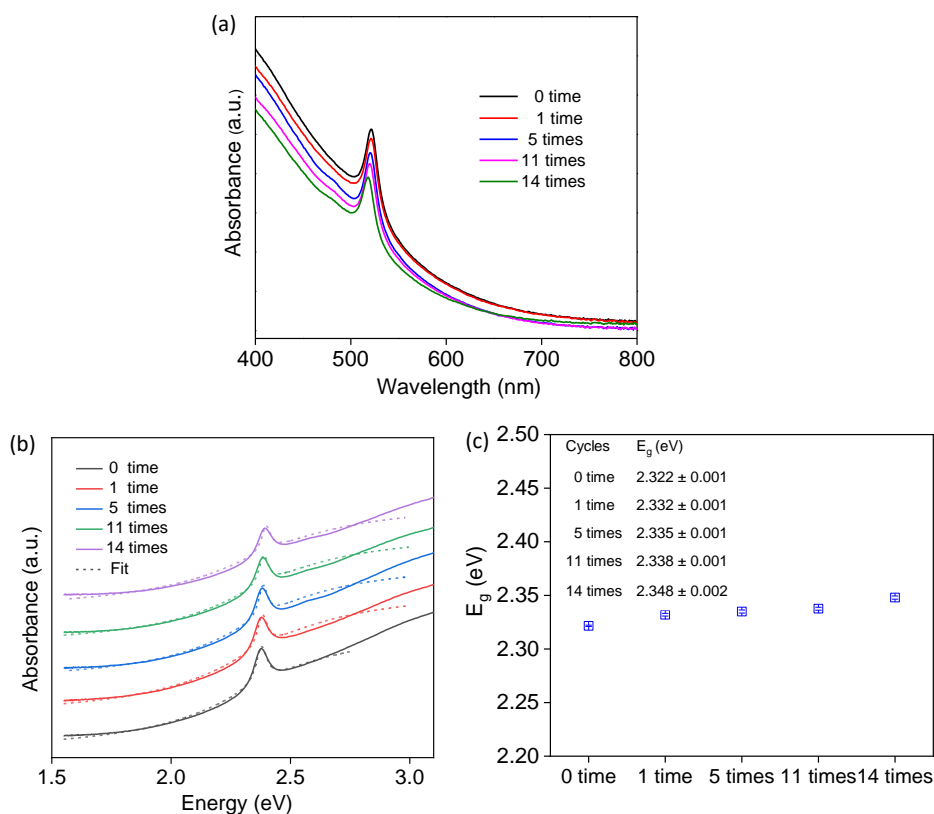


Fig. S10. (a) Absorption spectra of CsPbBr₃ thin films with repeated cycles ranging from 0 to 14 times. (b-c) Elliot model used to extract the bandgap energy, and the obtained bandgap values, respectively.

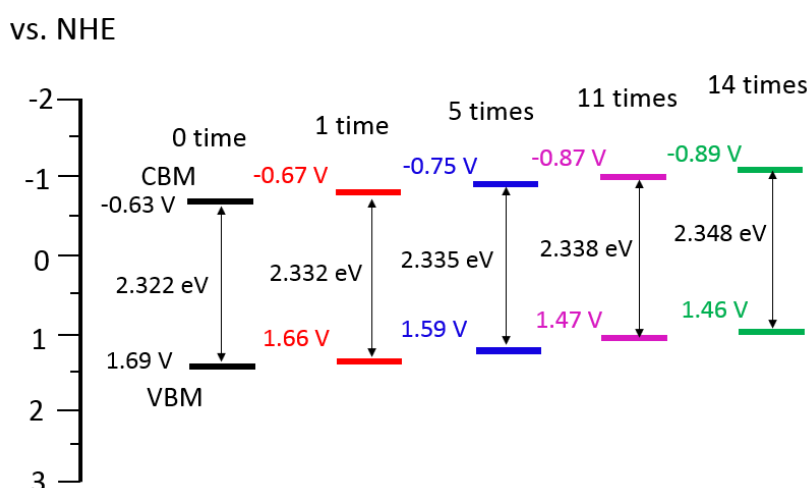


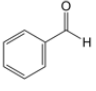
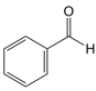
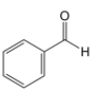
Fig. S11. The schematic illustration of the band structures of CsPbBr₃ with different cycle times from 0 to 14 times. Conduction band maximum (CBM) is determined from flat band plot (Fig. 8d) and valence band minimum (VBM) is evaluated using the band energy *via* UV-Vis absorption spectra (Fig. S10).

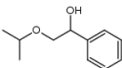
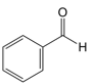
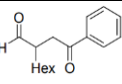
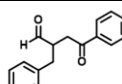
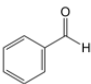
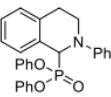
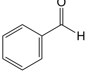
Table S1. Detailed Parameters for CsPbBr₃ Thin-Film with Different Precursor Concentrations.

Concentration (M)	0.05	0.15	0.25	0.35	0.45
Total area (cm ²)	1.2	1.2	1.2	1.2	1.2
Thickness (nm)	187	275	368	453	525
Surface coverage (%)	40.8	49.0	63.7	72.4	78.5
Mass (μg)	0.27	1.33	4.03	7.94	13.10
Bandgap (eV)	2.318	2.299	2.296	2.319	2.330

The mass of CsPbBr₃ photocatalyst with different precursor concentrations was calculated depending on the precursor solution concentration, the volume of CsPbBr₃ thin film (*i.e.*, the thickness of the film multiplied by the area) and the related surface coverage, with detailed parameters summarized in Table S1, in which the CsPbBr₃ amount was calculated according to the followed formula:
 $m = \text{active area} \times \text{thickness} \times \text{concentration} \times \text{molar mass} \times \text{surface coverage}$

Table S2. Comparison of the CsPbBr₃ Photocatalyst with Other Reported Metal Halide Perovskite-Based Photocatalysts Used for Organic Synthesis.

Perovskite photocatalyst	Solvent	Light source	Product and activity (mmol/g/h)	Measured time for stability (h)	TON	Ref.
CsPbBr ₃	trifluorotoluene	AM 1.5G	 (807)	92	45300	This work
Cs ₃ Bi ₂ Br ₉	benzyl alcohol	λ >420 nm	 (32.9)	12	-	[1]
FAPbBr ₃	toluene	AM 1.5G	 (3.8)	20	263	[2]

Cs ₃ Bi ₂ Br ₉	isopropanol	$\lambda > 420$ nm	 (1.333)	18	-	[3]
FAPbBr ₃	trifluorotoluene	AM 1.5G	 (0.25)	20	-	[4]
CsPbBr ₃	CH ₂ Cl ₂	Blue LED	 Hex	96	52000	[5]
CsPbBr ₃	CH ₂ Cl ₂	Blue LED		24	9100	[6]
FAPbBr ₃	toluene	AM 1.5G		40	-	[7]
CsPbBr ₃	CH ₂ Cl ₂	white LED		20	-	[8]
CsPbBr ₃	toluene	$\lambda > 420$ nm		8	-	[9]

Turnover number (TON) is calculated as follows: TON= sum of the molar of benzaldehyde in 23 cycles / the molar of perovskite catalyst

Table S3. Comparison of Selective Photocatalytic Oxidation of Benzyl Alcohol (BA) to Benzaldehyde (BAD) over Various Photocatalysts.

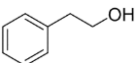
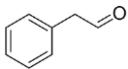
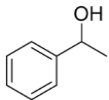
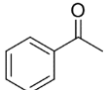
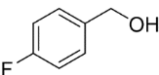
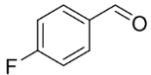
Photocatalyst	Reaction conditions	BA (mmol)	Selectivity (%)	Activity (mmol/g/h)	Measured stability time (h)	Ref.
NiO _x /CsPbBr ₃ /TiO ₂	150 W Xe lamp, AM 1.5G, trifluorotoluene, 4 h	0.5	99	783	92	This work
Cs ₃ Bi ₂ Br ₉ /SBA-15	300 W Xe lamp, visible light ($\lambda > 420$ nm), 4 h	48	> 99	32.9	12	[1]
G@ULDH/ BiVO ₄	300 W Xe lamp, AM 1.5G, H ₂ O, 1.2 V vs RHE, 4 h	2	>99	30.0	-	[10]

TiO ₂ /C	150 W Xe lamp, H ₂ O, AM 1.5G, 1.25 V vs RHE, 4 h	9.6	99	28.8	-	[11]
CN-Si-WO ₃	300 W Xe lamp, full light, acetonitrile, 3h	0.2	>99	2.82	15	[12]
WO ₃ /TiO ₂	450 W high- pressure mercury lamp, λ >350 nm, H ₂ O, 3h	0.1	56	1.87	6	[13]
CdS/TiO ₂	300 W Xe lamp, visible light (λ ≥ 420 nm), trifluorotoluene, 3 h	0.2	99	1.27	12	[14]
Au/BiOCl-Ov	300 W Xe lamp, visible light (λ >420 nm), acetonitrile, 8h	0.5	100	0.95	40	[15]
BiVO ₄	30 W blue LED (λ max = 470 nm), acetonitrile, 3 h	0.1	>99	0.78	12	[16]
In ₂ S ₃ -Sv	300 W Xe lamp, visible light (λ >420 nm), trifluorotoluene , 5 h	0.1	99	0.71	25	[17]
FAPbBr ₃ / Bi ₂ WO ₆	150 W Xe lamp, AM 1.5G, trifluorotoluene, 4 h	0.1	~100	0.25	20	[4]
yolk-shell WO ₃	300 W Xe lamp, full light, H ₂ O, 5h	0.1	>99	0.127	20	[18]

Table S4. Comparison of the NiO_x/CsPbBr₃/TiO₂ Photocatalyst Cell with Thin Film Based PEC/PEC-PV Systems.

Materials	Medium	Product	Production rate ($\mu\text{mol cm}^{-2} \text{h}^{-1}$)	Light source	Stability (h)	System	Ref.
NiO _x /CsPbBr ₃ /TiO ₂	trifluorotoluene	BAD	21.7	AM 1.5G	92	PV	This work [19]
TiO ₂ nanorod MAPbI ₃	HI solution	H ₂	~24 at 0.7 V vs. Ag/AgCl	25 mW cm ⁻² (white LED)	>5h	PEC	
TiO ₂ Co-doped hematite MAPbI ₃	HI solution	H ₂	33.3 at 0.14 V vs. Ag/AgCl	AM 1.5G	>8h	PEC	[20]
ICA-Mo:BiVO ₄ /Fe(Ni)OOH-FA _{0.83} CS _{0.17} PbI ₂ Br	H ₂ O	H ₂ , O ₂	H ₂ : 95.6 O ₂ : 50.8	AM 1.5G	6h	PEC-PV	[21]

Table S5. Results of the Selective Oxidation of Alcohols over NiO_x/CsPbBr₃/TiO₂ Solar Photocatalyst Cell^a

Substrate	Main product	Production rate (mmol/g/h)	Selectivity (%)	TON
		190.5	99.2%	442
		152.7	98.3%	352
		182.6	98.7%	423

^aReaction conditions: NiO_x/CsPbBr₃/TiO₂ photocatalyst cell, alcohols (0.5 mmol) in 2.5 mL trifluorotoluene solution with saturated molecular oxygen, simulated solar light illumination (AM 1.5G, 150 W Xe lamp), irradiation time (4 h). This result proves the versatility of the NiO_x/CsPbBr₃/TiO₂ solar photocatalyst cell for organic synthesis.

Table S6. The Effects of Various Radical Scavengers on the Photocatalytic Performance of BA Oxidation over Photocatalyst Cell^a

Scavenger added	Reaction intermediate targeted	Photocatalytic activity ($\mu\text{mol cm}^{-2} \text{h}^{-1}$)	
		Before	After
none	/	12.1	12.1
ammonium oxalate	holes (h^+)	12.1	1.1
potassium persulfate	electrons (e^-)	12.1	4.7
1,4-benzoquinone	superoxide radicals ($\cdot\text{O}_2^-$)	12.1	2.3
t-butanol	hydroxyl radicals ($\cdot\text{OH}^-$)	12.1	11.9

^aReaction conditions: $\text{NiO}_x/\text{CsPbBr}_3/\text{TiO}_2$ photocatalyst cell ($1.0 \times 1.2 \text{ cm}^2$), 0.5 mmol benzyl alcohol in 2.5 ml trifluorotoluene solution with saturated molecular oxygen, various scavengers, AM 1.5 G simulated solar light irradiation (150 W Xe lamp), reaction time (4 h).

Table S7. Detailed Parameters of XRD Structural Refinement Results for CsPbBr_3 Film with Different Cycle Times (Normalization of the γ -phase lattice is made *via* rescaling the orthorhombic unit cell by $(1/\sqrt{2}, 1/\sqrt{2}, 1/2)$).

Cycle (time)	a (\AA)	b (\AA)	c (\AA)	U	aNorm (\AA)	bNorm (\AA)	cNorm (\AA)	volNorm (\AA^3)
0	8.255	8.740	11.699	16.278	5.837	6.180	5.849	211.012
1	8.210	8.749	11.689	12.046	5.805	6.187	5.845	209.895
5	8.216	8.684	11.689	8.302	5.810	6.140	5.844	208.496
11	8.147	8.574	11.576	8.024	5.761	6.063	5.788	202.134
14	8.161	8.717	11.591	13.139	5.770	6.164	5.795	206.141

Table S8. Detailed Lifetime Parameters of CsPbBr₃ Film Before and After Recycling.

Cycle (time)	τ_1 (ns)	τ_2 (ns)	A_1 (%)	A_2 (%)
0	0.58	3.64	93.4	6.6
1	0.67	5.12	91.1	8.9
5	0.82	5.65	89.5	10.5
11	1.16	6.23	86.6	13.4
14	1.02	5.96	88.3	11.7

Table S9. Detailed Resistance Parameters of CsPbBr₃ Film with Different Cycle Times that Extracted from Nyquist plots

Cycle (time)	R_s (ohm)	R_{ct} (ohm)
0	46.6	259.2
1	44.9	212.3
5	43.7	195.1
11	41.5	172.1
14	42.4	175.0

References

- [1] Y. Dai, C. Poidevin, C. Ochoa-Hernandez, A.A. Auer, H. Tuysuz, A Supported Bismuth Halide Perovskite Photocatalyst for Selective Aliphatic and Aromatic C-H Bond Activation, *Angew. Chem. Int. Ed.*, 59 (2020) 5788-5796.
- [2] H. Huang, H. Yuan, J. Zhao, G. Solís-Fernández, C. Zhou, J.W. Seo, J. Hendrix, E. Debroye, J.A. Steele, J. Hofkens, J. Long, M.B.J. Roeffaers, C(sp³)-H Bond Activation by Perovskite Solar Photocatalyst Cell, *ACS Energy Lett.*, 4 (2018) 203-208.
- [3] Y. Dai, H. Tuysuz, Lead-Free Cs₃Bi₂Br₉ Perovskite as Photocatalyst for Ring-Opening Reactions of Epoxides, *ChemSusChem*, 12 (2019) 2587-2592.

- [4] H. Huang, J. Zhao, Y. Du, C. Zhou, M. Zhang, Z. Wang, Y. Weng, J. Long, J. Hofkens, J.A. Steele, M.B.J. Roeffaers, Direct Z-Scheme Heterojunction of Semicoherent FAPbBr₃/Bi₂WO₆ Interface for Photoredox Reaction with Large Driving Force, *ACS Nano*, 14 (2020) 16689-16697.
- [5] X. Zhu, Y. Lin, Y. Sun, M.C. Beard, Y. Yan, Lead-Halide Perovskites for Photocatalytic alpha-Alkylation of Aldehydes, *J. Am. Chem. Soc.*, 141 (2019) 733-738.
- [6] X. Zhu, Y. Lin, J. San Martin, Y. Sun, D. Zhu, Y. Yan, Lead halide perovskites for photocatalytic organic synthesis, *Nat. Commun.*, 10 (2019) 2843.
- [7] H. Huang, H. Yuan, K.P.F. Janssen, G. Solís-Fernández, Y. Wang, C.Y.X. Tan, D. Jonckheere, E. Debroye, J. Long, J. Hendrix, J. Hofkens, J.A. Steele, M.B.J. Roeffaers, Efficient and Selective Photocatalytic Oxidation of Benzylic Alcohols with Hybrid Organic–Inorganic Perovskite Materials, *ACS Energy Lett.*, 3 (2018) 755-759.
- [8] W.-B. Wu, Y.-C. Wong, Z.-K. Tan, J. Wu, Photo-induced thiol coupling and C–H activation using nanocrystalline lead-halide perovskite catalysts, *Catal. Sci. Technol.*, 8 (2018) 4257-4263.
- [9] S. Schunemann, M. van Gastel, H. Tuysuz, A CsPbBr₃/TiO₂ Composite for Visible-Light-Driven Photocatalytic Benzyl Alcohol Oxidation, *ChemSusChem*, 11 (2018) 2057-2061.
- [10] L. Luo, Z.-j. Wang, X. Xiang, D. Yan, J. Ye, Selective Activation of Benzyl Alcohol Coupled with Photoelectrochemical Water Oxidation via a Radical Relay Strategy, *ACS Catal.*, 10 (2020) 4906-4913.
- [11] R. Zhang, M. Shao, Z. Li, F. Ning, M. Wei, D.G. Evans, X. Duan, Photoelectrochemical Catalysis toward Selective Anaerobic Oxidation of Alcohols, *Chem. Eur. J.*, 23 (2017) 8142-8147.
- [12] L. Sun, B. Li, X. Chu, N. Sun, Y. Qu, X. Zhang, I. Khan, L. Bai, L. Jing, Synthesis of Si–O-Bridged g-C₃N₄/WO₃ 2D-Heterojunctional Nanocomposites as Efficient Photocatalysts for Aerobic Alcohol Oxidation and Mechanism Insight, *ACS Sustain. Chem. Eng.*, 7 (2019) 9916-9927.
- [13] D. Tsukamoto, M. Ikeda, Y. Shiraishi, T. Hara, N. Ichikuni, S. Tanaka, T. Hirai, Selective Photocatalytic Oxidation of Alcohols to Aldehydes in Water by TiO₂ Partially Coated with WO₃, *Chem. Eur. J.*, 17 (2011) 9816-9824.

- [14] X. Li, J. Wang, Y. Men, Z. Bian, TiO₂ mesocrystal with exposed (001) facets and CdS quantum dots as an active visible photocatalyst for selective oxidation reactions, *Appl. Catal. B: Environ.*, 187 (2016) 115-121.
- [15] H. Li, F. Qin, Z. Yang, X. Cui, J. Wang, L. Zhang, New Reaction Pathway Induced by Plasmon for Selective Benzyl Alcohol Oxidation on BiOCl Possessing Oxygen Vacancies, *J. Am. Chem. Soc.*, 139 (2017) 3513-3521.
- [16] C.A. Unsworth, B. Coulson, V. Chechik, R.E. Douthwaite, Aerobic oxidation of benzyl alcohols to benzaldehydes using monoclinic bismuth vanadate nanoparticles under visible light irradiation: Photocatalysis selectivity and inhibition, *J. Catal.*, 354 (2017) 152-159.
- [17] X. Sun, X. Luo, X. Zhang, J. Xie, S. Jin, H. Wang, X. Zheng, X. Wu, Y. Xie, Enhanced Superoxide Generation on Defective Surfaces for Selective Photooxidation, *J. Am. Chem. Soc.*, 141 (2019) 3797-3801.
- [18] Z. Chen, J. Wang, G. Zhai, W. An, Y. Men, Hierarchical yolk-shell WO₃ microspheres with highly enhanced photoactivity for selective alcohol oxidations, *Appl. Catal. B: Environ.* 218 (2017) 825-832.
- [19] J. Luo, H. Yang, Z. Liu, F. Li, S. Liu, J. Ma, B. Liu, Organic-inorganic hybrid perovskite–TiO₂ nanorod arrays for efficient and stable photoelectrochemical hydrogen evolution from HI splitting, *Mater. Today Chem.*, 12 (2019) 1-6.
- [20] S. Roy, G.G. Botte, Perovskite solar cell for photocatalytic water splitting with a TiO₂/Co-doped hematite electron transport bilayer, *RSC Adv.*, 8 (2018) 5388-5394.
- [21] S. Xiao, C. Hu, H. Lin, X. Meng, Y. Bai, T. Zhang, Y. Yang, Y. Qu, K. Yan, J. Xu, Integration of inverse nanocone array based bismuth vanadate photoanodes and bandgap-tunable perovskite solar cells for efficient self-powered solar water splitting, *J. Mater. Chem. A*, 5 (2017) 19091-19097.

Chapter 5. Conclusion and outlook

Besides the traditional photovoltaic applications, MHPs semiconductors have shown great potential in photocatalysis. The past few years have witnessed the rapid development of MHPs for photocatalytic solar-to-chemical conversion, but the inefficient charge separation of MHPs limits their photocatalytic performance. Besides, the poor stability of MHPs is considered the main bottleneck for practical applications. Further development needs to address these two issues.

In this thesis, we have developed some efficient strategies to improve both the photocatalytic activity and stability of the MHP photocatalysts. Firstly, by the design of a Pd/CsPbBr₃ Schottky junction, photocatalytic performance of Suzuki couplings over Pd/CsPbBr₃ composite is improved by over 11 folds compared to pure CsPbBr₃. Besides, the photo- and thermal- catalysis contribution to the overall performance was investigated, and the mechanism of the photocatalytic Suzuki reaction was clarified. Secondly, following a similar concept, a phase-engineered crystalline-amorphous Pd (APd) cocatalyst was developed to further improve the photocatalytic performance of Cs₃Bi₂B₉ for simultaneous H₂ evolution and BAD production. The effect of the APd cocatalyst on the photoactivity improvement, i.e., the charge separation dynamics and surface reaction kinetics, were experimentally and theoretically investigated. Finally, to simultaneously boost the photoactivity and stability of the MHPs, a planar heterojunction photocatalyst cell, NiO_x/CsPbBr₃/TiO₂, was constructed. The inorganic electron extracting layer (TiO₂) and hole extracting layer (NiO_x) were employed to not only facilitate the charge separation but also serves as MHP protecting layers.

In practical applications, the MHP photocatalyst not only requires high solar-to-chemical conversion efficiency to maximize economic benefits, but also needs to possess good stability to ensure long-term use. Overall, this PhD thesis has developed some useful approaches to improve the photocatalytic performance and stability of MHP-based photocatalysts. Based on and beyond this thesis, more possible strategies that can be taken into consideration are summarized as follows.

First, to suppress the charge carrier recombination of MHPs and thus improving the photocatalytic performance, the following proven or potential approaches can be considered. (1) The formation of a Schottky junction by loading cocatalysts. The decoration of cocatalysts on the surface of MHPs, such as Pd, Au, and Pt, can facilitate the interfacial charge transfer and promote charge separation of MHP photocatalysts, and ultimately boost the photocatalytic performance. (2) Construction of a heterojunction. Constructing heterojunctions by coupling other semiconductor materials with MHPs is another efficient approach. So far, type-II and Z-scheme heterojunctions are the most adopted approaches. Efficient charge transfer and separation can be achieved, thus contributing to higher catalytic activities. Many materials such as GO, rGO, TiO₂, g-C₃N₄, Fe₂O₃ and Bi₂WO₆, have been employed to form type-II or Z-scheme system.

Besides, several proven or promising methods can be adopted to improve the stability of MHPs. (1) Using low-polarity or nonpolar solvents such as toluene, ethyl acetate, hexane, isopropanol and dichloromethane, to create a stable photocatalytic reaction environment. (2) Suitable compositions and reengineering of the MHPs. For instance, replacing the organic cations (MA⁺, FA⁺) with inorganic Cs⁺ ion has been widely adopted. Furthermore, surface treatments with ligands are also reported to stabilize the MHPs photoactive materials. (3) Surface passivation, such as the surface passivation of CsPbBr₃ by g-C₃N₄ through the interaction between the amino group on the edges of heptazine in g-C₃N₄ and Br⁻ in CsPbBr₃, or the interaction between functional group (fluorophenyl, halide, etc.) in graphene oxide and Pb defects, has also been demonstrated as feasible approaches. (4) The precipitation-solubility approach was found to keep the MHP stable under photocatalytic environments. (5) The addition of drying agents (anhydrous Na₂SO₄) to absorb the water existed in the photocatalytic reaction process is an effective method. (6) The encapsulation of MHPs by forming a core-shell structure (core: MHP, shell: TiO₂, MOF, etc.) is a straightforward way to stabilize MHPs. Compared to surface passivation with functionalized group semiconductors, the core-shell structure has a better stability. This is attribute to the fact that the core-shell structure with near-perfect coverage that helps to limit contact between the MHPs and

polar products. (7) The construction of a planar heterojunction. Using inorganic materials to cover the MHPs layer and protect the MHPs from decomposition. In summary, although the number of remaining challenges, expanding the applications of MHPs in photocatalytic reactions such as CO₂ reduction, H₂ evolution, organic transformation, pollutant degradation and N₂ fixation, is promising. By applying the strategies acquired in this dissertation work together with other reported approaches, taking the acceleration of charge separation and improving the stability of the MHP photocatalyst into account, the use of MHP for solar-to-chemical conversion is expected to contribute to solving the energy crisis and environmental issues.

Safety Aspects

All the experimental work presented in this dissertation was conducted compliant with the Code of Practice for Safety in Lab¹ and Basic Rules For Chemistry Practicals.² Before the experiments, risk assessments were taken following the detailed information on the website of the Health, Safety, and Environment (HSE) service.³ More specifically, the chemicals used in this thesis were handled with necessary care (lab coat, safety goggles, and gloves) considering that they are harmful or fatal in case of skin irritation in contact with skin, swallowing or if inhaled (H310, H312, H330, H331). Pb, Ni, and Pd salts were manipulated correctly since they are most of them are toxic or teratogenic (H361d, H360D, H361f, H360F, H361fd, H360FD, H360Df, H360Fd), and they may cause organ damage or cancer if long-term exposure to these compounds (H371, H372, H370, H350, H350i). When using high risk (E4) products and some solvents (toluene, DMSO, acetonitrile), more caution was taken since they are extremely flammable (H220, H222, H224, H225) and may cause organ damage (H332, H373), skin irritation (H311) and eye damage (EUH070).

1. <https://admin.kuleuven.be/sab/vgm/kuleuven/risicoactiviteiten/cv/cglp>.
2. <https://admin.kuleuven.be/sab/vgm/kuleuven/en/riskactivities/cs/basic-rules-forchemistry-practicals>.
3. <https://admin.kuleuven.be/sab/vgm/kuleuven/en>.

List of publications

1. **C.H. Wang**, H.W. Huang,* B. Weng, D. Verhaeghe, M. Keshavarz, H.D. Jin, B. Liu, H.P. Xie, Y. Ding, Y.J. Gao, H. F. Yuan, J. A. Steele, J. Hofkens,* M. B. J. Roeffaers,* Planar Heterojunction Boosts Solar-Driven Photocatalytic Performance and Stability of Halide Perovskite Solar Photocatalyst Cell, *Appl. Catal. B: Environ.* **2022**, 301, 120760.
2. **C.H. Wang**, B. Weng,* M. Keshavarz, M.Q. Yang, H.W. Huang, Y. Ding, F.L. Lai, I. Aslam, H.D. Jin, G. Romolini, B.L. Su, J. A. Steele, Johan Hofkens,* Maarten B. J. Roeffaers,* Photothermal Suzuki Coupling Over a Metal Halide Perovskite/Pd Nanocube Composite Catalyst, *ACS Appl. Mater. Interfaces*, **2022**, 14, 17185-17194.
3. **C.H. Wang**, B. Weng,* M.Q. Yang, B. Liu, M. Keshavarz, Y. Ding, H.W. Huang, B. L. Su, J. Hofkens,* M. B. J. Roeffaers,* Simultaneous photocatalytic H₂ generation and organic synthesis over crystalline-amorphous Pd nanocube decorated Cs₃Bi₂Br₉ composite, *Chem. Comm.*, Accepted.
4. **C.H. Wang**, B. Weng,* B. Liu, Y. Ding, H.W. Huang, J. Hofkens,* M. B. J. Roeffaers,* Effect of Structural Discrepancy of Lead-free Cs₃Bi₂Br₉ and Cs₃BiBr₆ Perovskites on Photocatalytic Performance. *In preparation*.
5. Y. Ding, **C.H. Wang (co-first author)**, B. Weng, J. Hofkens,* M. B. J. Roeffaers,* B. L. Su,* Metal Halide Perovskites Coupled with Defect and Morphology Engineered g-C₃N₄ for Efficient Photocatalytic C–H Bond Activation, *In preparation*.